**UNIVERSIDADE FEDERAL DA BAHIA**

**INSTITUTO DE QUÍMICA**

**PROGRAMA DE PÓS-GRADUAÇÃO EM QUÍMICA**

**Planejamento, síntese e estudo de novos cristais líquidos luminescentes derivados da triazina**

FABRÍCIA NUNES DA SILVA

SALVADOR - BA

2023

**FABRÍCIA NUNES DA SILVA**

**Planejamento, síntese e estudo de novos cristais líquidos luminescentes derivados da triazina**

Tese apresentada ao Programa de Pós-Graduação em Química, área de concentração Química Orgânica, Instituto de Química, Universidade Federal da Bahia, como requisito parcial para a obtenção do grau de Doutora em Química - Área: Química Orgânica.

**Orientador:** Prof. Dr. André Alexandre Vieira

SALVADOR - BA

2023

**TERMO DE APROVAÇÃO**

FABRICIA NUNES DA SILVA

**DESIGN, SÍNTESE E ESTUDO DE NOVOS CRISTAIS LÍQUIDOS LUMINESCENTES DERIVADOS DA TRIAZINA**

Tese aprovada como requisito parcial para obtenção do grau de Doutora em Química, Universidade Federal da Bahia, pela seguinte banca examinadora:

Prof. Dr. André Alexandre Vieira
Doutorado em Química, Universidade Federal de Santa Catarina (UFSC)
Universidade Federal da Bahia

Prof. Dr. Harald Bock
Doutorado em Química, Technische Universität Berlin (TUB)
Centre de Recherche Paul Pascal

Profa. Dra. Juliana Eccher
Doutorado em Física, Universidade de Santa Catarina (UFSC)
Universidade Federal de Santa Catarina

Profª. Drª. Vanessa do Nascimento
Doutorado em Química, Universidade Federal de Santa Catarina (UFSC)
Universidade Federal Fluminense

Profª. Drª. Hugo Alejandro Gallardo Olmedo
Doutorado em Química, Universidad de Concepción (UDEC)
Universidade Federal de Santa Catarina

Salvador, 06 de março de 2023.

Ficha catalográfica elaborada pela Biblioteca Universitária de Ciências e Tecnologias Prof. Omar Catunda, SIBI - UFBA.

*"Il faut bien que je supporte deux ou trois chenilles si je veux connaître les papillons."*

*Antoine de Saint-Exupéry*

*Le petit prince*

**THANKS**

To God, for life and for every moment lived in pursuit of my dreams. To my family for all the support, encouragement and affection throughout this journey. To Prof. Dr. André Alexandre Vieira for believing in me, giving me the opportunity to grow as a professional, for all the dedication and friendship. To Dr. Harald Bock, for his immeasurable patience and dedication. To my supervisors, thank you very much!

To my laboratory colleagues, Brazilian or French, for the moments lived together, whether good or bad, they were precious moments for my formation, my thanks for the knowledge shared and for all the times they gave me a little of their time to help me: Suellen, Eunice, Rebeca, Abad, Ludmilla, Fred, Luc and Hugo.

To my friends for their friendship and support, especially Jaqueline, Oscar, Daniel, Henrique, Amanda, Thaiane, Leonardo, Rayanne, Isabelle, for their affection and companionship along the way, thank you for being there for me whenever I needed a video call.

The Federal University of Santa Catarina, for the thermal and optical analyses. And to the friends I made there during my brief stay: Suely, Pri, Will, Gustavo, José, Andres, Renêr.

To the friends I made in France, they were important in this experience.

The doctoral jury of this work for having accepted to participate in the examination of this thesis and for the valuable contributions to its final redaction.

To CAPES and to Campus France for the scholarships.

And to everyone who contributed in some way to the construction of this work.

*Ao meu pai, sábio homem analfabeto,
que sempre zelou pela minha educação
moral e a todos que me encorajaram
nessa jornada, sem cada torcida a
caminhada teria sido mais difícil.*

## TITRE: CONCEPTION, SYNTHÈSE ET ÉTUDE DE NOUVEAUX CRISTAUX LIQUIDES LUMINESCENTS À BASE DE TRIAZINE

**RÉSUMÉ**: Dans ce travail, deux séries de molécules discoïdales ont été conçues, synthétisées et caractérisées, l'une symétrique et l'autre non symétrique, toutes deux dérivées de l'hétérocycle s-triazine. La méthodologie utilisée employait initialement la trimérisation des benzonitriles en milieu acide et ensuite la triphényltriazine était fonctionnalisée avec un, deux ou trois bras du type phénanthryle ou [4]hélicényle à partir de réactions de Perkin-Mallory. Les molécules finales ont été planifiées avec des groupes de type ester d'alkyle à chaîne courte pour induire les transitions vitreuses et également le mésomorphisme colonnaire. Tous les composés ont été largement caractérisés à partir de techniques spectroscopiques et spectrométriques. Les propriétés thermiques des molécules finales ont été étudiées par les techniques DSC, TGA, POM et XRD. Les esters de triazine symétriques substitués par des phénanthryles ou [4]hélicényles ont montré des transitions vitreuses convenablement au-dessus de la température ambiante et à l'intérieur de la phase cristalline-liquide colonnaire hexagonale, résultant en un ordre colonnaire solide à température ambiante. Des températures de clarification > 375°C ont été enregistrées pour les dérivés phénanthryles. Pour un alignement optimal d'um cristal liquide, il est important que les températures de fusion et de clarification soient atteignables, ce qui n'a été réalisé que pour les dérivés [4]hélicényles symétriques modérément non planaires (> 205°C). Pour contourner ce défi, une deuxième série de molécules non symétriques a été préparée à partir de la fonctionnalisation de la triphényltriazine avec un ou deux bras phénanthryle ou [4]hélicényle, mais en conservant le groupe benzoate de méthyle dans la structure. Les triazines non symétriques ont également montré un comportement de cristaux liquides colonnaires hexagonaux, mais avec des températures de clarification plus basses (< 290°C). Des transitions vitreuses ont également été observées à environ 70, 50, 40 et 0°C pour les composés non symétriques, em fonction du motif de substitution. Les propriétés photophysiques ont été évaluées pour les triazines symétriques en solution et en phase solide. Les matériaux ont montré une absorbance entre 272-342 nm et une émission entre 409-458 nm. Le rendement quantique moyen était de 22 % pour les dérivés phénanthryle et de 12% pour les dérivés [4]hélicényle. Les données photophysiques ont permis de déduire les énergies du premier état singulet excité S1 de 3,31 eV pour le phénanthryle et de 2,9eV pour l'hélicényle. Les calculs DFT ont montré une bonne corrélation entre les valeurs d'énergie expérimentales et calculées pour S1 et ont permis une bonne estimation pour T1. Les valeurs calculées pour l'orbitale T1 des triazines symétriques sont proches de 2,5 eV. Par conséquent, ces matériaux peuvent être considérés comme des matrices pour les émetteurs TADF qui émettent de la lumière dans la gamme vert-jaune du spectre visible.

**Mots clés**: cristaux liquides, triazine, matrices anisotropes, transition vitreuse.

# TITLE: DESIGN, SYNTHESIS AND STUDY OF NEW LUMINESCENT LIQUID CRYSTALS TRIAZINE-BASED

**ABSTRACT**: In this work, two series of discoidal molecules were designed, synthesized and characterized, one symmetric and the other non-symmetric, both derived from the heterocycle s-triazine. The methodology used employed initially the trimerization of benzonitriles in acidic medium and subsequently the triphenyltriazine was functionalized with one, two or three arms of the phenanthryl or [4]helicenyl type from Perkin-Mallory reactions. The final molecules were planned with short-chain alkyl ester-type groups to induce the glassy transitions and also columnar mesomorphism. All compounds were extensively characterised from spectroscopic and spectrometric techniques. The thermal properties of the final molecules were investigated by DSC, TGA, MOLP and XRD techniques. The symmetric triazine esters substituted with phenanthryl and helicenyl showed glassy transitions conveniently above room temperature and within the hexagonal columnar liquid crystal phase, resulting in a solid columnar order at room temperature. Cleavage temperatures > 375°C were recorded for the phenanthryl derivatives. For optimal alignment of a liquid crystal it is important that the melting and clearing temperatures are achievable, which was achieved only for the moderately non-planar (> 205°C) symmetric helicenyl derivatives. To circumvent this challenge, a second series of non-symmetric molecules was prepared from the functionalisation of triphenyltriazine with one or two phenanthryl or helicenyl arms, but retaining the methyl benzoate group in the structure. The non-symmetric triazines also showed hexagonal columnar liquid-crystalline behaviour, but with lower clearing temperatures (< 290°C). Glass transitions were also observed at approximately 70, 50, 40 and 0°C for the non-symmetric compounds, depending on the substitution pattern. The photophysical properties were evaluated for the symmetric triazines in solution and solid phase. The materials showed absorbance between 272-342 nm and emission between 409-458 nm. The average quantum yield was 22% for phenanthryl derivatives and 12% for helicenyl. From the photophysical data it was possible to infer the energies of the first excited singlet state S1 of 3.31 eV for phenanthrene and 2.95 eV for helicenyl. DFT calculations showed good correlation between the experimental and calculated energy values for S1 and allowed a good estimate for T1. The calculated values for the T1 orbital of the symmetric triazines are close to 2.5 eV, therefore, these materials can be considered as arrays for TADF emitters that emit light in the green-yellow range of the visible spectrum.


**KEYWORDS**: Liquid crystals, Triazine, Anisotropic matrices, Glass transition.

# TÍTULO: PLANEJAMENTO, SÍNTESE E ESTUDO DE NOVOS CRISTAIS LÍQUIDOS LUMINESCENTES DERIVADOS DA TRIAZINA

**RESUMO**: Nesse trabalho, foram projetadas, sintetizadas e caracterizadas duas séries de moléculas discóticas, uma série simétrica e a outra não simétrica, ambas derivadas do heterociclo *s*-triazina. A metodologia utilizada empregou inicialmente a trimerização de benzonitrilas em meio ácido e posteriormente a trifeniltriazina foi funcionalizada com um, dois ou três braços do tipo fenantril ou [4]helicenil a partir de reações de Perkin-Mallory. As moléculas finais foram planejadas com grupamentos do tipo éster de cadeia alquílica curta para induzir as transições vítreas e também o mesomorfismo colunar. Todos os compostos foram amplamente caracterizados a partir de técnicas espectroscópicas e espectrométricas. As propriedades térmicas das moléculas finais foram investigadas por técnicas de DSC, TGA, MOLP e XRD. Os ésteres de triazina simétricos substituídos por fenantrila e helicenila mostraram transições vítreas convenientemente acima da temperatura ambiente e dentro da fase cristal líquido colunar hexagonal, resultando em uma ordem colunar sólida à temperatura ambiente. Temperaturas de clareamento > 375°C foram registradas para os derivados de fenantrila. Para o alinhamento ideal de um cristal líquido é importante que as temperaturas de fusão e clareamento sejam atingíveis, o que foi alcançado apenas para os derivados simétricos de helicenila (> 205°C) moderadamente não planares. Para contornar esse desafio, uma segunda série de moléculas não simétricas foi preparada a partir da funcionalização da trifeniltriazina com um ou dois braços fenantrila ou helicenila, mas mantendo o grupo benzoato de metila na estrutura. As triazinas não simétricas também apresentaram comportamento líquido-cristalino colunar hexagonal, mas com temperaturas de clareamento inferiores (< 290°C). Transições vítreas também foram observadas em aproximadamente 70, 50, 40 e 0°C para os compostos não simétricos, dependendo do padrão de substituição. As propriedades fotofísicas foram avaliadas para as triazinas simétricas em solução e fase sólida. Os materiais apresentaram absorbância entre 272-342 nm e emissão entre 409-458 nm. O rendimento quântico médio foi de 22% para derivados de fenantrila e 12% para helicenila. A partir dos dados fotofísicos foi possível inferir as energias do primeiro estado singleto excitado S1 de 3,31 eV para fenantrenos e de 2,95 eV para helicenos. Cálculos de DFT mostraram boa correlação entre os valores de energia experimentais e calculados para S1 e permitiram uma boa estimativa para T1. Os valores calculados para o orbital T1 das triazinas simétricas são próximos de 2,5 eV, portanto, esses materiais podem ser considerados como matrizes para emissores TADF que emitem luz na faixa verde-amarelo do espectro visível.

# LIST OF ABBREVIATIONS

Å – Ångström

$\delta$ – Chemical shift

$\lambda$ – Wavelength

LCs – Liquid crystals

CLCs – Columnar liquid crystals

DLCs – Discotic liquid crystals

Col – Columnar mesophase

$Col_{hex}$ – Hexagonal columnar mesophase

$Col_r$ – Rectangular columnar mesophase

$Col_{ob}$ - Oblique columnar mesophase

d – Doublet

dd – Double doublet

HOMO – Highest occupied molecular orbital

LUMO – Lowest unoccupied molecular orbital

m – Multiplet

OFETs –Organic field effect transistors

OLEDs –Organic light emitting diodes

OSCs –Organic solar cells

ppm – parts per million

q – Quartet

s – Singlet

t – Triplet

SmA - smectic A mesophase

SmC - smectic C mesophase

Tg- glass transition temperature

$S_0$- fundamental state

S1- first excited singlet state

T1- first excited triplet state

IC- internal conversion

SOC- spin-orbit coupling

ISC- intersystem crossing

RISC- Reverse Intersystem Crossing

TADF- Thermally Activated Delayed Fluorescence

TTA- triplet-triplet annihilation

PLQY- photoluminescence quantum yield

IQE- Internal quantum efficiency

TDM- transition dipolar moment

PAH- Polycyclic aromatic hydrocarbons

DBU-1,8- diazabicyclo[5.4.0]undec-7-ene

DHP- dihydrophenanthrene

THF- tetrahydrofuran

DFT- density functional theory

$J$- coupling constant

Hz- Hertz

**LIST OF FIGURES**

**LIST OF SCHEMES**

**LIST OF TABLES**

**SUMMARY**

## 1. INTRODUCTION

The research and development of novel organic light emitting diodes (OLEDs) have attracted considerable interest and made significant progress over the past two decades (Li et al., 2017). This effort has intensified further since the first report of thermally activated delayed fluorescence (TADF) applied to OLEDs in 2006 (Wong et al., 2017; Wang et al., 2020). However, only in 2011 were the first purely organic TADF emitters applied to OLEDs reported (Endo et al., 2011). Since then, publications on this topic have increased exponentially.

Recently, besides the structure and behavior of the TADF luminogen itself, other factors are being taken into consideration for designing more efficient OLEDs. There are efforts to find matrices that induce horizontal alignment in the emissive layer of the device, as this type of emission minimizes efficiency losses by light trapping by the device cavities. In this perspective, glassy matrices made of strongly anisotropic polyaromatic molecules, already widespread in organic electronics, are of particular interest, because the use of the glassy state circumvents electrical and optical problems related to grain boundaries and similar inhomogeneities (Tenopala-Carmona et al., 2021).

Liquid crystals (LC) are organic materials that combine fluidity with molecular alignment, are of interest in a vast number of research topics and have attracted the interest of the scientific community for more than a century. In particular, liquid crystals with light emitting properties are of great interest in the development of multifunctional molecular materials. Hexagonal columnar liquid crystals have stood out as a new type of organic semiconductors for organic electronics, and they tend to align homeotropically with respect to surfaces, favoring an emitter orientation with preferential emission perpendicular to the device plane (Wöhrle et al., 2016). Glassy liquid crystals are rare and provide the possibility to incorporate emitter materials in an oriented anisotropic solid, improving the efficiency of light emitting devices.

To obtain such multifunctional materials, the design of new molecules with the aid of theoretical chemistry and new synthetic methodologies is necessary. Thus, the structural improvement of already known molecules as well as the search for new systems that possess both semiconductor and liquid crystal properties in order to improve the

performance and efficiency of optoelectronic devices is a productive area within materials science.

## 1.2 Liquid Crystals

The liquid crystalline state is a condensed state that combines the anisotropic properties of a crystalline solid with a certain degree of fluidity (Kotian et al., 2020; Sagara et al., 2009; Wöhrle et al., 2016). LCs are classified as complex fluids, a category in which different types of fluids with self-organizing properties, such as organogels, are found (Bechtold, 2005). Many liquid crystals show phase transitions under external stimuli such as light, electric fields, and mechanical shear. These LC phase transitions are characterized by a change of the self-assembled structure (Kelly &O'Neil, 2001).

The formation of liquid crystalline phases, also called mesophases, can be explained by the anisotropic structure of the molecules, always having one or two of their axes more elongated than the other(s) (An et al., 2016; Kotian et al., 2020; Wöhrle et al., 2016) (**Figure 1**).

Figure 1. a) Schematic representation of rod-type anisometry: the molecule is much more elongated along the **a** axis than along the **b** and **c** axes; b) Schematic representation of disc-type anisometry: the molecule is much shorter along the **b** axis than along **a** and **c**.
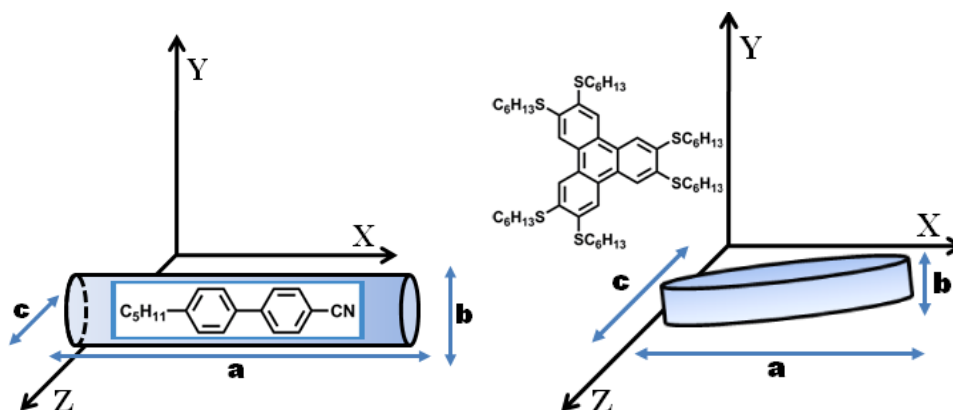


Source: Author

Liquid crystals exhibit some degree of molecular alignment that is between the long-range three-dimensional order of a crystalline solid and the short-range diffuse packing of the molecules in an isotropic liquid (Andrienko, 2018; Laschat, 2009; Pestov & Vill, 2018). A representative scheme of the molecular arrangements in crystalline solids, liquid crystals, and in the isotropic liquid is shown in **Figure 2**.

Figure 2. Schematic representation of molecular organizations in crystal, liquid crystal and isotropic liquid phases as a function of temperature.
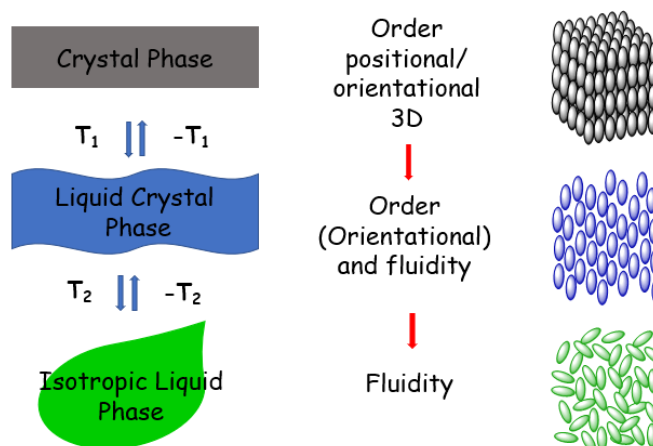


Source: Wöhrle, 2016

## 1.3 Classification of Liquid Crystals

Basically, there are two types of liquid crystals (LCs), the more common temperature-dependent thermotropic ones and the solvent/concentration-dependent lyotropic ones in certain colloidal solutions.

### 1.3.1. Lyotropic liquid crystals

Lyotropic liquid crystals have as their main characteristic the ability to induce mesophases according to solvent, concentration and temperature. In other words, in lyotropic liquid crystals, mesophases are formed by anisotropic molecules in an a priori isotropic solvent, often water. This phase is formed when amphiphilic molecules, with both hydrophilic and hydrophobic groups, are dissolved in a solvent forming aggregates of molecules. The concentration of amphiphilic molecules and the nature of the solvent directly interfere with the structure of the mesophase (Andrienko, 2018; Dierking, 2015;

Mueller-Goymann, 2002; Pestov & Vill, 2018). In **Figure 3** are shown representations of molecular arrangements in lyotropic liquid crystals.

Figure 3. Representation of the possible structural arrangements of amphiphilic compounds, forming more complex structures. a) Examples of amphiphilic molecules forming lyotropic mesophases; b) lamellar arrangement; c) micellar arrangement.
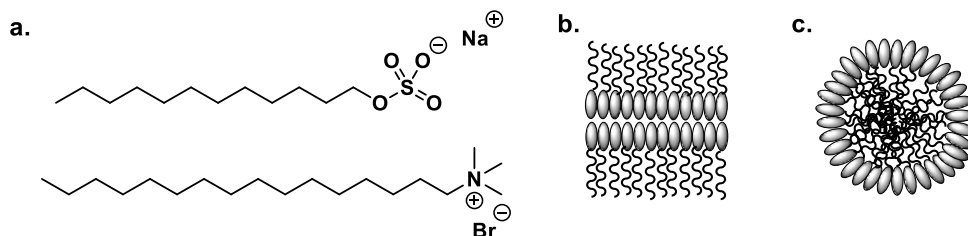


Source: Author

Lyotropic liquid crystals are vastly studied for biological applications, being employed for controlled drug release, cosmetics and soaps (Binot et al., 2018; Mueller-Goymann, 2002).

## 1.3.2. Thermotropic liquid crystals

Thermotropic liquid crystals have temperature as the dominant parameter for obtaining mesophases. They are made up of molecules that have strong anisotropy, and which are classified according to their anisometric shape, such as calamitic, discotic, banana, among others (Bhagavath et al., 2019; Wöhrle et al., 2016). The different

classifications depending both on the shape of the molecules and on the type of their arrangement are shown in **Figure 4** below.

Figure 4. Classification of thermotropic liquid crystals.
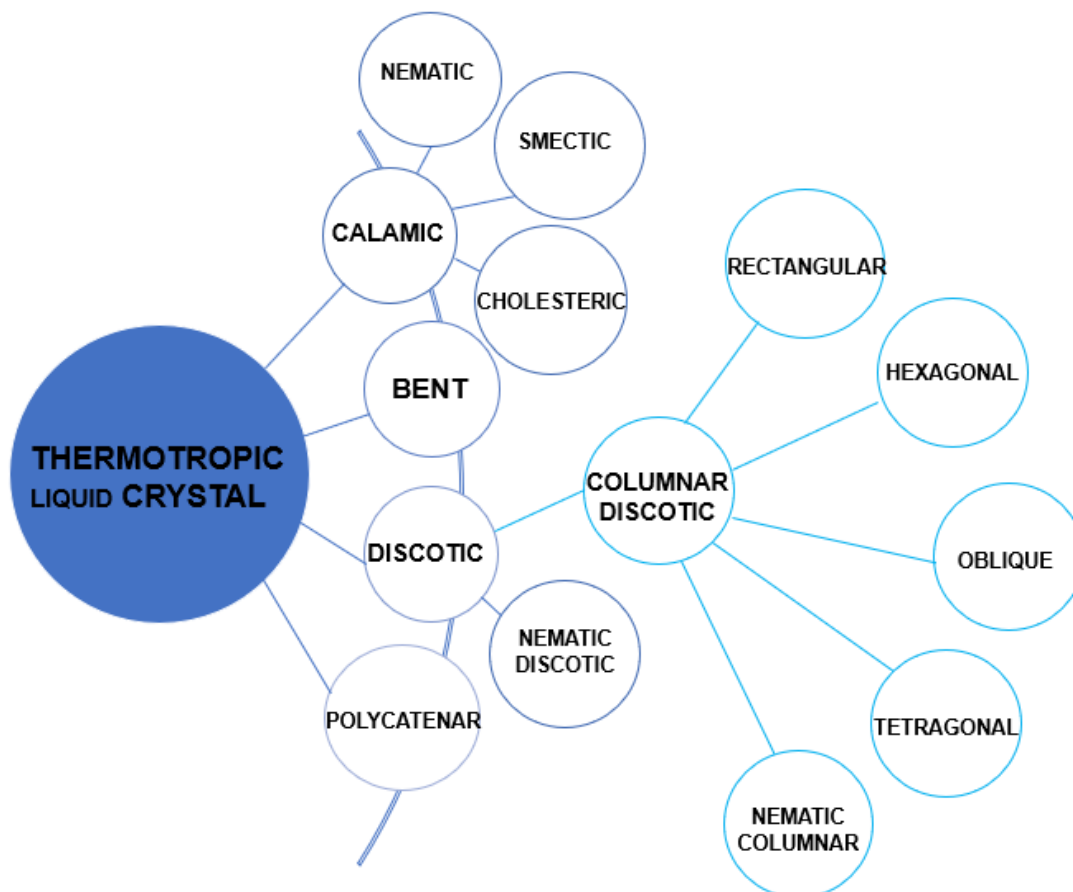
## 1.3.2.1. Calamitic thermotropic liquid crystals

Calamitic thermotropic liquid crystals are formed by elongated rod-like molecules (**Figure 5a**) (Ely et al., 2007). Many of these calamitic LC compounds contain heterocycles as central units, which may be of eg. of biomedical benefit (Silva et al., 2019). Calamitic LCs can be symmetric or non-symmetric, depending on the peripheral

groups connected to the core. In **Figure 5b**, there are examples of compound: symmetric (**5**) and non-symmetric (**6**) calamitic mesogens.

Figure 5. a) Schematic representation of the anisometry of a calamitic liquid-crystalline molecule: the molecular axis x is much more elongated than the y and z axes; b) Examples of liquid-crystalline calamitic compounds.
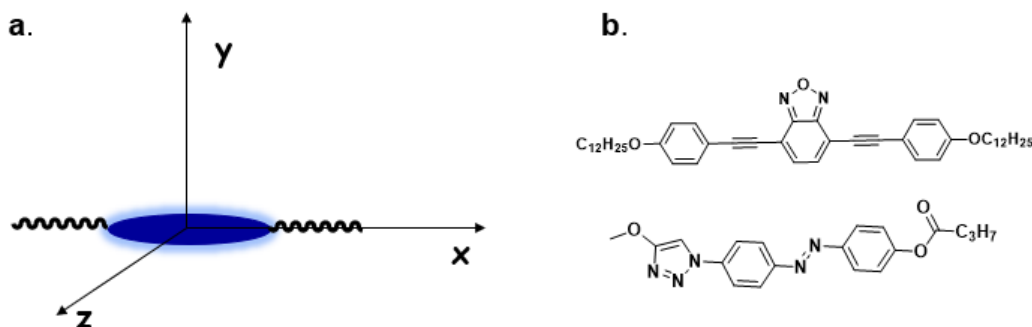


Source: Author

For calamitic mesogens the main types of mesophase observed are: nematic (**N**), cholesteric or chiral nematic (**N\***) and smectic (**Sm**).

In the nematic phase, the molecules are free to slide along each other, because there is no positional order of the centers of mass, but there is orientational order in the absence of positional order. The molecules orient themselves, on average, parallel to each other in a given preferential direction, which is associated with a unit vector **n**, called the director (**figure 6**). In systems with the presence of chirality, the nematic phase is called chiral nematic phase (**N\***) (Ely et al., 2007).

Figure 6. Schematic representation: a) nematic mesophase; b) isotropic liquid phase.
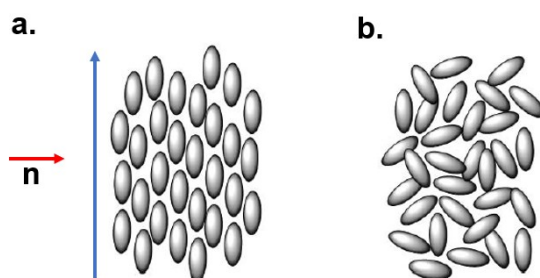


Source: Author

In the various smectic mesophases, the calamitic mesogens are more organized than in the nematic mesophase; there is a degree of positional as well as orientational order; a characteristic of these mesophases is the formation of layers. This layered organization leads to a lower fluidity, when compared to the nematic phase, and is closer

to the organization of the crystalline solid. Since the Van der Waals intermolecular forces between the layers are smaller than the lateral intermolecular forces between the molecules, the layers can slide over each other (Bechtold et al, 2005; Collings & Patel, 1997; Ely et al., 2007).

The most common smectic phases are smectic A (SmA) and smectic C (SmC). In the SmA mesophase the molecules are oriented parallel to the normal (i.e. the z axis), while in SmC the molecules are tilted. The molecules have freedom to move within the layers, but less freedom to move between the layers (Collings & Patel, 1997). **Figure 7** shows these two possible molecular organizations for calamitics.

Figure 7. Representations of the organization of the two main smectic mesophases.



SmA                           SmC
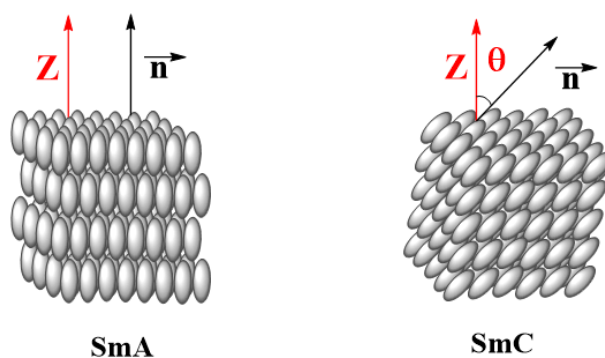
Source: Author

## 1.3.2.2. Thermotropic discotic liquid crystals

In 1977, Chandrasekhar identified some benzene hexa-alkanoates (**Figure 8a**) as the first discotic liquid crystals (Chandrasekhar et al., 1977). Following this discovery, several systems similar to this structure with a homo- or heteroaromatic central core linked to six aromatic or aliphatic substituents by different spacers were prepared and characterized. Thus, discotic liquid crystals typically consist of a rigid aromatic central

core and flexible side arms with two molecular axes longer than the third (x, z >> y) (S. Kumar, 2011; Wöhrle et al., 2016b; Yuvaraj et al., 2018), resembling a disc (**Figure 8b**).

Figure 8. a) Chemical structure of benzene hexa-alkanoates, the first discotic (columnar) LCs; b) Representation of the generic architecture of a discotic molecule.



a.

b.

$R= n\text{-}C_4H_9 \text{ or } n\text{-}C_9H_{19}$
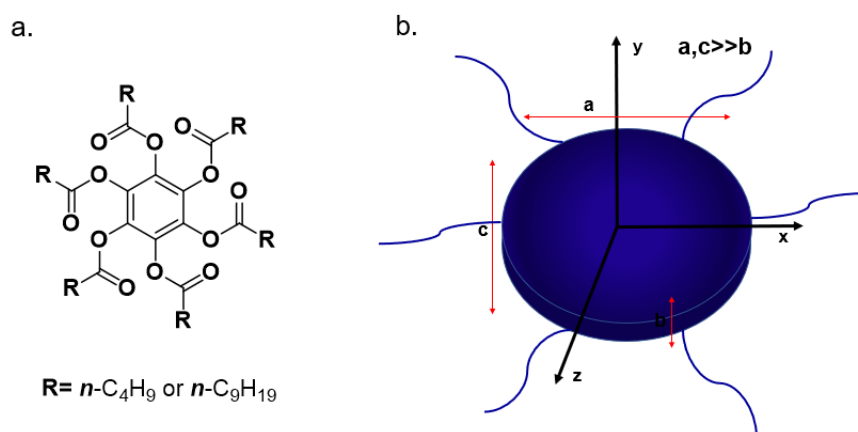
Source: Author

The way in which discotic liquid crystals self-organize as a function of their structures is key to distinguishing their mesophases. The stacking of these disk-like mesogens in 1D columns is common to most of these mesophases. The rigid, relatively flat nuclei organize themselves into columns. This is caused by steric packing and π-π interactions between the nuclei (Yasuda et al., 2011). The molecules within the columns exhibit only short-range positional order. The formation of a 3D crystal is hindered due to the high entropy and disorder of the flexible aliphatic chains at the periphery. Columnar stacking also leads to nanosegregation between the polarizable cores and the aliphatic tails (Wöhrle et al., 2016) (**Figure 9**).

Figure 9. Representation of the stacking of discotic mesogens made of several aromatic units and a multitude of aliphatic chains.
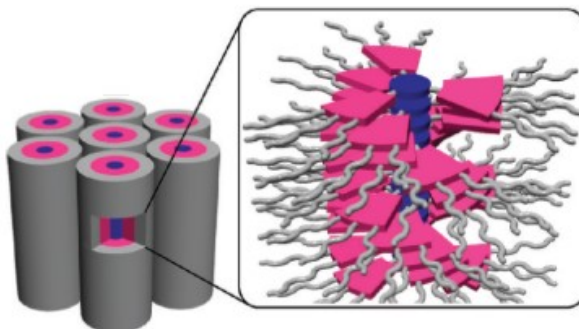


Source: Yasuda, 2011.

Different types of stacking can be found for (**Figure 10**): There are "disordered columns" with irregular stacking of the disks, "ordered columns" in which the cores are more equidistant but discs in adjacent columns still do not register with each other, as well as "tilted columns" with the cores tilted with respect to the column axis. These columns do not exhibit a true 3D order and therefore can be considered as 1D fluids (Wöhrle et al., 2016; Yasuda et al., 2011).

Figure 10. The different types of columnar stacking. a. ordered; b. disordered.
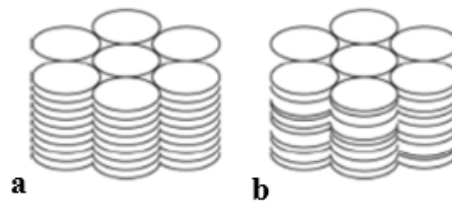
Discotic mesophases are classified into two types: nematic discotic and columnar discotic. In the columnar phase, positional order is present as the molecules themselves lie approximately on top of each other. Discotic mesogens tend to form columns, which are the building blocks of columnar phases, and discotic molecules forming nematic mesophase are rarer. In columnar mesophases, the columns are arranged in a 2D network with the axes of the columns parallel to each other. Columnar mesophases can have specific organizations, such as hexagonal ($Col_h$), oblique ($Col_{ob}$), and rectangular ($Col_r$) (**Figure 11**) (Bhagavath et al., 2019).

Figure 11. Representation of mesophases for discotic liquid crystals.
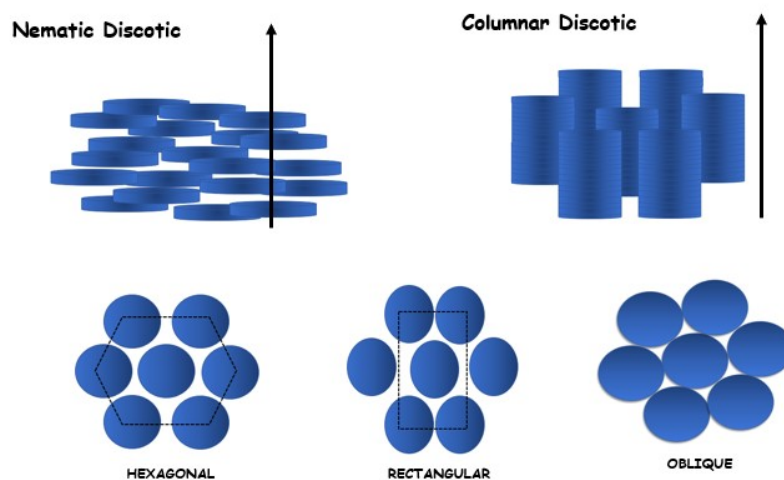
Columnar π-conjugated liquid crystals generated from discotic molecules feature an extensive intermolecular overlap of the π orbitals, resulting in uniaxial mobility of charge carriers and excitons along the columns (Bhagavath et al., 2019; Kumar, 2011; Wöhrle et al., 2016). They provide efficient hole and electron transport in electroluminescent and organic electronic devices (Yasuda et al., 2011) (**Figure 12**).

Figure 12. Schematic representation of a π-conjugated molecule and its self-assembled 1D conducting structure.
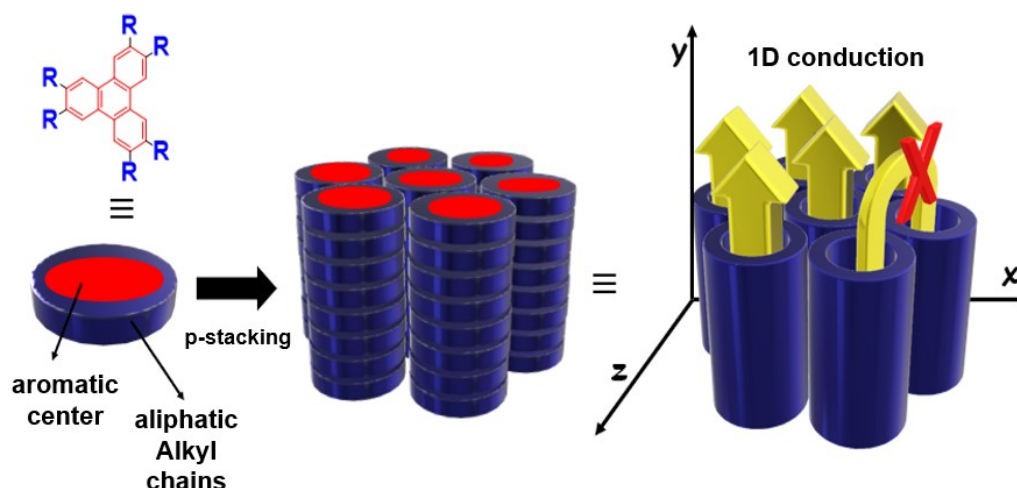


Source: Wöhrle, 2016.

The molecular design of discotic liquid crystals involves a flat rigid aromatic core and flexible peripheral arms that assist in creating columnar arrangements due to the microsegregation of these regions. Benzene and s-triazine are groups that can act as a central core, among which the s-triazine system is fascinating not only for its distinctive structural aspects, but also for its straightforward synthetic approaches. Moreover, the molecular architecture of these three-armed star-shaped mesogens arouses interest in the influence of incomplete space filling around the center. These tri-substituted systems can integrate multiple functional groups to sculpt the desired physical and chemical characteristics (Bhagavath et al., 2019; Pradhan et al., 2016; Taing et al., 2018).

## 1.4 Columnar liquid crystals and glass transitions

Glass dynamics relate to the glass transition temperature ($T_g$), which is an important phenomenon in soft materials science (Tenopala-Carmona et al., 2021). In general, the glass transition temperature $T_g$ in a non-crystalline solid is defined by a distinct inflection point in the change in specific volume as the temperature is varied. Due to the complexity in defining molecular packing in an amorphous network, the physics of glass transitions

remains imprecise. It is known that the glass transition is not a typical phase transition, as it does not involve abrupt changes in any observable physical properties (Debenedetti & Stillinger, 2001; H.-N. Yang & Lu, 2021). The formation of glassy states rather than crystals is favored by conformational multiplicity and the presence of viscosity-enhancing dipoles. This phenomenon in discotic liquid crystals is rarely observed (Yildirim et al., 2019). Detailed investigation of glass dynamics in anisotropic systems can help to understand the nature of the glass transition in general.

In Liquid crystalline glasses, the organization of liquid crystals is frozen without crystallization of the material, which consequently decreases its molecular mobility and modifies its conductivity (Wunderlich, 2007). This glassy mesophase can be considered as a solid, and thus robust, matrix capable of improving the optoelectronics of emitters, by intermolecular electronic influence and by orientation effects (Tenopala-Carmona et al., 2021).

Currently, the application of anisotropic glassy materials in the production of OLEDs is one of the basic strategies to control the orientation of organic emitters in vacuum processed films. These strategic procedures involve the optimization of molecular structures, the selection of host molecules with useful $T_g$ in co-evaporated systems, and the adjustment of substrate temperature during film deposition to modify the entropy and orientation of the glass (C. Liu et al., 2015; Tenopala-Carmona et al., 2021; Yokoyama, 2011a).

The higher the $T_g$, the less diffuse is the deposition of molecules onto the films. Therefore, materials that have higher $T_g$ may have better horizontal orientation of molecules in films (Tenopala-Carmona et al., 2021).

**1.5 Luminescence**

The phenomenon of photoluminescence has attracted human attention and curiosity since ancient times, however it was first described scientifically in 1852 by Stokes (Valeur & Berberan-Santos, 2013).

Luminescence according to IUPAC is the spontaneous emission of radiation from an electronically or vibrationally excited species in thermal disequilibrium with the environment. According to the method of excitation used, a different nomenclature is employed for the luminescent behavior, i.e. the type of luminescence can be classified

according to the excitation mode. **Table 1** shows the known excitation modes (Valeur & Berberan-Santos, 2013).

Table 1. Luminescence types and excitation modes.

| Type of Luminescence | Mode of excitation |
|---|---|
| Photoluminescence (fluorescence and phosphorescence) | Absorption of photons (light) |
| Radioluminescence | Radiation (X-rays, α, β, γ particles) |
| Cathodoluminescence | Electron beam |
| Electroluminescence | Electric field |
| Thermoluminescence | Heating |
| Chemiluminescence | Chemical reaction |
| Bioluminescence | Biochemical process (living organisms) |
| Triboluminescence | Friction and electrostatic forces |
| Sonoluminescence | Ultrasound |

Source: Valeur, 2013.

Photoluminescence is always preceded by the absorption of photons that causes an electron from a bonding orbital in the fundamental state to be excited generating an excited state. The return of the electron to the fundamental state can be accompanied by light emission which is called photoluminescence. Fluorescence, phosphorescence or delayed fluorescence are different types of this same phenomenon (Valeur & Berberan-Santos, 2013). Photoluminescence is only one of the possible pathways for relaxation of an excited species, as shown in **Figure 13**.

Figure 13. Possible pathways for relaxation of a molecule excited with photons.
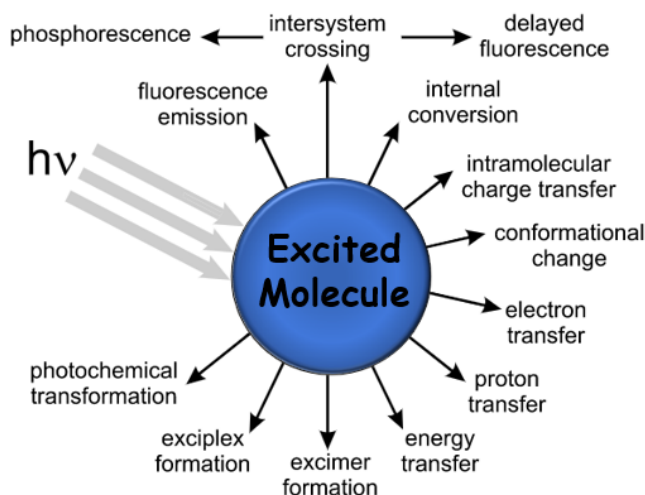


Source: Valeur, 2013.

Other relaxation pathways are possible, for example, a species can relax through the vibration of its bonds, thus returning to the fundamental state, but without light

emission. Relaxation can occur via a process called intersystem crossing between singlet and triplet excited states, which can result in phosphorescence and delayed fluorescence. Other relaxation pathways such as energy or charge transfer, and excimer or exciplex formation are associated with intermolecular interactions in the excited state.

Photoluminescence phenomena can be exemplified using the Perrin-Jablonski diagram (**Figure 14**), where $S_0$ symbolizes the fundamental state, $S_1$ the first excited singlet state, and $T_1$ the first excited triplet state (Z. Yang et al., 2017).

Figure 14. Jablonski's diagram.
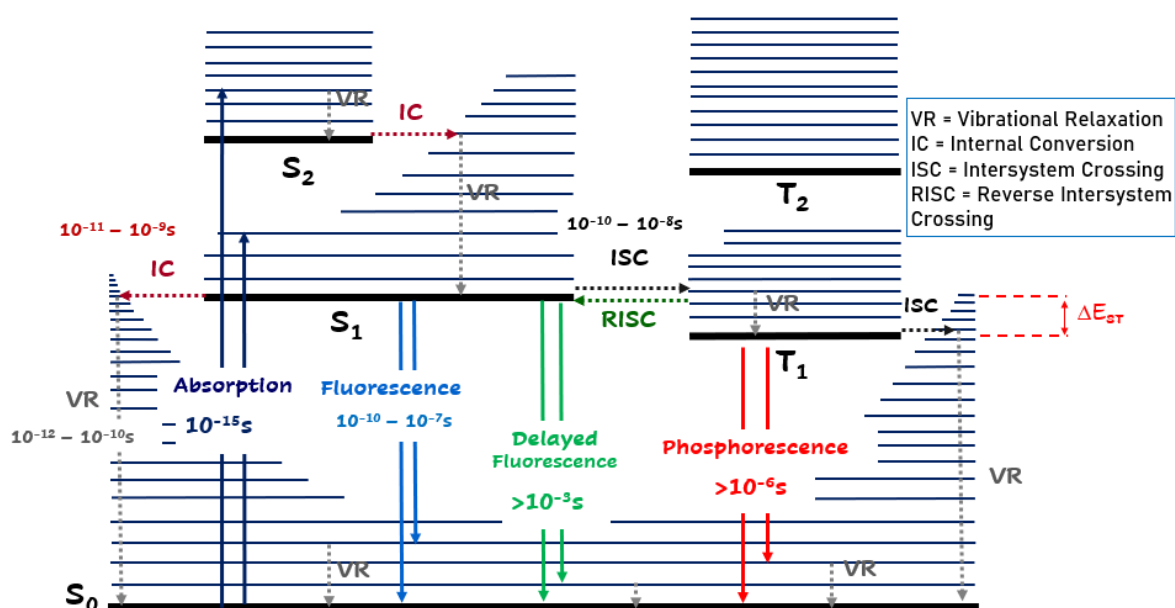


Source: Valeur, 2013.

The photoluminescence phenomenon occurs by fluorescence when by absorbing a photon of appropriate energy, a molecule can move from the fundamental state $S_0$ to one of the vibrational levels of the excited state of same multiplicity. Through a vibrational relaxation process, lasting $10^{-14}$ to $10^{-11}$ s, which does not involve the emission of radiation, the molecule is normally driven to the first vibrational level of the $S_1$ singlet state. Non-radiative transitions between states of the same multiplicity ($S_2{\rightarrow}S_1$ and $S_1{\rightarrow}S_0$) are called internal conversion (IC) and can occur as a result of vibrational energy transfer to other molecules, such as those in the solvent, through collisions. Since the transition is spin allowed, the lifetimes of the excited states in fluorescence processes are

small, on the order of $10^{-9}$ to $10^{-6}$ s (ns to µs) (Valeur & Berberan-Santos, 2013; Z. Yang et al., 2017).

A non-radiative electronic transition between excited states of different multiplicity ($S_1 \rightarrow T_1$), occurs when there is a possibility of spin-orbit coupling (SOC), allowing intersystem crossing (ISC). Thus, an electronic transition with changing spin multiplicity ($T_1 \rightarrow S_0$), of long duration ($10^{-6}$ to $10^2$ s), can occur, followed by photon emission, which characterizes phosphorescence. The emission band of phosphorescence is generally shifted to longer wavelengths (lower energy) relative to fluorescence because the $T_1$ state is of lower energy than $S_1$ (Valeur & Berberan-Santos, 2013; Z. Yang et al., 2017).

One of the characteristics of fluorescence is its short lifetime. However, in some molecules where the energies of $S_1$ and $T_1$ are close (small $\Delta E_{ST}$), another process occurs, this one with a longer lifetime, the delayed fluorescence. This phenomenon is essentially the process in which an absorbed photon is promoted to the $S_1$ state, then moves to the $T_1$ state, ($S_1 \rightarrow T_1$), through the process of intersystem crossing (ISC). Through some external excitation, the Reverse Intersystem Crossing (RISC) process is activated causing the $S_1$ state to be occupied again ($T_1 \rightarrow S_1$); and thus, a delayed photon decay occurs between ($S_1 \rightarrow S_0$) resulting in an increased fluorescence lifetime. For there to be a high probability of RISC (Reverse InterSystem Crossing), the energies of $T_1$ and $S_1$ must be very similar (Valeur & Berberan-Santos, 2013; Z. Yang et al., 2017).

IUPAC states that there are three types of delayed fluorescence: delayed fluorescence type (E), type (P), and recombination fluorescence.

The first type is E-type delayed fluorescence, in this phenomenon the RISC process is favored through a thermal activation (compounds with Thermally Activated Delayed Fluorescence (TADF)). In other words, the temperature allows the energy barrier of $\Delta E_{ST}$ to be compensated. The RISC internal quantum efficiency is theoretically 100% restricting the probability of the delayed E-type fluorescence being contaminated with phosphorescence. The second type of delayed fluorescence, P-type, on the other hand, unlike TADF, where the process occurs in individual molecules, implies an intermolecular collision in the triplet state (triplet-triplet annihilation (TTA)) giving rise to a molecule in the S1 state. This process has an internal quantum efficiency between 20% and 50%, and there is a higher probability of phosphorescence contamination. The

third delayed fluorescence mechanism is the population of the $S_1$ state through $T_1$ by recombination of ions and electrons and/or by recombination of oppositely charged ions (Hofbeck et al., 2015; Z. Yang et al., 2017).

## 1.6 Organic light-emitting diodes (OLEDs)

Organic light-emitting diodes (OLEDs) are solid-state electroluminescent device elements in which the light-emitting materials consist of organic, organometallic, dendrimer, or polymer molecules containing conjugated $\pi$-electron systems. OLEDs have been the subject of intense research since their discovery in 1987 by Tang and Van Slyke, as they signify an unprecedented advance in display and lighting technologies. Compared to existing liquid crystal displays (LCDs), OLEDs offer better image quality and contrast, faster response times, are visible at wider angles, and are thinner and lighter. In addition to the ability to fabricate these devices on flexible substrates, one of the most important features of OLEDs is energy efficiency (S. Wang et al., 2020b; Wong & Zysman-Colman, 2017a; Z. Yang et al., 2017; Yokoyama, 2011b).

To make OLEDs commercially viable for lighting applications, there are still some challenges to overcome, in addition to production cost reduction. OLEDs need to exhibit high photoluminescence quantum yields (PLQYs). The energy levels of the molecular frontier orbitals (HOMO-LUMO) of each of the layers in the device must be adjusted to: i) minimize the charge injection barrier, and ii) confine the recombination region within the device, which greatly affects both the efficiency and lifetime of the device. Thermal stability is another important point, these matrices must demonstrate sufficient thermal stability to be compatible with their deposition conditions to form the thin films (Tenopala-Carmona et al., 2021; Wong & Zysman-Colman, 2017b).

In addition to these problems, another issue to be addressed is the management of hole-electron recombination within the device. Unlike photoexcitation, in which mainly singlet excited states are produced in organic emitters, exciton formation through charge (hole and electron) recombination in OLED devices results in 25% singlets and 75% triplets (Z. Yang et al., 2017).

In the first generation OLEDs, the singlet state excitation leads to prompt fluorescence (**Figure 15a**) with short emission times (in the nanosecond range). Whereas

in the second generation of OLEDs, the phenomenon involved is phosphorescence (**Figure 15b**) with emission times extending to milliseconds due to the spin-forbidden nature of the emission. The very long emission lifetime makes the triplet excitons vulnerable to non-radiative deactivation. Devices based on organometallic complexes with nearly 100% IQE have been reported, since 2001 (Wong & Zysman-Colman, 2017).

Figure 15. Comparison of emission mechanisms in a) first-generation (prompt-fluorescent); b) second-generation (phosphorescent) OLEDs.
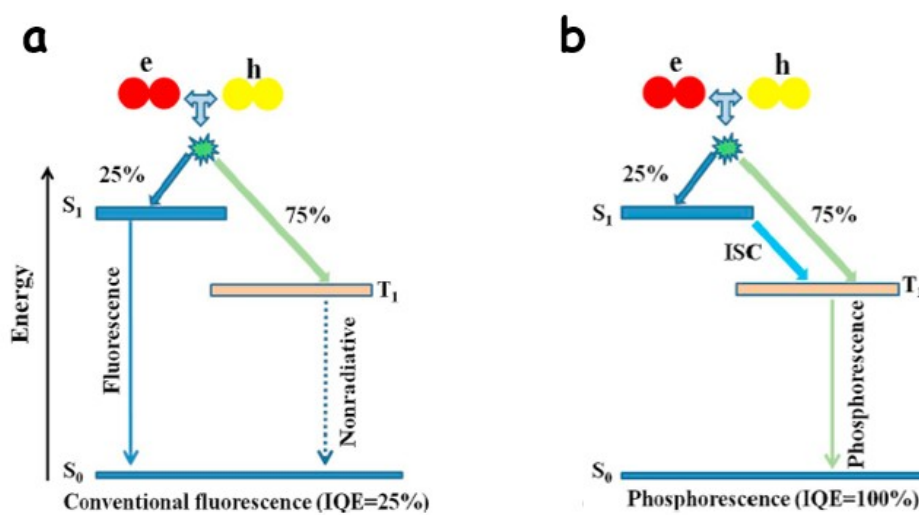


Source: Wang, 2020.

The point in using organometallic complexes as emitters is their ability to access triplet states via intersystem crossing (ISC) from the singlet excited state via a strong spin-orbit coupling (SOC) mediated by a heavy metal atom (iridium, platinum and other metals) in the complexes (Naveen et al., 2022; Wong & Zysman-Colman, 2017a).

Currently, commercialized displays rely on green and red emitting iridium complexes. The iridium metal is a low abundance element which ends up making the production of devices more expensive. Another relevant point is the inefficiency of blue-emitting complexes: so far, blue emitters continue to be the bottleneck of the OLED industry. Possible causes of this inefficiency in the blue include triplet polaron annihilation (TPA), resulting in highly energetic polarons that cause device degradation, and unstable radical cations in the complex, which cause complex dissociation or isomerization. Thus, achieving deep blue with stable emitters in OLEDs remains a challenge (Naveen et al., 2022; Wong & Zysman-Colman, 2017).

### 1.7 OLEDs and TADF

Emerging as an option for building efficient blue OLEDs, thermally activated delayed fluorescence (TADF) is the most promising mechanism for obtaining excitons in these devices. Since the first reported OLED based on an organic TADF emitter in 2011, tremendous attention has been devoted in recent years to improving its performance (**Figure 16**). Similar to phosphorescent organometallic emitters, purely organic TADF emitters can use emission from triplet excitons for light emission and thus can achieve 100% IQE. An important advantage of TADF emitters is that they can be purely organic, thus avoiding the problems associated with using metal-based organometallic complexes (Naveen et al., 2022; Wong & Zysman-Colman, 2017; Z. Yang et al., 2017). **Figure 16** below presents a brief summary of developments of TADF-based OLEDs.

Figure 16. Timeline of developments of TADF-based OLEDs.
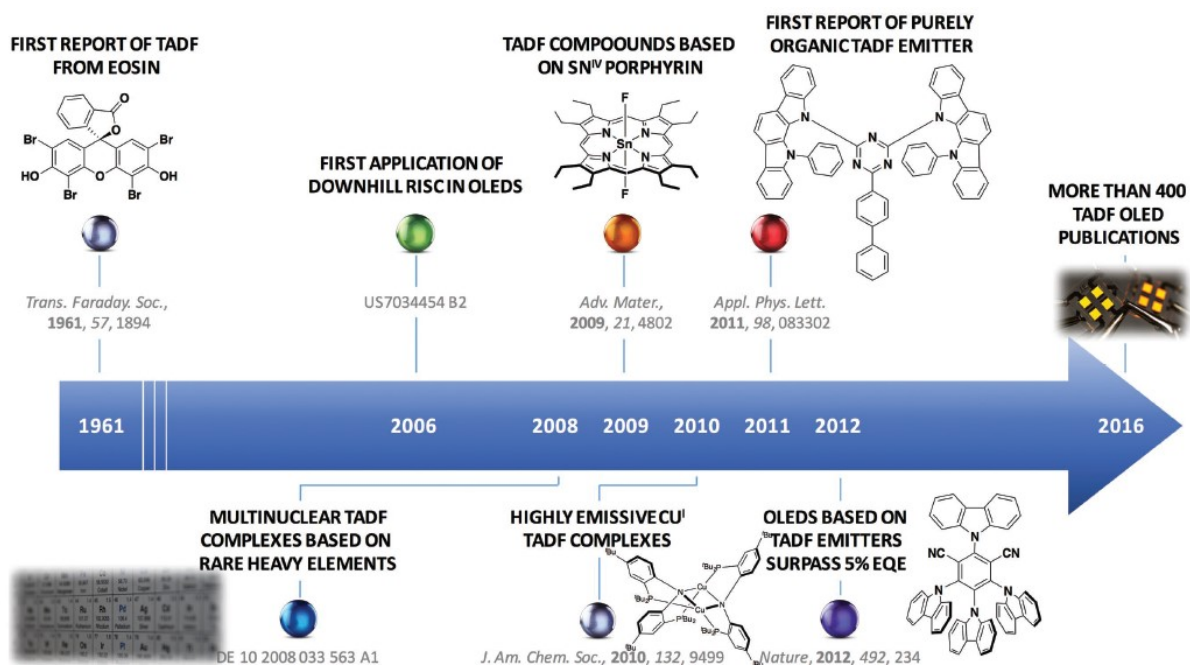


Source: Wong, 2017.

TADF relies on a small singlet-triplet energy gap, $\Delta E_{ST}$, defined as the gap between the lowest energy triplet state ($T_1$) and the lowest energy singlet state ($S_1$). When $\Delta E_{ST}$ is small enough, thermal conversion to from the triplet state to the singlet state by reverse intersystem crossing (RISC) becomes possible. TADF emitters typically show two types of photoluminescence: immediate fluorescence in which the singlet exciton pathway involves no communication with the triplet state, and delayed fluorescence, which is the

result of an initial ISC to the triplet state followed by repopulation of the singlet state via RISC (**Figure 17**).

Figure 17. Emission mechanism in third generation OLEDs.
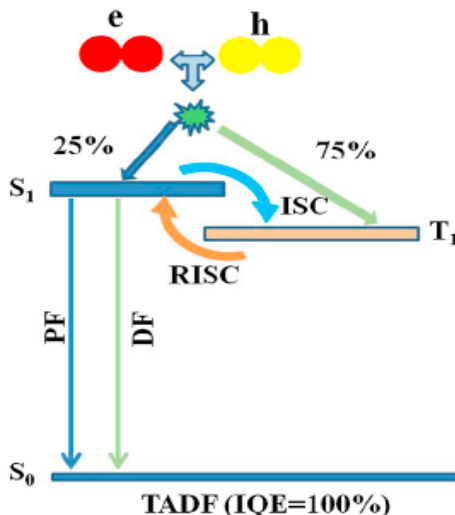


Source: Wang, 2020.

OLEDs have their emitter layer composed of a luminogen and a matrix to reduce self-quenching effects. When this emitting layer presents a randomly oriented state, the emission is isotropic, leading to a significant retention of emitted light in the device cavity. However, if the emissive transition dipolar moment (TDM) is oriented horizontally, this can improve the light coupling efficiency by up to 50% over random orientation, i.e. the emission is mainly perpendicular and light trapping is minimized, thus improving the energy performance of the device, as is detailed in **Figure 18**.

Figure 18. Examples of two structural schemes of OLEDs: with isotropic emitter layers and with anisotropic emitter layers.
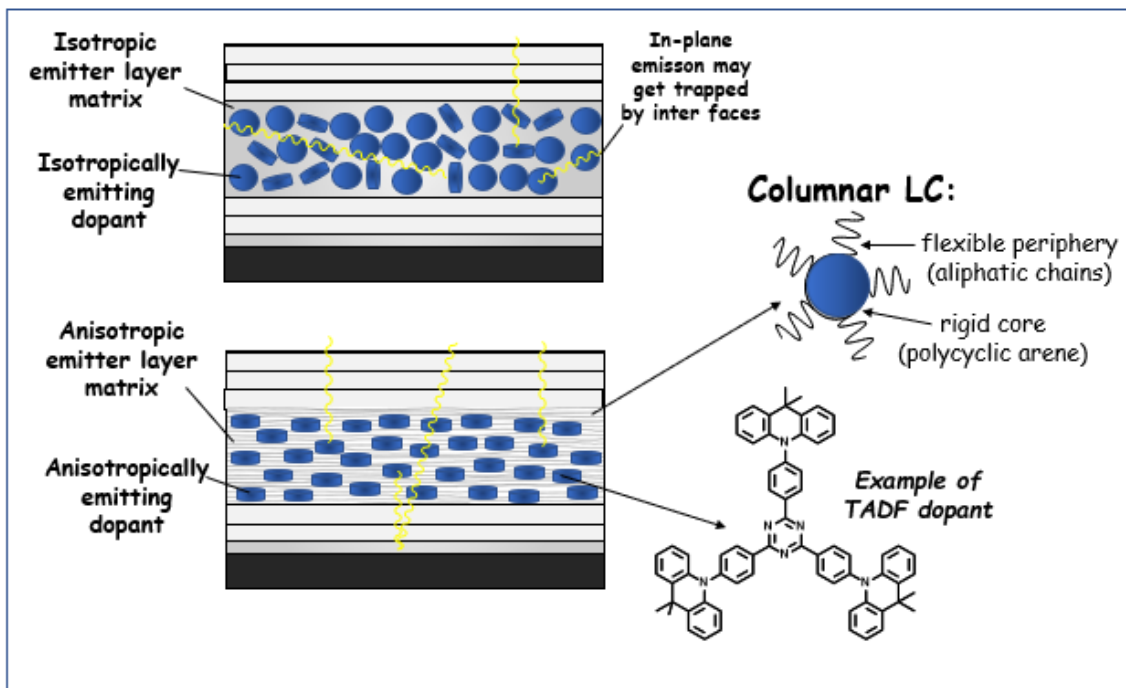


Source: Author.

Given the importance of these materials, there are currently great efforts to find arrays that perform this function of horizontal alignment in the emissive layer of the device. Some aspects have been studied such as the geometry of the emitting molecule and the glass transition temperature (Tg) of the films are currently considered important.

From this perspective, columnar liquid crystals that exhibit glass transitions emerge as promising materials as matrices for TADF OLEDs.

## 1.8 Triazines

The incorporation of nitrogen atoms into a π-conjugated nucleus allows the gap values between the HOMO and LUMO orbitals to change, and thus modulate optical, electrical properties, and intermolecular interactions (Bhagavath et al., 2019; Pradhan et al., 2016). The 1,3,5-triazine nucleus has a considerably higher electron affinity than other aromatic rings, thus being a unit of electron acceptor nature. Triazines are six-membered rings containing three nitrogen atoms and three carbon atoms (Glang et al., 2014; Kumar et al., 2014; Yasuda et al., 2011). The triazine isomers differ by the positions of their nitrogen atoms, and are described as 1,2,3-triazine (**1a**), 1,2,4-triazine (**1b**), and 1,3,5-triazine (**1c**), respectively (Bhagavath et al., 2019; R. Kumar et al., 2014) (**Figure 19**).

Figure 19. Structures of the triazine isomers.



|  |  |  |
|---|---|---|
| **1,2,3-triazine** | **1,2,4-triazine** | **1,3,5-triazine** |
| **or** | **or** | **or** |
| **v-triazine** | **a-triazine** | **s-triazine** |
| **(1a)** | **(1b)** | **(1c)** |
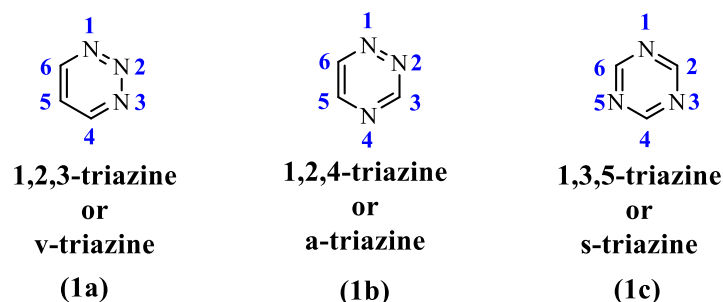
Among the triazine isomers, the 1,2,3-triazines are the least investigated because the system is considered the least stable and because their synthetic accessibility is limited and consequently, reports are scarce (Kumar et al., 2014). The chemistry of 1,2,4-triazine or a-triazine, on the other hand, has mainly focused on synthetic approaches for scaffold construction, i.e. molecules that serve as a support for the construction of others, as well as on their reactivity in hetero-Diels-Alder cycloaddition reactions. Regarding applications, 1,2,4-triazines have been studied mainly in the context of medicinal chemistry without a focus on the preparation of molecular materials such as polymers, dendrimers or liquid crystals (Zhang et al., 2018).

The use of 1,3,5-triazine in the field of functional molecular materials chemistry is mainly driven by three characteristics of s-triazine: its C3 symmetry, its electron-poor character, and its high thermal stability. The s-triazine core has the appropriate architecture to be employed in the synthesis of discotic liquid crystals: Due to the C3 symmetry, a star shape geometry is commonly obtained with s-triazine derivatives (Taing et al., 2018; Yasuda et al., 2011).

## 1.9 s-Triazines as the center of discotic liquid crystals

1,3,5-triazine has been intensively used in the field of materials, especially in the construction of organic devices such as OLEDs (Tan et al. 2020; Zassowski et al. 2018; Li et al. 2017). It has played this prominent role for structural reasons. It represents the electron deficient portion in the electron acceptor-type fluorescent emitters, with a relevant charge transport ability. Moreover, due to its threefold symmetry it has mainly stood out in reporting compounds capable of exhibiting hexagonal columnar liquid crystal

behavior when suitably extended with alkyl chain-bearing aryl substituents (Matulaitis et al., 2016; Mooibroek & Gamez, 2007).

The threefold symmetry present in this nucleus, a characteristic that favors the obtention of disk-shaped compounds, an ideal structure for columnar discotic liquid crystals, favors the self-organization into one-dimensional stacks of these derivatives, capable of electron and hole transport (Taing et al., 2018; Umar & Shamsuddin, 2018; Mooibroek & Gamez, 2007).

Recently new classes of nanostructured columnar liquid crystals based on 1,3,5-triazine with three symmetrically linked electron donor segments have been synthesized and studied (Yasuda, et al., 2011; Pradhan, et al., 2016) (**Figure 20**).

Figure 20. Compounds derived from s-triazine with liquid crystalline behavior.
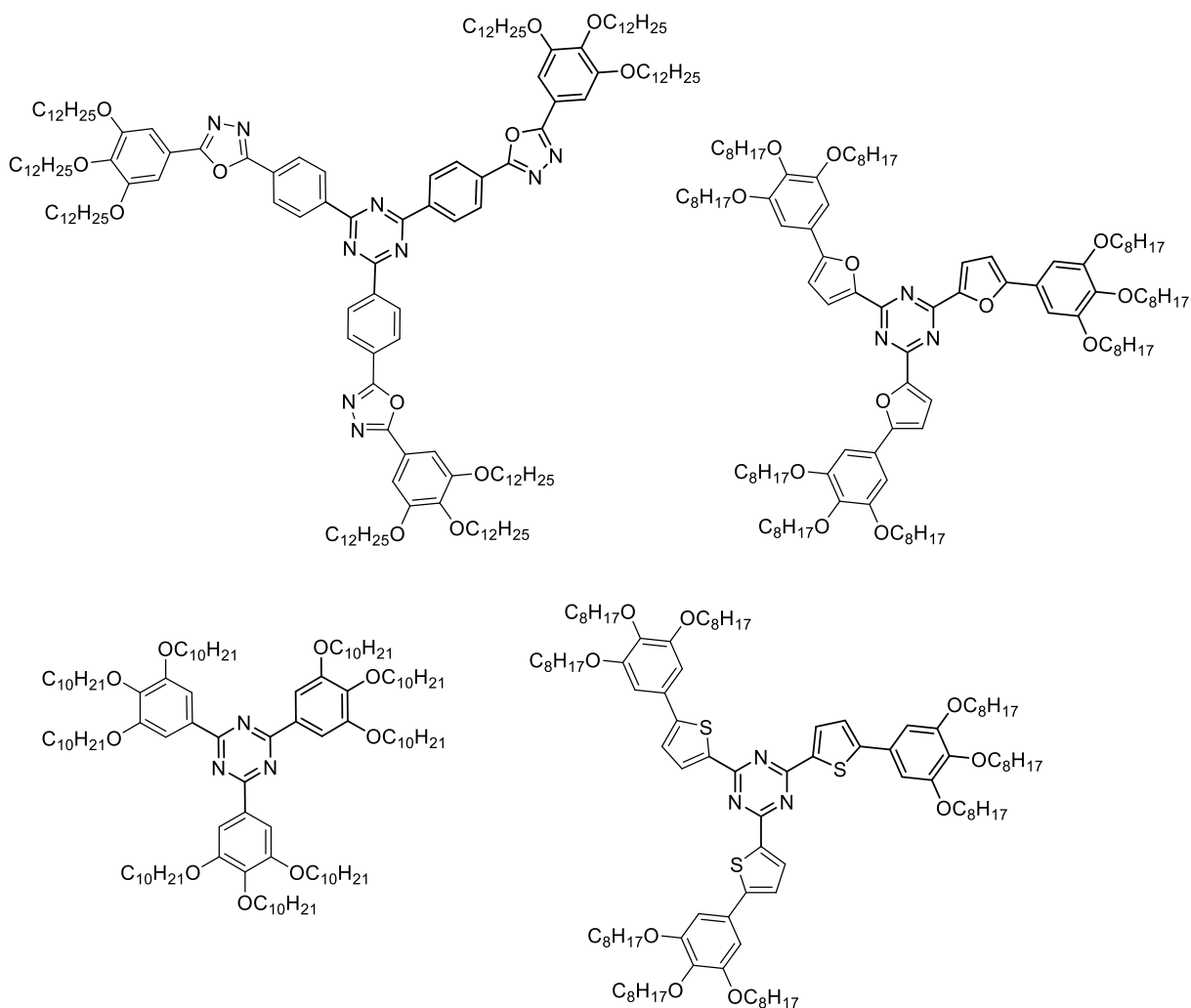
As for the application in OLEDs, triazines were also reported for TADF (Endo et al., 2011; Wada et al., 2015; Sharma et al. 2019; Kumar et al. 2020; Tanaka et al. 2012) (**Figure 21**).

Figure 21. 1,3,5-triazine derivatives with TADF properties.
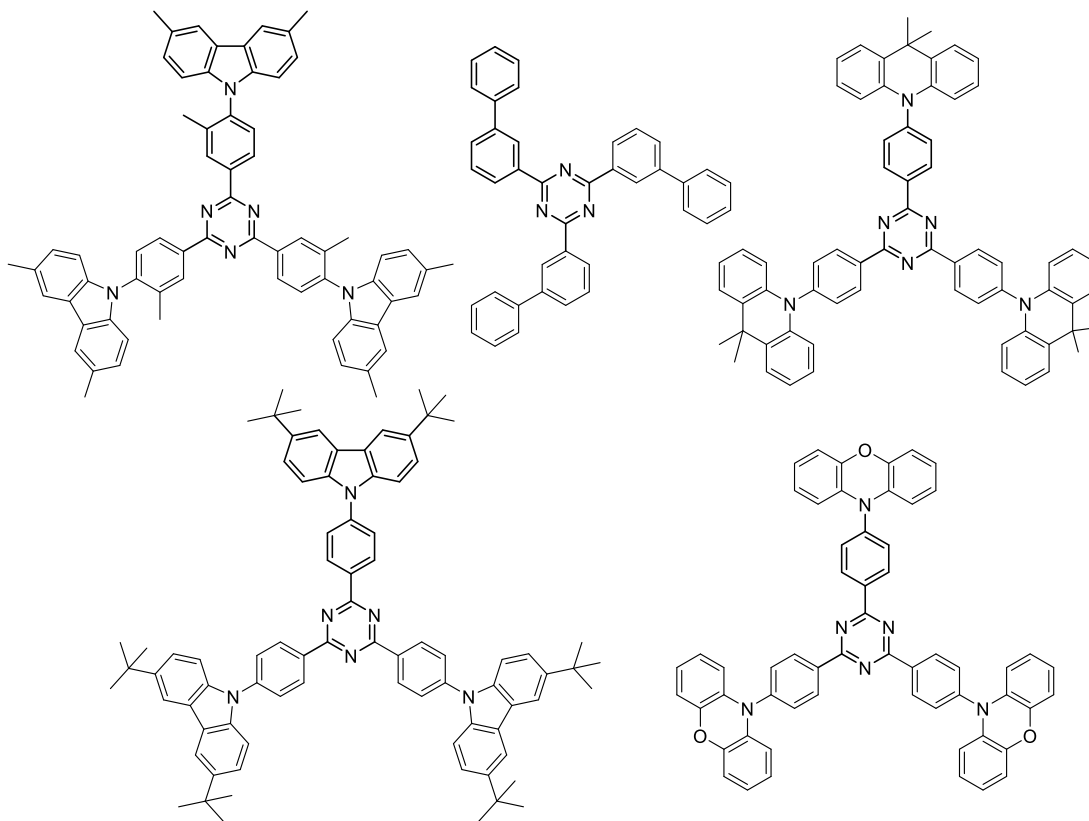


In several tris(triazolyl)triazine derivatives (Beltrán, et al. 2010; Beltrán, et al., 2012; Tober et al., 2019), glass transitions above room temperature could be detected after

melting and subsequent cooling, confirming the presence of an anisotropic columnar glass under standard conditions (**Figure 22**).

Figure 22. Examples of columnar s-triazine mesogens. The glass transition temperatures Tg in the columnar mesophase are given if observed by calorimetry.
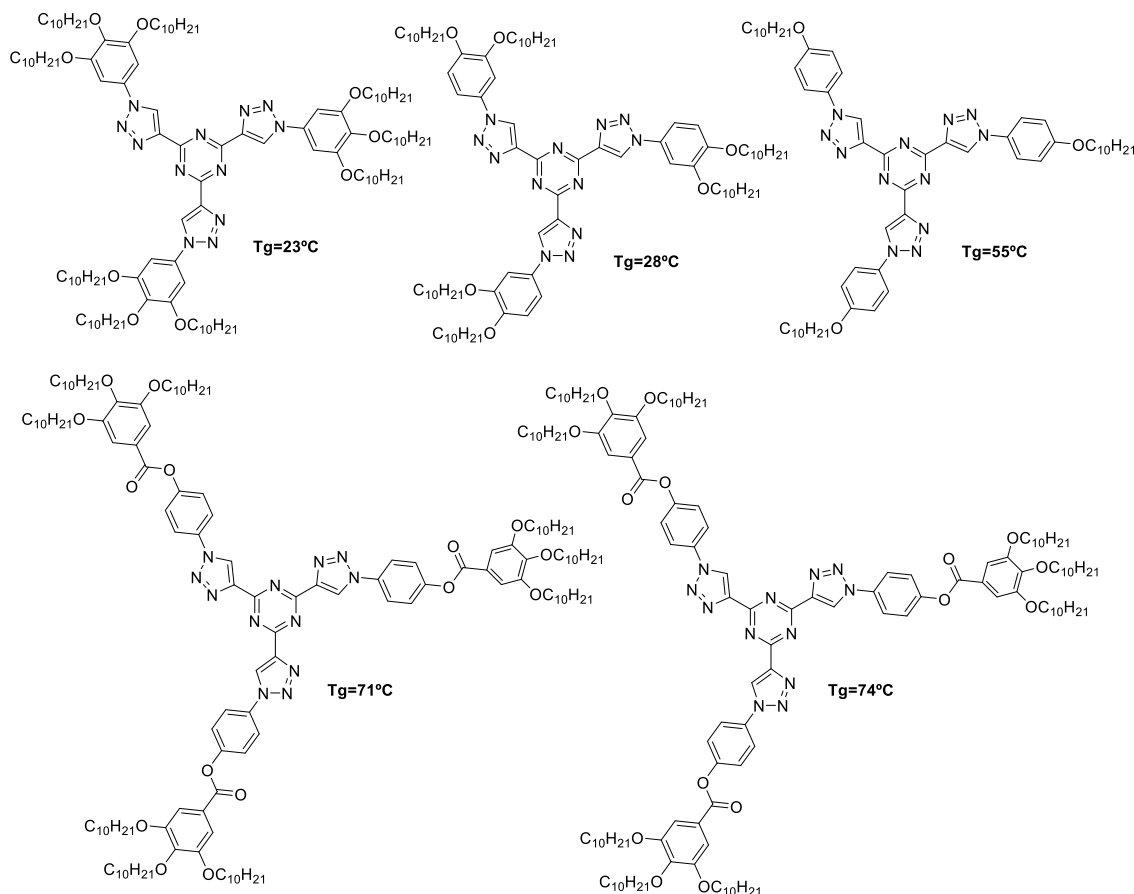


In recent work of my two thesis supervisors, ester-substituted triphenyltriazines, i.e. tris(3-alkoxycarbonylphenyl)-s-triazines (**2** and **3**) (Vieira, et al., 2021), have been obtained (**Figure 23**) readily from methyl 3-cyanobenzoate, and showed predominantly nematic liquid crystal behavior. Chain or core fluorination leads to columnar mesophases with a weak tendency to crystallize at room temperature, due to the flexibility of rotation at the single triazine-benzene bond that allows two in-plane configurations of each meta-conjugated ester group with respect to this bond. The limited conjugation between the three outer benzene units via meta-bonds across the central triazine cycle ensures that a large band gap is preserved, allowing the incorporation of blue emitters, as is desired for TADF (organic light-emitting diode) OLEDs. A robust glassy state was not achieved in

convenient temperature ranges above room temperature with these smallest representatives of the triarylazine esters.

Figure 23. Liquid crystalline triaryltriazine triesters.
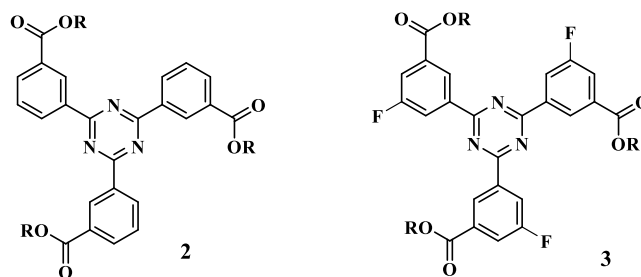


## 1.9.1 Preparation of triazines

In recent years several synthetic methodologies have been developed to obtain 1,3,5-triazines, among which are nucleophilic substitution of cyanuric chloride (Dudley & Thurston, 1949) and nitrile cyclization catalyzed by strong acids (a widely employed synthetic method) (Hayami & Inoue, 1999). Other methods involve weak bases or lanthanide (III) ions (Forsberg et al., 1988), however, these methods are associated with some limitations, such as requirement of halogenated substrates, production of undesirable residues, requirement of excess amine as a co-catalyst, oxidation of aldehyde in normal environment, and decarboxylation under adverse reaction conditions (Pardeshi et al., 2018; Sugimura et al., 2018).

A widely employed methodology for the preparation of 1,3,5-triazines is the cyclization of nitriles catalyzed by very strong acids. The work of Hayami and Inoue is an example of this type of synthesis. Here the authors use trifluormethanesulfonic acid (triflic acid) and chloroform as solvent. The acid was added at 0°C, and one hour after the addition the system was brought up to room temperature, and remained under stirring for approximately 24 hours. Although the reaction time was relatively long, the obtained yield of 85% is an advantage of this method (Hayami & Inoue, 1999) (**Scheme 1a**).

There are more recent reports in the literature of the use of strong acids without the use of solvents. The synthesis of tris(bromophenyl)triazine (**5**) by trimerization of 4-bromobenzonitrile (**4**), using only triflic acid, shows better yields than with the use of solvent and also needs less reaction time (Vieira et al., 2021) (**Scheme 1b**).

Scheme 1. Synthesis of 1,3,5-triazine trought nitrile ciclization.

**a.** With solvent: CHCl$_3$ (Hayami e Inoue, 1999**)**
**b.** With out solvent (Vieira, 2021)

CF$_3$SO$_3$H

**4**

**5**
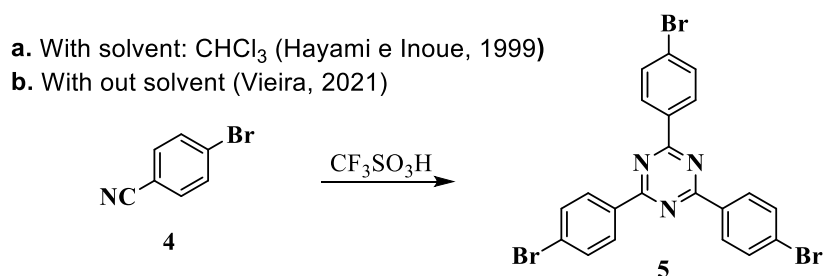
## 1.10 Polyaromatic compounds

Polycyclic aromatic hydrocarbons (PAHs) have played an important role in the recent development of organic electronic devices (Jabłoński et al., 2019; Ravat, 2021; Storch et al., 2022) such as in: photovoltaics, field effect transistors and solar cells, conductors, semiconductors (Doyranlı et al., 2017; Hopf, 2014; Ryan & Fuchter, 2022). They took this prominent role due to their electronic characteristics of resonance, stability and inter- and intramolecular interactions (Hasan & Borovkov, 2018). These compounds are synthesized in an atomically precise and structurally well-defined manner using well-established synthetic organic chemistry tools (Storch et al., 2022).

Polycyclic aromatic hydrocarbons are basically fused aromatic rings, which have no heteroatoms (Barnes et al., 2013). Among the types of polycyclic aromatic hydrocarbons their classes are distinguished by the amount and manner in which the rings are bonded. Benzene (**6**), naphthalene (**7**), anthracene (**8**) are examples of linear and planar aromatic structures (**Figure 24**), in these compounds the benzene rings are fused linearly; when the rings are ortho-fused we have the class of angular acenes; the simplest of them and still planar, is the angular homologue of anthracene, phenanthrene (**9**). When the number of ortho-fused aromatic rings is increased beyond three units (**10-12**) (**Figure 24**), the spatial crowding in the molecule is also increased, forcing it to adopt a non-planar helical arrangement: these compounds are known as helicenes (Hasan & Borovkov, 2018).

Figure 24. Examples of polycyclic aromatic hydrocarbons (PAHs), linear compounds (**6-8**), and angular compounds (**9-12**).

benzene

naphthalene

anthracene

phenanthrene

**6**

**7**

**8**

**9**

[4]helicene

**10**

[5]helicene

**11**

[6]helicene

**12**
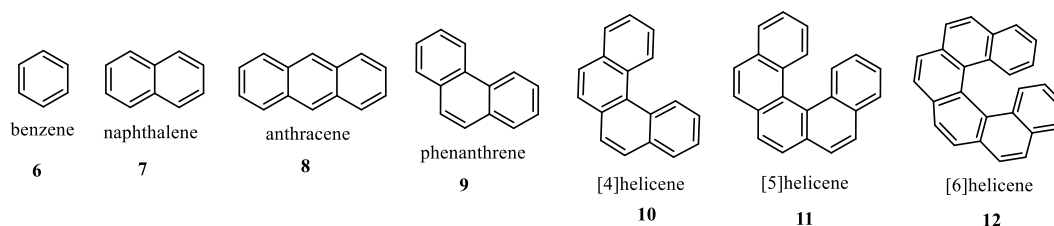
The development of polycyclic aromatic hydrocarbon syntheses has made enormous progress during the past decades. However, the photochemical approach still prevails as an important, efficient, and quite generally applicable method for obtaining these compounds (Storch et al., 2022). From a variation of the Perkin reaction (Sarkar et al., 2013) a useful and versatile tool for the synthesis of polycyclic arenes was devised, and the functionalization of these substrates became facilitated.

### 1.10.1 Polyaromatic compounds: phenanthrenes and helicenes

Phenanthrene is the simplest member of the phenacene family, a class of compounds formed by benzene rings fused together in an alternating pattern (extended zig-zag structure) (Mallory et al., 1997). Phenacenes are a class of hydrocarbons with attractive physical properties such as high charge mobility (Doyranlı et al., 2017; X. F. Wang et al., 2011).

Phenanthrene derivatives were first synthesized via the oxidative photocyclization reaction of stilbenes (Smakula, 1934), but their structure was not elucidated until 1950 by Parker and Spoerri (Parker & Spoerri, 1950). Today, its synthesis has been improved and its molecular skeleton is used in the construction of more complex polyaromatic compounds.

Helicenes are a class of non-planar molecules formed of at least four angularly condensed benzene rings, which have been known to chemists since 1956, when Lednicer reported the first helicene (Hopf, 2014). Due to their structural chirality, their π-extended system, and their intriguing optical and electronic properties, helicenes have found application in various fields of chemistry, from non-symmetric catalysis (Verbiest et al., 2002), biomolecular recognition, materials for optoelectronic devices and sensors (Storch et al., 2015), to starting materials for the construction of chiral conducting polymers (Hrbac et al., 2014).

Despite the unquestionable potential of these compounds, helicenes have disadvantages regarding their obtainability. For a long time, these materials were difficult to obtain in large quantities and their functionalizations were limited (Jakubec & Storch, 2020). Functionalization of helicenes is discussed with emphasis on different types of transformations, their versatility and regioselectivities. These limitations were circumvented by the advancement of new synthetic methodologies (Jakubec et al., 2018).

With respect to liquid crystals, some phenanthrene and helicene derivatives exhibit mesomorphism, especially columnar mesophases. They constitute the main structures (aromatic center) (Scherowsky & Chen, 1995; Verbiest et al., n.d.; Vyklický et al., 2003) and/or make up the arms of these structures. Some examples of this type of structure are shown below (**Figure 25**).

Figure 25. Examples of phenanthrenes and helicenes with liquid crystal properties.
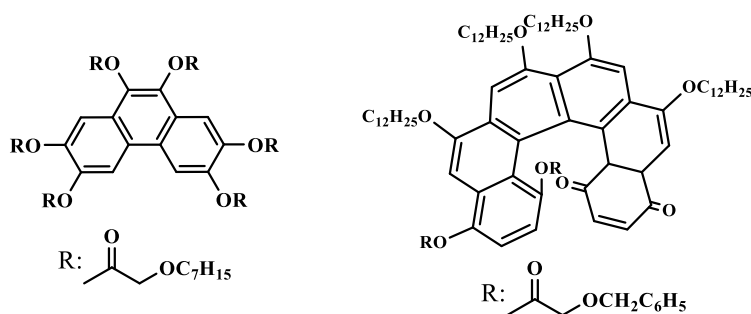


## 1.11 The Perkin reaction

British chemist Sir Willian Henry Perkin (1838-1907) became known, in 1868, for discovering a chemical process that allowed unsaturated carboxylic acids to be obtained, a process now known as the Perkin reaction (Sturm et al., 2022). Perkin's reaction or condensation involves the condensation of an aromatic aldehyde (**13**) and an aliphatic anhydride (**14**), in the presence of a weak base, into an α-β-unsaturated carboxylic acid (**15**), such as cinnamic acid (**Scheme 2**) (Perkin, 1877).

Scheme 2. General scheme of the Perkin reaction.
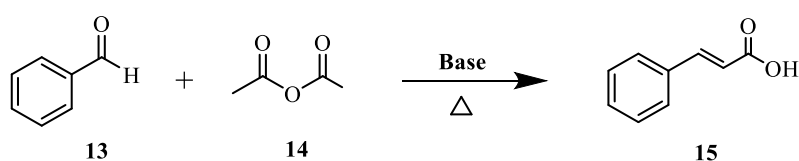


Over the years, Perkin's reaction has undergone several modifications and extensions, broadening the scope and utility of the original synthesis, since, the resulting α-β-unsaturated acids can undergo a variety of chemical transformations, allowing access to several other compound types (Crawford & Shaw, 1953; Tarbell et al., 1954). One of the earliest known modifications to the original synthesis was described in 1941 by Koelsch and Wawzonek, who reacted a salt of phenylglyoxylic acid with a phenylacetic acid in acetic anhydride, in this case involving not an aldehyde but a phenylglyoxylic acid as an electrophile.

## 1.12 The "glyoxylic" Perkin reaction

From this variation of the Perkin reaction (Fields et al., 1990), an anhydride intermediate is obtained, but the lack of solubility and the reactivity towards water and nucleophilic functions make its isolation unadvisable. To obtain compounds with better solubility and less reactivity, the maleic anhydride is transformed into a diester (**Scheme 3**) (Sturm et al., 2022).

Scheme 3. General scheme of the glyoxylic Perkin reaction followed by esterification.
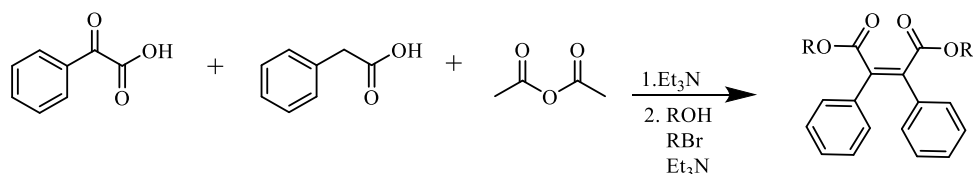


The mechanism of the traditional Perkin reaction and the glyoxylic Perkin reaction are not yet fully elucidated. In **Scheme 4** a mechanistic proposal for the glyoxylic Perkin reaction - obtaining the maleic anhydride in 10 steps - is presented.

The mechanism begins with the deprotonation of arylacetic acid (I) by the base (triethylamine), forming the carboxylate ion (II), which then reacts with acetic anhydride (II') in a nucleophilic substitution reaction to the carbonyl that has as leaving group the acetate ion (IV'), generating the anhydride (IV).  Next, the intermediate (IV) is deprotonated from the more acidic α hydrogen and forms the anhydride enolate (V). It is possible that the slow step of the reaction involves the anhydride enolate (V) attacking the carbon of the "softer" carbonyl of the glyoxylic portion, by Pearson's theory, of (VI') in an aldol-type reaction, generating the carboxy-alcohol anhydride (VII). The reaction continues via intramolecular acylation providing a six-membered ring derived from 1,3-dioxane (VIII) which, with the repositioning of the double bond to the carbonyl, generates the acetoxycarboxylate ion (IX). This is followed by β-elimination of the acetate ion (X') and formation of the maleic carboxylate with the aryl groups in cis position. The last step occurs by the addition of the inorganic acid providing the diacid (XI) and, with dehydration (if subjected to elevated temperatures), formation of the maleic anhydride derivative (XII).

Scheme 4. Proposed mechanism for the glyoxylic Perkin reaction. Part 1: obtaining the maleic anhydride
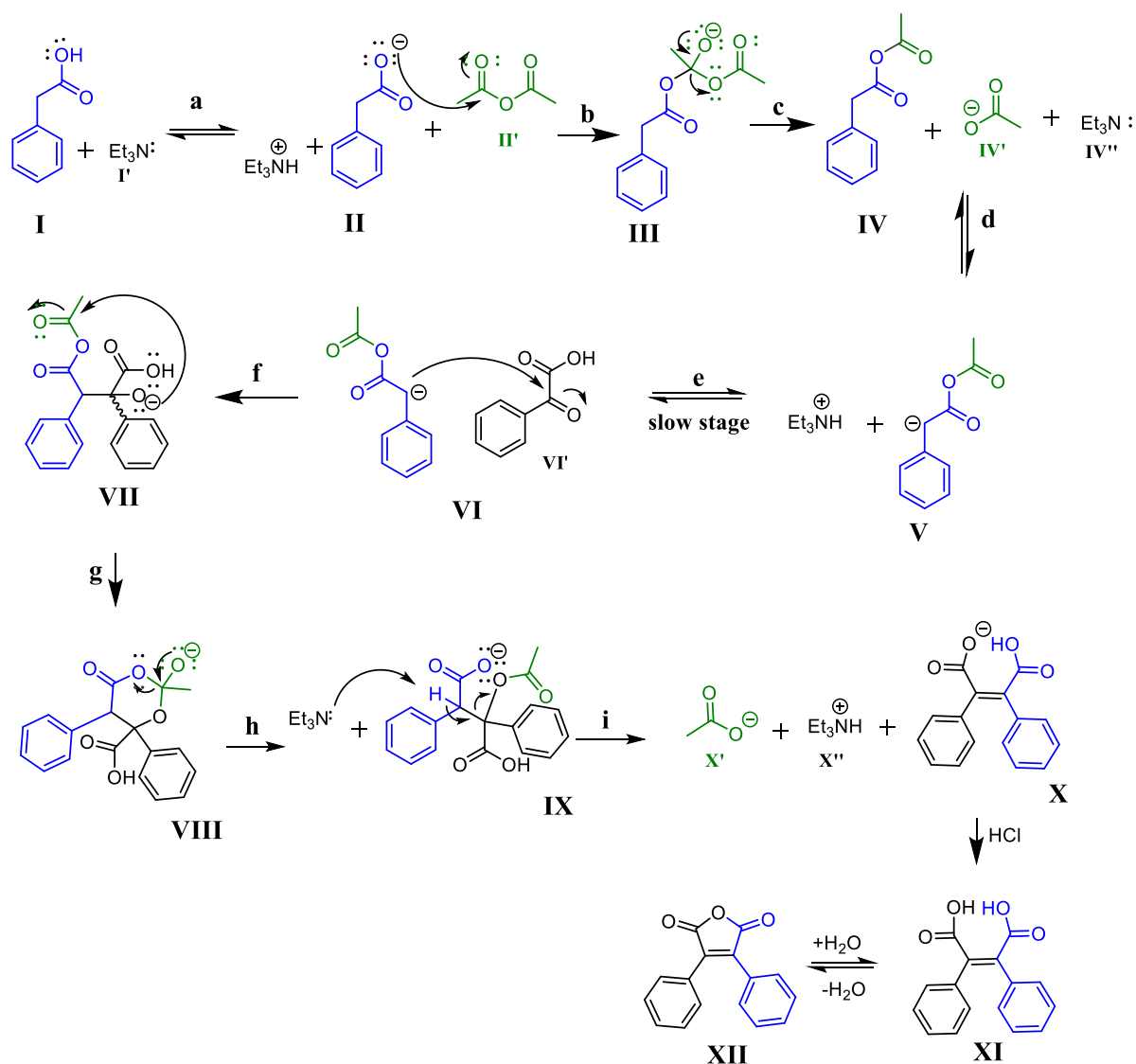


The second part of the mechanism of the glyoxylic Perkin reaction is shown below (**Scheme 5**). In situ esterification occurs from an alkyl alcohol and a halogenalkane in the presence of a base (DBU (1,8- diazabicyclo[5.4.0]undec-7-ene) or triethylamine). Initially the base removes the proton from the alcohol giving rise to the alkoxy species, which in turn attacks the anhydride (XII), inducing its opening (XIV). After this step, the substitution by the halogenoalkane occurs, and the alkyl maleate is obtained (XV).

Scheme 5. Proposed mechanism for the glyoxylic Perkin reaction. Part 2: obtaining the final maleate.

$$R_1OH + B: \rightleftharpoons R_1O^- + \overset{+}{B}H$$



XII          XIII          XIV          XV
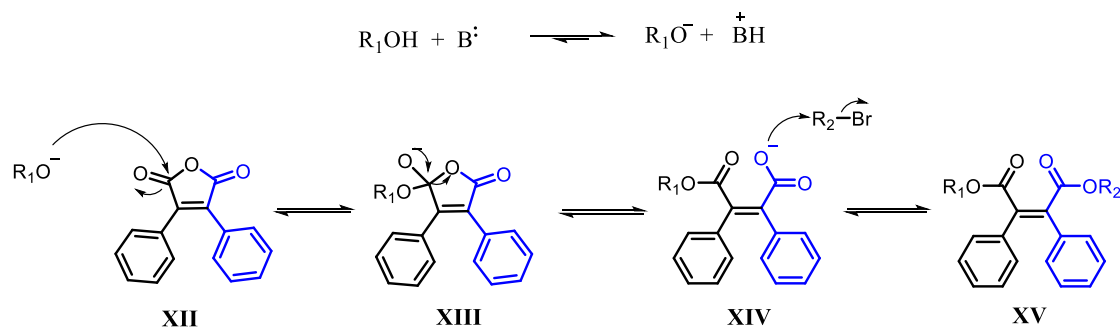
## 1.13    The Mallory reaction: oxidative photocyclization

Mallory's photocyclization reaction is the coupling of two aromatic carbons transforming stilbene derivatives into phenanthrene derivatives with ultraviolet irradiation in the presence of an oxidant (Mallory & Mallory, 1984). The reaction can be used to form homo- and heteroaromatic polycycles.

The oxidative photocyclization reaction of stilbenes had already been described in the 1930s (Jørgensen, 2010; Li & Twieg, 2015; Smakula, 1934; Weber & Clennan, 2019), but it was only after Mallory described in 1964 the use of iodine as a catalyst for this photochemical cyclization (**Scheme 6),** that this reaction proved its efficiency in the synthesis of phenanthrenes and other polycyclic aromatic hydrocarbons, providing a good collection of phenacenes with a variety of substituents (Mallory et al. , 1964; Mallory & Mallory, 1984; Q. Yang et al., 2018).

Scheme 6. Oxidative photocyclization reaction of stilbene, described by Mallory.
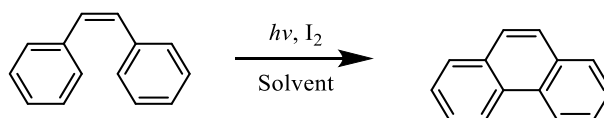


Two decades after Mallory's publication, the oxidative stilbene photocyclization reaction had much progressed, and Mallory himself proposed a detailed review in which he discusses various aspects and applications of the reaction (Mallory & Mallory, 1984). In more concentrated solutions, stilbenes can form dimers in a cyclic [2+2] condition. However, Mallory's reaction conditions circumvent this limitation, because when we use iodine in catalytic amounts along with $O_2$, it is proposed that the iodine is photochemically cleaved into chain-reacting radicals (Mallory & Mallory, 1984).

Increasing the iodine concentration, on the other hand, leads to the formation of more hydrogen iodide that can saturate the initial stilbene and can also contribute to other side reactions (L. Liu et al., 1991). Other oxidants besides iodine have also been used, but have not shown more prominent results for this synthesis (Jørgensen, 2010).

The proposed mechanism of the reaction known as Malorry photocyclization is presented below (**Scheme 7**). From a synthetic point of view, photochemical isomerization of the double bond (cis/trans-isomerization) occurs rapidly under the reaction conditions, such that different compositions of cis- and trans- stilbenes (I↔I') can provide the same products. Thus, stilbenes can be used as isomeric mixtures in photocyclization, although only the cis-isomer is capable of further cyclization (Jørgensen, 2010; Mallory & Mallory, 1984; Weber & Clennan, 2019).

Scheme 7. Proposed mechanism of the Mallory reaction.
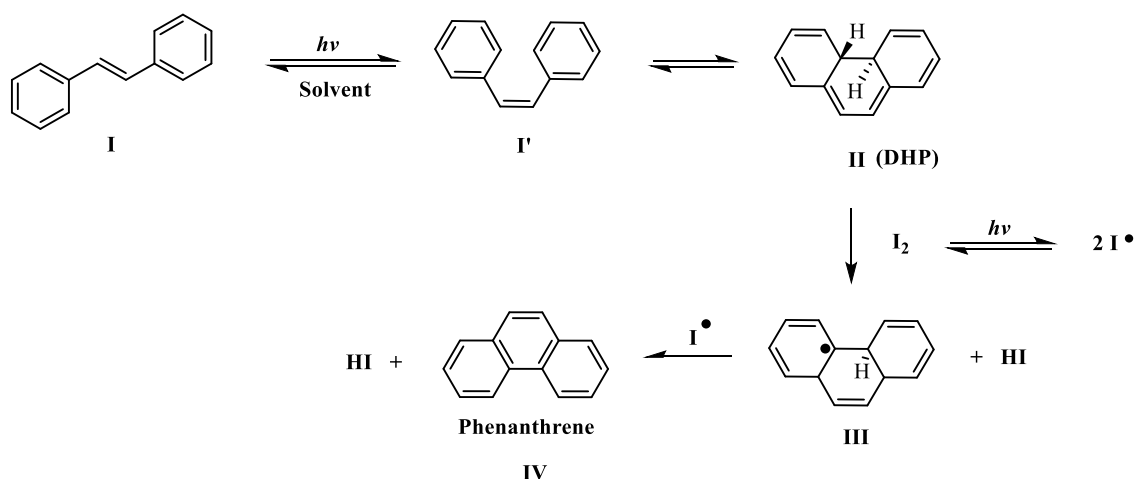


The key point of Mallory's mechanism is the formation of the trans-dihydrophenanthrene (DHP) (II) intermediate by an orbital-symmetry-allowed conrotatory electrocyclic closure. This skeletal rearrangement in many diaryl-ethylenes has been used in the construction of a large number of photocyclized units. Dihydrophenanthrene, DHP, however, is an intermediate, not a final product, which is subsequently converted to another intermediate (III), and thereupon into the final product phenanthrene (IV) by hydrogen abstraction and HI formation (Weber & Clennan, 2019).

## 2. OBJECTIVES

### 2.1 General Objective

The proposal of this work is the synthesis and study of new 2,4,6-triphenyl-1,3,5-triazine derivatives, which are candidates to present columnar mesomorphism and high charge mobility, as well as glass transitions in the mesophase, in view of later application as matrices for OLEDs.

### 2.2 Specific Objectives

1. Optimize the synthesis of extended triaryltriazine esters via glyoxylic Perkin reactions.

2. From these intermediate Perkin products, synthesize symmetric triply aryl-substiuted compounds based on the triazine core with phenanthrene or [4]helicene arms and six short alkyl ester chains (**Figure 26**).

Figure 26. Symmetric compounds proposed in this work.



**F₃Et**: R= Ethyl;
**F₃Pr**: R= Propyl;
**F₃Bu**: R= Butyl.

Phenanthrene

**H₃Et**: R= Ethyl;
**H₃Pr**: R= Propyl;
**H₃Bu**: R= Butyl;
**H₃Hex**: R= Hexyl.
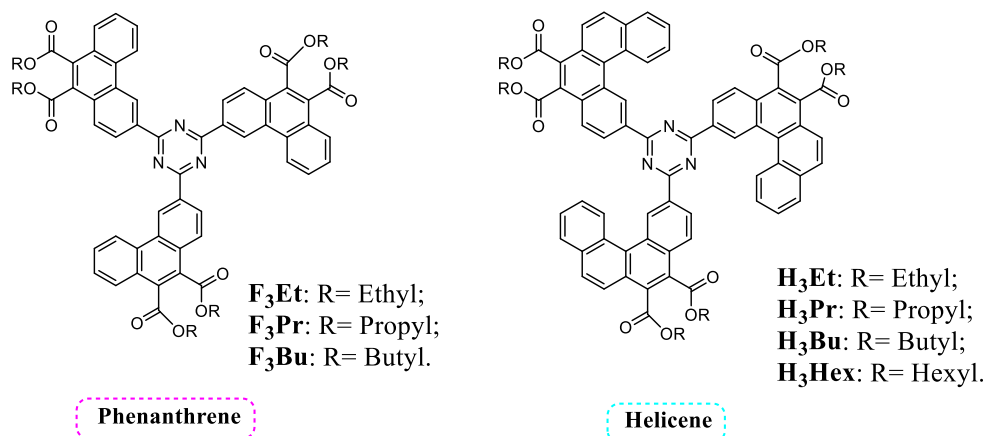
Helicene

3. Prepare non-symmetric compounds based on the triazine core and one or two phenanthrene or [4]helicene diethylester arms associated with two or one phenyl arms bearing one methyl ester in meta position, in analogy to the previously obtained triply meta-ester-substituted triphenyltriazines (**Figure 27**);

Figure 27. Non-symmetric compounds proposed in this work.
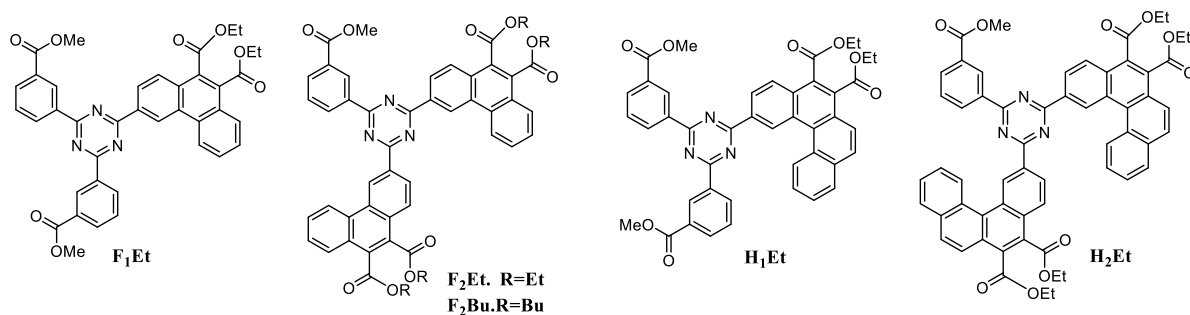


4. Characterize the compounds obtained by analytical techniques that can confirm them, such as: $^1$H NMR, $^{13}$C NMR and high resolution mass spectrometry (HRMS);

5. To study the thermal properties of the target molecules in order to verify their stability by thermogravimetric analysis (TGA) and the existence of mesophases by polarized optical microscopy (POM), differential scanning calorimetry (DSC) and X-ray diffraction (XRD), thus establishing their liquid crystalline self-assembly and the formation of a mesomorphic glass;

6. To analyze the photophysical properties of these materials in order to evaluate their luminescence properties.

## 3. RESULTS AND DISCUSSION – PART 1

*Series 1: Symmetric molecules derived from 2,4,6-triphenyl-1,3,5-triazine with phenanthrene or [4]helicene arms.*

### 3.1 Structural design and synthetic strategy

In the elaboration of this thesis subject, several aspects were considered, among them, the recent reports of the group about obtaining anisotropic and columnar glassy compounds (Vieira *et al*, 2021). In addition to the selection by means of DFT of electron acceptors and donors already used in the literature, in order to obtain properties such as delayed thermally activated fluorescence associated with anisotropic properties, an association not reported in the literature until recently.

One of the valid strategies, and currently widespread in organic synthesis, is modeling using density functional theory (DFT), which is a type of structural calculation that has gained a lot of notoriety in recent years. This study is used in the design of new molecules, becoming an advantage when it comes to theoretically evaluating, among several aspects, the photophysical properties. For the materials area, pre-establishing a relationship between the structure to be synthesized and the desired properties is an approach already used. For molecules with TADF, this theoretical DFT approach is indispensable, since, through these calculations, we have access to the theoretical values of the gaps between the S1 and T1 states, besides the SOC values, thus it is possible to select the best electron acceptor and donor groups for the final design of the molecules.

The DFT calculations were performed for the simplest analogs with methyl chains (not synthesized in this work, used for comparison to facilitate obtaining the calculations) and the theoretical results were promising. The energies of the theoretical singlet states for **F₃Me** was 3.347 eV and for **H₃Me** was 2.963 eV, and of the triplet states was 2.637 eV for **F₃Me** and 2.464 eV for H₃Me, therefore, the phenanthrene-type derivatives will

possibly emit in the sky-blue region, while the helicene-type derivatives in the green region (Yang, *et al.*, 2017; Wong, *et al.*, 2017).

Figure 28. Representation of the minimized symmetric molecules for this work.
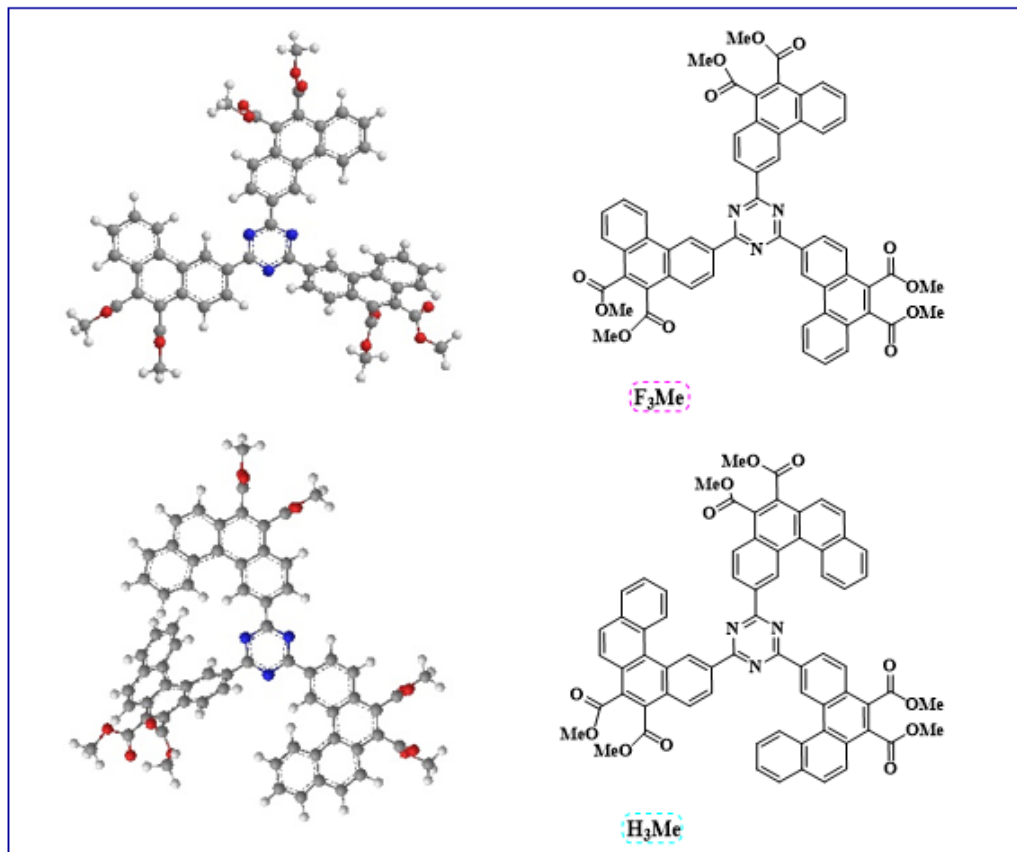


In **Scheme 8** a brief retrosynthetic analysis is presented for the series of triphenanthryltriazine hexaesters. In it, two possible routes are presented. The first step of this retrosynthetic analysis involves a disconnection between the $Csp^2$-$Csp^2$ carbons of **F₃R**(I), resulting in the synthetic equivalent (II). The second step involves a disconnection between the $C_a$-$C_b$ carbons, involving two different synthetic routes, which results in the possibility of four synthetic equivalents, in the first route (III+ IV) and in the second (III' + IV'). Following route 1, the next disconnection occurs between oxygen and the acid hydrogen, resulting in the equivalent (V). The next step in the retrosynthetic analysis of route 1, is the disconnection between the $C_c$-$C_d$ carbons, resulting in the synthetic equivalent (VI). In the retrosynthetic sequence there is a disconnection between the heterocycle carbon and nitrogen, resulting in the synthetic equivalent (VII). For route 2, after the disconnections that result in the synthetic equivalents (III' + IV'), the next disconnection occurs between the carbon and nitrogen of the heterocycle of (III'), resulting in the synthetic equivalent (IV')

Scheme 8. General retrosynthetic analysis for symmetric compounds.
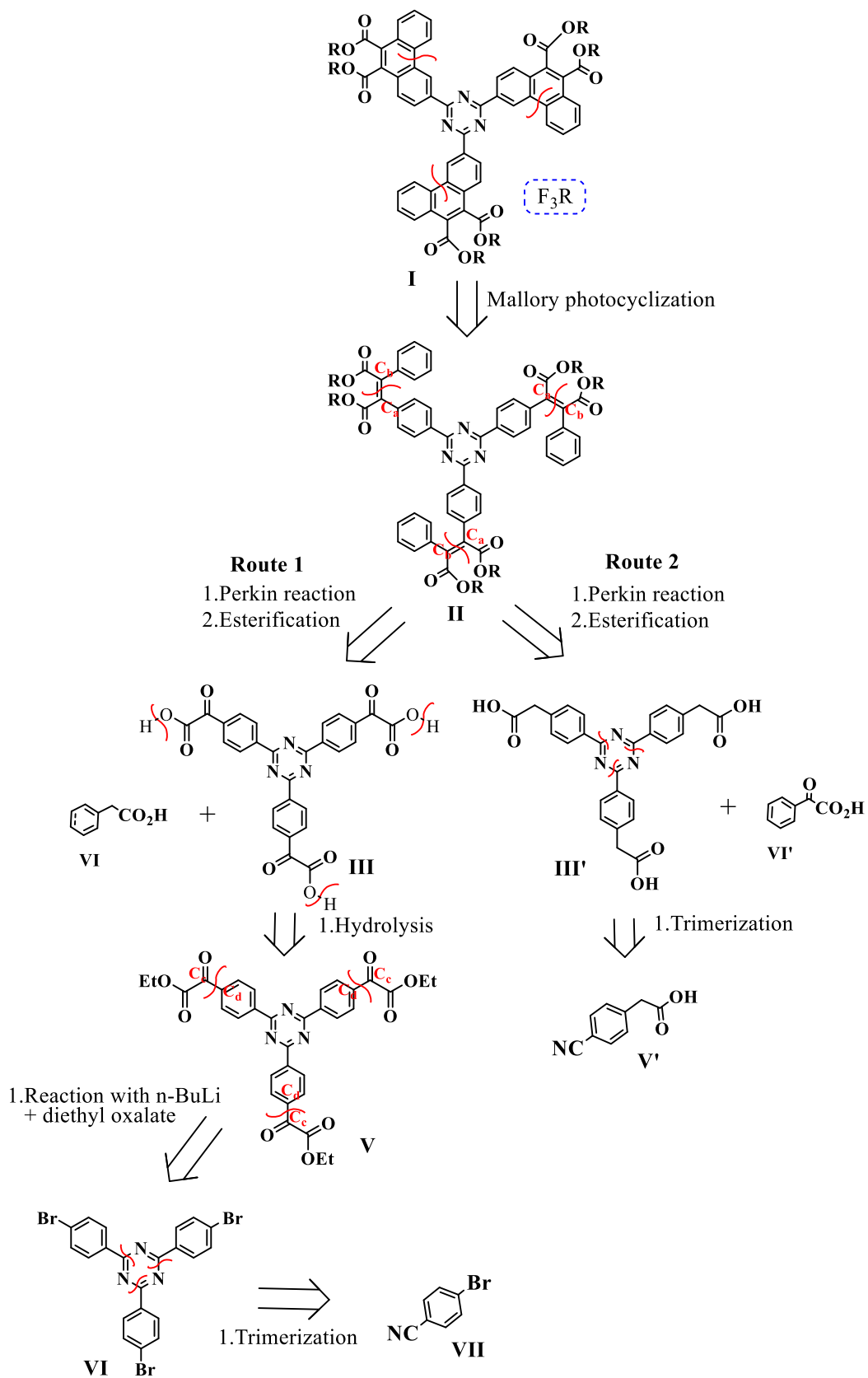
From this retrosynthetic analysis, two possible routes are evaluated, the first of them (**Scheme 9**) somewhat longer, which involves three more synthesis steps than its analogue. However, the availability and cost of the starting nitrile of route 1 drives us to optimize each synthetic step and thus overcome the possible problems with overall yields.

Scheme 9. Proposed synthetic route 1, for the synthesis of the compounds planned for this work.
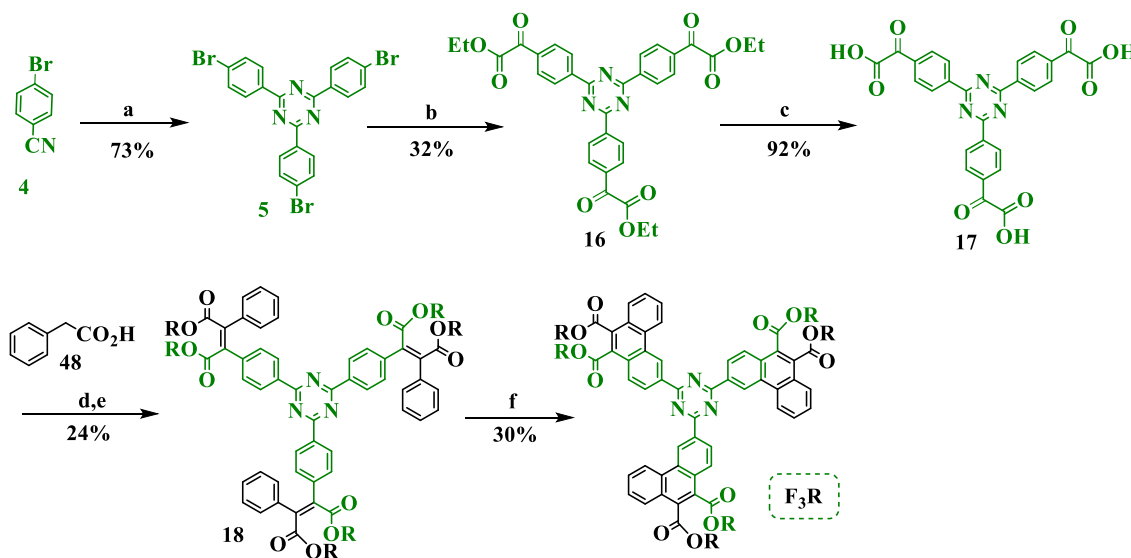


**Reagents and conditions:** a. Triflic acid, 0ºC, overnight; b. n-BuLi, THF dry, -78ºC, diethyl oxalate; c. NaHCO$_3$, H2O/EtOH, HCl 1M; d. Acetic anhydride, TEA, THF; e. alkyl alcohol, alkyl bromide, TEA; f. iodine, ethyl acetate.

On the other hand, route 2 (**Scheme 10**), with a smaller number of steps, is notably better from the synthetic point of view (better yield). However, the starting nitrile is more expensive.

Scheme 10. Proposed synthetic route 2, for the synthesis of the compounds planned for this work.
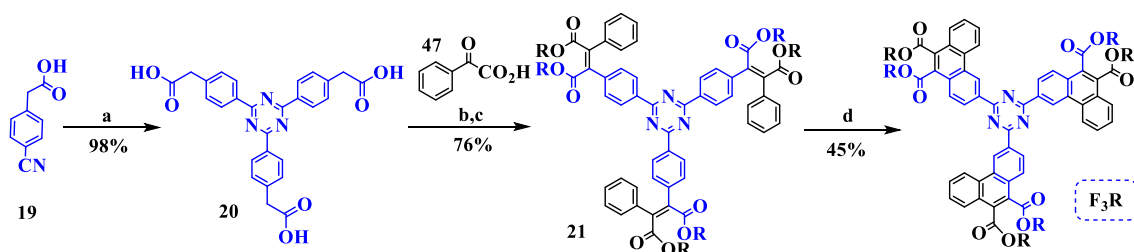


**Reagents and conditions:** a. Triflic acid, 0ºC, overnight; b. Acetic anhydride, TEA, THF; c. alkyl alcohol, alkyl bromide, TEA; d. iodine, ethyl acetate.

However, regarding the synthetic planning and subsequent execution, both routes will be experimentally evaluated in this work the reaction of Perkin glyoxyl is a reaction between an arylacetic acid and an arylglyoxylic acid, allowing us to evaluate how the

reactivity of the reaction is affected by the presence of different acid groups attached to a strong electron acceptor group, here triazine.

## 3.2 Synthesis and characterization of phenanthrene and helicene derivatives and their intermediates

All the syntheses employed in this work will be detailed below, as well as the characterization of the compounds by characterized by $^1$H NMR. The final compounds were also characterized by $^{13}$C NMR and mass spectrometry (see appendix).

### 3.3.1 Synthesis of the building block: s-triazine

The first route evaluated was route 1. The formation reaction of 2,4,6-tris(4-bromophenyl)-1,3,5-triazine (**5**) was the initial step for the synthesis of the molecules. This reaction has a satisfactory yield (around 72%) and simple treatment and purification. The *s*-triazine block is constructed via a trimerization reaction of 4-bromobenzonitrile (**4**) in triflic acid and without solvent (**Scheme 11**) (Vieira, *et al*., 2021).

Scheme 11. Synthesis of 2,4,6-tris(4-bromophenyl)-1,3,5-triazine (**5**).
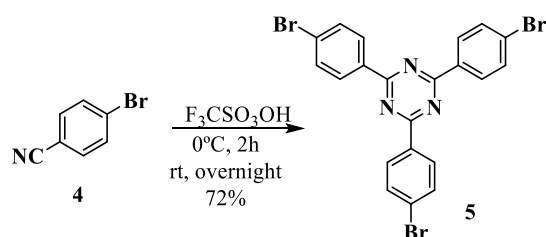


In the first attempt to obtain the triazine nucleus the methodology employed had dichloromethane as the reaction solvent and the reaction time of 72 h. But using triflic acid as the solvent for this reaction was the best method, decreasing the average reaction time to 14 h (overnight) and also improving the yield, which in the solvent version was approximately 39% and in the solventless methodology increased to 72%.

In **Figure 29**, we compare the hydrogen nuclear magnetic resonance spectra of the starting material 4-bromobenzonitrile (**4**) and 2,4,6-tris(4-bromophenyl) -1,3,5-triazine (**5**). It is possible to observe a shift of the signals of the hydrogens that in the starting material are at a chemical shift of 7.64 (H1) and 7.53 (H2) ppm, two doublets with coupling constants $J = 8.0$ and 8.8 Hz, respectively and for (**5**) there is a smaller field shift in the product formed at 8.57 (H1) and 7.72 (H2) ppm, doublets with coupling constants $J = 8.7$ and 8.6 Hz.

Figure 29. Comparison of the $^1$H NMR spectra of the starting nitrile (**4**) and the trimerization product (**5**) in 1,1,2,2-tetrachloroethane-$d_2$, 400 MHz .
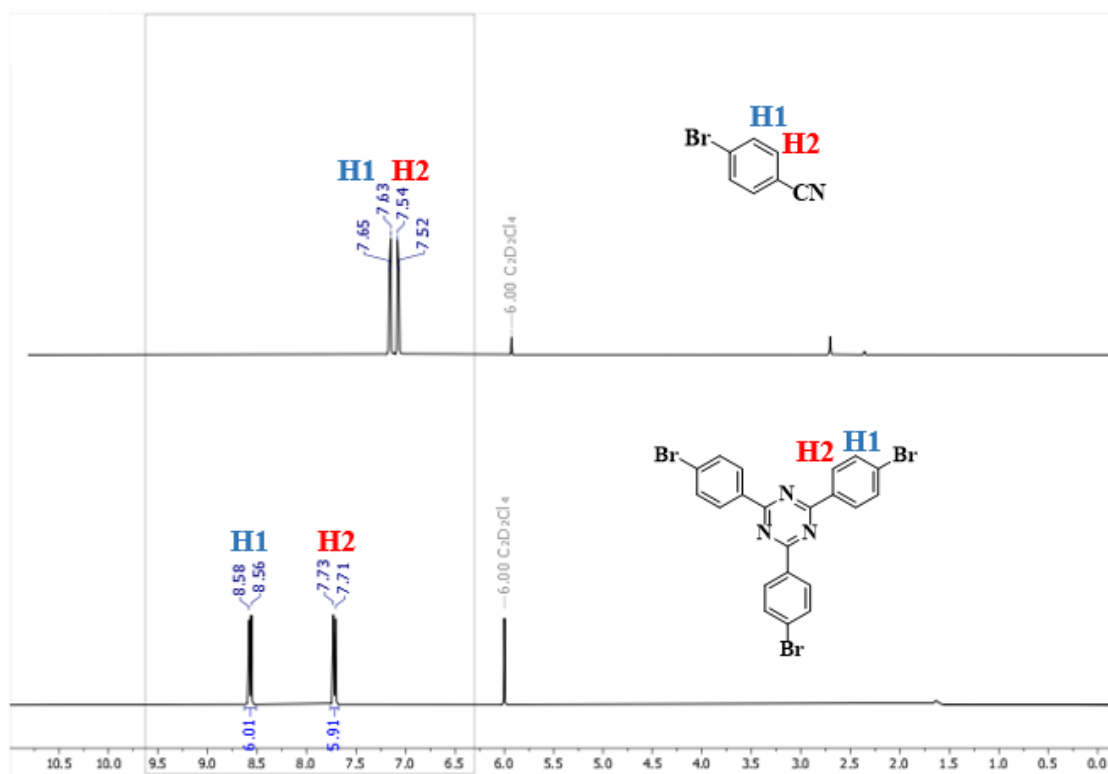


After the preparation of 2,4,6-tris(4-bromophenyl)-1,3,5-triazine (**5**), the next synthetic steps were aimed at the construction of the glyoxylic acid group attached to triazine. To construct glyoxylic acid, the first reaction was the lithiation of compound (**4**) with n-butyl lithium, at -78°C, in 1 litre of THF (dry), after 2 hours of reaction under strong stirring, the temperature was increased until it reached room temperature and after 1 hour, the temperature was lowered again to -78°C and then diethyl oxalate was added, after the addition of ethyl oxalate the temperature was raised again and then the reaction was treated with 1M hydrochloric acid solution, compound (**5**) was formed with an average yield of 32%.

Scheme 12. Synthesis of triethyl 2,2',2''-((1,3,5-triazine-2,4,6-triyl)tris(benzene-4,1-diyl))tris(2-oxoacetate) derivative (**16**).
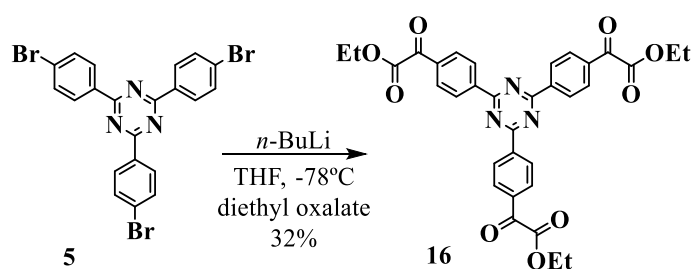
In the $^1$H NMR spectrum of compound (**16**) (**Figure 30**), it is possible to observe two doublets (*d*) referring to hydrogens of the aromatic region at 8.2 ppm (H2) and 8.8 ppm (H1), the integral of the signals confirms the ratio 6 hydrogens. The coupling constants (*J*) for the (*d*) were determined as *J* = 8.4 Hz and *J* = 8.5 Hz, respectively. In the aliphatic region, we have a signal referring to the methyl hydrogens of the ethyl ester portion (-O-CH$_2$-) at 4.48 ppm and at 1.45 ppm referring to the signals of the methyl hydrogens (-O-CH$_2$-CH$_3$).

Figure 30. $^1$H NMR spectrum of compound (**16**) in 1,1,2,2-tetrachloroethane-$d_2$, 400 MHz.
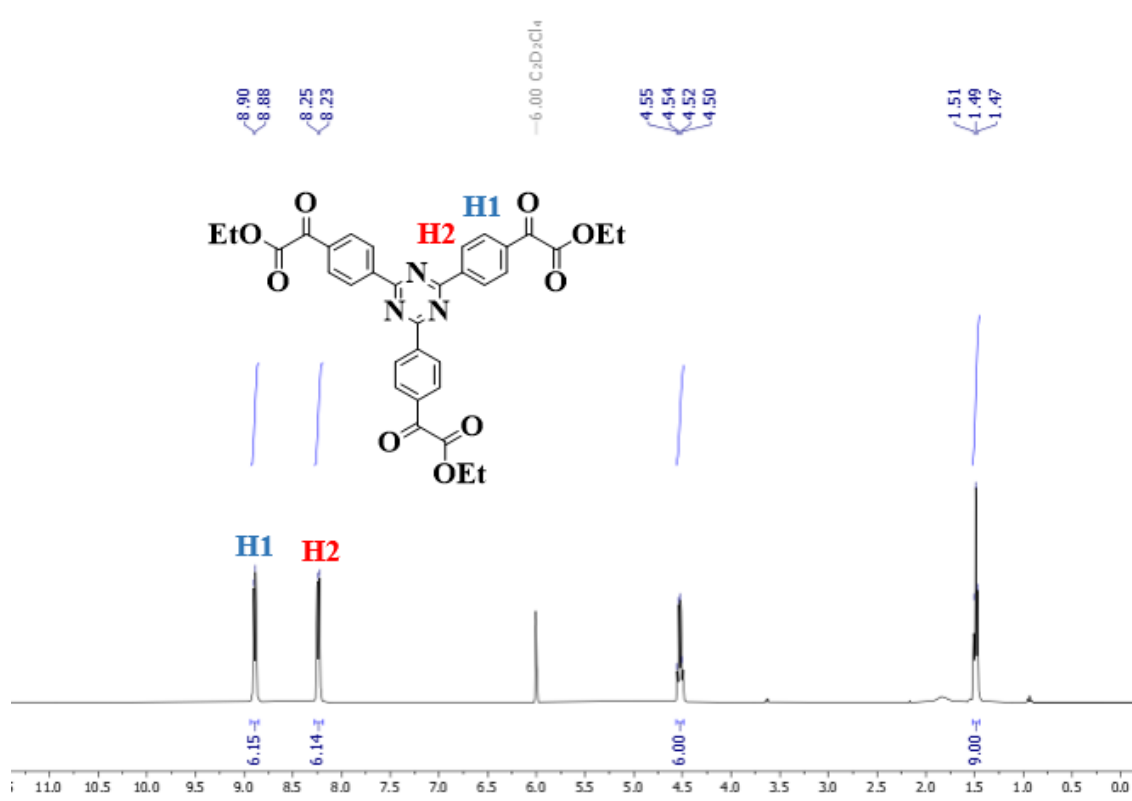


This compound (**16**) undergoes hydrolysis in basic medium to generate the glyoxlic acid (**17**) (Robert et al., 2017), obtained in 92% yield.

Scheme 13. Hydrolysis of ester (**16**), formation of 2,2',2''-((1,3,5-triazine-2,4,6-triyl)tris(benzene-4,1-diyl))tris(2-oxoacetic acid) (**17**).
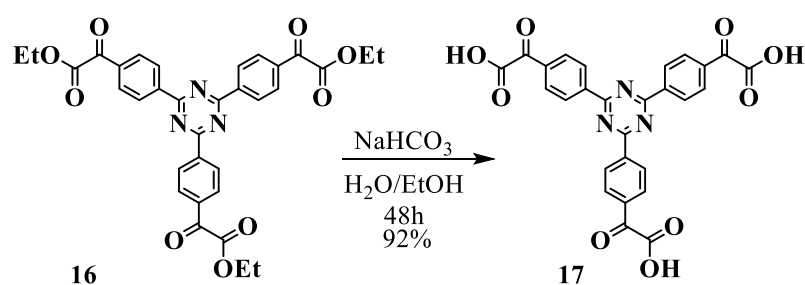
As observed in the ${}^1$H NMR spectrum (**Figure 31**) after the hydrolysis reaction, the ethyl group is eliminated and only the signals referring to the aromatic region are observed. The relative integral between the signals remained proportional. Due to the presence of the carboxylic acid function, the two doublets (*d*) at 9.0 (H1) and 8.3 (H2) ppm, with coupling constants of $J = 8.8$ Hz and $J = 8.8$ Hz, showed a slight shift to smaller field when compared to the starting ester. It was, as usual, not possible to observe the signals referring to the hydrogen of the acid.

Figure 31. ${}^1$H NMR spectrum of compound (**17**) in acetone-$d_6$, 400 MHz.
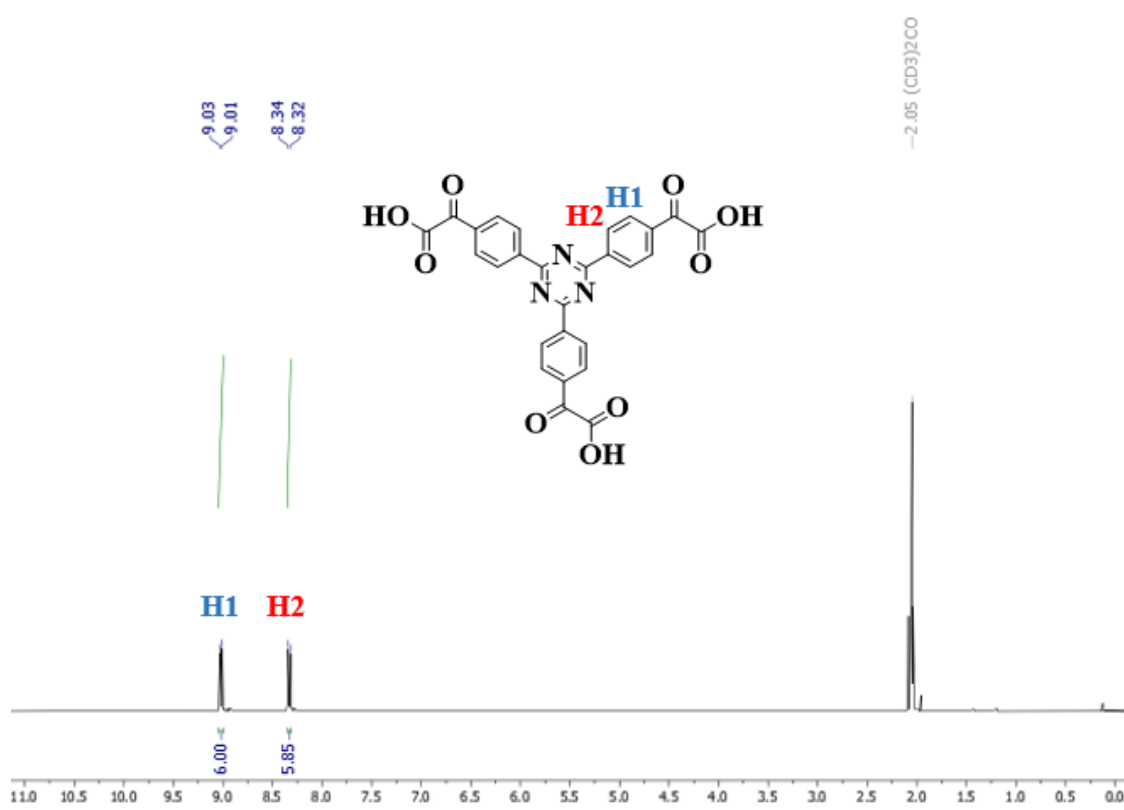


The synthesis of compound (**17**) finalizes the first step of route 1. Next, the synthetic steps to obtain the acid unit of the second route, compound (**18**), will be discussed.

To obtain the second acid building block (**20**), an attempt was made to selectively reduce the carbonyl of the oxalic acid of the triazine (**17**) in order to obtain the arylacetic acid derivative (**Scheme 14**). This attempt to selectively reduce the glyoxylic carbonyl is an alternative to the high cost of the nitrile, 2-(4-cyanophenyl)acetic acid, (**19**), used in the trimerization reaction.

The selective reduction reaction, was already part of the expertise of the group (Robert et al., 2017). However, for the triazine system, the conditions used for polycyclic

aromatic hydrocarbon compounds did not work, so we tried to vary the reaction time, reducing it from four days to two days, as well as varying the proportions of the acids used, without success: the starting triazine was degraded, on all occasions.

Scheme 14. Selective reduction to form 2,2',2"-((1,3,5-triazine-2,4,6-triyl)tris(benzene-4,1-diyl))triacetic acid (**20**).
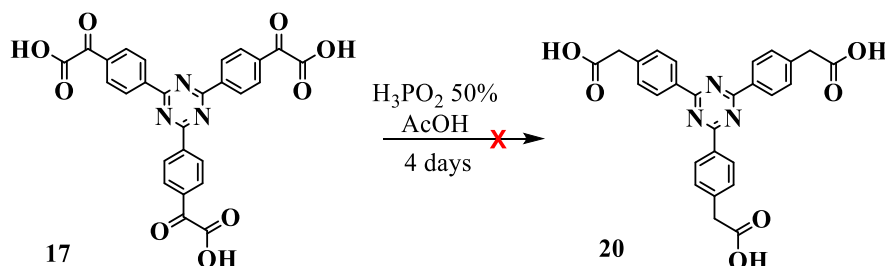


Given this impasse, we returned to the original synthetic route to obtain 2,2',2"-((1,3,5-triazine-2,4,6-triyl)tris(benzene-4,1-diyl))triacetic acid, (**20**): The trimerization reaction of 4-cyano-phenylacetic acid (**19**) (**Scheme 15**) under the same conditions as the trimerization of 4-bromobenzonitrile (**4**), which was obtained with a yield of approximately 98%.

Scheme 15.Trimerization of 4-cyanophenylacetic acid (**19**), to result 2,2',2"-((1,3,5-triazine-2,4,6-triyl)tris(benzene-4,1-diyl))triacetic acid, (**20**).
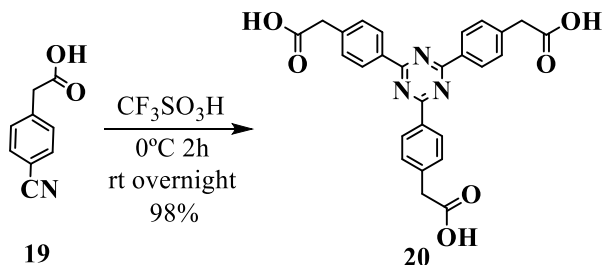


Below is a comparison of the $^1$H NMR spectra of the starting material 4-cyanophenylacetic acid (**19**) with 2,2',2"-((1,3,5-triazine-2,4,6-triyl)tris(benzene-4,1-diyl))triacetic acid (**20**). The signal referring to the methylenic hydrogens of acetic acid in both appears at a chemical shift of 3.79 ppm (H3). The doublets (*d*) in the aromatic region suffer a slight shift to smaller field in the spectrum of the product formed when compared to the starting material. For the starting material the signals of aromatic region appear at 7.74 (H1) and 7.55 (H2) ppm ($J = 8.5$ and $J = 8.6$ Hz, respectively) and in the product they appear around 8.7 and 7.6 ppm with coupling constants of $J = 8.5$ Hz and $J = 8.5$ Hz, the integral corresponding to six hydrogens.

Figure 32. Comparison of the $^1$H NMR spectra of the starting nitrile (**19**) with product (**20**) (both in acetone-$d_6$, 400 MHz).
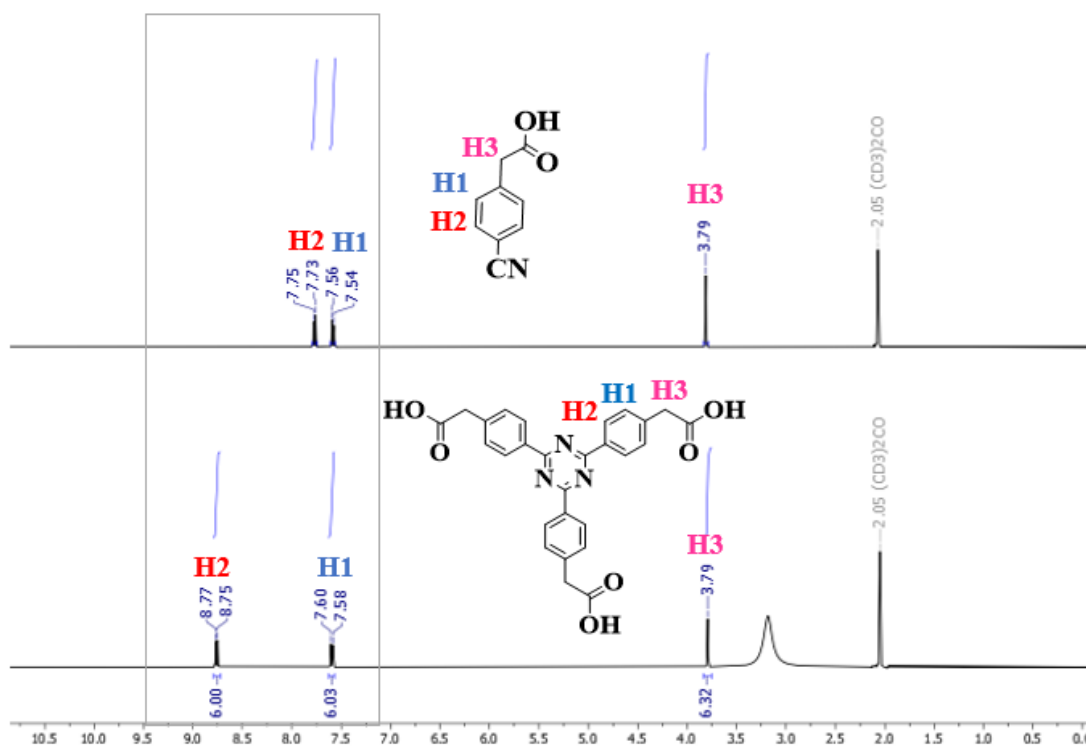


## 3.3.2 Perkin products: construction of the phenanthrene and [4]helicene arms

Since the acid building block of route 1 was obtained by hydrolyzing the ester (**16**) to the glyoxylic acid derivative (**17**), a triple Perkin reaction to form the first derivatives with three phenanthrene-like arms was performed between compound (**17**) and 2-phenylacetic acid (**22**). This reaction is followed by an *in situ* esterification to generate the hexa-ester (**18**) (**Scheme 16**). The latter compound obtained was isolated, purified and properly characterized.

Scheme 16. Glyoxylic Perkin reaction, followed by esterification to form the intermediate (**18**).
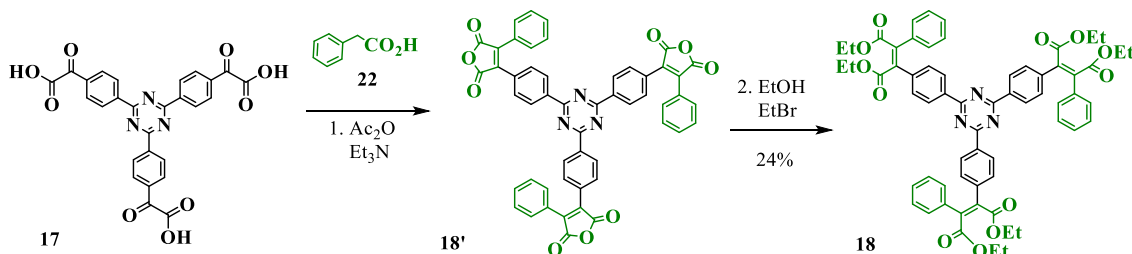


The Perkin reaction between triazine-triglyoxylate (**17**), commercial 2-phenylacetic acid (**22**), acetic anhydride, triethylamine and dry THF was carried out under reflux for an average period of 24 hours and led to the anhydride (**18**). The anhydride obtained in the first step was not isolated but *in situ* esterified. In the second step, alcohol (ethanol),

alkyl bromide (bromoethane) and triethylamine were added and the reaction was brought to reflux for another 24 hours to form (**18**). Purification of the hexa-ester (**18**) was done on a silica gel chromatographic column followed by precipitation in methanol. The yield of the reaction for both steps was 30%. The intermediate (**18**) was characterized by $^1$H NMR (**Figure 33**).

In the following spectrum one can observe signals referring to the hydrogens of the 2,4,6-triphenyl-triazine center (highlighted in black) as the two most short-field shifted (Ar-**H**) doublets (H1) and (H2) at 8.48 and 7.28 ppm, with coupling constants of $J = 8.7$ Hz and $J = 8.6$ Hz. The doublets have integrals corresponding to six hydrogens each one. The signals from the five hydrogens of the phenyl that was added via the Perkin reaction are observed in the form of two larg undefined signals at 7.20 ppm, with an integral corresponding to fifteen hydrogens. In the aliphatic region of the spectrum the signal is observed, an undefined signal, probably the result of the superposition of several quartets, methylenic hydrogens (-CO$_2$C**H**$_2$-) with chemical shift at 4.30 ppm and integral for twelve hydrogens. A multiplet is also observed at 1.31 ppm, referring to the signal of the methyl hydrogens of the ester alkyl chain (-CO$_2$CH$_2$C**H**$_3$), corresponding to eighteen hydrogens.

Figure 33. $^1$H NMR spectrum of compound (**18**) in CD$_2$Cl$_2$, 400 MHz.
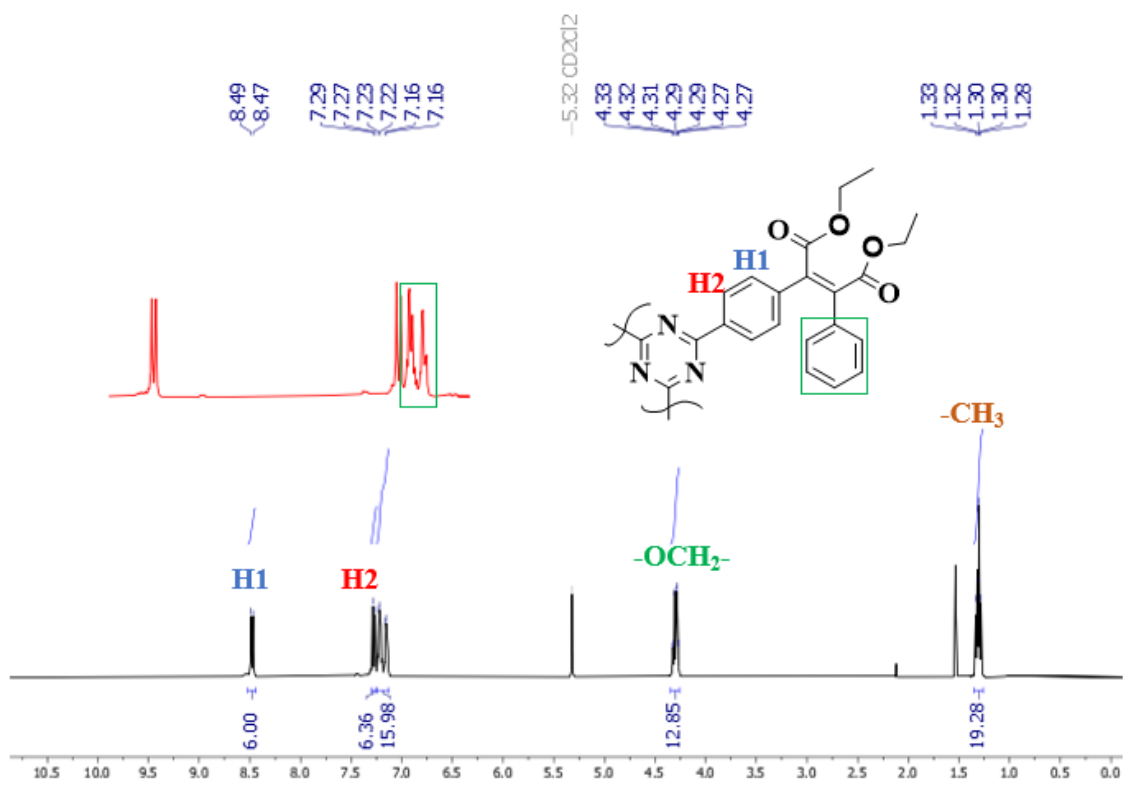
To synthesize the precursor hexa-esters of the [4]helicene derivatives, such as compound (24), the same methodology was followed as for the phenanthrene analogs starting from triphenyltriazine-4',4'',4'''-triglyoxylic acid (17) and commercial 2-naphthylcetic acid (23). The reaction conditions for the Perkin reaction and esterification were the same as for the phenanthrene-type derivatives. The yield obtained in these two transformations was 31%, similar to the phenanthrene analog.

Scheme 17. Perkin reaction, followed by esterification, to form intermediate (24).
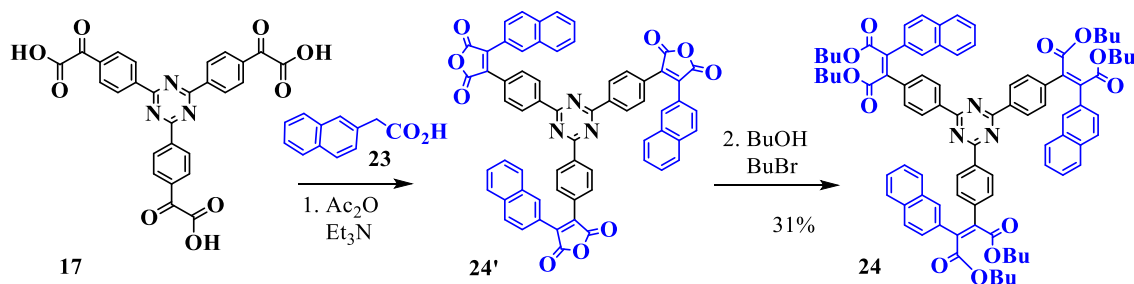


This derivative was characterized by $^1$H NMR in deuterated chloroform (CDCl$_3$). A discussion of the signals confirming its obtention is presented below.

The signals that are observed in the aromatic region of the spectrum correspond to the signals of the 2,4,6-triphenyl-s-triazine system (H2) and (H1) and the naphthalene system added by the Perkin reaction (highlighted in blue). The most shifted duplet with coupling constant of $J = 8.1$ Hz at 8.41 ppm (H2) stems from six hydrogens of the 2,4,6-triphenyl-s-triazine system closest to s-triazine (Ar-**H**). The signals that are observed at 7.69 ppm correspond to the signals of the naphthalene system, (H5) and (H8), an undefined signal. And at 7.66 ppm, the (*dd*) of smaller intensity with coupling constants $J = 7.6$ and $J = 2.1$ Hz corresponds to (H9). The doublet (*d*) at 7.57 ppm corresponds to (H3), with coupling constant $J = 8.6$ Hz, integrating for three hydrogens. The multiplet at 7.42 ppm is a signal referring to the hydrogens (H6) and (H7), with integral proportional to six hydrogens. At 7.27 ppm we have an (H1) duplet with a coupling constant of $J = 8.6$ Hz, the integral does not correspond to the expected six hydrogens, possibly due to the signals from the solvent residue that appears at the same shift. And a signal at 7.11 ppm corresponds to (H4), a double doublet with $J = 10.8$ and $J = 6.8$ Hz, integrating for three hydrogens.

One signal that is observed at 4.27 ppm is referring to the hydrogens neighboring the oxygen of the ester group (CO$_2$-C**H**$_2$-), the other three signals at 1.65, 134 and 0.90 ppm are the hydrogens further away from the ester group.

Figure 34. ¹H NMR spectrum of compound (**24**) in CDCl₃, 400 MHz.
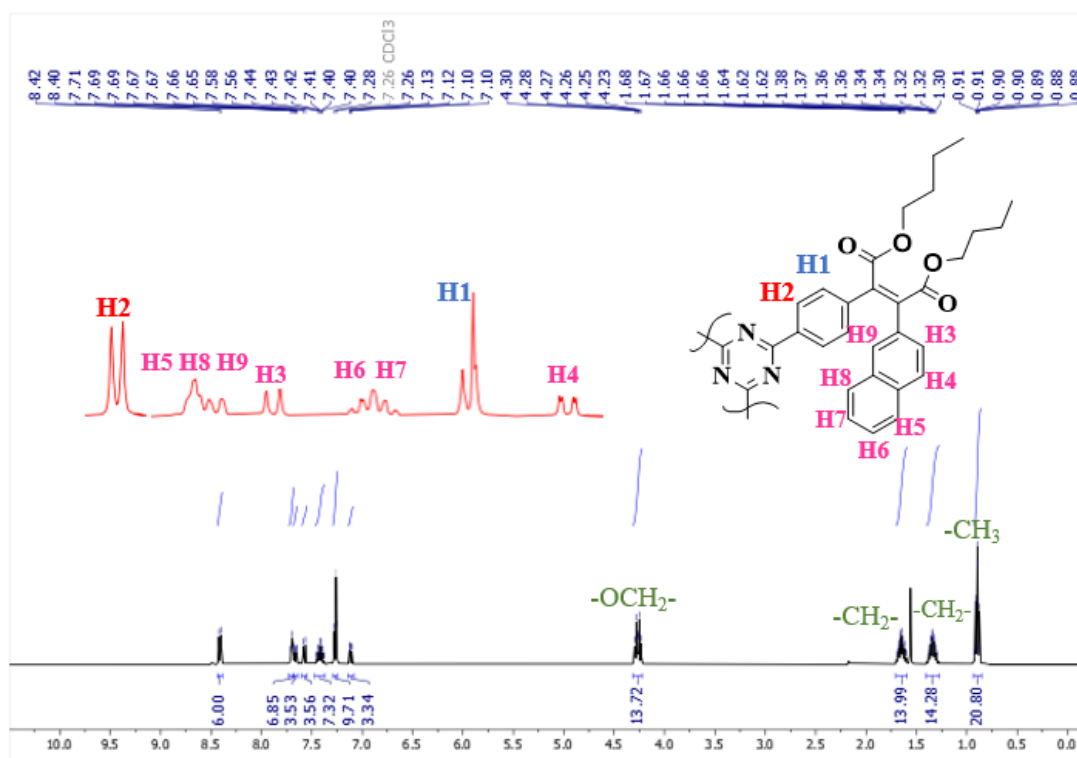


Alternatively, in order to try to improve the yields obtained for the Perkin reactions, hence the overall yield of the products, the Perkin reaction was tested with acetic acid bound to s-triazine and glyoxylic acid bound to phenylene or naphthalene (**Scheme 18**).

Scheme 18. Perkin reaction starting from the percursor (**20**), followed by esterification to form the hexa-ester intermediate.
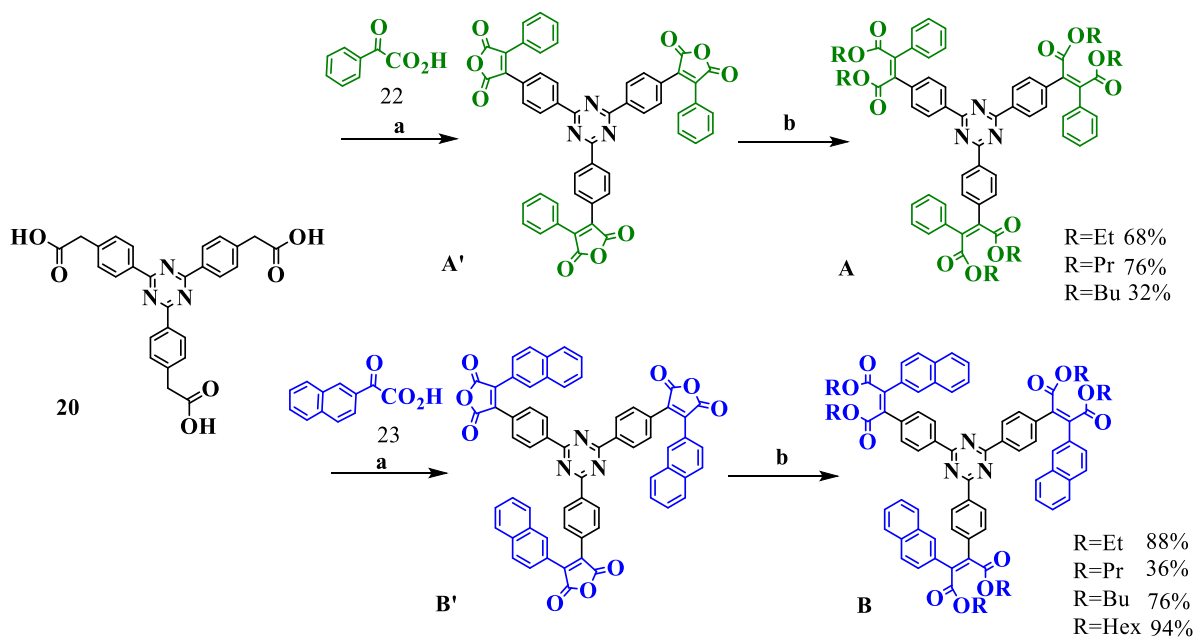


**Reagents and conditions**: a. Acetic anhydride, TEA, THF; b. alkyl alcohol, alkyl bromide, TEA.

When comparing the values of efficiency of Perkin's reaction for the same hexa-ester, e.g. the butyl derivative, it was observed that the yield more than doubled, going from 30% to 68%. From this result it was decided to follow this second method to obtain the symmetric products of this work, both the phenanthrene and [4]helicene derivatives.

Thus, for the other phenanthrene derivatives, Perkin's reaction occurs between the tri(acetic acid) (**20**) and phenylglyoxylic acid (**22**) under the same conditions described previously, but in the *in situ* esterification, the alcohol (ethanol, propanol, or butanol) and the alkyl bromide (bromoethane, bromopropane, or bromobutane) were varied according to the length of the alkyl chain desired in the esters. Purification was performed under the same conditions, obtaining the three derivatives with yields of 68%, 76%, and 32%, respectively.

Following the same methodology for the hexa-ester derivatives derived from [4]helicene, using 2-naphthylglyoxylic acid (**23**), esterification was additionnally performed with a long-chain alcohol and the corresponding alkyl halide (hexanol/bromohexane).

A total of four [4]helicene derivatives with ester groups and alkyl chains with two, three, four, and six carbon atoms were obtained. The yields of these steps were 80%, 36%, 76%, and 94%, respectively. All intermediates were properly characterized by ^{1}H NMR (see Appendix).

### 3.3.3 Photo-oxidative intramolecular cyclization: formation of polyaromatic arms

After the identification of all Perkin products we proceeded to the last step, the intramolecular photo-oxidative cyclization to obtain the targeted phenanthrene and [4]helicene arms.

The final compounds were obtained from the respective hexa-esters, in ethyl acetate solution, in the presence of oxygen and with a catalytic amount of iodine (0.3 g), by irradiation with a 150 W mercury lamp, inside a borosilicate immersion tube, in which cooling water circulated. After 48 hours, some of these materials precipitated in the solution and were then filtered, in some cases the solution was concentrated in the rotary evaporator, in both cases the products were purified by silica gel chromatographic column, using as eluent cyclohexane/acetone with increasing polarity, and finally recrystallized in butanol.

Figure 35. System used for preparation of the final compounds, at end of reaction with precipitated product stirred in iodine-colored ethyl acetate.



Characterization of the inedit compounds was performed by $^1$H and $^{13}$C NMR and high resolution mass spectrometry (HRMS). Two proton NMR spectra for each series, phenanthryl and [4]helicenyl, are discussed below by way of example. All spectra are presented in Appendix.

Scheme 19. Intramolecular photo-oxidative cyclization to form compounds **F₃R**.
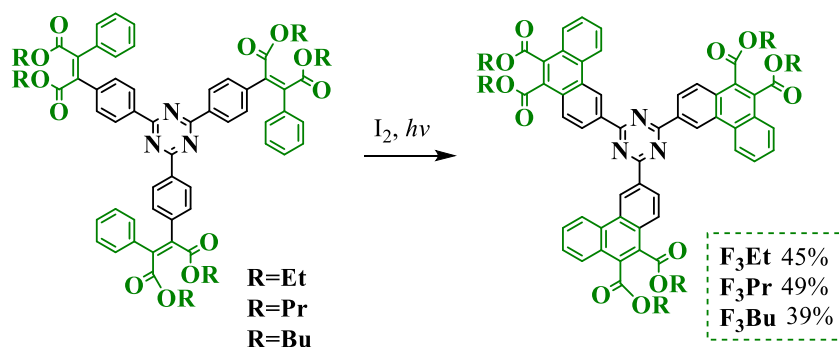


The phenanthryl derivatives have alkyl ester groups with two (**Et**), three (**Pr**) and four (**Bu**) carbon atoms on each aliphatic chain. For the homologue with six ethyl chains (**F₃Et**) the characterization is shown below.

In the aliphatic region of the $^1$H NMR spectrum (**Figure 36**) there are the signals referring to the methylene protons (-OCH$_2$-), this signal does not appear as a defined quartet due to the presence of two different ethyl chains in the molecule whose methylene signals overlap. Another signal in the aliphatic region is a triplet at 1.5 ppm referring to the methyl (-CH$_3$) signals, where no difference between the two ethyl groups is discerned. In the aromatic region one can clearly see the seven signals referring to the phenanthrene

system, all signals in the aromatic region integrating for three hydrogens each. The singlet is the signal most displaced to smaller field, at 9.29 ppm, referring to the hydrogen signal (H1) closest to the triazine ring, which possibly can make a hydrogen bond with the nitrogen of the triazine, which would justify its strong displacement. The double-doublet at 8.37 ppm, (H4) hydrogens, has coupling constants of $J1 = 8.4$ and $J2 = 1.5$ Hz. At 8.06 ppm, the doublet can be assigned to (H2) ($J = 8.1$ Hz), in proximity to the triazine ring. And at 7.80 there is a doublet referring to (H3), with a coupling constant of 8.3 Hz. The double-doublet at 7.71 ppm can be attributed to (H7), with coupling constants $J1 = 8.1$ and $J2 = 1.3$ Hz. The triplets are the most shielded signals, at 7.38 and 7.28 ppm, with coupling constants $J = 8.0$ and $J = 8.0$ Hz and are referring to the farthest hydrogens from the triazine, (H5) and (H6), the outermost portion of the phenanthrene.

Figure 36. $^1$H NMR spectrum of **F$_3$Et** in CD$_2$Cl$_2$, 400 MHz.
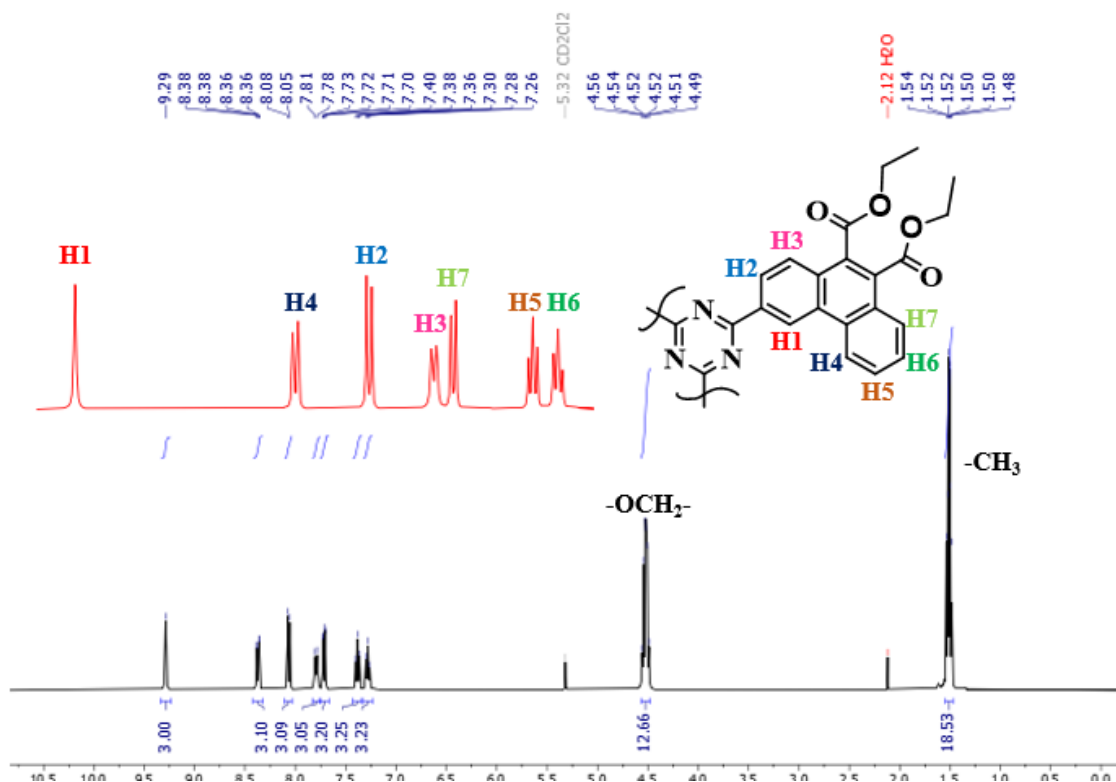


In the analysis of carbon nuclear magnetic resonance ($^{13}$C NMR) (**Figure 37**) it is confirmed that the compound **F$_3$Et** was obtained; because it is a theefold symmetric molecule it is observed only one set of signals corresponding to any of the three arms. Thus, seventeen signals are observed in the smaller field region of the spectrum, one signal corresponding to the three carbons of s-triazine (CN)$_3$ at 170.5 ppm, two signals referring to the six carbonyl carbons (C=O) at 167.8 and 167.7 ppm, and fourteen signals corresponding to the forty-two carbons of the three phenanthrene systems between 134.4

and 121.9 ppm. In the aliphatic region three signals are observed, two of them at 62.3 62.2 ppm referring to the methylenic carbons and the signal at 14.4 ppm corresponds to the methyl carbons.

Figure 37. $^{13}$C NMR spectrum of compound **F$_3$Et** in CD$_2$Cl$_2$, 100 MHz.
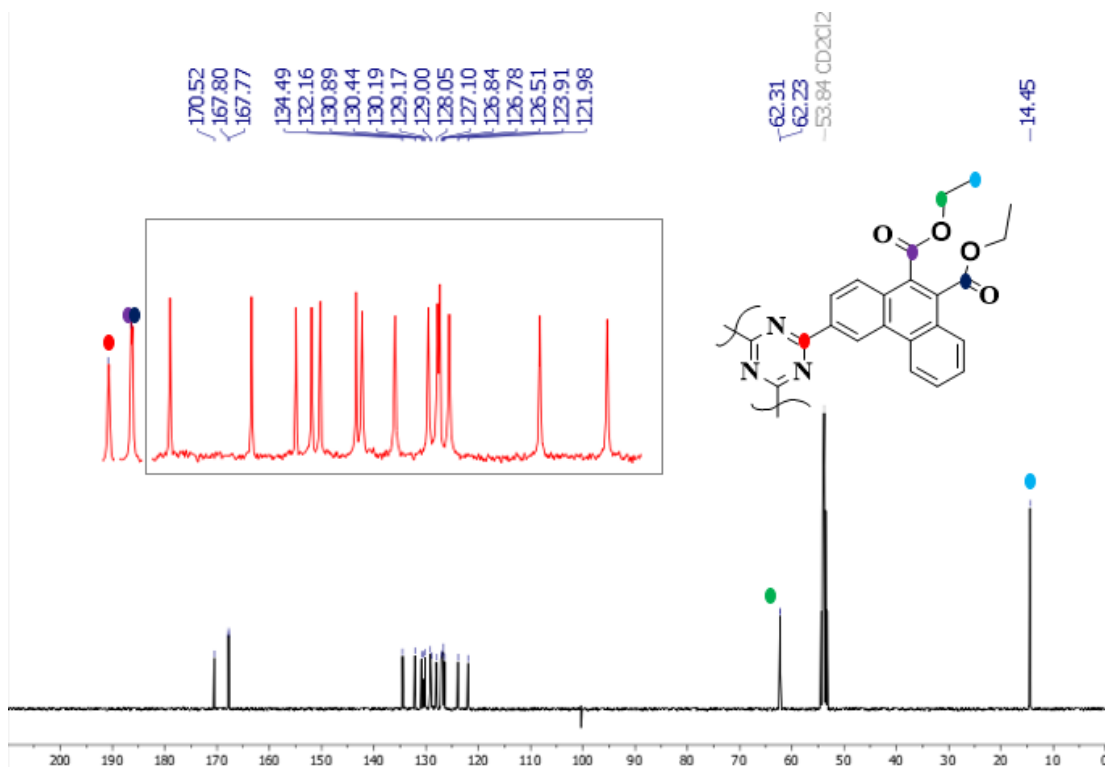


The helicene analogues vary in their ester chain length from two (**H$_3$Et**), via three (**H$_3$Pr**) and four (**H$_3$Bu**) to six carbons (**H$_3$Hex**) in each aliphatic chain. For the butyl homolog (**H$_3$Bu**), the formation and characterization are presented in the following.

Scheme 20. Intramolecular photo-oxidative cyclization to form compounds **H$_3$R**.
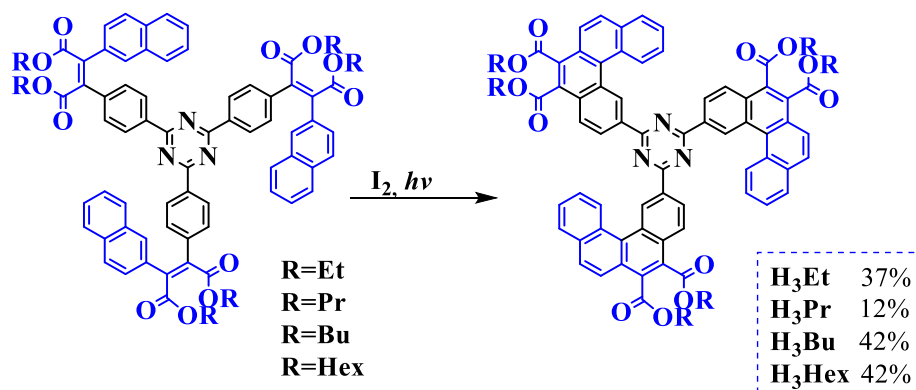


In the $^1$H NMR spectrum (**Figure 38**) in the aliphatic region the signals referring to the six alkyl chains linked to the six esters consist of those of the oxygen-neighboring methylene hydrogens (-O-CH$_2$-), this signal does not appear as a well-defined triplet due

to the two kinds of ethyl esters present in the molecule, and at 1.88 ppm, there is a multiplet with integral for 12 hydrogens, which can be assigned to the hydrogens of the second methylene. At 1.57 ppm, there is a further multiplet, referring to the signals of the third methylene next to the methyl; its integral is larger than what was expected, which may be due to overlap with the signal referring to the deuterated solvent's residual water. And at 1.06 ppm, the methyl signal can be observed as two overlapping triplets, integrating for eighteen hydrogens.

In the aromatic region, seven signals are present referring to the [4]helicene system. The singlet is the signal most shifted to smaller field, above 10 ppm, referring to the signal of the hydrogen closest to the triazine ring, (H1), which possibly can make a hydrogen bond with the nitrogen of the $s$-triazine; this would justify its shift, the integral of this signal corresponds to three hydrogens. The doublet coupling constant ($J = 8.5$ Hz), referring to the (H2) hydrogens is at a chemical shift of 9.02 ppm and integrates for three hydrogens. The most unshielded doublet, coupling constant ($J1 = 8.67$ Hz and $J2 = 1.5$ Hz), which can be assigned to (H9), with a 3H integral. At 8.45, there is a doublet that can be assigned to (H3), with coupling constant $J = 8.7$ Hz, integrating for three hydrogens. The signal at 7.99 ppm, a doublet that is fused to the double-doublet at 7.95 ppm; the coupling constant identified for the duplet at 7.99 ppm is $J = 3.0$ Hz and the constants assigned to ($dd$) are $J1 = 8.1$ Hz and $J2 = 1.5$ Hz, these signals together have integration for nine hydrogens, they can be assigned to the hydrogens H4, H5 and H6. The triplets are the most shielded signals, at 7.41 and 7.23 ppm, and are referring to the hydrogens farthest from the triazine, (H7) and (H8), with coupling constants $J = 7.5$ Hz and $J = 7.7$ Hz, both with integral for three hydrogens.

Figure 38. $^1$H NMR spectrum of compound **H₃Bu** in CD₂Cl₂, 400 MHz.
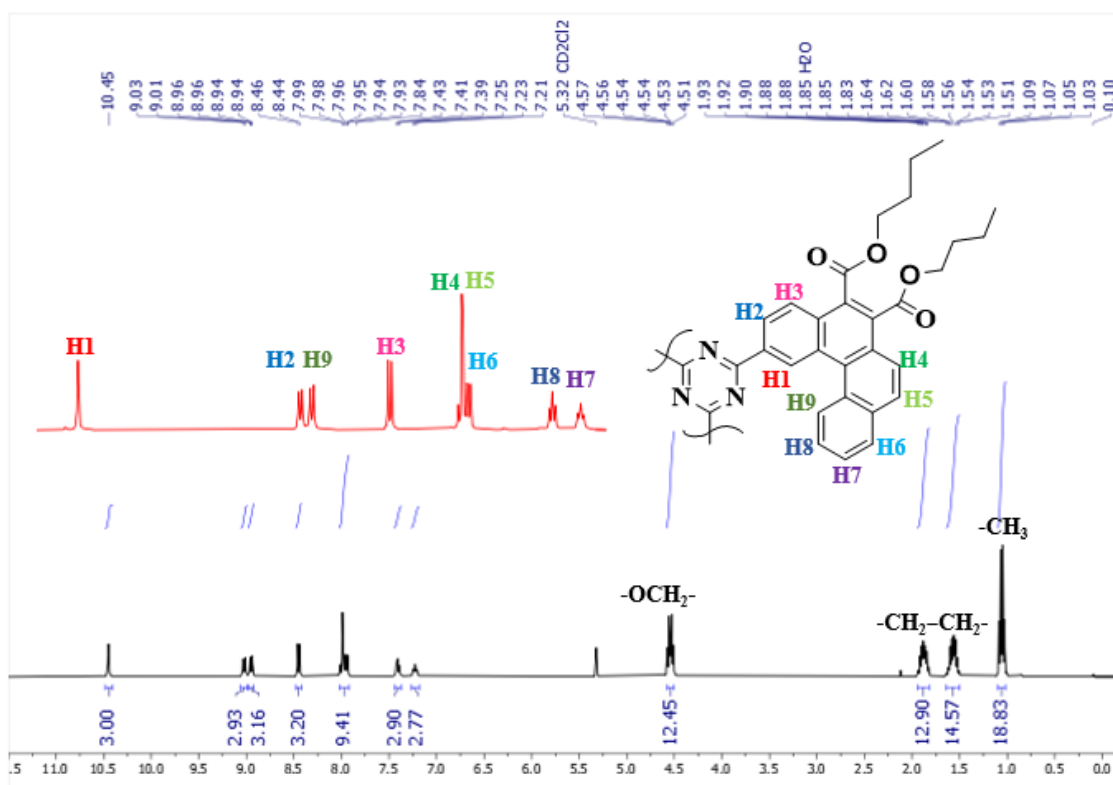


The obtainment of compound **H₃Bu** was confirmed by $^{13}$C NMR (**Figure 39**). Twenty signals are observed in the aromatic region of the spectrum, one signal corresponding to the three carbons of s-triazine (CN)₃ at 171.8 ppm, two signals referring to the six carbonyl carbons (C=O) at 168.4 and 167.9 ppm, and seventeen signals corresponding to the carbons of the three [4]helicene systems between 134.8 and 123.3 ppm. In the aliphatic region eight signals are observed, two of them at 66.6 and 66.5 ppm referring to the oxygen-bound methylenic carbons (-O-CH₂-), at 31.1 and 31.0 ppm to the following carbons of the alkyl chain, the signals at 19. 7 ppm match the signals of the methyl subsituted methylene carbons and the signals at 14.0 and 13.9 ppm correspond to the methyl carbons.

Figure 39. $^{13}$C NMR spectrum of compound **H$_3$Bu** in CD$_2$Cl$_2$, 100 MHz.
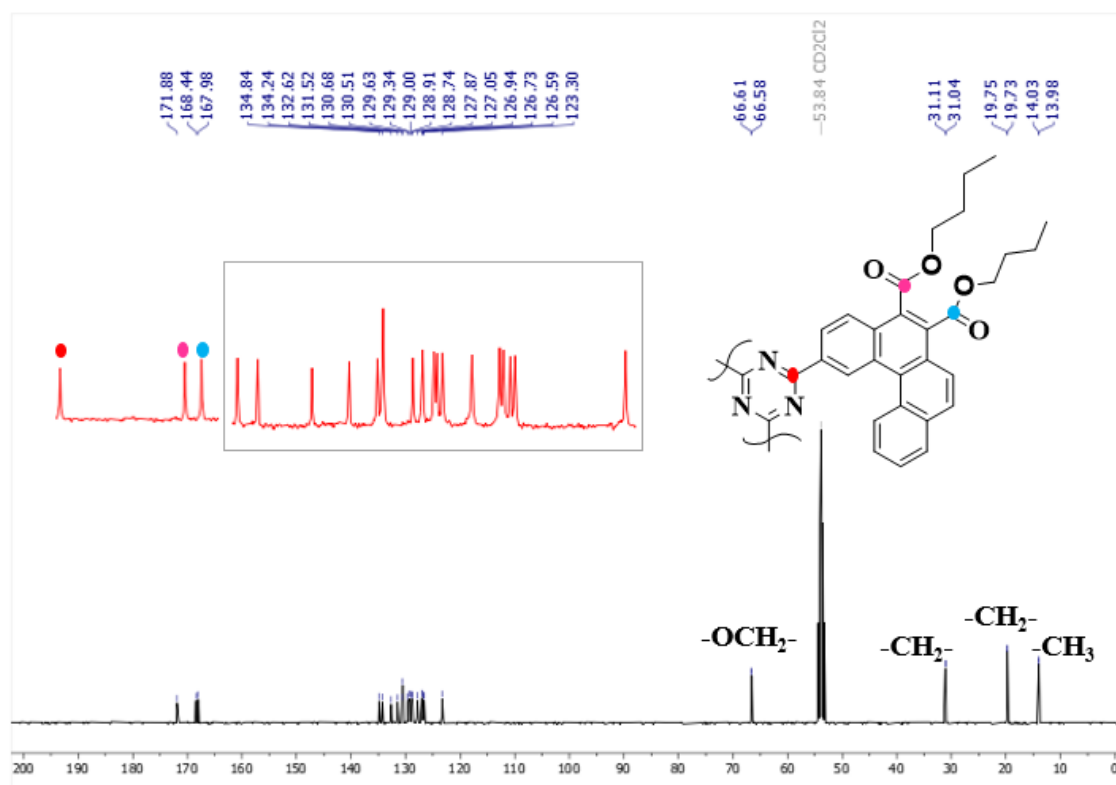


In addition to nuclear magnetic resonance characterization, all the final compounds were also characterized by high resolution mass spectrometry (HRMS) and the data are arranged in **Table 2**.

Table 2. High resolution mass spectrometry (HRMS) results.

| Compound | Molecular formula | Theoretical mass (Da) | Experimental mass (Da) | Error (Da) |
|:---:|:---:|:---:|:---:|:---:|
| **F$_3$Et** | [C$_{63}$H$_{51}$N$_3$O$_{12}$+Na]$^+$ | 1064.33650 | 1064.3378 | 0.0013 |
| **F$_3$Pr** | [C$_{69}$H$_{63}$N$_3$O$_{12}$+Na]$^+$ | 1148.43040 | 1148.4310 | 0.0006 |
| **F$_3$Bu** | [C$_{75}$H$_{75}$N$_3$O$_{12}$+Na]$^+$ | 1232.52430 | 1232.5245 | 0.0002 |
| **H$_3$Et** | [C$_{75}$H$_{57}$N$_3$O$_{12}$+Na]$^+$ | 1209.43822 | 1209.4396 | 0.00138 |
| **H$_3$Pr** | [C$_{81}$H$_{69}$N$_3$O$_{12}$+Na]$^+$ | 1298.47735 | 1298.4778 | 0.00045 |
| **H$_3$Bu** | [C$_{87}$H$_{81}$N$_3$O$_{12}$+Na]$^+$ | 1309.50646 | * | * |
| **H$_3$Hex** | [C$_{99}$H$_{105}$N$_3$O$_{12}$+Na]$^+$ | 1634.63531 | * | * |

*The compounds **H$_3$Bu** and **H$_3$Hex**, did not have their masses confirmed by HRMS, due to a limitation of the equipment, these compounds having very high molar masses.

The errors of the HRMS measurements ranged from 0.0002 to 0.00138 Da. The mass spectrometry values confirm the identity of the synthesized triazine-phenanthrene and triazine-helicene symmetric series.

### 3.3 Thermal properties of the final compounds

The presence of glass and mesophase transitions in the synthesized compounds was investigated. The studies were carried out, in sequence, by means of polarized light optical microscopy (POM), differential scanning calorimetry (DSC) and X-ray diffraction (XRD), by which the phase transition temperatures as well as the transition enthalpy are determined. Thermal stability was investigated by thermogravimetric analysis (TGA), by which the decomposition temperature of the materials was determined.

Some of the seven compounds showed LC mesomorphism. The presence of glass transitions ($T_g$) was also observed for some of them.

The thermal stability of the compounds was evaluated by thermogravimetric analysis (TGA) under nitrogen atmosphere and showed good thermal robustness with decomposition temperatures between 389 ºC for **F₃Bu** and 387 ºC for **H₃Bu**, data that demonstrate that the extension of the polyaromatic system and the vicinal ester substitution did not drastically affect the thermal stability of these compounds. Likewise, the increase of the alkyl chain length has no big influence on the stability, since the temperature observed for the short-chain phenanthrene homolog, **F₃Et**, was 385ºC (all temperatures correspond to a 5% mass loss).

The textures observed by polarized light optical microscopy (POM) were predominantly homeotropic (pseudo-isotropic), indicative of the hexagonal columnar mesophase in face-on alignment. The DSC analyses confirmed the existence of glass transitions.

Table 3 shows the thermal behavior of the seven compounds synthesized in this series.

Table 3. Summary of thermal data of the final triaryltriazine hexaesters.

| Compound | Transition | Tg (°C) on heating | T/°C, Heating (ΔH/kJ mol⁻¹) | T/°C, Cooling (ΔH/kJ mol⁻¹) |
|---|---|---|---|---|
| F₃Et | Cr-Cr(I) | - | 224 (26.14) | 174 (9.62) |
| | Cr-Iso | | > 375 | - |
| F₃Pr | Cr-Col | 81 | 150 (13.86) | * |
| | Col-Iso | | > 375°C | - |
| F₃Bu | Cr-Col | 19 | 108 (12.70) | * |
| | Col-Iso | | > 375°C | - |
| **H₃Et** | **Cr-Cr(I)** | **-** | **153 (13.27)** | ***** |
| | **Cr(I)-Iso** | | **325 (30.94)** | **298 (5.88)** |
| **H₃Pr** | **Cr-Iso** ₁°Ciclo | | **232 (45.4)** | **-** |
| | **Iso-Col₂** ₁°Ciclo | | **-** | **226°C (2.8)** |
| | **Col₂-Col₁** ₂°Ciclo | **-** | **179 (45.4)** | **142°C (2.8)** |
| | **Col₂-Iso** ₂°Ciclo | | **223 (2.8)** | |
| **H₃Bu** | **Cr-Iso** ₁°Ciclo | | **208 (35.3)** | ***** |
| | **Iso-Col** ₁°Ciclo | **39** | **-** | **143 (1.4)** |
| | **Col-Iso** ₂°Ciclo | | **149 (1.8)** | **205 (31.9)** |
| **H₃Hex** | **Cr-Iso** | **27** | **123 (31.93)** | ***** |

*Not observed in DSC.

The first compound studied is the hexa-ester with ethyl chains (**F₃Et**), which by thermal analyses, as by powder X-ray diffraction (XRD) (**Figure 40**), shows a phase transition between two different crystalline states upon heating at temperatures above the onset of melting at 224°C, and no transition to the isotropic liquid is observable by polarized light optical microscopy (POM) until our experimental limit of 375°C.

Figure 40. Comparison of powder X-ray spectra of **F₃Et** at room temperature and at 250°C.
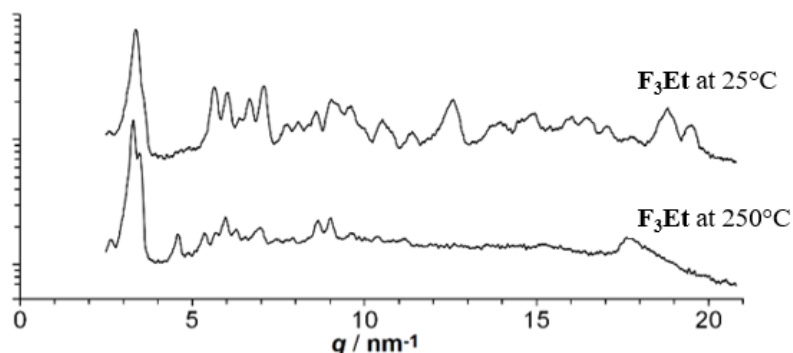


The hexa-ester homologue with propyl chain, **F₃Pr**, after melting at 150°C, also shows no clearing to the isotropic liquid below the equipment detection limit temperature, 375°C, but the state identified after its melting at 150°C was characterized as a columnar hexagonal mesophase, featuring (11) and (21) secondary peaks of the column lattice in the XRD corresponding to distances related by factors of √3 and √7 to the main lattice peak (**Figure 41**), which upon cooling to room temperature becomes rigid but maintains the organization achieved in mesophase.

The powder XRD spectra at 250 and 25°C for compound **F₃Pr**, (**Figure 41**) give evidence of a 10% contraction of the column-to-column distances (from 23.0 Å to 20.7 Å) over this temperature range, accompanied by modification of the diffraction pattern in the small angle region, but without loss of peaks (11) and (21).

Figure 41. X-ray spectra of powder of compound **F₃Pr** at room temperature and at high temperature. The root values indicate the q ratio with the main network peak on the left and correspond to a column lattice of hexagonal symmetry.
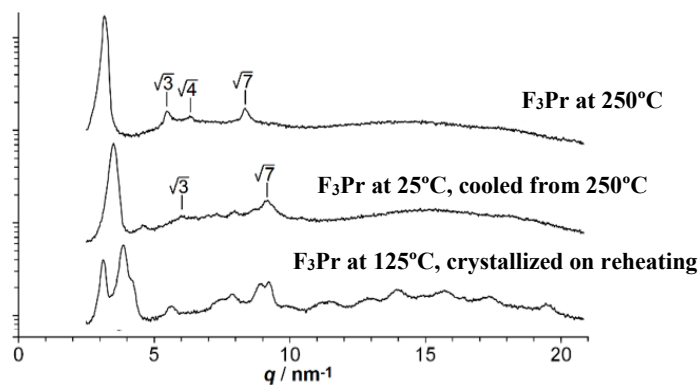


The diffractogram of compound **F₃Bu**, (**Figure 42**) shows the same pattern observed for the propyl homologue. Like its homologue **F₃Pr**, compound **F₃Bu** also

showed in the diffractogram secondary (11) and (21) peaks characteristic of at hexagonal columnar mesophase, which are conserved at 25°C.

Figure 42. Comparison of powder X-ray spectra of compound **F₃Bu** at room temperature and at high temperature.
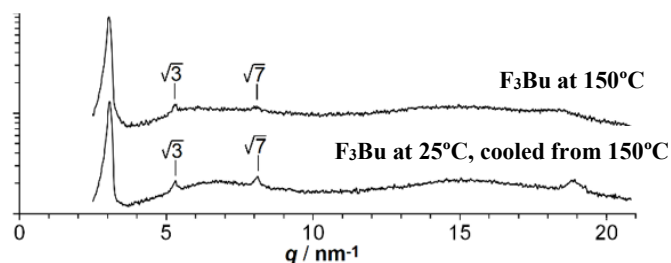


When analyzing the thermograms as for **F₃Pr**, a notable feature of the phenanthrene derivatives is an apparent slope change in the calorimetric cooling curve between 85 and 63°C (at -10°C/min), (**Figure 43**) while on the heating ramp a similar feature is observed above 81°C (heating ramp at 10°C/min; calorimetric glass transition temperatures are most commonly recorded on heating at this rate) with heating induced crystallization between 100 and 130°C. A glass transition at 81°C that restricts crystallization to the temperature domain between this temperature and the onset of melting at 150°C can be inferred.

In the butyl homologue, **F₃Bu**, which also shows a hexagonal columnar mesophase after melting at 108°C, the calorimetric glass transition is significantly reduced to 19°C, while, unlike **F₃Pr**, immediate crystallization after heating above this glass transition is not observed. Like its two smaller-chain counterparts, **F₃Bu** does not go isotropic below 375°C. The hexagonal lattice parameter of **F₃Bu** is preserved on cooling from 150°C to room temperature, with a column-to-column distance of 23.8 Å. The π stacking order within the columns, corresponding to an interdisk distance of about 3.3 Å, was improved at room temperature **(Figure 42)**, suggesting facilitated charge transport. The π stacking order was not clearly observed for **F₃Pr (Figure 41)**.

Although we were able to obtain with **F₃Pr** an anisotropic mesomorphic glassy state with a conveniently high glass transition temperature of 81°C, the lack of clearing to the isotropic liquid at practical temperatures and the drop of the glass transition temperature to only 19°C with **F₃Bu** prompted us to redesign the molecular structure.

Figure 43. Differential calorimetry scans on heating (red) of **F₃Pr**, **F₃Bu**, **H₃Bu** and **H₃Hex** at +10°C/min (after initial heating above the melting point and subsequent cooling with -10°C/min) and cooling scan (blue) of **F₃Pr** at -10°C/min.
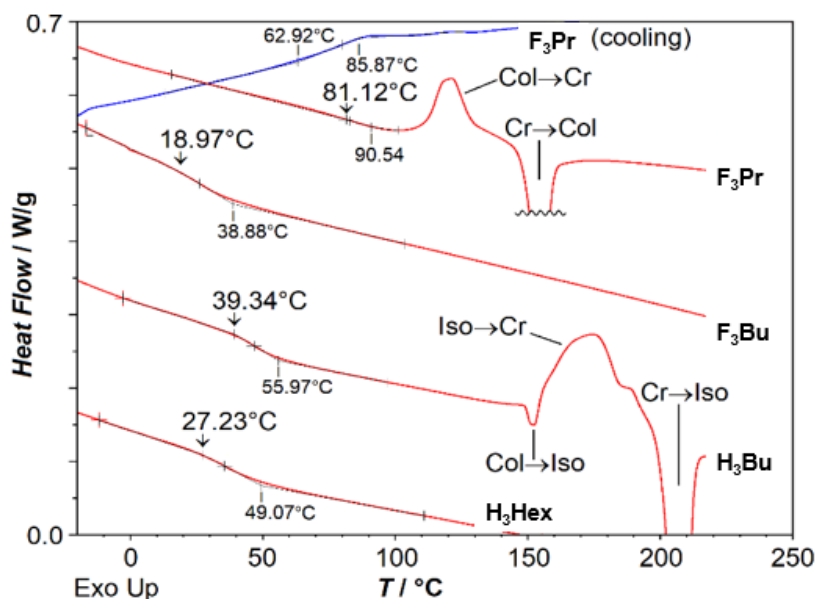


\* Glass transition onset temperatures on heating are indicated above vertical arrows; phase transitions are marked between Col = hexagonal columnar mesophase, Cr = crystalline state, and Iso = isotropic liquid.

To achieve the extension of the three arms forming a helicene-type polyaromatic system, 2-naphthylglyoxylic acid was used as Perkin adduct for the target esters with out-of-plane [4]helicenyl units. This system offered the prospect of both lowering the clarification temperature due to a less planar and relatively compact molecular shape, and hindering the crystallization tendency due to increased conformational variations, both in-plane and out-of-plane.

Thus, we analogously prepared helicenyl hexa-ester derivatives with ethyl, propryl and butyl chains (**H₃Et**, **H₃Pr** and **H₃Bu**). All three homologues show direct melting from the crystalline state to the isotropic liquid at attainable temperatures of 325°C, 232°C, and 205°C, respectively.

As observed for the **F₃Et** analog, no mesophase is identified for **H₃Et** on cooling from the isotropic liquid, and a crystal-crystal transition is observed by DSC (at 153°C on heating). In the diffractogram all crystal phases are of hexagonal symmetry, showing the characteristic (10), (11), (20), (21), (30), (22) and (31) peaks corresponding to hexagonal lattice distances in ratios of $1:\sqrt{3}:\sqrt{4}:\sqrt{7}:\sqrt{9}:\sqrt{12}:\sqrt{13}$, in addition to a multitude of other peaks (**Figure 44**).

Figure 44. Powder X-ray spectra of **H₃Et** at room temperature and elevated temperature. The root values indicate the q-ratio to the main nlattice peak on the left and correspond to a column lattice of hexagonal symmetry.
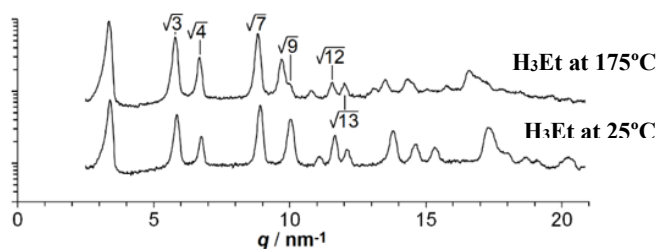


The consequence of the slight deplanarization of the aromatic core by the three [4]helicene arms is the destabilization of the hexagonal mesophase, enough to provide accessible clarification temperatures with **H₃Pr** and **H₃Bu** (in contrast to the analogues with phenanthrene arms), whereas for **H₃Et** the mesophase is suppressed in favor of the formation of a hexagonal crystal. On cooling and reheating, **H₃Pr** shows a reversible low enthalpy transition with onset temperatures on cooling and reheating with 10 ºC /min of 143 and 179°C, respectively (**Figure 45**).

Figure 45. Differential calorimetric scans on cooling (blue) and subsequent heating (red) of **H₃Pr** at -/+10°C/min (after initial heating above the melting point); with phase transitions between two hexagonal columnar mesophases (Col).
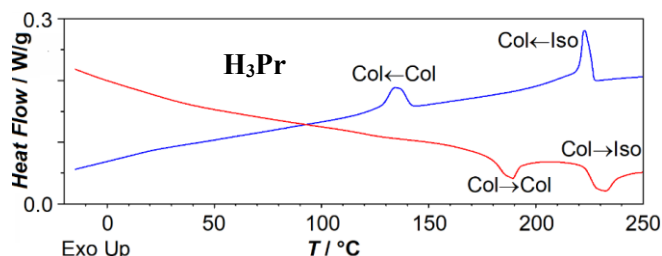


When attempting to associate this behavior observed in the thermogram with those characterized in the diffractogram (**Figure 46**) for **H₃Pr**, this transition is not associated with any change in the hexagonal symmetry of the mesophase and no appearance of peaks not associable with a 2D hexagonal lattice, but the higher order peaks of the column lattice increase significantly in relative intensity with respect to the primary lattice peak (and peaks √7, √9, √12 and √13 are now clearly expressed). Thus, the diffractogram showed an increase in the correlation length of the column lattice. Similar to **F₃Pr**, a slight contraction of the column-to-column distance (from 22.6 Å to 22.2 Å) and the π-stacking distance (from 3.8 Å to 3.7 Å) was also observed for **H₃Pr**.

Figure 46. X-ray spectra of **H₃Pr** and **H₃Bu**.
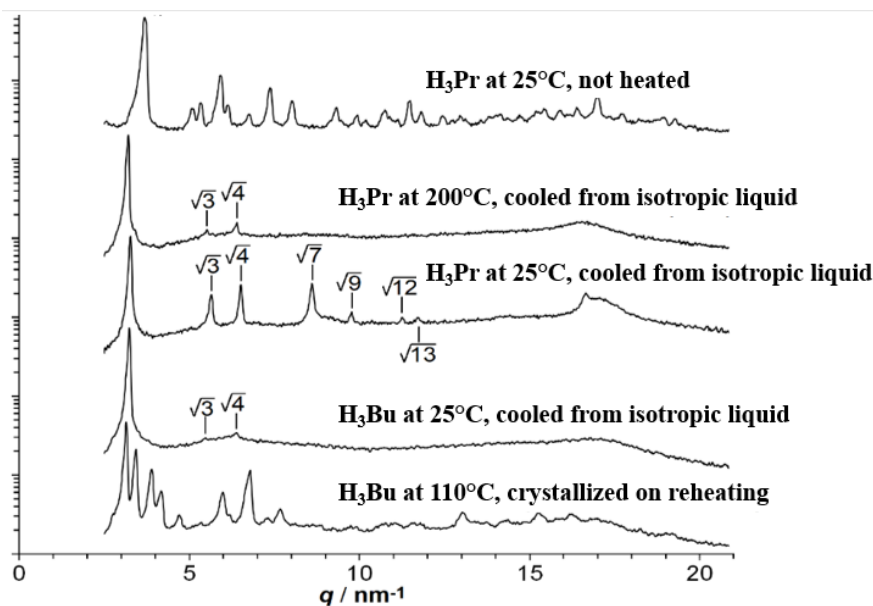


The diffractograms of as-obtained **H₃Pr** and **H₃Bu** show no prominent peaks associable with a hexagonal lattice prior to heating. They show monotropic mesophases upon cooling below their clearing points at 223 and 149°C, respectively, and associated √3 and √4 peaks.

No glass transition could be observed with **H₃Pr** within the temperature range. For the homologue **H₃Bu**, a mesomorphic glass was observed at room temperature with a calorimetric glass transition at 39°C upon reheating (+10°C/min). Thus, in **H₃Bu** the mesomorphic hexagonal columnar glassy state persists at room temperature (with a column-to-column distance of 21.9 Å and an intracolumnar distance of 3.7 Å). Melting and clearing temperatures are conveniently accessible at 205°C and 149°C. By polarized light microscope (POM), the observed textures are typical of the hexagonal columnar mesophase (**Figure 47**).

Figure 47. a) Growth between glass plates of the hexagonal columnar mesophase of **H₃Bu** in homeotropic alignment on cooling through the isotropic-columnar phase transition (POM with

slightly uncrossed poolarizers); b) Fan-shattered texture in hexagonal columnar mesophase of **H₃Bu** on cooling by isotropic-columnar phase transition;
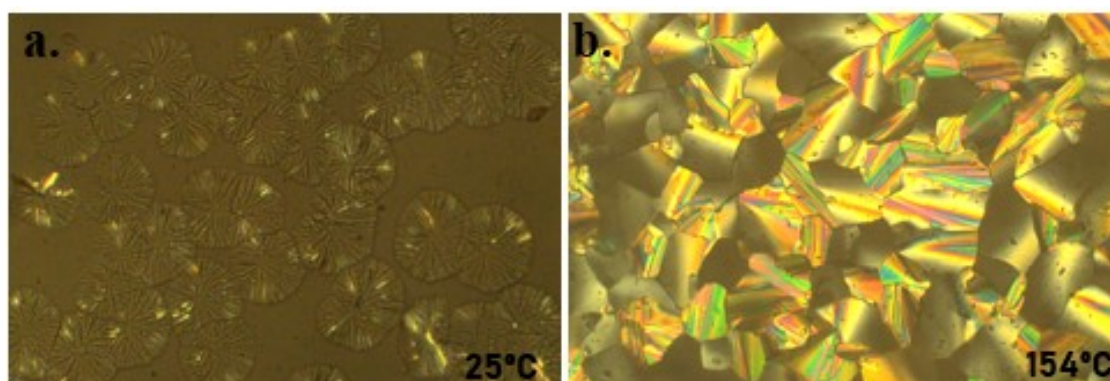


In order to assess whether the elongation of alkyl chains into derivatives with three [4]helicene arms would still allow a mesomorphic glass at room temperature, we prepared the homologue **H3Hex** with n-hexyl-ester substituents, and were surprised to find that it is not mesogenic, but forms an isotropic glass (Tg = 27°C upon reheating at +10°C/min) after melting at 123°C and cooling back to room temperature.

Thus, the modification of the molecular shape from a more planar structure with phenanthrene arms to a not fully planar structure with [4]helicene arms resulted in a drastic reduction of the thermal range of the mesophase, while the glass transitions increased from 19°C in **F3Bu** to 39°C for its analogue **H3Bu** allowing to obtain a material that combines a mesomorphic hexagonal glassy columnar state at room temperature with the formation of an isotropic liquid at conveniently achievable temperatures.

### 3.4 Photophysical properties of the final compounds

The photophysical properties of the two series of symmetric compounds were investigated both in dilute chloroform solution and in thin films.

In the solution studies the main absorption and emission bands were investigated. For the phenanthrene series, **F3R**, the UV spectra in chloroform solution ($10^{-5}$ M) (**Figure 48 right**), show an intense band with absorption maxima between 342 and 272 nm attributed to the π-π* electronic transitions throughout the aromatic portion of the molecules. The spectra are similar (dark blue and light blue) as the chromophore is the same in **F3Pr** (dark blue) and **F3Bu** (light blue). As for the helicene derivatives, **H3Et**, **H3Pr** and **H3Bu** (brown, red and pink) show absorption maxima around 361, 345 and 316 nm and a weaker absorption band near 405 nm.

The emission of these compounds was also investigated (also in chloroform solution). In the fluorescence spectra (**Figure 48 right**) a single emission peak can be observed at 409 nm for the **F₃R** series and at 458 nm for **H₃R**; all homologues emit in the same region within their series, there is no distinction between any of them.

Figure 48. Normalized spectra of **F₃Pr**, **F₃Bu** (dark blue and light blue); **H₃Et**, **H₃Pr** and **H₃Bu** (brown, red, pink), in CHCl₃ (10⁻⁵ M) solution; left: Absorption spectra; right: Emission spectra.
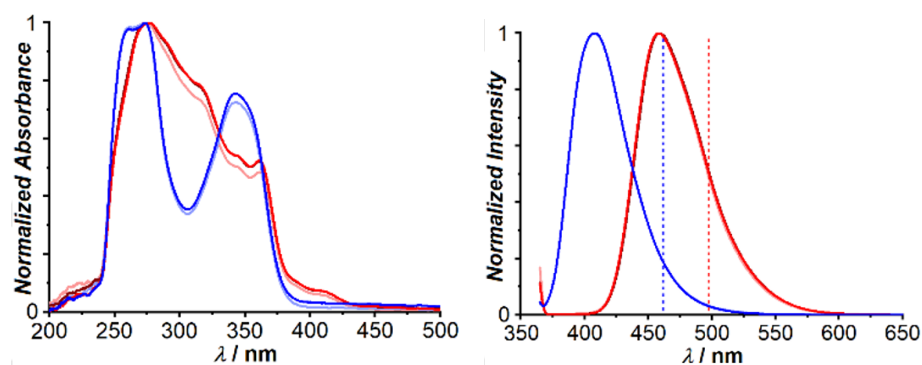


While the absorption and emission behavior in solution was quite similar between the **F₃R** homologues and between the **H₃R** homologues, the behavior observed for the emission from films of these compounds varied significantly between homologues, especially after heating of the films (**Figure 49**).

The emission of the compounds that exhibit hexagonal columnar mesomorphism and subsequent glassy transitions at room temperature: **F₃Pr**, **F₃Bu** and **H₃Bu**, remained unchanged after the heating treatment of the films and subsequent cooling back to room temperature, which suggests to us that the same mesogenic state is obtained when preparing the films at room temperature and after returning to room temperature after heating to melting temperature. On the other hand, the emission spectra of **H₃Et** and **H₃Pr**, which adopt respectively a hexagonal crystal state and a second columnar mesophase of greater order, show a small bathochromic shift after heating, oft 28 nm (**H₃Et**) and 11 nm (**H₃Pr**). Thus, the higher order of these films is apparently obtained only after heating the film.

When comparing the behavior in solution and in film of these compounds, we observe that the batochromic shift from solution emission to columnar mesophase emission is more pronounced for the phenanthrene-derived, planar, **F₃R** series of compounds than for the non-planar helicene-derived **H₃R** series. The implication is that the flatter core of **F₃R** allows for more pronounced chromophore aggregation in the mesophase than the less easily stacked, non-planar **H₃R** system.

Figure 49. Normalized spectra of **F₃Pr**, **F₃Bu** (dark blue and light blue); **H₃Et**, **H₃Pr** and **H₃Bu** (brown, red, pink), in drop-cast thin films; left: Emission spectra before heating; Right: Emission spectra after heating.
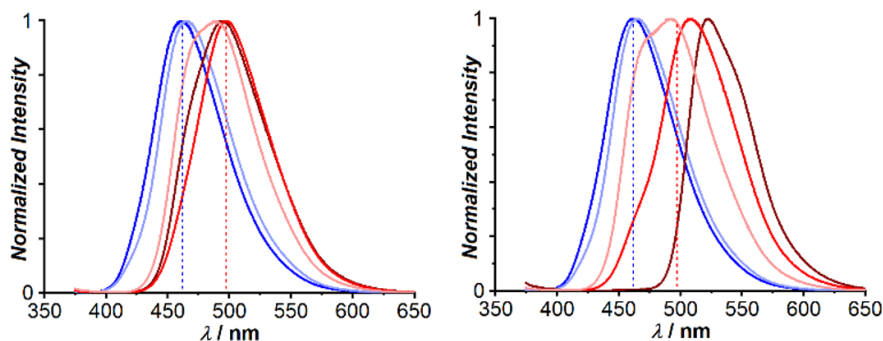


Table 4 summarizes the photoluminescence quantum yield (PLQY) data, which show that columnar aggregation tends to increase the emission yield, as the thin films show higher PLQYs than the solutions. No significant change in PLQY is observed upon heating. The increase in PLQY for the columnar film constitutes a peculiar form of aggregation-enhanced emission.

Table 4. Photoluminescence quantum yield and emission maximum in chloroform solution and in drop-cast film, upon excitation at 360 nm.

|  | F₃Et | F₃Pr | F₃Bu | H₃Et | H₃Pr | H₃Bu | H₃Hex |
|---|---|---|---|---|---|---|---|
| **Solution (CHCl₃)** | 22% 409 nm | 21% 407 nm | 22% 409 nm | 12% 459 nm | 12% 458 nm | 12% 459 nm | 12% 459 nm |
| **As-cast film** | 27% 462 nm | 45% 462 nm | 49% 465 nm | 20% 495 nm | 23% 498 nm | 14% 489 nm | 17% 500 nm |
| **Annealed film** | n/a (does not melt) | 44% 461 nm | 46% 466 nm | 24% 523 nm | 23% 509 nm | 13% 493 nm | 16% 505 nm |

DFT and TD-DFT calculations were performed on optimized geometries of the methyl homologues **F₃Me** and **H₃Me** to gain insights into the configurations of the excited states. For **F₃Me** the low-energy band is related to π-π* transitions mainly centered on the triazine core, while the high-energy band is also due to π-π* transitions, but mainly scattered through the phenanthrene structure. In **H₃Me** the adopted geometry with lower planarity leads to a different absorption profile: The low intensity band near 400 nm arises from a charge transfer state from helicene to triazine. The other transitions are similar to those of F₃Me, with intermediate energy bands related to π-π* transitions centered on the triazine and those of high energy scattered through the helicene structure.

From the emission in solution at 375 nm for **F₃R** and at 420 nm for **H₃R**, energies of the first excited state S₁ of 3.31 eV for **F₃R** and 2.95 eV for **H₃R** can be inferred. From TD-DFT calculations on optimized geometries, S₁ energies were obtained that are very

close to the values inferred from emission in solution: 3.347 eV for **F₃Me** and 2.963 for **H₃Me**. We also calculated the energy of $T_1$ excited triplet states on the same geometries using SOC-TD-DFT, obtaining 2.637 eV for **F₃Me** and 2.464 eV for **H₃Me**. The good correspondence of the experimental and DFT-calculated energy values for $S_1$ indicates that the $T_1$ energies obtained over the same geometries can also be good estimates. Materials such as these with $T_1$ energies around 2.5 eV can be considered as matrices for TADF emitters that emit light of slightly lower energy, i.e., in the green-yellow range of the visible spectrum.

# 4. RESULTS AND DISCUSSION – PART 2

*Series 2: Non-symmetric molecules derived from 1,3,5-triazine.*

## 4.1 Structural design and synthetic strategy

The results of the two series of symmetric compounds were quite promising. However, some materials still have thermal limitations, such as inconvenient clearing points and low glass transition temperatures.

Seeking to overcome these difficulties, in the first step of the work (chapter 3) the ester alkyl chains were varied (**F₃R**), which did not bring sufficient results, but showed that the useful range of chain lengths is limited to butyl and shorter. Then, in a second attempt to improve the performance of the triaryltriazine derivatives, the aromatic system was increased modifying the planar phenanthrene type arms to [4]helicene (**H₃R**), slightly non-planar, which brought improvement in some thermal aspects, but still with glass transition temperatures far from those desired.

In this perspective, the present work proposes to prepare a series of non-symmetric compounds. The non-symmetric molecules are based on the designs of the triphenylthriazine triesters published by Vieira and co-workers (2021) (compound **2**), but integrating one or two phenanthrene- or [4]helicene-diester groups replacing two or one m-benzoate groups (**F₃R** and **H₃R**) (**Figure 50**).

Figure 50. Conceptual precursor compounds of the non-symmetric targets.
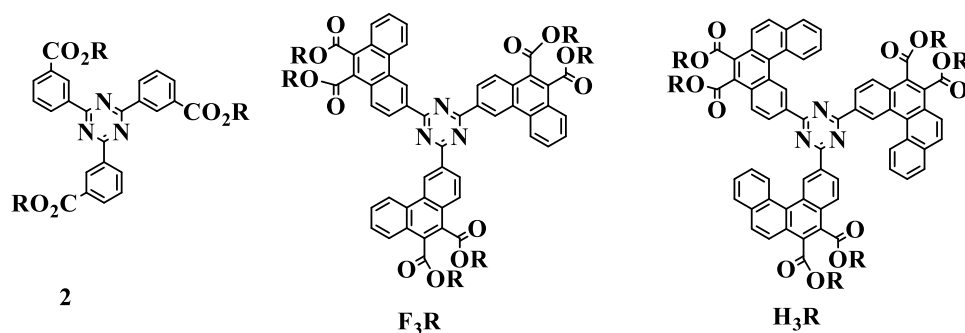


Despite not being symmetric the proposed molecules have not completely lost the star shape favored by the C3 symmetry of s-triazine, remaining with a discotic shape, the symmetry lost only in the arms. We will try to minimize of the alkyl chain length of the esters attached to the phenanthrene and/or helicene systems to ethyl (hoping that the reduced symmetry and lower molecular weight will allow for the appearance of a

mesophase at shorter alkyl lengths than in the symmetric series), and we will stick to methyl at the ester of the 3-benzoate system.

There are two proposals for non-symmetric molecules, in the first case, we will fix two m-MeO$_2$C-C$_6$H$_4$- arms on the triazine ring and we will vary only one arm between phenanthrene diester and [4]helicene diester. And in the second case, only one arm of the methyl m-benzoate type will be fixed and the other two, symmetrical to each other, will have the aromatic systems modified. The retrosyntheses for the two types of structures for these series are illustrated below (**Scheme 21**).

Scheme 21. Retrosynthetic analysis of the compounds **F$_1$Et** and **F$_2$Et**.
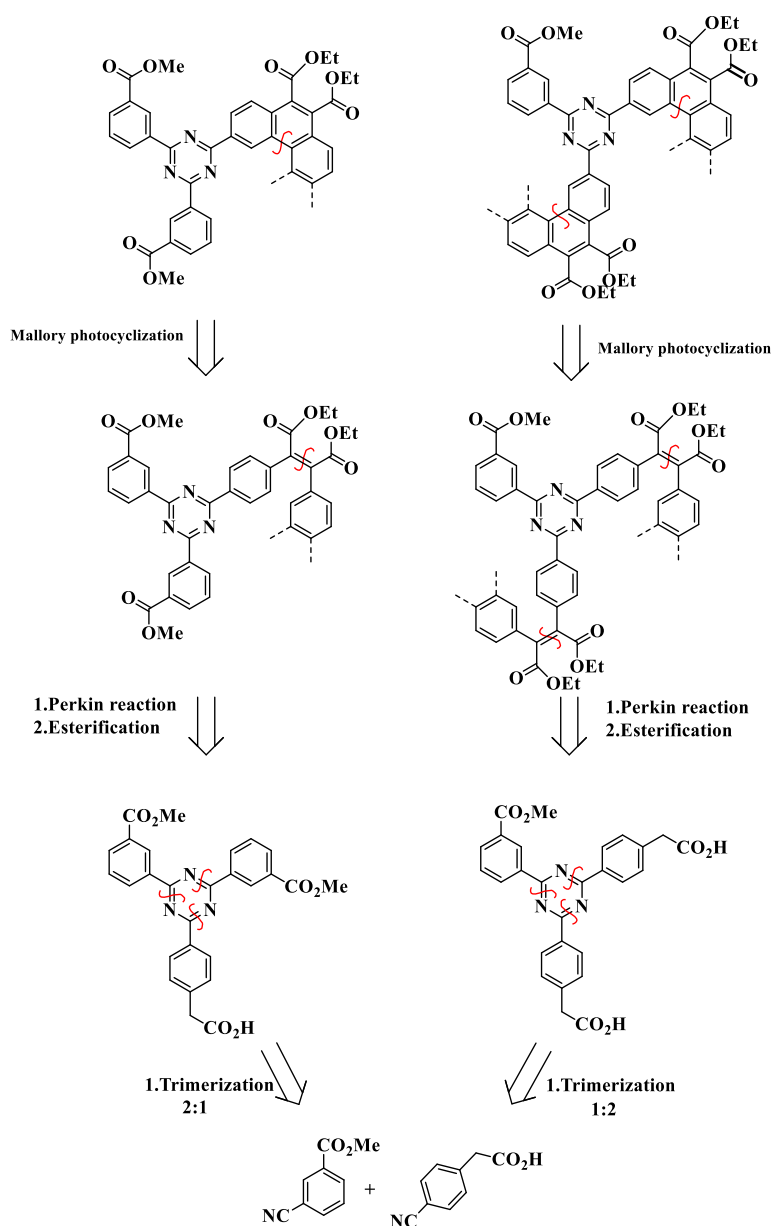
The synthetic methods used to construct the molecules will be the same as already described for the symmetric molecules (chapter 3): i. trimerization, ii. glyoxylic Perkin reaction/esterification and iii. photocyclization forming the final polyaromatic systems (**Scheme 22**).

Scheme 22. Proposed synthetic route for the phenanthrylderivatives $F_1R$ and $F_2R$.
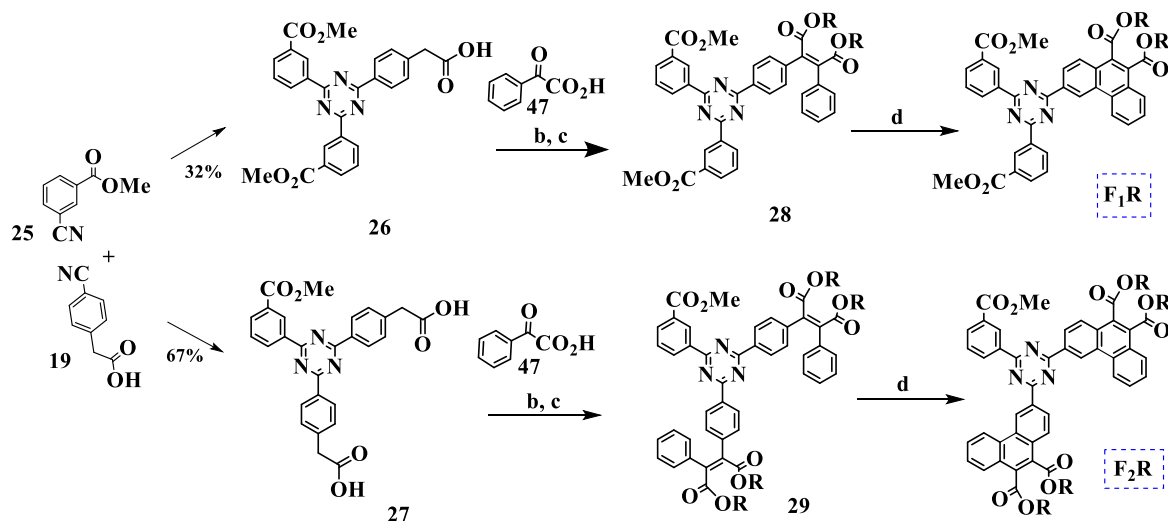


**Reagents and conditions:** a. Triflic acid, 0ºC, overnight; b. Acetic anhydride, TEA, THF; c. alkyl alcohol, alkyl bromide, TEA; d. iodine, ethyl acetate.

## 4.2 Synthesis and characterization of non-symmetric derivatives

The syntheses employed in this part of the work will be detailed below, and the characterizations of the synthesized compounds will be presented and discussed. The Hydrogen Nuclear Magnetic Resonance ($^1$H NMR) technique was used to characterize the intermediates and the final compounds besides $^1$H NMR were also characterized by Carbon Nuclear Magnetic Resonance ($^{13}$C NMR) and Mass Spectrometry (see appendix A).

### 4.2.1 Synthesis of the building block: non-symmetric triphenyl-s-triazine

Just as for symmetric compounds, the triazine formation reaction is the initial step for synthesis of the designed molecules. The non-symmetrical s-triazine is formed via the trimerization reaction of methyl 3-cyanobenzoate and 4-cyanophenylacetic acid, in triflic acid in the absence of solvent. This reaction has satisfactory yields and a simple workup, but the purification and separation of this product mixture is somewhat laborious. As shown in **Scheme 23**, the co-trimerization of these two nitriles generates four possible products, among them the two building blocks used in the two series of compounds discussed in this chapter.

Scheme 23. Non-symmetric trimerization reaction.
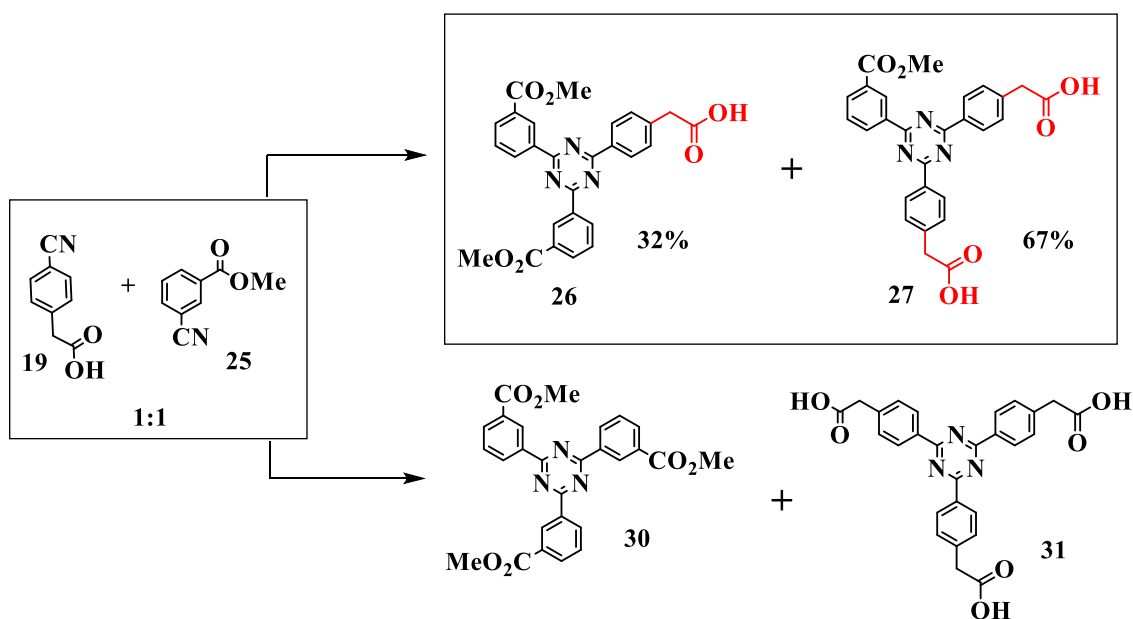


The purification and separation of this mixture of trimerization products was an important and difficult step of the work, due to the similar polarities of the diacid (**27**) and monoacid (**26**) products. However, using a silica gel chromatographic column and a variable chloroform:acetone elution system with increasing polarity, it was possible to separate these compounds with average yields of 32 % and 67%, respectively.

The various attempts to optimize the yields of the two desired products by varying the ratio between starting nitriles were not very efficient, the equimolar ratio of methyl 3-cyanobenzoate and 4-cyanophenylacetic acid was the best ratio found. Attempts to favor the formation of products (**26**) and (**27**), were not successful by varying the ratio to 2:1 or 1:2. This variation only favored the formation of a greater amount of the tri-ester (**30**) or the tri-acid (**31**).

In the $^1$H NMR spectrum shown in **Figure 51**, the s-triazine with two methyl 3-benzoate arms and one phenylacetic acid arm is identified (**26**). In the aromatic region there are six signals referring to the six different types of hydrogens present in the molecule. All signals in the aromatic region integrate for two hydrogens, confirming the identity of (**26**). The signal at 8.80 ppm is the smaller field signal and is a singlet, which can be assigned to the signal of the hydrogen of the methyl 3-benzoate portion (Ar-H3), between the s-triazine ring and the methyl ester; probably this hydrogen is in an intramolecular hydrogen bond interaction. At 8.54 ppm there is a doublet corresponding to the other hydrogen signal of the methyl 3-benzoate ring close to the s-triazine ring (Ar-

H4), with a coupling constant of $J = 7.8$ Hz. In the sequence there follows another doublet at 8.29 ppm, $J = 8.4$ Hz, this signal can be attributed to the hydrogen of the phenylacetic acid arm closer to s-triazine (Ar-H1); this proximity facilitates a hydrogen bond, which would explain the shift to smaller field. At 8.03 ppm there is a doublet, $J = 6.2$ Hz, corresponding to the external hydrogen neighboring the methyl ester group (Ar-H6). The triplet that appears at 7.65 ppm, $J1 = 7.8$ Hz, refers to the hydrogen of the methyl 3-benzoate ring with two neighboring hydrogens (Ar-H5). The most high-field doublet at 7.41 ppm, $J = 8.4$ Hz, is the signal referring to the remaining hydrogens of the phenylacetic acid arm (Ar-H2). In the aliphatic region there are two singlets, one signal with higher intensity corresponds to the signal of the methyl ester hydrogens at 3.89 ppm (Ar-COO-CH$_3$) and the other singlet with lower intensity at a chemical shift of 3.66 ppm corresponds to the signal of the methylene hydrogens (Ar-CH$_2$-CO$_2$H).

Figure 51. Non-symmetric precursor compound **26** in DMSO-$d_6$, 400 MHz.
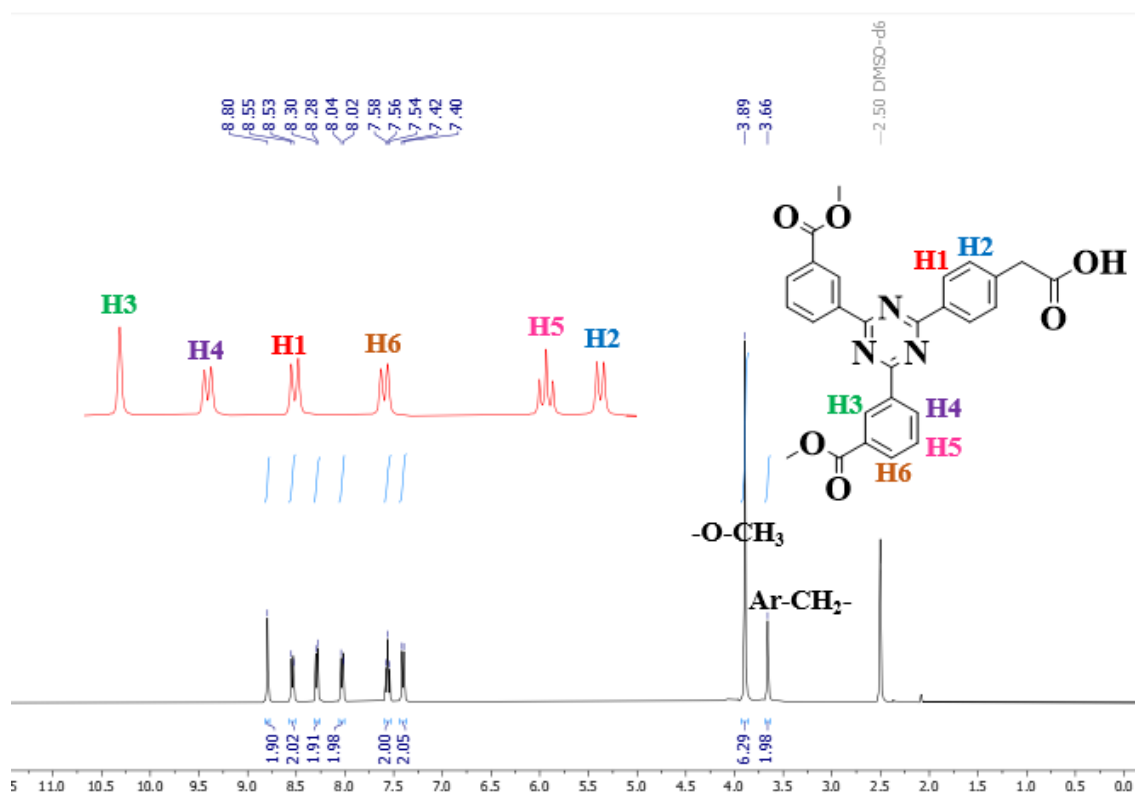


The second trimeric intermediate obtained from the trimerization of methyl 3-cyanobenzoate and 4-cyanophenylacetic acid is s-triazine with one methyl 3-benzoate arm and two phenylacetic acid arms, compound (**27**). Its obtainment is confirmed by $^1$H NMR as presented in **Figure 52**. At 9.10 ppm there is a signal of a singlet integrating for

one hydrogen, which is possibly the signal of the hydrogen of the methyl 3-benzoate portion (Ar-H3) between the s-triazine ring and the methyl ester; this hydrogen may be in a hydrogen bond with the nitrogen of s-triazine (Ar-H---N), which would explain its shift to smaller field. Next, a doublet is observed at 8.85 ppm, $J = 9.0$ Hz, of the methyl 3-benzoate ring, close to the s-triazine ring (Ar-H4). There is another doublet at 8.57 ppm, $J = 8.4$ Hz, integrating for four hydrogens, attributed to the hydrogens of the phenylacetic acid ring closer to s-triazine (Ar-H1). At a chemical shift of 8.18 ppm there is a doublet, $J = 7.8$ Hz, corresponding to the other hydrogen neighboring the methyl ester group (Ar-H6). The triplet that appears at 7.73 ppm, $J = 7.8$ Hz, refers to the hydrogen of the methyl 3-benzoate ring with two neighboring hydrogens (Ar-H5). The most high-field shifted signal can be attributed to the outer hydrogens of the phenylacetic acid arms (Ar-H2), a doublet with a coupling constant, $J = 8.4$ Hz, inetrating for four hydrogens. In the aliphatic region there are two singlets, one corresponding to the methyl ester at 3.93 ppm and the other at 3.73 ppm corresponding to the methylene next tot the acid group.

Figure 52. $^1$H NMR spectrum of compound **27** in DMSO-$d_6$, 400 MHz.
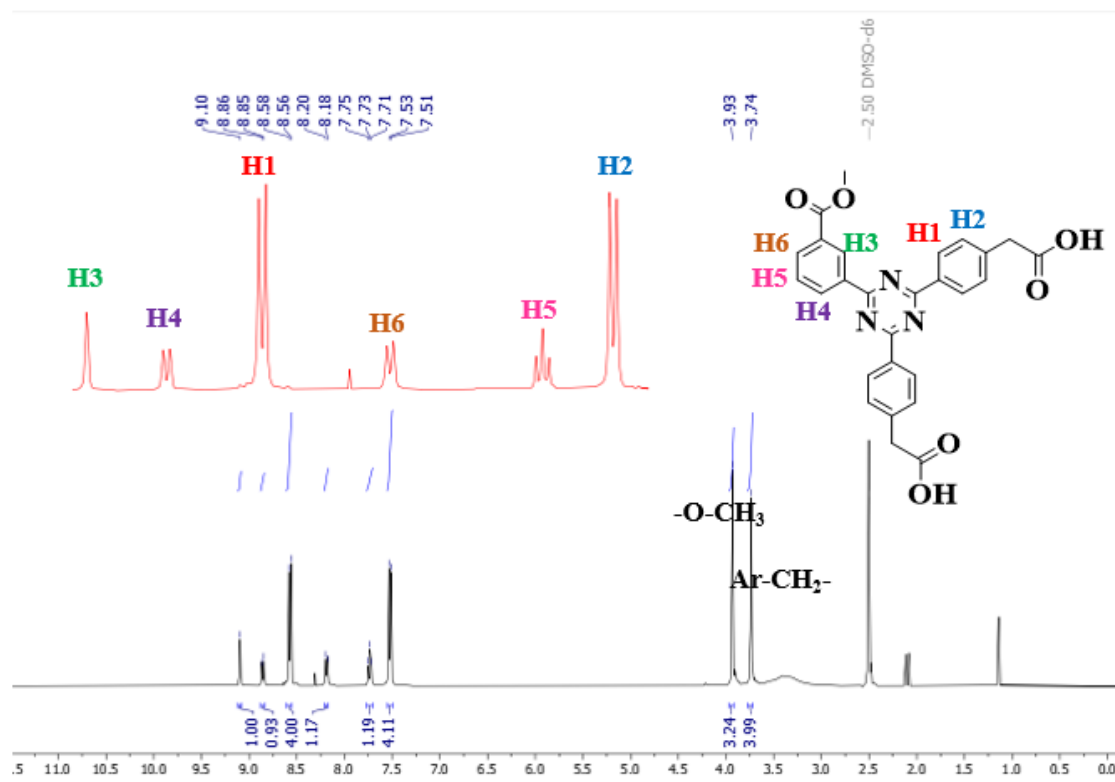
### 4.2.2. Perkin products: construction of the non-symmetric compounds with stilbene and methyl 3-benzoate arms

Figure 53. Building blocks of the non-symmetric series.



26

27
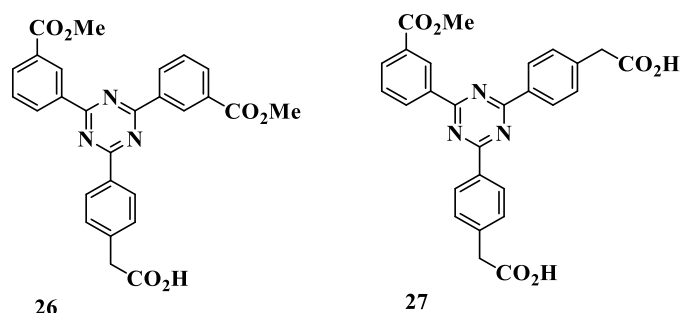
With these key molecules in hands, the next step is the Perkin reaction to form the derivatives with stilbene type arms. This reaction occurs between the building block (**26**) and commercial phenylglyoxylic acid (**22**), in a molar ratio of 1 equivalent of **65** to 2.3 equivalents of (**22**), in acetic anhydride, triethylamine and dry THF under reflux for an average period of 24 hours and led to the anhydride (**28'**). The anhydride obtained in the first step was not isolated, as an *in situ* esterification reaction is carried out by adding ethanol, bromoethane and triethylamine and refluxing for another 24 hours to form (**28**). Purification of the tetra-ester (**28**) was done on silica gel chromatographic column (eluent cyclohexane:acetone) followed by recrystallization in butanol (**Scheme 24**). The yield over both steps was 62%. Intermediate (**28**) was characterized by ^{1}H NMR (**Figure 54**).

Scheme 24. Perkin reaction of compound **26**, followed by *in situ* esterification, forming compound **28**.



26

28'

28

In the hydrogen nuclear magnetic resonance spectrum, it is possible to observe in the aromatic region the signals referring to both the stilbene system and to the methyl 3-benzoate. At 9.19 ppm th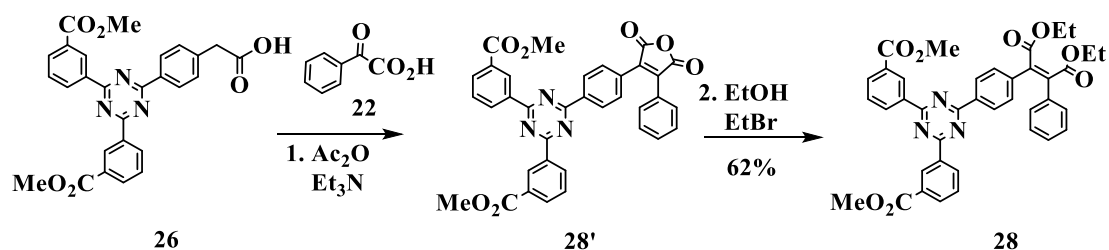ere is the signal of the hydrogens of methyl 3-benzoate between the triazine ring and the methyl ester (H3), integrating for two hydrogens, since the molecule has two methyl 3-benzoate arms. At 8.80 ppm there is a doublet ($J$ = 7.8 Hz), from the hydrogen (H4). At 8.54 ppm appear hydrogens (H1), a doublet with coupling constant $J$ = 8.2 Hz, integrating for two hydrogens. At 8.21 ppm comes (H6), a

doublet ($J = 7.7$ Hz). The triplet at 7.59 ppm ($J = 7.7$ Hz) can be attributed to (H5), which has two other hydrogens in its vicinity. The doublet at 7.35 ppm can be assigned to the hydrogens (H2), $J = 8.2$ Hz. And the multiplet at 7.25 ppm can be assigned to the five hydrogens of the phenyl that was added via the Perkin reaction (highlighted in grey).

Figure 54. $^1$H NMR spectrum of compound **28** in CD$_2$Cl$_2$, 400 MHz.
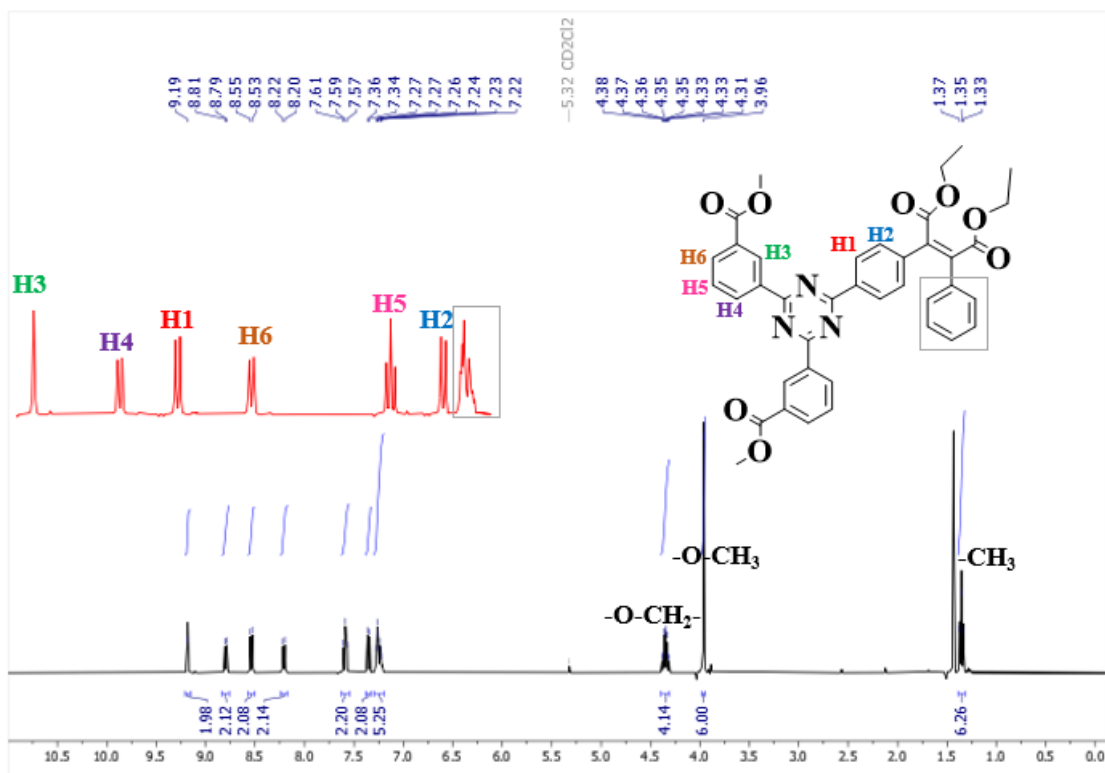


Between 4.38-4.31ppm there are two overlapping quartets from the methylenes of the ethyl esters and at 3.96 ppm it is possible to observe a signal referring to the methyls of methyl 3-benzoate more shifted to largest field in relation to the signals of the methylenes of the ethyl esters, and at 1.35 ppm appears the signal referring to the methyls of the ethyl esters linked to stilbene.

For the compound with two phenanthrene arms, the synthetic procedure followed the same sequence varying only the building block, using (**27**) and the ratio of Perkin reactants, with 1 molar equivalent of (**27**) for 4.3 equivalents of acid (**22**). In the esterification step ethanol and bromoethane were employed. The yield over these two steps was 58%.

Scheme 25. Perkin reaction of **27**, followed by *in situ* esterification, forming **29**.
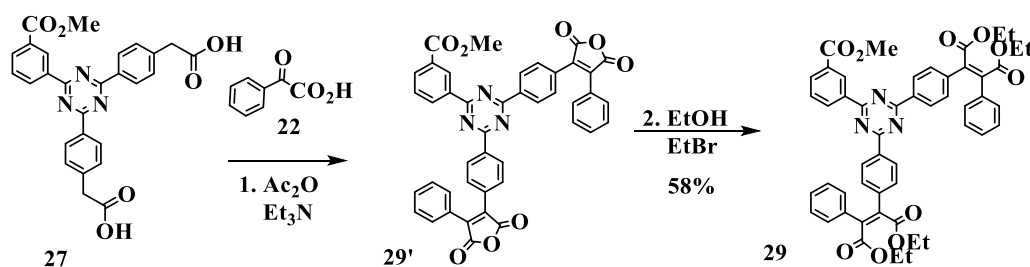


This compound was characterized by $^1$H NMR, as shown in **Figure 55**. The spectrum of this compound is similar to the spectrum of the compound with one stilbene arm, only the intensity of the signals and hence the integrals are proportionally different. In the aromatic region we have the same set of signals shown in the spectrum of compound **(29)**, with different signal intensities. The hydrogen signal (H3), a singlet, is slightly shifted to smaller field and integrates for one hydrogen. The signal from hydrogen (H4) is a doublet at 8.89 ppm ($J = 8.0$ Hz), integrating for one hydrogen. At 8.57 ppm, a doublet ($J = 8.8$ Hz) referring to hydrogens (H1) is observed, integrating for four hydrogens. The signal at 8.26 ppm can be assigned to hydrogen (H6), a doublet with coupling constant $J = 8.0$ Hz. The triplet at 7.66 ppm ($J = 8.0$ Hz) can be assigned to hydrogen (H5), which has two neighboring hydrogens, integrating for one hydrogen. At 7.32 ppm, there is a doublet, referring to hydrogens (H2), $J = 8.8$ Hz, integrating for four hydrogens. Between 7.24 and 7.15 ppm there are two blocks of signals (highlighted in grey), which are assigned to the two phenyls added via the Perkin reaction.

At 4.30 ppm the quartet ($J = 7.2$ Hz) integrating for eight hydrogens, corresponds to the methylene hydrogens of the ethyl esters and next there is a signal, a singlet, at 3.97 ppm, corresponding to the methyl ester. And between 1.34 and 1.29 ppm there are two overlapping triplets, corresponding to the methyls of the ethyl esters.

Figure 55. $^1$H NMR spectrum of compound **29** in CD$_2$Cl$_2$, 400 MHz.
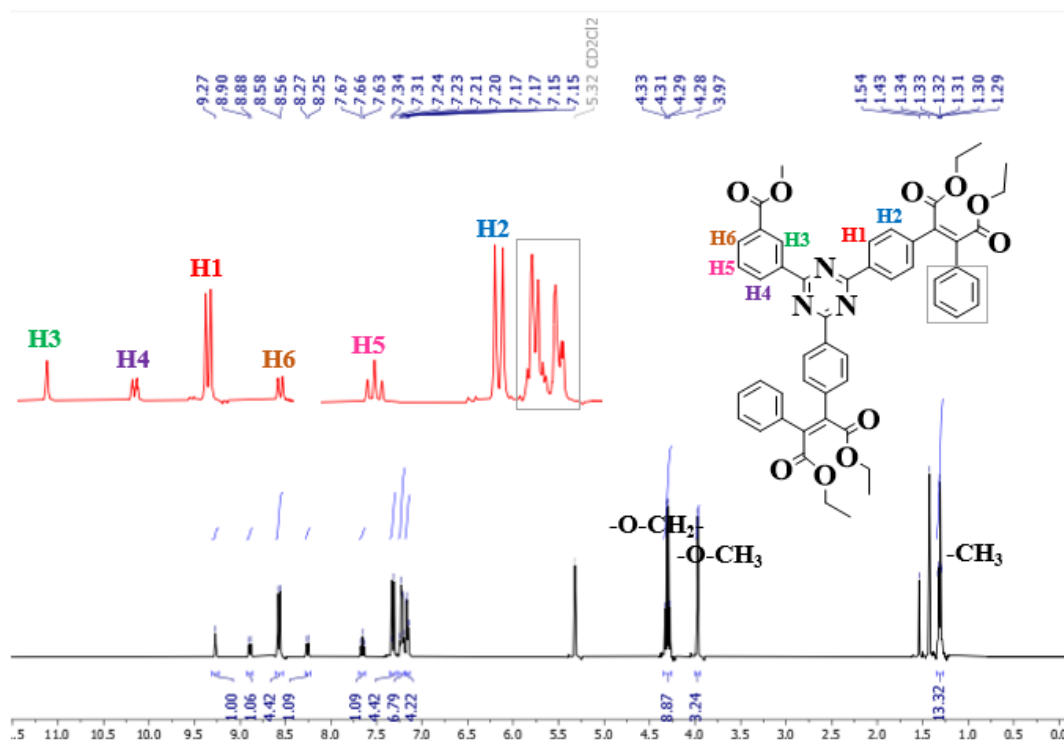


For compounds with two stilbene/phenanthrene arms a homolog with butyl chain was synthesized. The reactions to synthesize this compound were the same as for the short-chain homologue. The step that differs is only the esterification, by the use of butanol and bromobutane. The yield was 72% (**Scheme 26**).

Scheme 26. Perkin reaction of **27**, followed by *in situ* esterification, forming **32**.
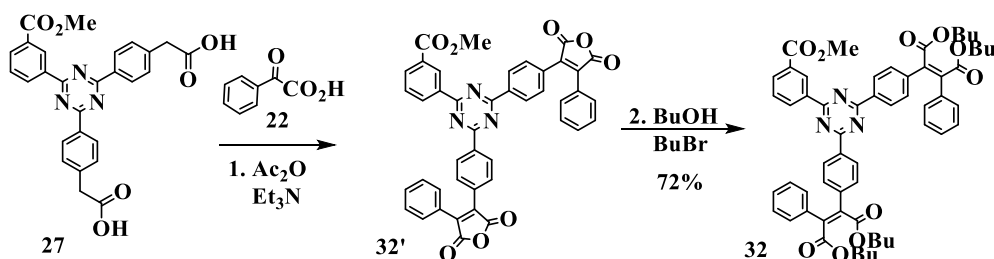


## 4.2.3. Perkin products: construction of non-symmetric compounds with benzostilbene arms

From building blocks (**26**) and (**27**) disssymmetric compounds with one and two benzostilbene (= styrylnaphthalene) arms were likewise obtained. The first reaction was performed to obtain the non-symmetric compound (**33**) with one benzostilbene arm

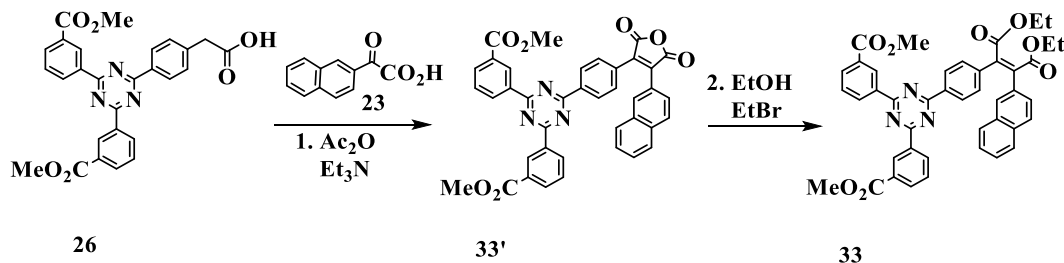(**Scheme 27**). This reaction followed the same methodology described on page 92 for the stilbene intermediate, but replacing the phenylglyoxylic acid with naphthylglyoxylic acid.

Scheme 27. Perkin reaction of **26**, followed by *in situ* esterification, forming **33**.



The obtainment of this compound is confirmed by hydrogen nuclear magnetic resonance. The elucidation of the spectrum of (**33**) is presented below.

Figure 56 shows the ^{1}H NMR spectrum of compound (**33**), in which it is possible to see in the aromatic region the signals referring to the two methyl 3-benzoate systems and to the helicene precursor system. The signal corresponding to the hydrogen (H3) is observed at 9.33 ppm, a singlet, whose shift can be justified by hydrogen bonds with nitrogen from the triazine, the integral corresponds to two hydrogens. At 8.91 ppm, ($J = 7.9$ Hz), there is a doublet integrating for two hydrogens corresponding to (H4). The doublet at 8.61 ppm, ($J = 8.3$ Hz) corresponds to the hydrogen closest to the triazine in the 1,4-substituted phenyl, (H1). At 8.27 ppm there is a doublet ($J = 7.8$ Hz) probably corresponding to the hydrogen (H6). At 7.75 to 7.70, there is a multiplet, seemingly an overlap of a doublet and a triplet, maybe hydrogens (H9), (H10) and (H12). The signal at 7.64 is a triplet ($J = 7.8$ Hz) that possibly corresponds to (H5) and (H11), whose integral corresponds to three hydrogens. The signal at 7.40 ppm is a multiplets corresponds to (H2). At 7.19 ppm a double-doublet (*dd*, $J1 = 8.7$ Hz and $J2 = 1.8$ Hz) is observed, which may correspond to (H13), integrating for one hydrogen. The signals of (H8) and (H7), are not clearly identified, possibly part of the multiplets.

The signals of the ester methylenes can be seen at 4.36 ppm, a multiplet with integral for four hydrogens. Next is a singlet with an integral for six hydrogens at 4.00 ppm, the methyl esters. And at 1.34 ppm, there is a triplet corresponding to the methyls of the ethyl esters.

Figure 56. $^1$H NMR spectrum of compound **33** in CDCl$_3$, 400 MHz.
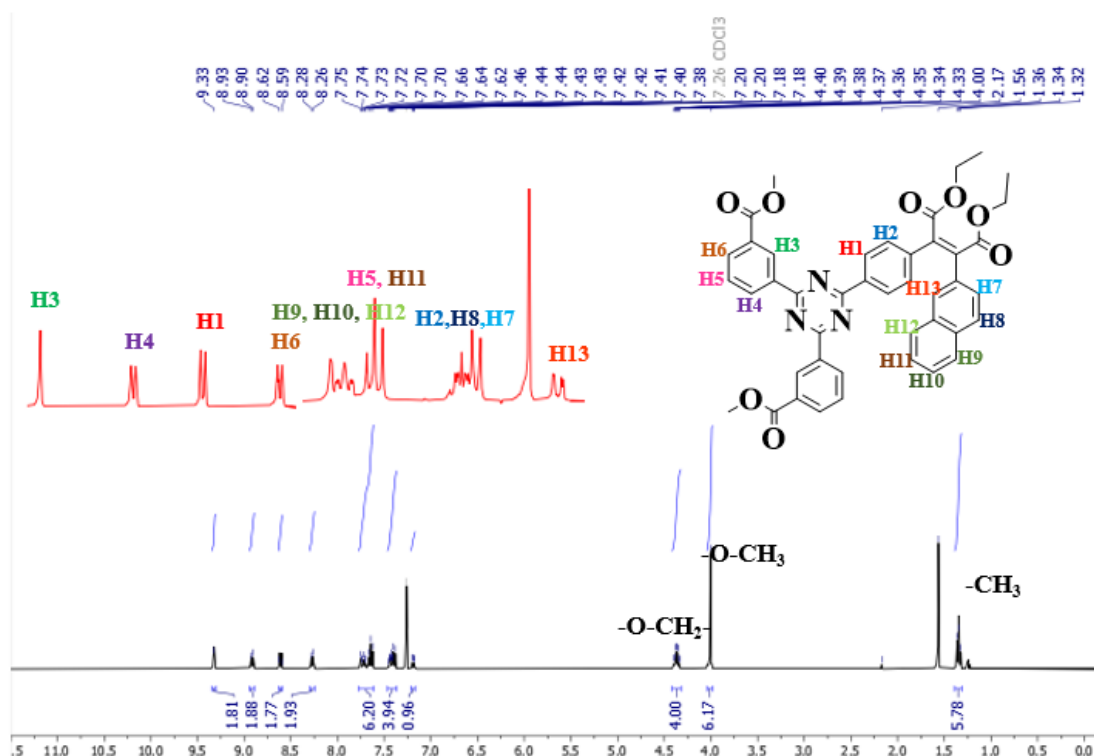


In **Scheme 18** is shown the formation of (**34**). The reaction followed the methodology described on page 92 for the stilbene intermediate, but replacing the phenylglyoxylic acid with naphthylglyoxylic acid. The yield over these reaction steps was 20%.

Scheme 28. Perkin greaction of **26**, followed by *in situ* esterification, forming **34**.
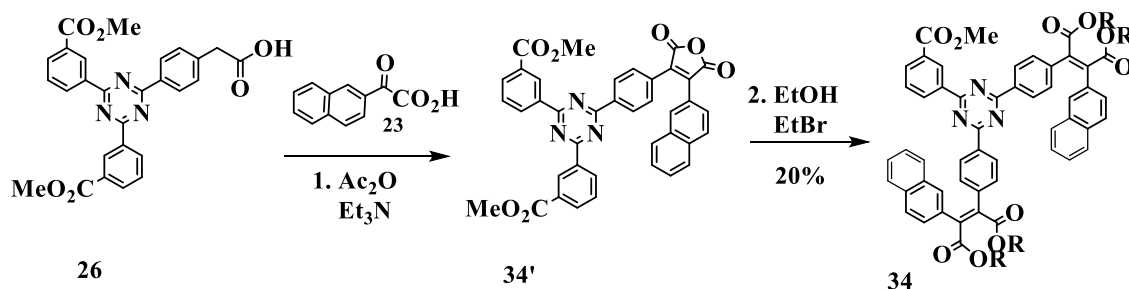


**Figure 57** shows the $^1$H NMR spectrum of (**34**), in which a set of signals with integrations in the ratio 1:1:4:1 is observed. In the aromatic region the signal corresponding to the hydrogen (H3) is at 9.25 ppm, a singlet with integral for one hydrogen, quite displaced to smaller field, a fact that can be attributed to hydrogen bonds with the nitrogen of the triazine. At 8.85 ppm there is a doublet ($J$ = 6.6 Hz) ntegrating for one hydrogen corresponding to (H4). The doublet at 8.61 ppm, with coupling constant ($J$ = 6.8Hz) is corresponding to the hydrogen closest to the triazine, (H1), the integral

corresponds to four hydrogens. At 8.27 ppm there is a doublet ($J$ = 9.0 Hz), a signal probably corresponding to the hydrogen (H6). At 7,74 ppm there is a signal probalgy corresponds to (H9), (H10) and (H12), integrating for 6H. At 7.66 to 7.60, there is a multiplet, likely a doublet overlapping with a triplet, integrating for three hydrogens, that possibly corresponds to (H5) and (H11). The signal at 7.45 is a multiplet, possibly corresponding to the (H8) and (H7) hydrogens, integrating for two hydrogens. At 7.34 ppm is a doublet ($J$ = 6.8 Hz) corresponding to (H2), integrating for 4H. At 7.17 ppm a doublet ($J$ = 8.6 Hz), can be assigned to (H13), integrating for two hydrogens. At 4.36 ppm there is a multiplet integrating for eight hydrogens, which can be assigned to the methylene hydrogens of the ethyl ester. In the following there is a singlet with integral for three hydrogens, at 4.00 ppm, corresponding to the methyl ester and at 1.34 ppm, ($J$ = 7.2 Hz) there is a triplet corresponding to the methyls of the ethyl esters, integrating for twelve hydrogens.

Figure 57. $^1$H NMR spectrum of **34** in C$_2$D$_2$Cl$_4$, 400 MHz.
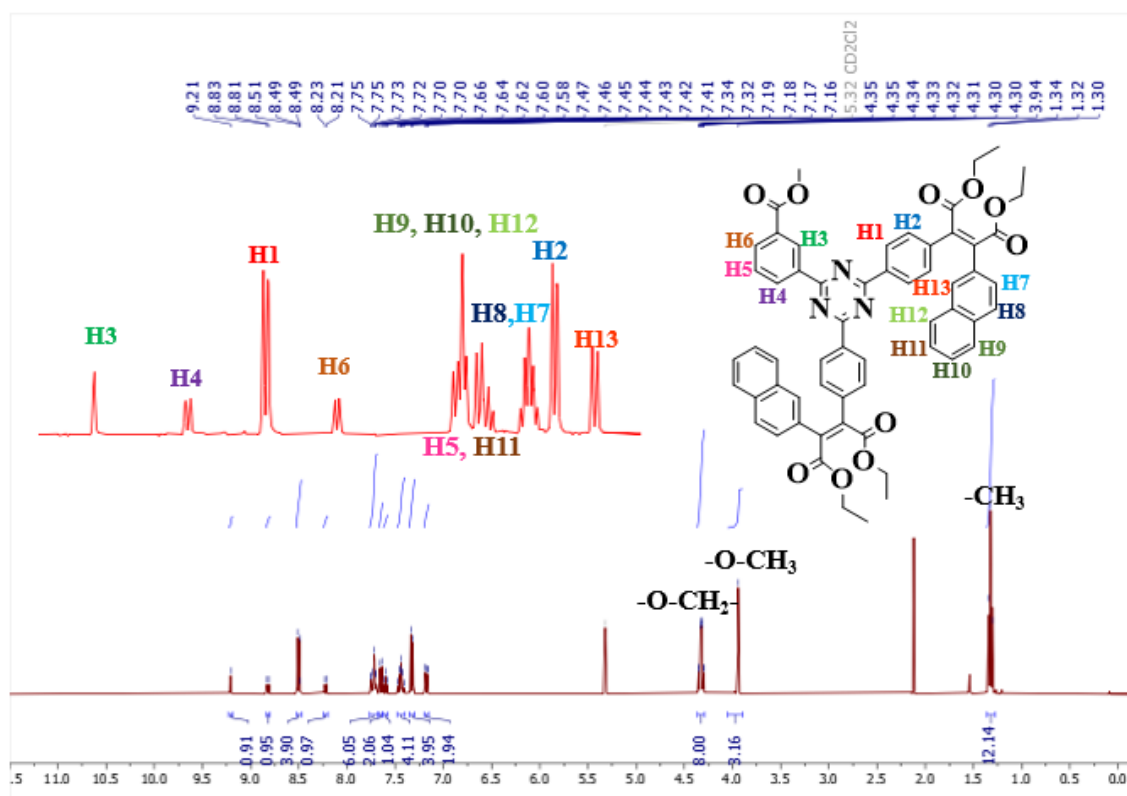
## 4.2.4. Photo-oxidative intramolecular cyclization: formation of polyaromatic arms in non-symmetric systems mono- and di-phenanthrenes.

The final compounds were obtained from intramolecular cyclization reactions with the respective intermediates (**28**), (**29**) and (**32**). The reactions were carried out in ethyl acetate, in the presence of oxygen and with a catalytic amount of molecular iodine (0.3 g) and irradiation with a 150 W mercury lamp, inside a borosilicate immersion tube in which cooling water circulates, the same system used in the photocyclization of the symmetric compounds. After an average period of 24 to 48 hours, some of these materials precipitated in the solution and were then filtered, in other cases the solution was concentrated, in both cases purification was done on a silica gel chromatographic column, eluting with cyclohexane/acetone with increasing polarity, and finally recrystallized in butanol, with an average yield of 20%.

Characterization of the compounds was done by $^1$H and $^{13}$C NMR. Two spectra for each system are discussed below. All spectra of the series are presented in Appendix A.

For the non-symmetric phenanthrene series, the derivative with one phenanthrene arm and two methyl benzoate groups **F$_1$Et** was prepared as indicated in the following scheme (**Scheme 29**).

Scheme 29. Intramolecular photo-oxidative cyclization to form **F$_1$Et**.
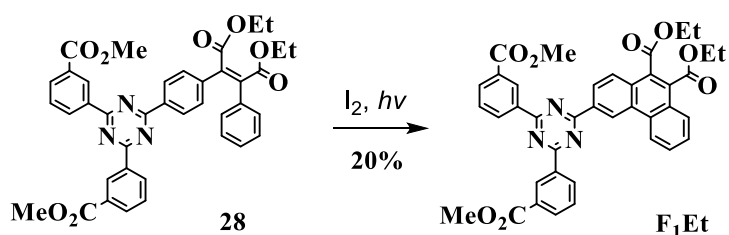


The $^1$H nuclear resonance spectrum confirms that **F$_1$Et** is obtained. The elucidation of the signals will be discussed below.

In the $^1$H NMR spectrum (**Figure 58**) a very smaller field singlet is observed at 9.76 ppm, that can be assigned to the hydrogen (H5). At 9.02 ppm there is another singlet with integral for two hydrogens, which possibly corresponds to (H1). The doublet at 8.68 ppm, ($J = 8.1$ Hz), with integral for one hydrogen, corresponds to the hydrogen (H6). The signal at 8.65 ppm is a doublet ($J = 8.9$ Hz) with integral for one hydrogen, referring to (H7). At

8.61 ppm there is a doublet ($J$ = 8.1 Hz), which corresponds to (H2). The doublet at 8.19 ppm ($J$ = 8.9 Hz), with integral for one hydrogen is a signal referring to the hydrogen (H8). The signal at 8.08 ppm is a doublet ($J$ = 7.9 Hz), referring to (H11) and (H4). At 7.77 ppm there is a triplet ($J$ = 8.2 Hz) with integral for one hydrogen, corresponding to (H9). The triplet at 7.69 ppm ($J$ = 8.2 Hz) with integral for one hydrogen corresponds to (H10). The signal at 7.46 ppm, a triplet ($J$ = 7.6 Hz) with integral for two hydrogens, corresponds to (H3). In the aliphatic region a set of signals is observed at 4.5, 4.0 and 1.5 ppm with integrals of value 4, 6 and 6, respectively.

Figure 58. $^1$H NMR spectrum of **F₁Et** in CD₂Cl₂, 400 MHz.
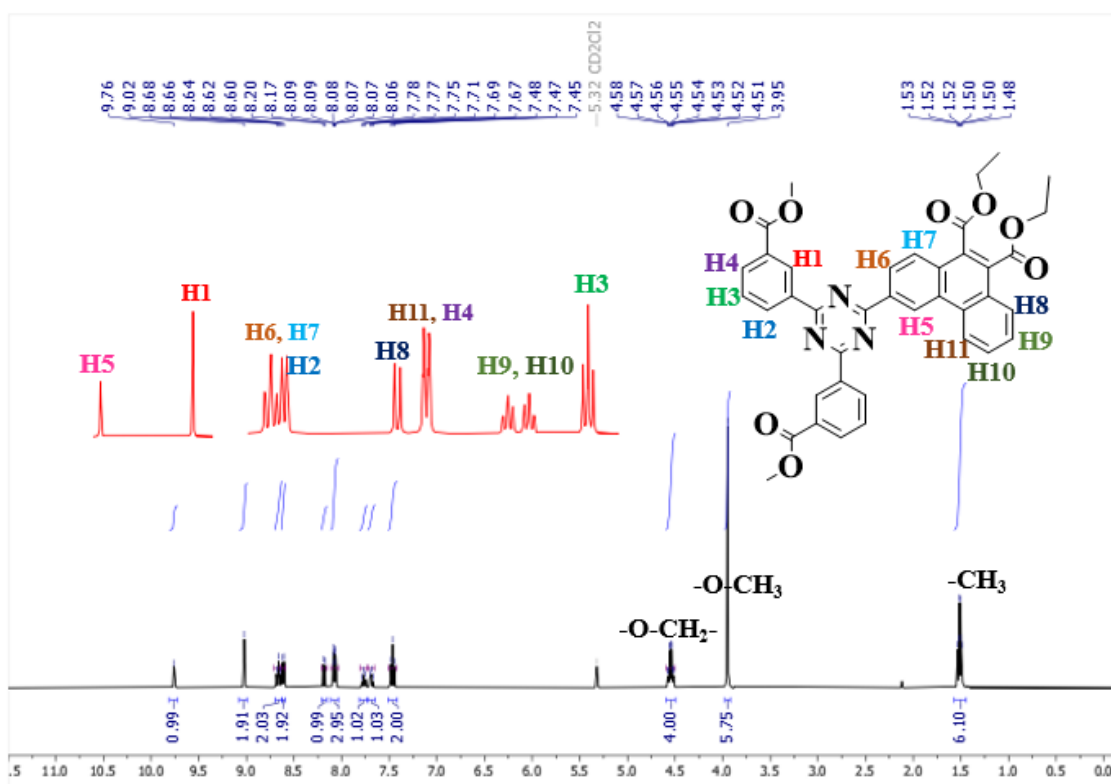


The $^{13}$C nuclear magnetic resonance analysis (**Figure 59**), confirms that **F₁Et** is obtained. 25 signals are observed in the smaller field region of the spectrum, one signal corresponding to the carbon of s-triazine attached to the phenanthrene arm at 171.1 ppm and the other two carbons of s-triazine are observed in a single signal at 170.9 ppm. The carbonyl carbons (C=O) are observed at 167.9, 167.4 and 166.5 ppm. There are twenty signals corresponding to the carbons of the phenanthrene system and the two methyl 3-benzoate rings, between 136.1 and 123.3 ppm. In the aliphatic region five signals are observed, two of them at 62.5 and 62.4 ppm referring to ethyl methylene carbons. At 52.5

ppm there is a signal referring to the oxygen-bound methyl carbon and the signals at 14.43 and 14.40 ppm correspond to the methyl carbons of the ethyl groups.

Figure 59. $^{13}$C NMR spectrum of **F$_1$Et** in CD$_2$Cl$_2$, 100 MHz.
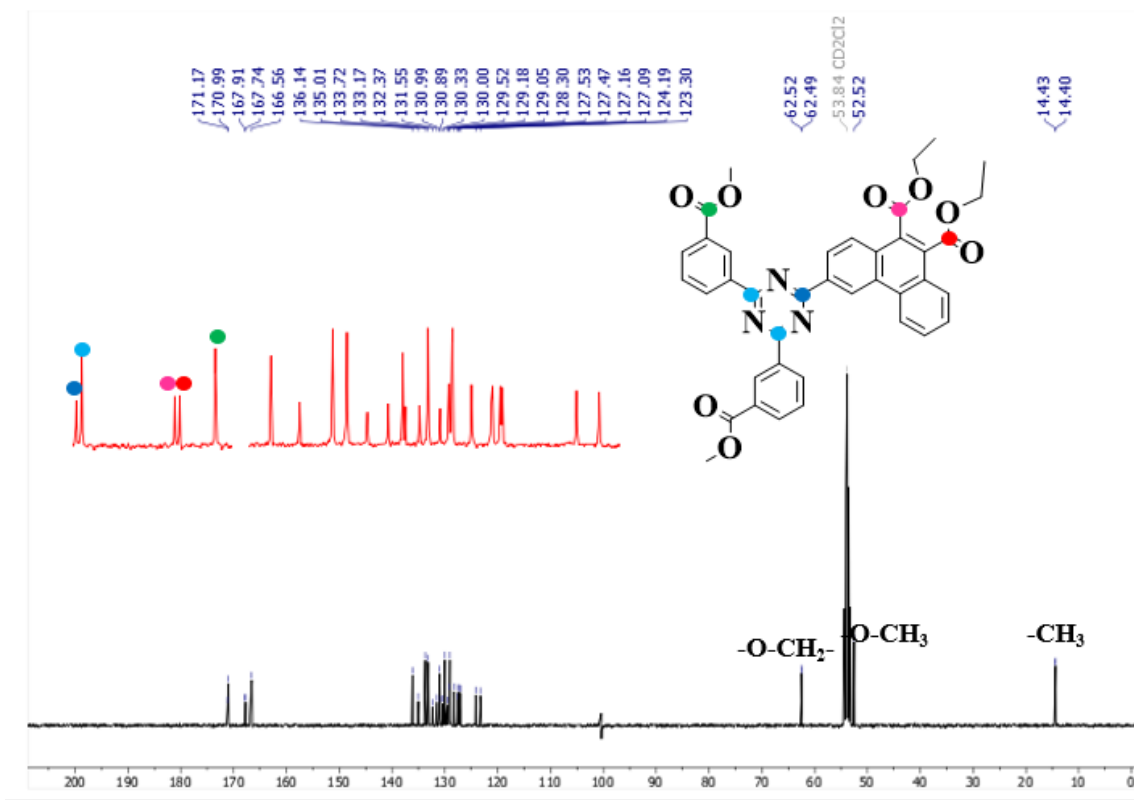


Homologues with two phenanthrene arms were studied after varying the chain lengths of the esters attached to the phenanthrenes (ethyl vs. butyl).

The first homologue to be prepared was **F$_2$Et**, according to **Scheme 30**, following the procedure already established for the photo-oxidative intramolecular cyclization reactions in this work, in 45% yield.

Scheme 30. Intramolecular photo-oxidative cyclization to form **F$_2$Et**.
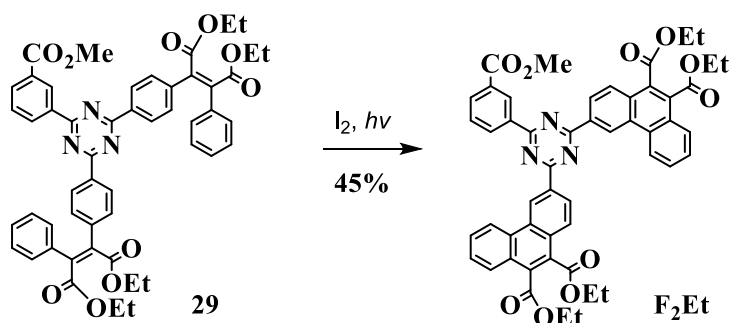


**Figure 60** presents the $^1$H NMR spectrum of **F$_2$Et**. At 10.15 ppm, there is a signal that corresponds to the (H5) hydrogens, with an integral for two hydrogens. At 9.38 ppm there is another singlet with integral for one hydrogen, which possibly corresponds to the

(H1) hydrogen. The signal at 8.99 ppm, ($J$ = 8.8Hz), a doublet with integral for two hydrogens, corresponds to the hydrogen (H6). At 8.89 ppm there is a doublet ($J$ = 8.6 Hz) with integral for two hydrogens, of the (H7) hydrogens. At 8.39 ppm there is a doublet ($J$ = 8.8 Hz), which corresponds to (H2). The doublet at 8.27 ppm ($J$ = 8.7 Hz), with integral for one hydrogen stems from (H4). The signal at 8.13 ppm is a doublet ($J$ = 7.9 Hz), referring to the hydrogens (H11). At 7.86 ppm there is a triplet ($J$ = 7.9 Hz) with integral for two hydrogens, correspondsing to the (H9) hydrogens. The triplet at 7.75 ppm ($J$ = 7.9 Hz) with integral for two hydrogens corresponds to the (H10) hydrogens. The signal at 7.73 ppm, a doublet ($J$ = 8.1 Hz) with integral for two hydrogens, corresponds to (H8). The signal at 7.70 ppm, a triplet ($J$ = 8.2 Hz) with integral for one hydrogen, corresponds to (H3).

Figure 60. $^1$H NMR spectrum of **F$_2$Et** in CD$_2$Cl$_2$, 400 MHz.
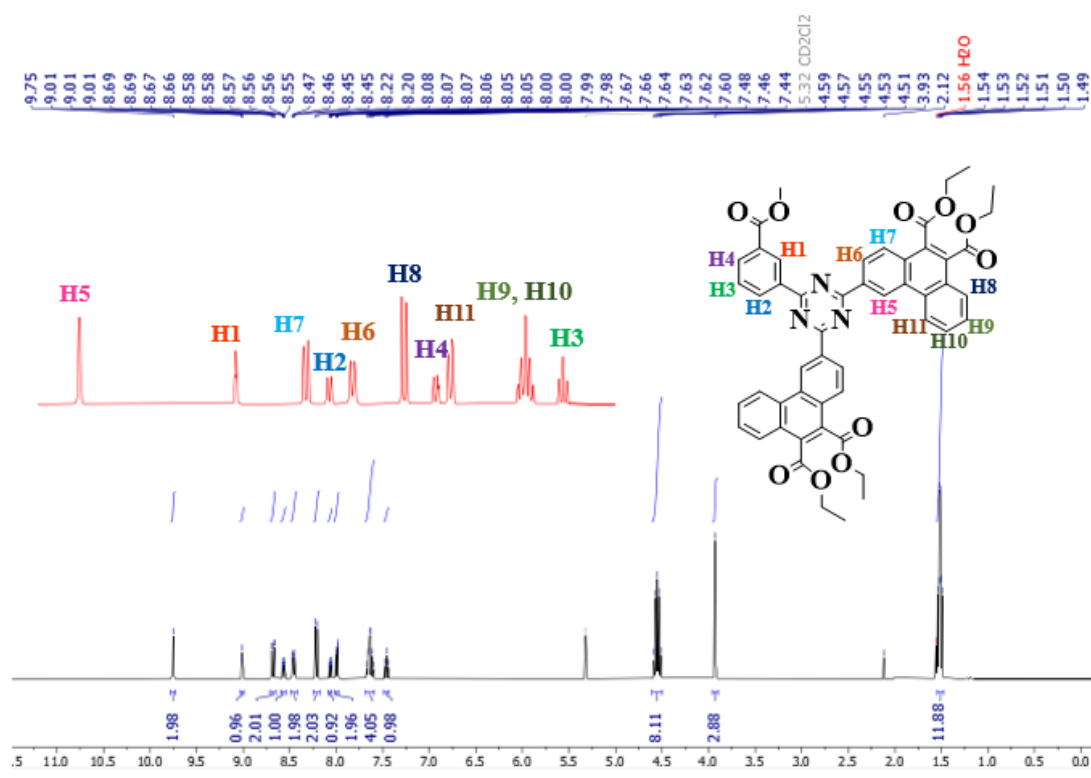


In the $^{13}$C NMR analysis (**Figure 61**) of **F$_2$Et**, 25 signals are observed in the aromatic region of the spectrum. The signal referring to the s-triazine carbons attached to the phenanthrene arms is observed at 171.1 ppm and the other carbon of s-triazine is observed at 170.9 ppm. The carbonyl carbons (C=O) are observed at 167.8, 167.7 and 166.5 ppm. There are 20 signals corresponding to the carbons of the phenanthrene system and the two methyl 3-benzoate rings, between 136.0 and 122.9 ppm. There are five signals in the aliphatic region, at 62.5 and 62.4 ppm referring to the methylene carbons, at 52.5

ppm referring to the ester methyl carbon and at 14.46 and 14.43 ppm corresponding to the methyl carbons of the ethyl groups.

Figure 61. $^{13}$C NMR spectrum of **F₂Et** in CD₂Cl₂, 100 MHz.
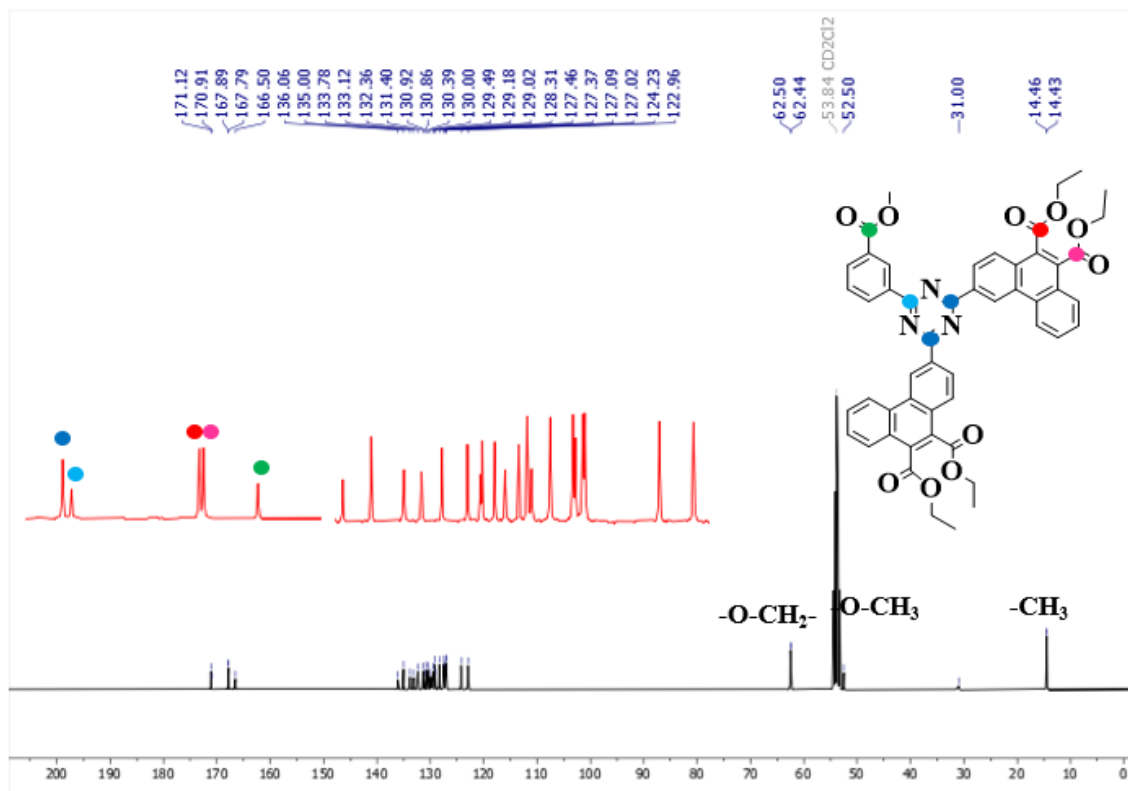


The second non-symmetric homologue with phenanthrene arms, **F₂Bu** (Scheme 31) was obtained in about 38% yield.

Scheme 31. Intramolecular photo-oxidative cyclization to form **F₂Bu**.
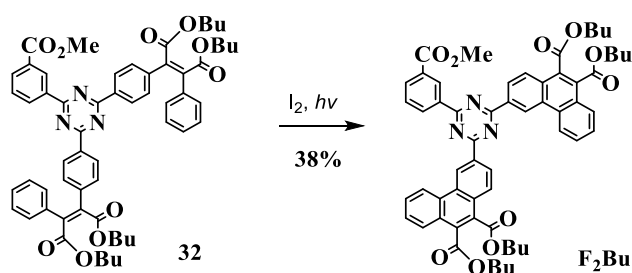


The confirmation that these compounds were obtained was done by $^1$H and $^{13}$C NMR, and will be in Appendix. They will not be discussed at this time; what differentiates them from the homologous **F₂Et** is the aliphatic region, which has signals from two more methylenic carbons than the previous one.

In addition to nuclear magnetic resonance, hydrogen and carbon characterization, all final compounds were also characterized by high resolution mass spectrometry (HRMS) and the data are arranged in the **Table 5**.

Table 5. Table High resolution mass spectrometry (HRMS) of the non-symmetric compounds.

| Compound | Molecular formula | Theoretical mass (Da) | Experimental mass (Da) | Error (Da) |
|---|---|---|---|---|
| F1Et | $[C_{39}H_{31}N_3O_8+Na]^+$ | 692.20034 | 692.1992 | 0.00114 |
| F2Et | $[C_{51}H_{41}N_3O_{10}+Na]^+$ | 878.26842 | 878.2682 | 0.00022 |
| F2Bu | $[C_{59}H_{57}N_3O_{10}+Na]^+$ | 990.3962 | 990.3940 | 0.0022 |

## 4.2.5 Photo-oxidative intramolecular cyclization: formation of polycyclic aromatic arms in non-symmetric systems: mono- and di-[4]helicenes.

**H₁Et** and **H₂Et** were obtained from the respective precursors (**33**) and (**34**).

The photo-cyclization was carried out as previously discussed. The reaction period varied between 24 and 28 h. The purification was performed on a silica gel chromatographic column, eluting with cyclohexane/acetone of increasing polarity, and finally recrystallized in butanol.

The two homologues **H₁Et** and **H₂Et** differ only in the number of polyaromatic arms. The homologue with one [4]helicene arm has two ethyl esters attached. For this homologue, the reaction is shown in **Scheme 32** and the characterizations are shown below in **Figures 62 and 63**.

Scheme 32. Intramolecular oxidative photo-cyclization to form compound **H₁Et.**
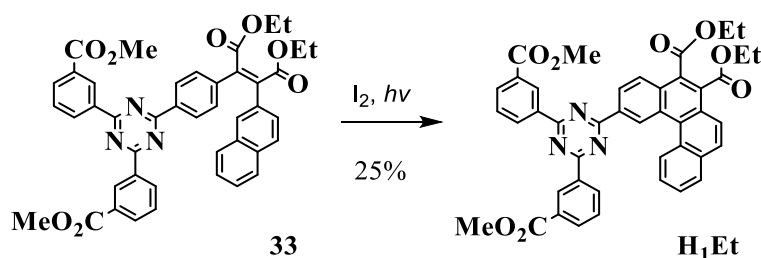


The spectrum in **Figure 62** confirms that **H₁Et** was obtained, in which it is possible to see in the aromatic region the signals referring to the two methyl 3-benzoate systems and to the [4]helicene system. The singlet of the helicene system, (H5), is observed with a strong smaller field shift, at 10.49 ppm. The signal corresponding to the hydrogen (H1) is observed at 9.30 ppm, a singlet, with an integral for two hydrogens. At 9.20 ppm there is a doublet, ($J$ = 8.8 Hz), with integral for one hydrogen possibly

corresponding to (H6). The doublet at 8.94 ppm, ($J$ = 7.8 Hz), can be assigned to the signal from the hydrogens (H2) and (H7), with integral for three hydrogens. At 8.45 ppm there is a doublet, ($J$ = 8.8Hz), a signal probably corresponding to the hydrogen (H8). At 8.23 ppm, (H4), integral for two hydrogens, there is a doublet, ($J$ = 7.8 Hz). At 8.12 ppm there is a doublet, ($J$ = 8.8 Hz), probably corresponding to (H9), integral for one hydrogen. At 8.05 ppm there is a singlet with an integral for two hydrogens, probably (H10) and (H13). The signal at 7.91 is a triplet, ($J$ = 6.9 Hz) possibly corresponding to the (H12) hydrogen. The triplet at 7.80 ppm, ($J$ = 6.9 Hz) corresponds to (H11). The triplet at 7.64 ppm, ($J$ = 7.8 Hz) corresponds to (H3). The ester signals are visualized at 4.57 ppm, 3.97 ppm and 1.51 ppm, with 4:6:6 integrals, which confirms the identity of a tetra-ester, diethyl and dimethyl.

Figure 62. $^1$H NMR spectrum of **H₁Et** in CD₂Cl₂, 400 MHz.
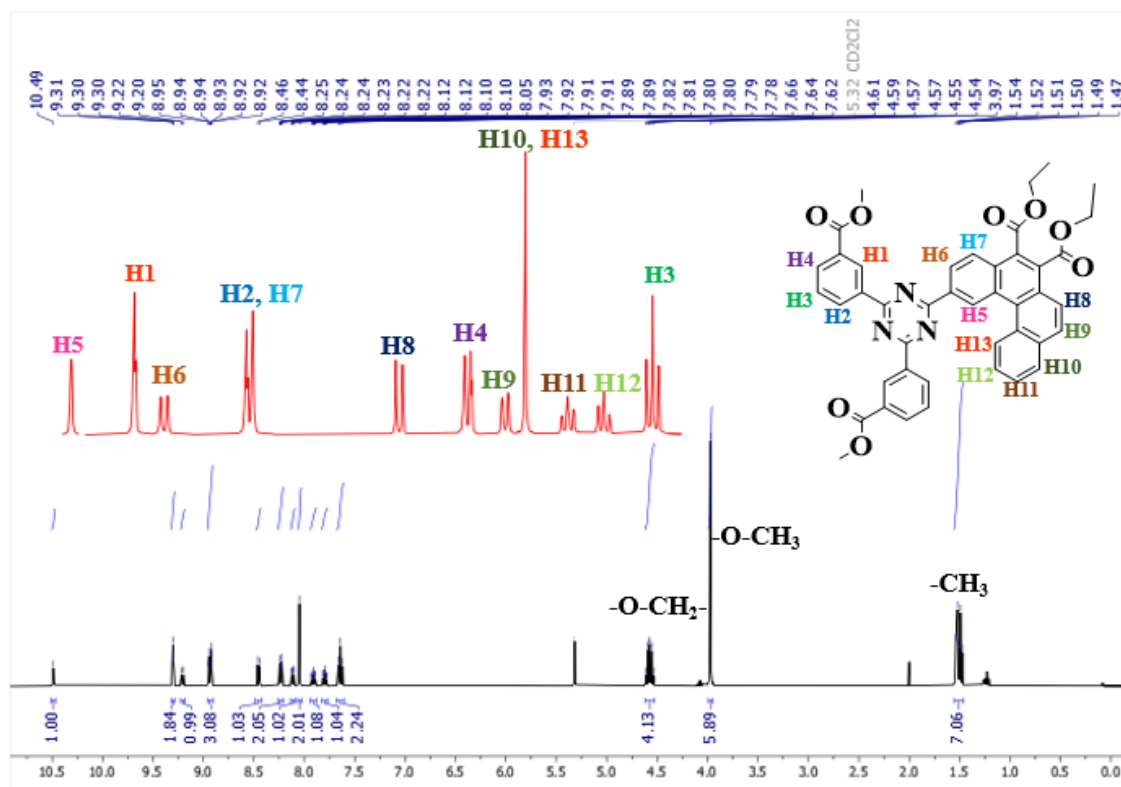


In the $^{13}$C NMR spectrum (**Figure 63**) of **H₁Et**, 28 signals are observed in the smaller field region of the spectrum, one signal corresponding to the carbon of s-triazine attached to the helicene arm at 171.9 ppm, and the other two carbons of s-triazine are observed in a single signal at 171.4 ppm. The carbonyl carbons (C=O) are observed at 168.2, 167.8 and 166.7 ppm. There are 23 signals corresponding to the carbons of the

helicene system and the two methyl 3-benzoate rings, between 136.5 and 123.4 ppm. In the aliphatic region five signals are observed, two of them at 62.6 ppm referring to methylene carbons. At 52.6 ppm there is a signal of the methyl ester carbon and the signals at 14.47 and 14.40 ppm correspond to the methyl carbons of the ethyl chains. The signals appearing at 206.80 and 31.00 ppm are residual signals from the solvent, acetone.

Figure 63. $^{13}C$ NMR spectrum of **H₁Et** in CD₂Cl₂, 100 MHz.
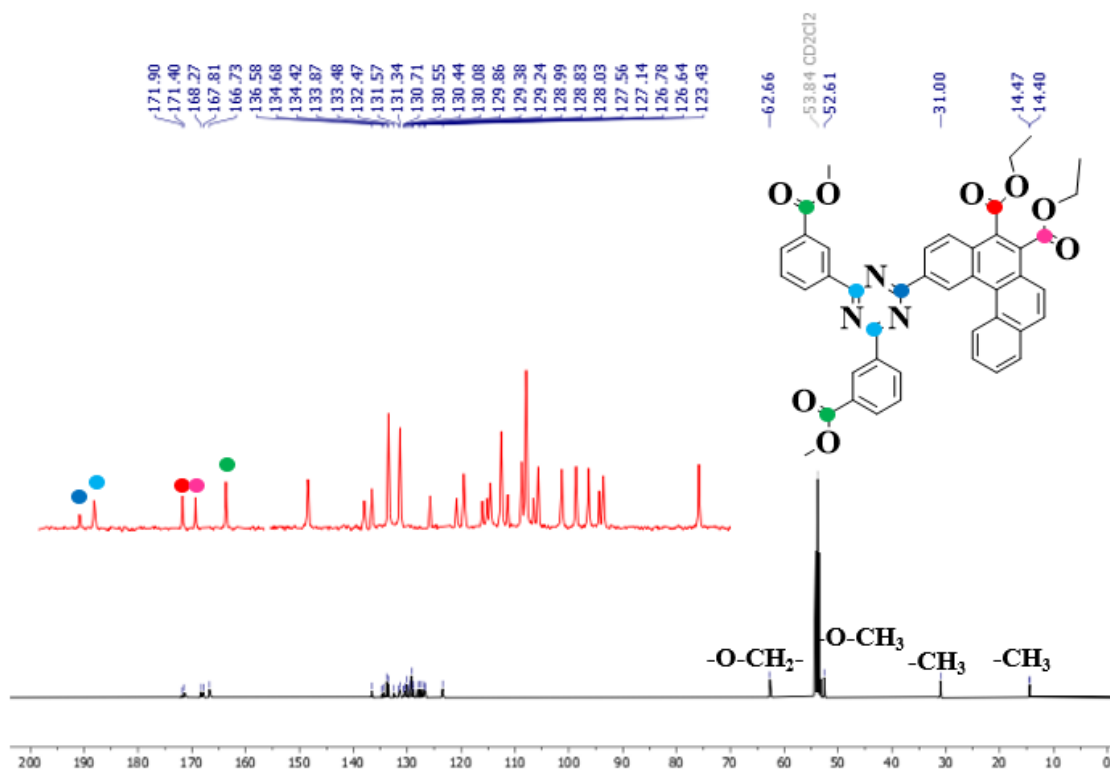


The second non-symmetric homologue with helicene arms, **H₂Et**, gives very similar spectra, only differing in the relative signal strengths.

Scheme 33. Intramolecular oxidative photo-cyclization to form **H₂Et**.
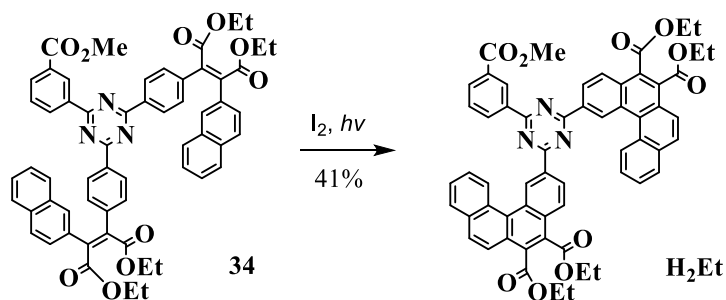


The $^1H$ NMR spectrum of **H₂Et** (**Figure 64**) shows signals between 10.52 and 1.52 ppm. In the aromatic region are the signals referring to the two helicene systems and

the methyl 3-benzoate system. The singlet of the helicene systems, (H5), is observed at 10.52 ppm. The signal corresponding to the hydrogen (H1) is observed at 9.36 ppm, a triplet, ($J = 1.8$ Hz), with integral for one hydrogen. At 9.15 ppm there is a multiplet with integral for two hydrogens, possibly corresponding to (H6). The signal at 8.99 ppm integrates for one hydrogen, (H2) and (H7), with integral for three hydrogens. At 8.48 ppm there is a doublet, ($J = 8.7$ Hz) a signal probably corresponding to the hydrogens (H8). The signal at 8.25 ppm, (H4), integrates for one hydrogen, a doublet ($J = 7,9$ Hz). At 8.04 ppm there is a multiplet, with integral for six hydrogens. The signal at 7.68 ppm is another multiplet, with an integral for five hydrogens. At 4.57 ppm there is a multiplet with integral for eight hydrogens, which can be assigned to the methylene hydrogens of the ethyl esters. Next there is a singlet with integral for three hydrogens at 3.96 ppm, from the methyl ester. And at 1.51 ppm, there is a multiplet corresponding to the methyl hydrogens of the ethyl ester.

Figure 64. [^1]H NMR spectrum in of **H₂Et** in CD₂Cl₂, 400 MHz.
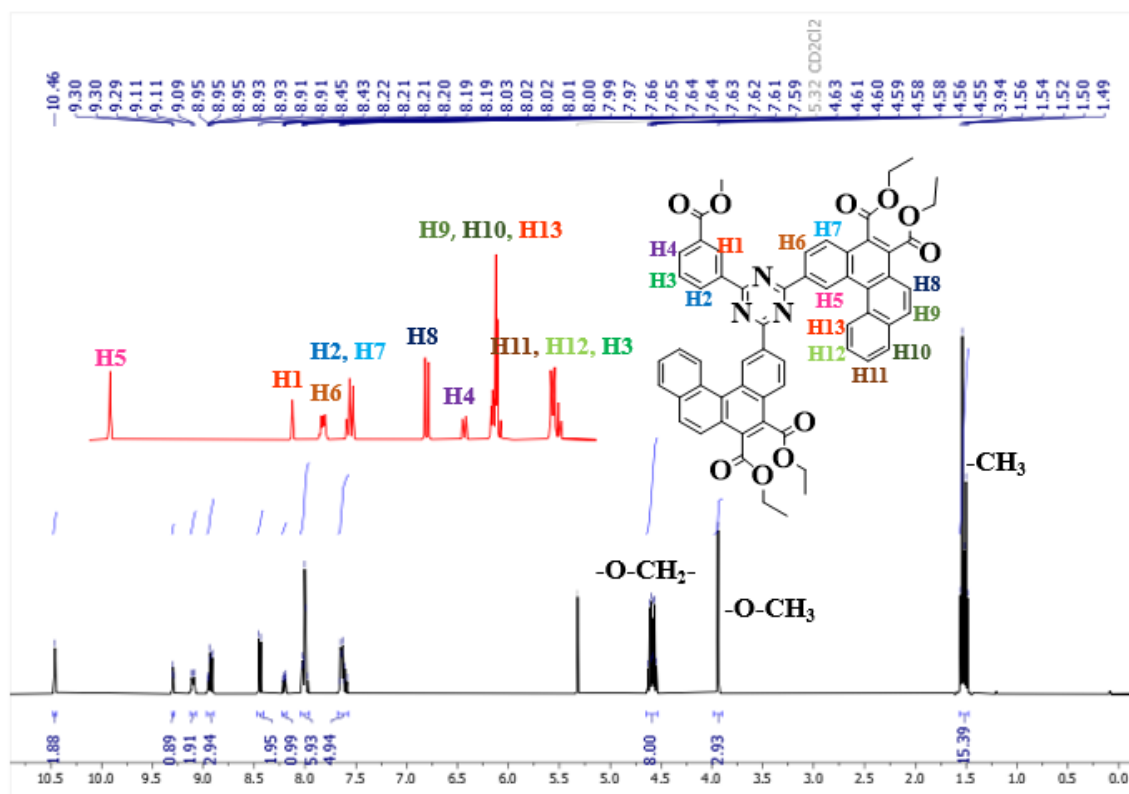


In the [^13]C NMR spectrum (**Figure 65**) of **H₂Et**, 28 signals are observed in the smaller field region of the spectrum. The signal of the s-triazine carbons attached to the helicene arms is observed at 171.9 ppm and the other carbon of s-triazine is observed at

171.3 ppm. The carbonyl carbons (C=O) are observed at 168.2, 167.8 and 166.7 ppm. There are 23 signals corresponding to the carbons of the helicene systems and the methyl 3-benzoate ring, between 136.7 and 123.3 ppm. In the aliphatic region four signals are observed, at 62.6 ppm referring to methylene carbons, at 52.6 ppm referring to the methyl ester and at 14.47 and 14.41 ppm to the methyl carbons of the ethyls.

Figure 65. $^{13}$C NMR spectrum of **H₂Et** in CD₂Cl₂, 100 MHz.
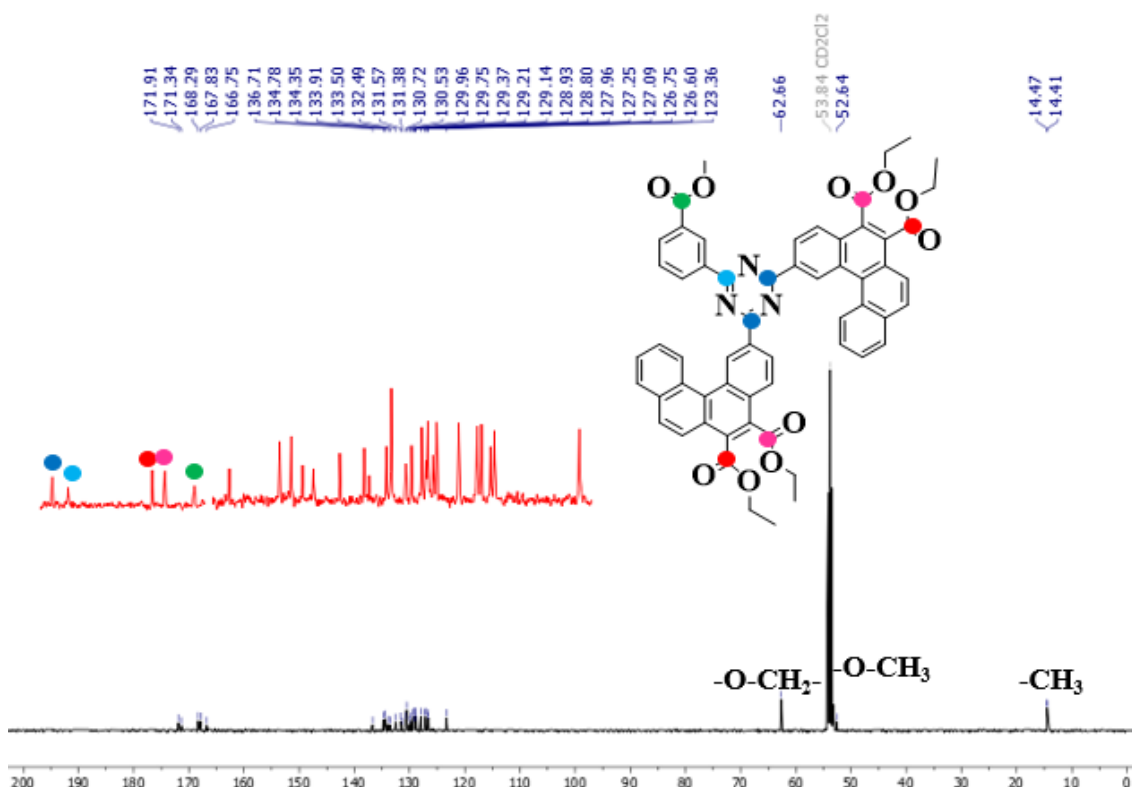


All final compounds were also characterized by high resolution mass spectrometry (HRMS) and the data are arranged in the Table 6.

Table 6. High resolution mass spectrometry (HRMS) of the non-symmetric [4]helicenyl compounds.

| Compound | Molecular formula | Theoretical mass (Da) | Experimental mass (Da) | Error (Da) |
|---|---|---|---|---|
| H1Et | $[C_{43}H_{33}N_3O_8+Na]^+$ | 742.21599 | 742.2161 | 0.00011 |
| H2Et | $[C_{59}H_{45}N_3O_{10}+Na]^+$ | 978.29972 | 978.3007 | 0.00098 |

## 4.3 Thermal properties of the non-symmetric compounds

The thermal behavior of the non-symmetric compounds **F₁Et**, **F₂Et**, **F₂Bu**, **H₁Et** and **H₂Et** was investigated to evaluate the presence of glass transitions and mesophases.

All compounds showed mesomorphism as well as glass transitions (Tg). In order to evaluate the thermal stability of the compounds, thermogravimetric analysis (TGA) was performed under nitrogen atmosphere and the observed decomposition temperatures prove the good thermal stability of the non-symmetric compounds, with decomposition onset around 363°C. In a parallel comparison with the symmetric compounds we observed a slight decrease, around 20ºC (all temperatures were obtained from the thermograms for 5% mass loss).

The textures observed by polarized light optical microscopy (POM) indicate the presence of mesophases typical of hexagonal columnar systems as expcted. DSC analyses confirmed the existence of glass transitions ($T_g$) within the mesophase (**Table 7**).

Table 7. Thermal data of the non-symmetric series.

| Compound | Transition | $T_g$ (°C) on heating | T/°C, Heating ($\Delta H$/kJ mol$^{-1}$) | T/°C, Cooling ($\Delta H$/kJ mol$^{-1}$) |
|---|---|---|---|---|
| $F_1Et$ | Col-Iso | 42 | 145 (1.6) | 149 (1.7) |
| $F_2Et$ | Col-Iso | 57 | 291 (5.0) | 292 (5.2) |
| $F_2Bu$ | Col-Iso | -0.7 | 200 (2.9) | 207 (2.40) |
| **$H_1Et$** | **Col-Iso** | **50** | **144 (3.5)** | **140 (3.3)** |
| **$H_2Et$** | **Col-Iso** | **72** | **227 (3.5)** | **228 (3.3)** |

The compound **$F_1Et$**, the first to be studied, a tetraester containing two methyl and two ethyl groups, forms a hexagonal columnar mesophase, which does not crystallize at room temperature, unlike the symmetric analog **$F_3Et$** that had no mesomorphic behavior. The hexagonal symmetry of the mesophase is evident by its growth into homeotropic domains upon cooling of the isotropic liquid (**Figure 66**), because the homeotropic growth is not compatible with the less common rectangular and oblique symmetries sometimes found with in columnar mesogens.

Figure 66. Texture observed by POM of **F₁Et.**
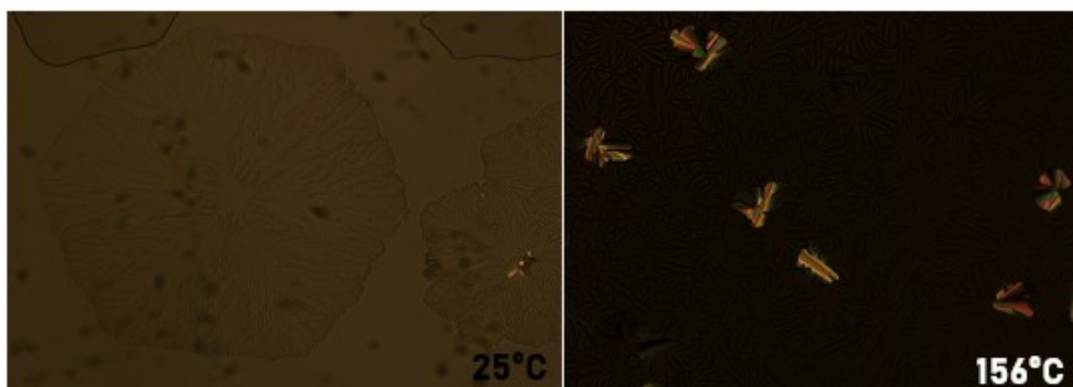


As an expected result of the non-symmetry, compound **F₁Et** shows in its thermogram (**Figure 67**) a lower clearing temperature of 145 °C (all clearing and melting temperatures shown are calorimetric onset temperatures upon heating at 10 K/min) than its homologue **F₂Et** which clears at 291 °C. In the symmetric analogue, **F₃Et**, it was not possible to observe the clearing temperatures because they are too high, beyond the detection limit of the apparatus. The glass transition (Tg) of this compound is observed particularly neatly as a step with onset around 38ºC in the second heating cycle.

Figure 67. Thermogram of **F₁Et.** In blue cooling and in red heating ramps (10 °C/min).
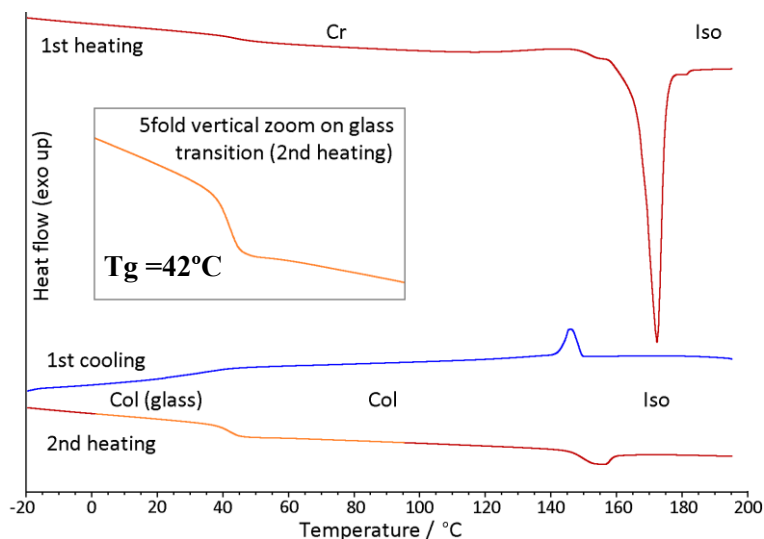


The **F₂Et** homolog, containing one methyl group and four ethyl groups, also shows hexagonal columnar mesophase, but with a much higher clearing temperature of 291°C. The greater amount of phenanthrene groups raised the clearing temperature, a fact that is even clearer when the comparison is made with the symmetric compound **F₃Et**, with three phenanthrene groups and no accessible clearing point.

To obtain a pentaester homologue with a lower clearing temperature, we also prepared the **F₂Bu** homologue with one methyl and four butyl groups, which clears at 200°C (**Figure 68**).

Figure 68. Thermogram of **F₂Bu**.
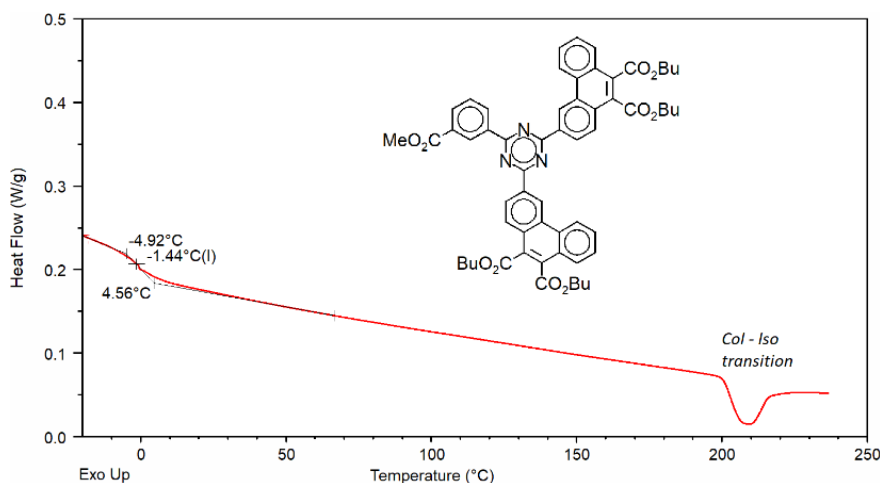


When comparing compound **F₂Bu** with its symmetric analog **F₃Bu**, the asymmetry brought some advantages such as a clearing temperature achievable at 200 °C. However, regarding melting temperatures and Tg, the non-symmetric compound presents disadvantages, as the $T_g$ of **F₃Bu** was observed at 19ºC and in **F₂Bu** it was reached at -4ºC, both disadvantageous temperatures. And as for $T_m$, in the symmetric analog it was 108ºC, but in the symmetric compound this transition was not reachable.

**F₁Et**, **F₂Et** and **F₂Bu** vary greatly in their propensity to show a crystalline state: the mesophase of **F₁Et** is monotropic with a melting point of 167 °C, the mesophase of **F₂Et** is enantiotropic with a melting temperature of 205 °C, 86 °C below the clearing point, and in **F₂Bu** the mesophase is formed with no crystalline state observed by calorimetry. But in all three cases, a columnar mesomorphic glassy state is obtained upon cooling these materials from the melting and clearing temperatures. The glass transition temperatures ($T_g$), as observed according to the common standard, at the beginning of DSC heating with 10 K/min, are 38 °C for **F₁Et**, 49 °C for **F₂Et**, and -4 °C for **F₂Bu**. The large decrease in the glass transition temperature from **F₂Et** to **F₂Bu** illustrates the importance of keeping the alkyl tails short in these structures.

Upon realizing that increasing the chain length offered no improvement in thermal behavior, as well as that the greater amount of phenanthrene groups improved so little, we once again extended the polyaromatic system to [4]helicene. 2-naphthylglyoxylic acid

was again used as Perkin adduct for the target esters with [4]helicenyl units. This extension of the polyaromatic system brought the prospect of both lowering the clearing temperature and hindering the crystallization further, due to a less planar and relatively compact molecular shape of the helicenyl system and the increased conformational variations, both in-plane and out-of-plane. But unlike in the symmetric series, we were confident that short ethyl plus methyl chains are the best option.

Thus, we analogously prepared tetraester and pentaester [4]helicenyl derivatives with two or one methyl groups and two or four ethyl groups, **H₁Et** and **H₂Et**. The thermal results of the first non-symmetric helicenyl analog synthesized and studied, **H₁Et**, proved to be very satisfactory. As expected the mesophase obtained for this compound was columnar hexagonal (**Figura 69**).

Figure 69. Texture observed by POM of **H₁Et**.
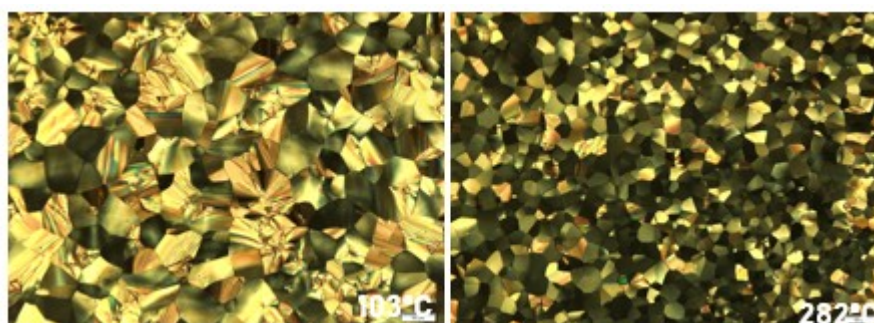


The clearing temperature obtained by calorimetry (**Figure 70**) is 144ºC, a temperature similar to that found for **F₁Et** (145ºC). However, the enlargement of the aromatic system fled to a $T_g$ twelve degrees above that found for **F₁Et**.

Figure 70. Thermogram of **H₁Et**.
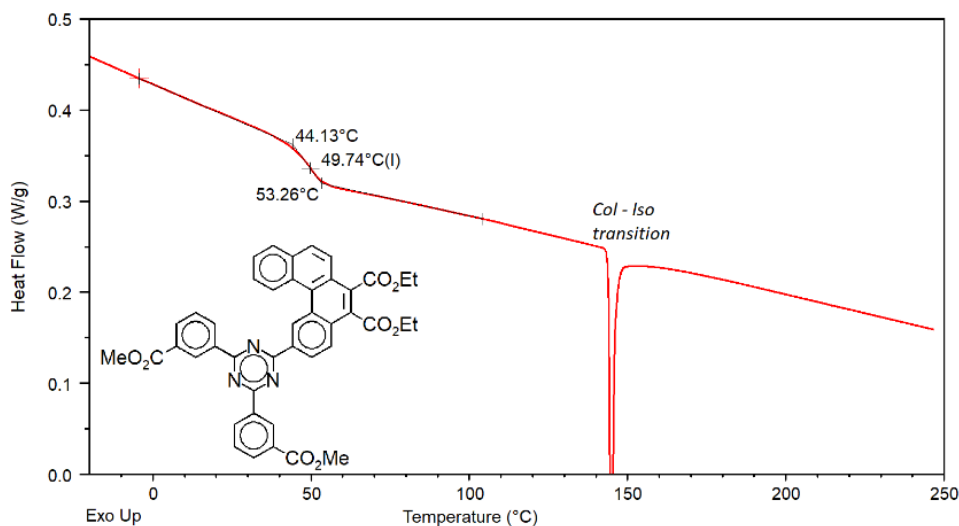
In **H₂Et**, similarly to what was observed with the non-symmetric compounds with phenanthryl groups, the greater amount of polyaromatic groups led to an increase of the clearing temperature, which for the compound with one helicenyl group was observed at 144°C, while the addition of a second helicenyl group raised it to 227°C. The glass transition was also obtained at a higher temperature, 72°C (**Figure 71**).

Figure 71. Thermogram of **H₂Et**.
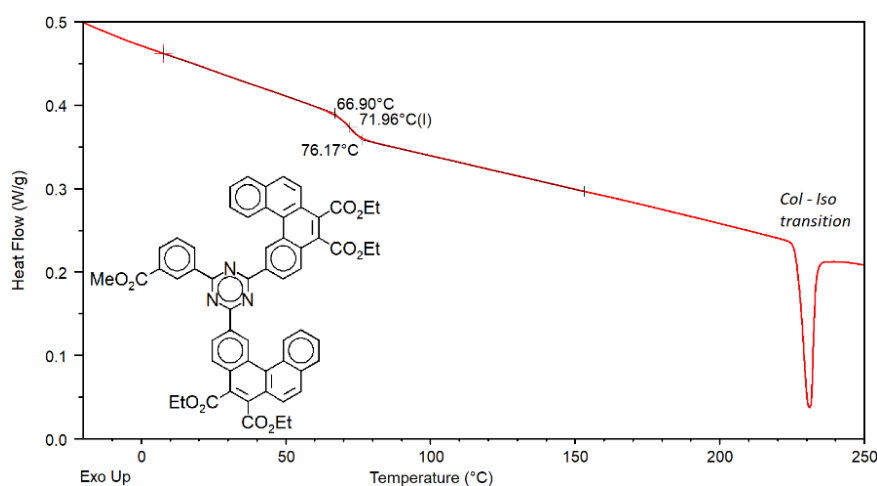


In order to directly analyze the expansion of the polyaromatic system and the resulting loss of planarity, we compare the thermal behaviors of the **H₂Et** and **F₂Et** analogues. In this direct comparison of the aromatic systems, the expansion favored the reduction of the clearing temperatures and raised $T_g$. For **F₂Et**, $T_c$ was observed around 291°C and with the increase of the aromatic system this temperature dropped to 227°C for **H₂Et**, whereas Tg was observed 13°C higher with the helicenyl analog.

Another comparison can be made between **H₁Et**, **H₂Et** and **H₃Et**. Here, as in the analysis of the phenanthrene derivatives, we observe that the amount of helicenyl groups modulates the clearing temperatures and $T_g$. The most significant feature in this comparison is the influence of Non-symmetry on the improvement in temperatures.

Symmetric **H₃Et** is not a liquid crystal. It is a hexagonal crystal and shows a crystal-crystal transition at 153°C. Non-symmetric **H₂Et**, on the other hand, is a hexagonal columnar discotic liquid crystal, with a clearing temperature of around 227°C. This temperature is greatly reduced in **H₁Et** to 144°C. The non-symmetric analogues show glass transitions at 50°C and 72°C, which are rather high values given their reduced molecular weight compared to the symmetric series. The non-symmetry has provided us

with two compounds with useful glass transition temperatures for TAFD OLED device studies.

The non-symmetric compounds **F₁Et**, **F₂Et**, **F₂Bu**, **H₁Et** and **H₂Et** vary greatly in their propensity to show a crystalline state. Only compounds with two polyaromatic groups, both phenanthrene and helicene are enantiotropic, **F₂Et** and **H₂Et**. For these compounds the clearing temperatures and Tg, were observed at relatively high temperatures, but desirable for the production of a device. The increase of the alkyl chain, from ethyl (**F₂Et**) to butyl (**F₂Bu**), disfavoured the temperature at which Tg was obtained. As for the comparison between the number of polyaromatic groups in these compounds in both cases, the higher number of polyaromatic groups raised the bleaching temperatures and the Tg temperatures.

The stabilisation of a columnar hexagonal mesophase at room temperature, combined with an accessible transition to the isotropic liquid to allow the formation of surface aligned samples by cooling from the liquid, is thus demonstrated by a molecular design based on configurable flexibility, together with a well-dosed intrinsic deviation from planarity and short alkyl ester substituents. It is a good proposal to obtain ordered arrays for OLDEs-TADF. What are reinforced poles promising preliminary photophysical results, since the experimentally observed values match with those calculated by DFT. Indicating that some of these compounds are promising candidates as OLDEs-TADF matrices.

## 5. CONCLUSIONS

The triphenanthryl-triazine hexaesters, phenanthrene derivatives with alkyl ester substituents longer than ethyl, i.e., **F₃Pr** and **F₃Bu**, showed enantiotropic columnar hexagonal mesophases that can be cooled without crystallization to form a mesomorphic glass. The glass transition temperature ($T_g$) is strongly dependent on chain length, with the Tg of the **F₃Pr** homologue being about 60°C higher than that of **F₃Bu**. Thus, a glassy state at room temperature and above can only be obtained with short alkyl chains, which implies relatively high clearing temperatures. A solution was found through a new series, the tris[4]helicenyl-triazine hexaesters, larger but less planar helicene derivatives, which with the same short alkyl chains produce monotropic hexagonal columnar mesophases with conveniently achievable melting and clearing temperatures, and, in the case of **H₃Bu**, an improved glass transition temperature, i.e. 20°C higher than that of its phenanthrene analogue **F₃Bu**. The short-chain homologue **H₃Pr** shows on cooling, instead of a glass transition, an unusual and intriguing first-order transition to a second columnar hexagonal mesophase with an extremely well-ordered hexagonal column lattice.

The non-symmetric compounds **F₁Et**, **F₂Et**, **F₂Bu**, **H₁Et** and **H₂Et** vary greatly in their propensity to show a crystalline state. Only compounds with two polyaromatic groups, either phenanthrene or [4]helicene, are enantiotropic, i.e. **F₂Et** and **H₂Et**. For these compounds the clearing temperatures and $T_g$ were observed at relatively high temperatures, which is desirable for the elaboration of devices. The increase of the alkyl chain length from ethyl (**F₂Et**) to butyl (**F₂Bu**), reduced $T_g$ greatly. As for the comparison between the number of polyaromatic groups in these compounds, in both cases, the higher number of polyaromatic groups raised the clearing temperatures as well as $T_g$.

The stabilization of a columnar hexagonal mesophase at room temperature, combined with an accessible transition to the isotropic liquid to allow the formation of surface aligned samples by cooling from the liquid, is thus demonstrated by a molecular design based on configurational flexibility, together with a well-dosed intrinsic deviation from planarity and short alkyl ester substituents. The materials obtained gave promising preliminary photophysical results, and the experimentally observed values matched those calculated by DFT rather closely. Some of these compounds are promising candidates as matrices for TADF OLEDs.

# 6.  EXPERIMENTAL PART

## 6.2 Instrumentation and materials

### 6.1.1 Materials

The reagents were obtained from commercial sources and used without prior purification.  In general, the synthesized compounds were purified by recrystallization in P.A. grade solvents and/or by column chromatography under compressed air using silica gel 60 for flash chromatography (pore size - 60 Å; particle size 35-75 µm).

### 6.1.2 Nuclear Magnetic Resonance

The $^1$H Nuclear Magnetic Resonance spectra ($^1$H NMR) and $^{13}$C ($^{13}$C NMR) were performed in a JEOL ECS-40 spectrometer (400 MHz). The chemical displacements are presented in parts per million (ppm), and are relative to tetramethylsilane (TMS). (TMS).

### 6.1.3  Mass spectrometry

Mass spectrometry analyses were obtained using a QStar Elite mass spectrometer (Applied Biosystems) in positive mode.

### 6.1.4 Thermal Analysis

The transition temperatures and mesomorphic textures were analysed on an Olympus BH-2 polarized light microscope or a BX50, equipped with a Mettler Toledo FP 82 HT Hot Stage heating plate. Meanwhile, the DSC analyses were performed in a Perkin-Elmer DSC7 equipment or in a DSC-Q 2000. The TGA analysis, in turn, was performed using a Shimadzu analyzer with the TGA-50 module.

### 6.1.5 X-Ray Diffraction Analysis

Powder X-ray diffraction (XRD) measurements were performed on powder samples placed onto a glass plate. The X'Pert-PRO (PANalytical) diffractometer used a linear monochromatic Cu Kα beam (λ = 1.5405 Å), with an applied power of 1.2 kVA. The scans were performed in continuous mode from 2° to 30° (2θ angle) and the temperature controlled with the TCU2000 temperature control unit (Anton Paar).

### 6.1.6  Optical analysis

UV-Vis spectra were collected with an Ocean Optics USB4000 spectrophotometer and the photoluminescence collected with a Hitachi fluorescence spectrophotometer, model F-7000, with excitation at 360 nm. The quantum yields were determined using a Hamamatsu Photonics Absolute Quantum Yield Measurement System model c9920-02G.

## 6.2 Synthesis

### 6.2.1 Synthesis of symmetric compounds
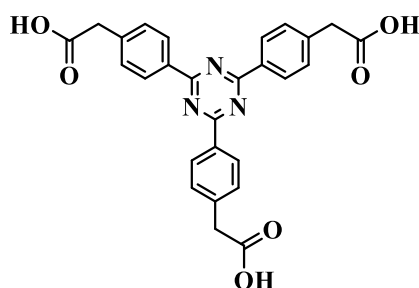


**2,4,6-triphenyl-*s*-triazine-4',4'',4'''-triacetic acid (59)**: Under ice bath cooling, triflic acid (10 mL) is added to 4-cyanoacetic acid (3 g, 160.2 g/mol, 18.7 mmol) and the mixture is stirred under exclusion of moisture for 16 h at room temperature. The ensuing viscous yellow-orange solution is poured into a stirred ice-water, mixture and stirred for 2 h. The formed white precipitate is filtered off, washed with water and air-dried. The obtained crude triacid (powder white) is used in the next step without further purification. Yield: 2.76 g (480.5 g/mol, 5.74 mmol, 92%). $^1$H NMR (400 MHz, DMSO-d$_6$): δ = 8.66 (*d*, 6 H, 8 Hz), 7.54 (*d*, 6 H, 8 Hz), 3.74 (*s*, 6 H) ppm.
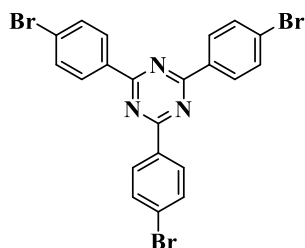


**2,4,6-tris(4-bromophenyl)-1,3,5-triazine (53)**: Under ice bath cooling, triflic acid (14 mL) is added to 4-bromobenzonitrile (5 g, 180.3 g/mol, 27.7 mmol) and the mixture is stirred under exclusion of moisture for 14 h at room temperature. The ensuing viscous yellow solution is poured into a stirred ice-water mixture and stirred for 2 h. The formed white precipitate is filtered off, washed with water and air-dried. The obtained crude tribromine was purified by chromatographic column on hot chloroform is used in the next

step (obtaining a white powder). Yield: 3.6 g (542.8 g/mol, 6.63 mmol, 72%). ^{1}H NMR (400 MHz, (CD$_3$)$_2$CO-d$_6$): δ = 8.57 (*d*, 6 H, 8.7 Hz), 7.72 (*d*, 6 H, 8.6 Hz) ppm.
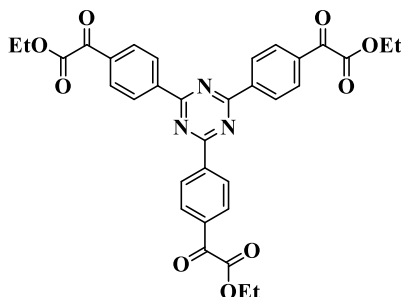


**Triethyl 2,2',2''-((1,3,5-triazine-2,4,6-triyl)tris(benzene-4,1-diyl))tris(2-oxoacetate) (54)**: Compound was added to a 1L round bottom flask, previously flamed and under argon flow. After the addition of the solid, it was alternated between vacuum and argon (2x) and then the THF was transferred via cannula. The system was cooled to -78°C with an acetone-nitrogen bath. After 20 min the n-BuLi was added slowly and monitoring the temperature. It was noticed that after adding a few drops of BuLi the solution turned orange/red. After 40 min at -78°C the bath was removed, and the system comes into equilibrium with the environment for 30 min. Subsequently, the system was again cooled to -78°C and the diethyl oxalate was rapidly added to the system. The reaction mixture was kept under cooling for ~1 h, then the cooling was removed and the flask is kept under stirring for a further 1 h. Finally, 300 mL of 1M HCl was added to the system and the organic phase was separated and dried with sodium sulfate, concentrated on the rotary evaporator, the resulting oil is precipitated in ice-cold ethanol and the precipitate was recrystallized from butanol (to a slightly yellow powder). Yield: 1.89 g (609.18 g/mol, 3.1 mmol, 32%). ^{1}H NMR (400 MHz, C$_2$D$_2$Cl$_4$): δ = 8.89 (*d*, 6H, 8.4Hz), 8.24 (*d*, 6H, 8.4Hz), 4.48 (*q*, 6 H, 7,1 Hz), 1,48 (*t*, 7,1 Hz, 9H) ppm.
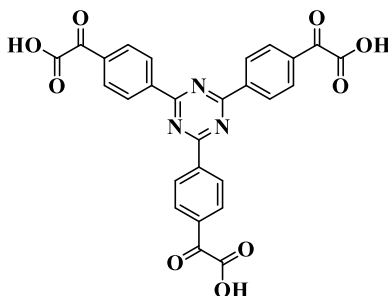


**2,2',2''-((1,3,5-triazine-2,4,6-triyl)tris(benzene-4,1-diyl))tris(2-oxoacetic acid) (55)**. The trimester (**54**) was added to a 1 L round bottom flask. After addition of the solid, it

was transferred to 0.3 L ethanol and 0.2 L water and 9 molar equivalents of $NaHCO_3$. The system was kept under strong stirring and reflux for 24 hours. After that period, the system is cooled to room temperature and then 0.2 L of 2M HCl was added to the system cautiously. The gelatinous precipitate was filtered off and washed, first with dilute hydrochloric acid and then with water (obtaining a white powder). Yield: 1.65 g (525.5 g/mol, 3.13 mmol, 92%). $^1H$ NMR (400 MHz, $C_2D_2Cl_4$): δ = 9.0 (*d*, 6 H, 8.8 Hz), 8.3 (*d,* 6 H, 8.8 Hz) ppm.

**General procedure for the condensation of 2,4,6-triphenyl-s-triazine-4',4'',4'''-triacetic acid 3 with arylglyoxylic acids to ester-substituted phenanthrenyl- and [4]helicenyl-triazines.**

2,4,6-triphenyl-s-triazine-4',4'',4'''-triacetic acid (**59)** (2 mmol, 480.5 g/mol, 0.96 g) and phenylglyoxylic acid (12 mmol, 150.1 g/mol, 1.80 g) or 2-naphthylglyoxylic acid (12 mmol, 200.2 g/mol, 2.40 g) are stirred at reflux in a mixture of acetic anhydride (40 mmol, 102.1 g/mol, 4.1 g), triethylamine (30 mmol, 101.2 g/mol, 3.0 g) and dry THF (60 mL) for 24 h under argon. Then the reaction is cooled to room temperature, a mixture of alkyl alcohol (240 mmol), bromoalkane (180 mmol) and triethylamine (120 mmol, 12 g) and dry THF (30 mL) is added and stirring at reflux is continued for another 24 h. Then the mixture is cooled to room temperature, poured into a stirred 1:1:1 mixture (300 mL) of ice, water and concentrated aqueous hydrochloric acid and extracted with ethyl acetate. The ethyl acetate extract is dried over magnesium sulphate and concentrated, and the residue is dissolved in a minimum amount of ethyl acetate and crystallized by adding ethanol. The obtained precipitate is dissolved in ethyl acetate (1 L), iodine (0.3 g) is added, and the solution is irradiated for 48 h at room temperature under air in a Peschl photoreactor with irradiation from a medium-pressure 150 W mercury immersion lamp inside a borosilicate immersion tube in which cooling water circulates. The solvent is evaporated, and the residue is purified by column chromatography on silica eluting with chloroform containing 1% of ethanol, followed by recrystallization from chloroform/ethanol to yield the desired triaryltriazine alkylester in 12 to 49% (on average 38%) overall yield over three steps (Perkin condensation, esterification, oxidative photocyclization).
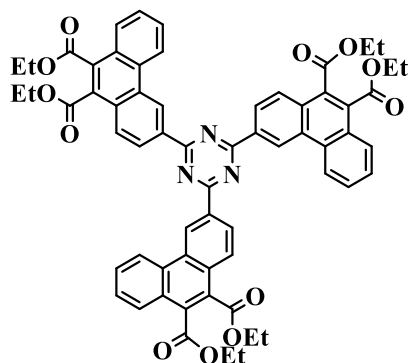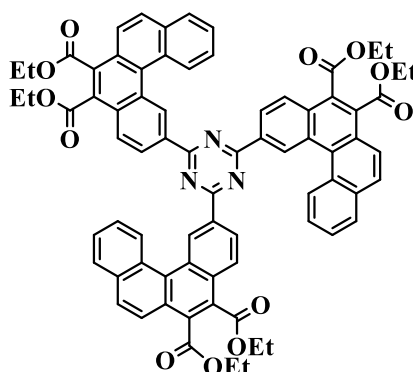
**2,4,6-tris-(9,10-bis(ethoxycarbonyl)phenanthren-3-yl)-*s*-triazine (F₃Et):** yield: 0.94 g (1042.1 g/mol, 45%), powder lightly yellow. $^1$H NMR (400 MHz, CD$_2$Cl$_2$): δ = 9.29 (*s*, 3 H), 8.37 (*dd*, 3 H, 8.4 Hz, 1.5 Hz), 8.06 (*d*, 3 H, 8.1 Hz), 7.80 (*d*, 3 H, 8.3 Hz), 7.71 (*d*, 3 H, 8.1 Hz, 1.3 Hz), 7.38 (*t*, 3 H, 8.0 Hz), 7.28 (*t*, 3 H, 8.0 Hz), 4.53 (*q*, 6 H, 7Hz), 4.52 (*q*, 6 H, 7Hz), 1.52 (*t*, 9 H, 7 Hz), 1.50 (*t*, 9 H, 7 Hz) ppm. $^{13}$C NMR (100 MHz, CD$_2$Cl$_2$): δ = 170.5, 167.95, 167.93, 134.7, 132.3, 131.0, 130.6, 130.4, 129.3, 129.2, 128.2, 127.3, 127.0, 126.9, 126.7, 124.1, 122.1, 62.5, 62.4, 14.4 ppm. ESI-HRMS: m/z calcd for C$_{63}$H$_{51}$N$_3$O$_{12}$Na [M+Na]$^+$: 1064.33650, found 1064.3378.
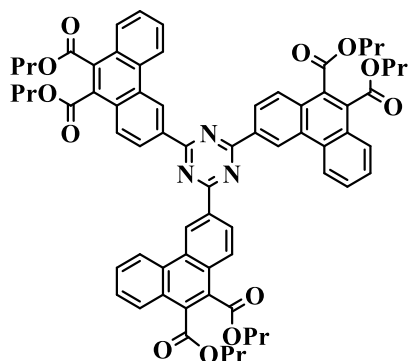


**2,4,6-tris-(9,10-bis(propoxycarbonyl)phenanthren-3-yl)-*s*-triazine (F₃Pr):** yield: 1.10 g (1126.3 g/mol, 49%), powder lightly yellow. $^1$H NMR (400 MHz, CDCl$_3$): δ = 10.25 (*s*, 3H), 9.11 (*d*, 3 H, 8 Hz), 8.93 (*d*, 3 H, 8 Hz), 8.50 (*d*, 3 H, 8 Hz), 8.17 (*d*, 3 H, 8 Hz), 7.89 (*t*, 3 H, 8 Hz), 7.76 (*t*, 3 H, 8 Hz), 4.51 (*t*, 6 H, 7 Hz), 4.48 (*t*, 6 H, 7 Hz), 1.90 (*m*, 12 H, 7 Hz),1.30 (*t*, 9 H, 7 Hz), 1.05 (*t*, 9 H, 7 Hz) ppm. $^{13}$C NMR (100 MHz, CDCl$_3$): δ = 170.1, 167.7, 167.6, 134.1, 131.8, 130.5, 130.1, 129.9, 128.9, 128.7, 127.7, 126.7, 126.5, 126.4, 126.1, 123.6, 121.5, 67.6, 67.5, 22.1, 10.7, 10.7 ppm. ESI-HRMS: m/z calcd for C$_{69}$H$_{63}$N$_3$O$_{12}$Na [M+Na]$^+$: 1148.43040, found 1148.4310.
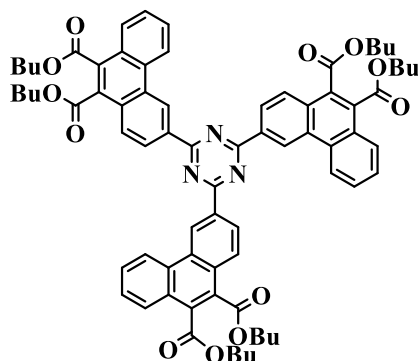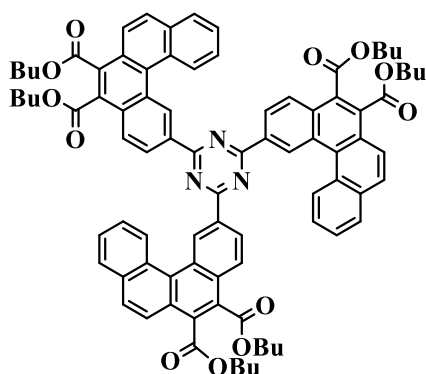
**2,4,6-tris-(9,10-bis(butoxycarbonyl)phenanthren-3-yl)-s-triazine (F₃Bu)**: yield: 0.95 g (1210.4 g/mol, 39%), powder lightly yellow. $^1$H NMR (400 MHz, CDCl$_3$): δ = 10.15 (*s*, 3 H), 9.01 (*d*, 3 H, 9 Hz), 8.80 (*d*, 3 H, 8Hz), 8.44 (*d*, 3 H, 9 Hz), 8.11 (*d*, 3 H, 8 Hz), 7.81 (*t*, 3 H, 8 Hz), 7.70 (*t*, 3 H, 8 Hz), 4.55 (*t*, 6 H, 7 Hz), 4.51 (*t*, 6 H, 7 Hz), 1.88 (*quint*, 6 H, 7 Hz), 1.86 (*quint*, 6 H, 7 Hz), 1.57 (*sext*, 6 H, 7 Hz), 1.55 (*sext*, 6 H, 7 Hz), 1.05 (*t*, 9 H, 7 Hz), 1.04 (*t*, 9 H, 7 Hz) ppm. $^{13}$C NMR (100 MHz, CD$_2$Cl$_2$): δ = 171.3, 168.13, 168.11, 135.1, 132.7, 131.4, 131.0, 130.7, 129.6, 129.4, 128.5, 127.6, 127.4, 127.3, 127.0, 124.6, 122.6, 66.7, 66.5, 31.4, 20.0, 14.23, 14.19 ppm. ESI-HRMS: m/z calcd for C$_{75}$H$_{75}$N$_3$O$_{12}$Na [M+Na]$^+$: 1232.52430, found 1232.5245.



**2,4,6-tris-(9,10-bis(ethoxycarbonyl)[4]helicen-2-yl)-s-triazine (H₃Et)**: yield: 0.88 g (1192.3 g/mol, 37%), powder lightly yellow. $^1$H NMR (400 MHz, CDCl$_3$): δ = 10.58 (*s*, 3H), 9.11 (*d*, 3 H, 8 Hz), 9.05 (*dd*, 3 H, 1 and 8 Hz), 8.53 (*d*, 3 H, 8 Hz), 8.07 (*d*, 3 H, 8 Hz), 8.01 (*d*, 3 H, 8 Hz), 8.00 (*d*, 3 H, 8 Hz) 7.50 (*t*, 6 H, 7 Hz), 7.33 (*t*, 6 H, 7 Hz), 4.61 (*sext*, 12 H, 7 Hz), 1.55 (*t*, 9 H, 7 Hz), 1.52 (*t*, 9 H, 7 Hz) ppm. $^{13}$C NMR (100 MHz, CDCl$_3$): δ = 171.4, 168.3, 167.7, 134.4, 133.9, 132.2, 131.2, 130.3, 130.3, 130.1, 129.3, 129.0, 128.7, 128.4, 127.5, 126.7, 126.5, 126.4, 126.3, 123.0, 77.5, 77.16, 76.8, 62.2, 14.4 ppm. ESI-HRMS: m/z calcd for C$_{74}$H$_{64}$N$_3$O$_{12}$Na [M+Na]$^+$: 1209.43822, found 1209.4396.
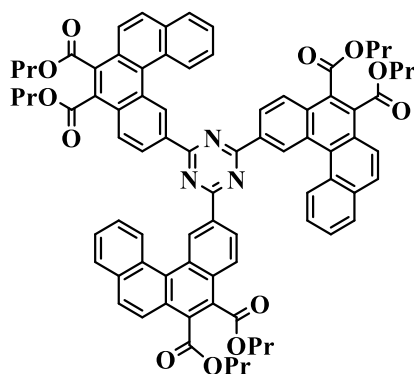
**2,4,6-tris-(9,10-bis(propoxycarbonyl)[4]helicen-2-yl)-s-triazine (H₃Pr)**: yield: 0.31 g (1276.4 g/mol, 12%), powder lightly yellow. $^1$H NMR (400 MHz, CDCl$_3$): δ = 10.65 (*s*, 3H), 9.16 (*d*, 3 H, 8 Hz), 9.10 (*dd*, 3 H, 1 and 8 Hz), 8.56 (*d*, 3 H, 8 Hz), 8.10 (*d*, 3 H, 8 Hz), 8.05 (*d*, 6 H, 8 Hz), 7.54 (*t*, 3 H, 7 Hz), 7.39 (*t*, 3 H, 7 Hz), 4.53 (*t*, 6 H, 7 Hz), 4.49 (*t*, 6 H, 7 Hz), 1.92 (*m*, 12 H), 1.15 (*t*, 9 H, 7 Hz), 1.09 (*t*, 9 H, 7 Hz) ppm. $^{13}$C NMR (100 MHz, CDCl$_3$): δ = 171.5, 168.4, 167.9, 134.5, 133.9, 132.4, 131.3, 130.4, 130.3, 130.2, 129.3, 129.0, 128.8, 128.5, 128.4, 127.5, 126.8, 126.5, 126.5, 126.3, 123.0, 68.0, 22.2, 22.1, 10.8, 10.7 ppm. ESI-HRMS: m/z calcd for C$_{81}$H$_{69}$N$_3$O$_{12}$Na [M+Na]$^+$: 1298.47735, found 1298.4778.



**2,4,6-tris-(9,10-bis(butoxycarbonyl)[4]helicen-2-yl)-s-triazine (H₃Bu)**: yield: 1.13 g (1360.6 g/mol, 42%), powder lightly yellow. $^1$H NMR (400 MHz, CD$_2$Cl$_2$): δ = 10.45 (*s*, 3H), 9.02 (*d*, 3 H, 8.5 Hz), 8.95 (*dd*, 3 H, 8.6 Hz, 1.5 Hz), 8.45 (*d*, 3 H, 8.7 Hz), 7.99 (*d*, 3 H, 3.0 Hz), 7.97 (d, 3 H, 8.1 Hz), 7.95 (*d*, 3 H, 8.4 Hz), 7.41 (*t*, 3 H, 7.5 Hz), 7.23 (*t*, 3 H, 7.7 Hz), 4.56 (*t*, 6 H, 7.0 Hz), 4.53 (*t*, 6 H, 7.1 Hz), 1.90 (*quint*, 6 H, 6.9 Hz), 1.87 (*quint*, 6 H, 6.8 Hz), 1.59 (*sext*, 6 H, 7.3 Hz), 1.55 (*sext*, 6 H, 7.2 Hz), 1.07 (*t*, 9 H, 7.0Hz), 1.05 (*t*, 9 H, 7.1 Hz) ppm. $^{13}$C NMR (100 MHz, CD$_2$Cl$_2$): δ = 172.0, 168.6, 168.1, 135.0, 134.4, 132.8, 131.7, 130.8, 130.7, 129.8, 129.5, 129.2, 19.1, 128.9, 128.0, 127.2, 127.1, 126.9, 126.7, 123.5, 66.8, 66.7, 31.3, 31.2, 19.19, 19.18, 14.0, 13.9 ppm.
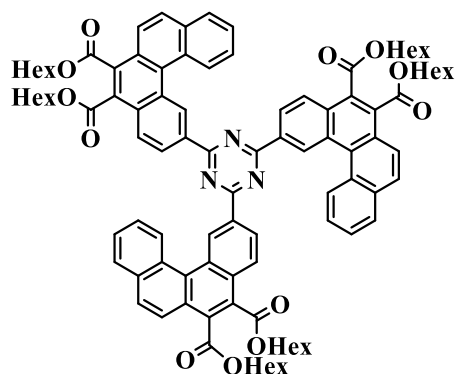
**2,4,6-tris-(9,10-bis(hexyloxycarbonyl)[4]helicen-2-yl)-s-triazine (H₃Hex)**: yield: 1.28 g (1528.9 g/mol, 42%), powder lightly yellow. $^1$H NMR (400 MHz, CDCl$_3$): δ = 10.63 (*s*, 3 H), 9.15 (*d*, 3 H, 8 Hz), 9.09 (*dd*, 3 H, 1 and 8 Hz), 8.55 (*d*, 3 H, 8 Hz), 8.09 (*d*, 3 H, 8 Hz), 8.04 (*d*, 6 H, 8 Hz), 7.53 (*t*, 3 H, 7 Hz), 7.37 (*t*, 3 H, 7 Hz), 4.55 (*t*, 6 H, 7 Hz), 4.52 (*t*, 6 H, 7 Hz), 1.88 (*m*, 12 H), 1.52 (*m*, 12 H), 1.38 (*m*, 24 H), 0.92 (*t*, 18 H, 7 Hz) ppm. $^{13}$C NMR (100 MHz, CDCl$_3$): δ = 172.0, 168.4, 167.9, 134.8, 134.2, 132.4, 131.5, 130.7, 130.6, 130.5, 129.6, 129.2, 128.9, 128.7, 128.6, 127.8, 127.0, 126.8, 126.6, 123.3, 66.7, 31.7, 28.8, 28.7, 25.9, 22.7, 14.2 ppm.

### 6.2.2 Synthesis of non-symmetric compounds

**4',4''-bis(methoxycarbonyl)-2,4,6-triphenyl-s-triazine-4'''-acetic acid (65)** and **4'-methoxycarbonyl-2,4,6-triphenyl-s-triazine-4,''4'''-diacetic acid (67)**

Under ice bath cooling, triflic acid (10 mL) is added to an intimate mixture of 4-cyanoacetic acid (2 g, 160.2 g/mol, 12.5 mmol) and methyl 3-cyanobenzoate (2.00 g, 160.2 g/mol, 12.5 mmol), and the mixture is stirred under exclusion of moisture for 16 h at room temperature. The ensuing viscous yellow-orange solution is poured into a stirred ice-water mixture and stirred for 2 h. The formed white precipitate is filtered off, washed with water and air-dried. The product mixture is separated by column chromatography on silica: The unwanted triester **(70)** is eluted with pure chloroform, the diester-monoacid **(65)** is eluted thereafter with chloroform containing 5% of acetone, and finally the monoester-diacid **(67)** is eluted with chloroform containing 10% of acetone, leaving the unwanted triacid **(69)** on the column. The two separated cotrimerization products are used in the next step without further purification. Yields for **(65)** and **(67)** varied from batch to batch between 0.3 g and 0.6 g for either of them, with an average yield of 0.45 g each. The statistically expected yield presuming ideal mixing of the two starting materials

leading to a 1:3:3:1 ratio between products (**70**), (**65**), (**67**) and (**69**) is 1.5 g of both (**65**) and (**67**), thus the average isolated yields of each the two co-trimerization products correspond to 30 % of the theoretical value.
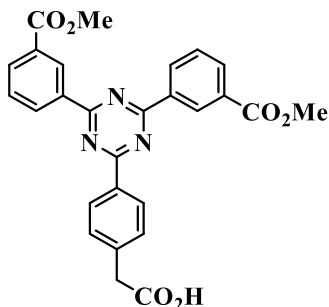


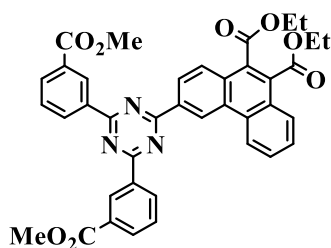**(2-(4-(4,6-bis(3-(methoxycarbonyl)phenyl)-1,3,5-triazin-2-yl)phenyl) acetic acid) (65):** yield: 32%, powder white.^{1}H NMR (400 MHz, DMSO-d$_6$): δ = 8.93 (*s*, 2 H), 8.67 (*d*, 2 H, 7.8 Hz), 8.41 (*d*, 2 H, 8.4 Hz), 8.12 (*d*, 2 H, 6.2 Hz), 7.65 (*t*, 2 H, 7.8 Hz), 7.46 (*d*, 2 H, 8.4 Hz), 3.89 (*s*, 6 H), 3.66 (*s*, 2 H) ppm.
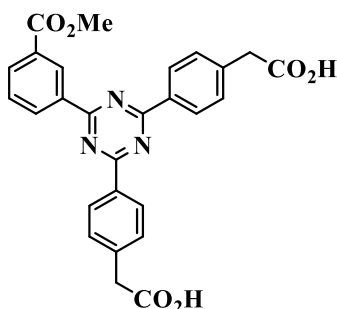


**2,2'-((6-(3-(methoxycarbonyl)phenyl)- 1,3,5-triazine-2,4-diyl) bis (4,1-phenylene)) diacetic acid (67)**: yield: 32%, powder white. ^{1}H NMR (400 MHz, DMSO-d$_6$): δ = 9.09 (*s*, 1 H), 8.85 (*d*, 1 H, 9.0 Hz), 8.57 (*d*, 4 H, 8.4 Hz), 8.18 (*d*, 1 H, 7.8 Hz), 7.73 (*t*, 1 H, 7.8 Hz), 7.49 (*d*, 4 H, 8.4 Hz), 3.91 (*s*, 3 H), 3.72 (*s*, 4 H) ppm.

**General procedure for the condensation of triazine-acetic acids with arylglyoxylic acids to ester-substituted phenanthrenyl- and [4]helicenyl-triazines**

Triazine-mono- or -diacetic acid (**65**) or (**67**) (2 mmol, 480.5 g/mol each, 0.96 g) and a two fold excess (i.e. 4 or 8 mmol) of phenylglyoxylic acid or 2-naphthylglyoxylic acid are stirred at reflux in a mixture of acetic anhydride (40 mmol, 102.1 g/mol, 4.1 g), triethylamine (30 mmol, 101.2 g/mol, 3.0 g) and dry THF (60 mL) for 24 h under argon. Then the reaction is cooled to room temperature, a mixture of alkyl alcohol (240 mmol), bromoalkane (180 mmol) and triethylamine (120 mmol, 12 g) and dry THF (30 mL) is added and stirring at reflux is continued for another 24 h. Then the mixture is cooled to room temperature, poured into a stirred 1:1:1 mixture (300 mL) of ice, water and

concentrated aqueous hydrochloric acid and extracted with ethyl acetate. The ethyl acetate extract is dried over magnesium sulphate and concentrated, and the residue is dissolved in a minimum amount of ethyl acetate and crystallized by adding ethanol or purified by column chromatography, chloroform-cyclohexane eluent. The obtained precipitate is dissolved in ethyl acetate (1 L), iodine (0.3 g) is added, and the solution is irradiated for 48 h at room temperature under air in a Peschl photoreactor with irradiation from a medium-pressure 150 W mercury immersion lamp inside a borosilicate immersion tube in which cooling water circulates. The solvent is evaporated, and the residue is purified by column chromatography on silica eluting with chloroform containing 1% of ethanol, followed by recrystallization from chloroform/ethanol to yield the desired triaryltriazine alkylester in 20 to 45% (on average 34%) overall yield over three steps (Perkin condensation, esterification, oxidative photocyclization).



**2,4-bis(3-(methoxycarbonyl)phenyl)-6-(9,10-bis(ethoxycarbonyl)phenanthren-3-yl)-*s*-triazine F$_1$Et.** Yield: 0.27 g (669.7 g/mol, 20%), powder lightly yellow. ^{1}H NMR (400 MHz, CD$_2$Cl$_2$): δ = 9.76 (*s*, 1 H), 9.02 (*s*, 2 H), 8.68 (*d*, 1 H, 8.1 Hz), 8.65 (*d*, 1 H, 8.9 Hz), 8.61 (*d*, 2 H, 8.1 Hz), 8.19 (*d*, 1 H, 8.9 Hz), 8.08 (*d*, 3 H, 7.9 Hz), 7.77 (*t*, 1 H, 8.2 Hz), 7.69 (*t*, 1 H, 8.2 Hz), 7.47 (*t*, 2 H, 7.6 Hz), 4.55 (*q*, 2 H, 7.1 Hz), 4.54 (*q*, 2 H, 6.8 Hz), 3.95 (*s*, 6 H), 1.52 (*t*, 3 H, 7.2 Hz), 1.50 (*t*, 3 H, 6.9 Hz) ppm. ^{13}C NMR (100 MHz, CD$_2$Cl$_2$): δ = 171.3, 171.1, 168.1, 167.9, 166.7, 136.3, 135.2, 133.9, 133.3, 132.5, 131.7, 131.1, 131.0, 130.5, 130.2, 129.7, 129.3, 129.2, 128.4, 127.7, 127.6, 127.3, 127.2, 124.3, 123.5, 62.7, 62.6, 52.7, 14.59, 14.57 ppm. ESI-HRMS: m/z calcd for C$_{39}$H$_{31}$N$_3$O$_8$Na [M+Na]$^+$: 692.20034, found 692.1992.
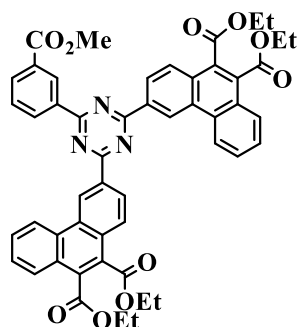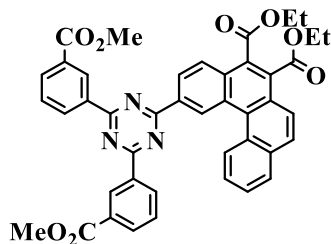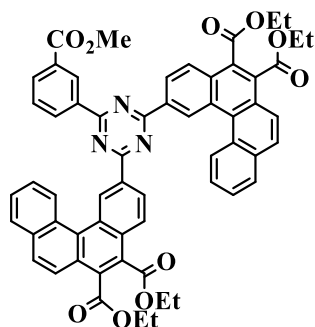
**2-(3-(methoxycarbonyl)phenyl)-4,6-bis(9,10-bis(ethoxycarbonyl)phenanthren-3-yl)**
**-*s*-triazine F₂Et:** Yield: 0.77 g (855.9 g/mol, 45%), powder lightly yellow. $^1$H NMR (400
MHz, CD$_2$Cl$_2$): δ = 10.15 (*s*, 2 H), 9.38 (s, 1H), 8.99 (*d*, 2 H, 8.8 Hz), 8.89 (*d*, 1 H, 8.6
Hz), 8.39 (*d*, 2 H, 8.8 Hz), 8.27 (*d*, 2 H, 8.7 Hz), 8.13 (*d*, 1 H, 7.9 Hz), 7.86 (*d*, 2 H, 7.9
Hz), 7.75 (*t*, 2 H, 7.9 Hz), 7.73 (*t*, 2 H, 8.1 Hz), 7.70 (*t*, 1 H, 8.2 Hz), 4.56 (*q*, 4 H, 7.1
Hz), 4.54 (*q*, 4 H, 7.2 Hz), 3.93 (*s*, 3 H), 1.52 (*t*, 6 H, 6.9 Hz), 1.51 (*t*, 6 H, 6.8 Hz) ppm.
$^{13}$C NMR (100 MHz, CD$_2$Cl$_2$): δ = 171.3, 171.1, 168.1, 167.9, 166.7, 136.3, 135.2, 133.9,
133.3, 132.5, 131.7, 131.1, 131.0, 130.5, 130.2, 129.7, 129.3, 129.2, 128.4, 127.7, 127.6,
127.3, 127.2, 124.3, 123.5, 62.7, 62.6, 52.7, 14.59, 14.57 ppm. ESI-HRMS: m/z calcd for
C$_{51}$H$_{41}$N$_3$O$_{10}$Na [M+Na]$^+$: 878.26842, found 878.2682.
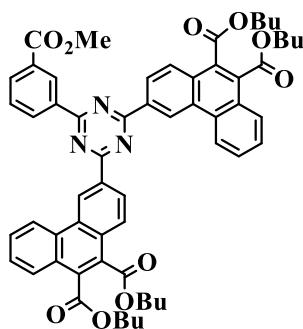


**2-(3-(methoxycarbonyl)phenyl)-4,6-bis(9,10-bis(butoxycarbonyl)phenanthren-3-yl)**
**-*s*-triazine F₂Bu:** Yield: 0.74 g (968.1 g/mol, 38%), powder lightly yellow. $^1$H NMR (400
MHz, CDCl$_3$): δ = 10.14 (*s*, 2 H), 9.41 (*s*, 1 H), 9.00 (*d*, 2 H, 9 Hz), 8.96 (*d*, 1 H, 8 Hz),
8.88 (*d*, 2 H, 8 Hz), 8.40 (*d*, 2 H, 9 Hz), 8.30 (*d*, 1 H, 8 Hz), 8.14 (*d*, 2 H, 8 Hz), 7.85 (*t*,
2 H, 8 Hz), 7.72 (*t*, 2 H, 8 Hz), 7.70 (*t*, 1 H, 8 Hz), 4.52 (*t*, 4 H, 7 Hz), 4.49 (*t*, 4 H, 7 Hz),
4.06 (*s*, 3 H), 1.85 (*quint*, 4 H, 7 Hz), 1.84 (*quint*, 4 H, 7 Hz), 1.54 (*sext*, 4 H, 7 Hz), 1.52
(*sext*, 4 H, 7 Hz), 1.03 (*t*, 6 H, 7 Hz), 1.01 (*t*, 6 H, 7 Hz) ppm. $^{13}$C NMR (100 MHz,
CD$_2$Cl$_2$): δ = 171.2, 171.0, 168.1, 168.0, 166.6, 136.1, 135.1, 133.9, 133.2, 132.6, 131.5,
131.0, 130.6, 130.1, 129.7, 129.3, 129.1, 128.4, 127.6, 127.5, 127.2, 127.1, 124.4, 123.0,

66.62, 66.56, 52.6, 31.3, 19.9, 14.19, 14.17 ppm. ESI-HRMS: m/z calcd for $C_{59}H_{57}N_3O_{10}Na$ [M+Na]$^+$: 990.39362, found 990.3940.



**2,4-bis(3-(methoxycarbonyl)phenyl)-6-(5,6-bis(ethoxycarbonyl)[4]helicen-2-yl)-*s*-triazine H₁Et:** Yield: 0.36 g (719.7 g/mol, 25%), powder lightly yellow. $^1$H NMR (400 MHz, CDCl$_3$): δ = 10.49 (*s*, 1 H), 9.30 (*s*, 2 H), 9.20 (*d*, 1 H, 8.8 Hz), 8.94 (*d*, 3 H, 7.8 Hz), 8.45 (*d*, 1 H, 8.8 Hz), 8.23 (*d*, 2 H, 7.8 Hz), 8.12 (*d*, 1 H, 8.8 Hz), 8.05 (*d*, 1 H, 8.9 Hz), 8.02 (*d*, 1 H, 8.9 Hz), 7.91 (*t*, 1 H, 6.9 Hz), 7.80 (*t*, 1 H, 6.9 Hz), 7.64 (*t*, 2 H, 7.8 Hz), 4.60 (*q*, 2 H, 6.8 Hz), 4.58 (*q*, 2 H, 6.9 Hz), 4.02 (*s*, 6 H), 1.53 (*t*, 3 H, 7.4 Hz), 1.49 (*t*, 3 H, 7.4 Hz) ppm. $^{13}$C NMR (100 MHz, CD$_2$Cl$_2$): δ = 172.0, 171.5, 168.4, 167.9, 166.9, 136.7, 134.8, 134.6, 134.0, 133.6, 132.6, 131.7, 131.4, 130.8, 130.7, 130.6, 130.2, 130.0, 129.5, 129.4, 129.1, 129.0, 128.2, 127.7, 127.3, 126.9, 126.8, 123.6, 62.8, 52.8, 14.62, 14.57 ppm. ESI-HRMS: m/z calcd for $C_{43}H_{33}N_3O_8Na$ [M+Na]$^+$: 742.21599, found 742.2161.



**2-(3-(methoxycarbonyl)phenyl)-4,6-bis(9,10-bis(ethoxycarbonyl)[4]helicen-2-yl)-*s*-triazine H₂Et.** Yield: 0.79 g (956.0 g/mol, 41%), powder lightly yellow. $^1$H NMR (400 MHz, CDCl$_3$): δ = 10.52 (*s*, 2 H), 9.36 (*t*, 1 H, 1.8 Hz), 9.15 (*d*, 2 H, 8.2 Hz), 8.99 (*d*, 1 H, 8.2 Hz), 8.97 (*d*, 2 H, 8.1 Hz), 8.48 (*d*, 2 H, 8.7 Hz), 8.25 (*d*, 1 H, 7.9 Hz), 8.09 (*d*, 2 H, 8.3 Hz), 8.06 (*d*, 2 H, 8.8 Hz), 8.02 (*d*, 2 H, 8.8 Hz), 7.71-7.65 (*m*, 5 H), 4.62 (*q*, 4 H, 6.9 Hz), 4.59 (*q*, 4 H, 6.9 Hz), 4.02 (*s*, 3 H), 1.54 (*t*, 6 H, 6.7 Hz), 1.51 (*t*, 6 H, 6.7 Hz) ppm. $^{13}$C NMR (100 MHz, CD$_2$Cl$_2$): δ = 172.1, 171.5, 168.4, 168.0, 166.9, 136.9, 134.9, 134.5, 134.1, 133.7, 132.6, 131.7, 131.5, 130.9, 130.7, 130.1, 129.9, 129.5, 129.4, 129.3,

129.1, 129.0, 128.1, 127.4, 127.2, 126.9, 126.8, 123.5, 62.8, 52.8, 14.63, 14.57 ppm. FD-HRMS: m/z calcd for $C_{59}H_{45}N_3O_{10}Na$ [M+Na]$^+$: 978.29972, found 978.3007.

## 7.  BIBLIOGRAPHIC REFERENCES

ANDRIENKO, D.. Introduction to liquid crystals. **Journal of Molecular Liquids**, *267*, 2018. https://doi.org/10.1016/j.molliq.2018.01.175

AN, J. G. et al. Characterization of liquid crystals: A literature review. In **Reviews on Advanced Materials Science**, Vol. 44, Issue 4, 2016.

BARNES, J. C. et al. ExBox: A polycyclic aromatic hydrocarbon scavenger. **Journal of the American Chemical Society**, *135*(1), 183–192, 2013. https://doi.org/10.1021/ja307360n

BECHTOLD, I. H.. Cristais líquidos: um sistema complexo de simples aplicação. **Revista Brasileira de Ensino de Física**, *27*(3), 333–342, 2005. https://doi.org/10.1590/S1806-11172005000300006

BELTRÁN, E, Serrano, JL, Sierra, T & Giménez, R.. Tris(triazolyl)triazine via click-chemistry: A C3 electron-deficient core with liquid crystalline and luminescent properties. **Organic Letters**. 12(7):1404–1407, 2010. doi.org/10.1021/ol902900y.

BELTRÁN, E, SERRANO, JL, SIERRA, T & GIMÉNEZ, R.. Functional star-shaped tris(triazolyl)triazines: Columnar liquid crystal, fluorescent, solvatofluorochromic and electrochemical properties. **Journal of Materials Chemistry**. 22(16):7797–7805, 2012. doi.org/10.1039/c2jm15648b.

BHAGAVATH, P., SHETTY, R., & SUNIL, D.. 1 , 3 , 5-Triazine-Based Liquid Crystals : An Up-to-Date Appraisal of Their Synthetic Design and Mesogenic Properties. **Critical Reviews in Solid State and Materials Sciences**, *0*(0), 1–32, 2019. https://doi.org/10.1080/10408436.2019.1632794

BINOT, C., SADOC, J. F., & CHOUARD, C. H.. Oncogenesis, lipids rafts and liquid crystals: A nanoscopic supplementary field for applied researches and a new hope of advances in cancer. **Heliyon**, *4*(7), 687, 2018. https://doi.org/10.1016/j.heliyon.2018.e00687

CHANDRASEKHAR, S., SADASHIVA, B. K., & SURESH, K. A. **Liquid crystals of disc-like molecules**.Vol. 9, Issue 5, 1977.

COLLINGS, P. J., & PATEL, J. S. (1997). **Handbook of liquid crystal research**. Oxford University press: New York, 1997.

CRAWFORD, M., & SHAW, J. A. M. (1953). The course of the Perkin coumarin synthesis. Part I. **Journal of the Chemical Society (Resumed)**, 3435–3439, 1953. https://doi.org/10.1039/jr9530003435

SILVA, F. N. da et al. Luminescent liquid crystals based on 2,1,3-benzoxadiazole: conducive heterocycle or poor cousin of benzothiadiazole? **Liquid Crystals**, *46*(11), 1707–1717, 2019. https://doi.org/10.1080/02678292.2019.1595754

DEBENEDETTI, P. G., & STILLINGER, F. H. **Supercooled liquids and the glass transition**, 2001.

www.nature.com

DIERKING, I..Handbook of liquid crystals. In **Liquid Crystals Today**.Vol. 24, Issue 1, 2015.
 https://doi.org/10.1080/1358314X.2014.973266

DOYRANLI, C. et al. Effect of the planar center moiety for a donor-acceptor polymeric electrochrome. **Polymer,** *108*, 423–431, 2017.
https://doi.org/10.1016/j.polymer.2016.12.016

DUDLEY, B. Y. J. R., & THURSTON, J. T. *Cyanuric Chloride Derivatives. 111. Alkoxy-s-triazines BY. 1946*(1945), 1949.

ELY, F., MAMORU, M. H., HAMANAKA, O., & Pellegrini , A. Cristais Líquidos Colestéricos: a quiralidade revela as suas cores. In **Quim. Nova**.Vol. 30, Issue 7, 2007.

Endo, A. et al. Efficient up-conversion of triplet excitons into a singlet state and its application for organic light emitting diodes. **Applied Physics Letters**, *98*(8), 2011.
https://doi.org/10.1063/1.3558906

Fields, E. K. et al. Diaryl-Substituted Maleic Anhydrides. **J. Org. Chem,** *55*, 5165–1570, 1990.

FORSBERG, J. H., SPAZIANO, V. T., KLUMP, S. P., & SANDERS, K. M. Lanthanide(III) ion catalyzed reaction of ammonia and nitriles: Synthesis of 2,4,6-trisubstituted-s-triazines. In **Journal of Heterocyclic Chemistry**.Vol. 25, Issue 3, pp. 767–770, 1988.
 https://doi.org/10.1002/jhet.5570250312

GLANG, S. et al. Arylethynyl-substituted tristriazolotriazines: Synthesis, optical properties, and thermotropic behavior. **European Journal of Organic Chemistry**, (15), 3116–3126, 2014.
https://doi.org/10.1002/ejoc.201400088

HASAN, M., & BOROVKOV, V. Helicene-based chiral auxiliaries and chirogenesis. In **Symmetry**,Vol. 10, Issue 1. MDPI AG, 2018.
https://doi.org/10.3390/sym10010010

HAYAMI, S., & INOUE, K. Structure and magnetic property of the organic triradical with triazine skeleton; 2,4,6-tris{p-(N-oxy-N-tert-butylamino)phenyl}triazine. In **Chemistry Letters**, Issue 7, pp. 545–546, 1999.
https://doi.org/10.1246/cl.1999.545

HOFBECK, T., MONKOWIUS, U., & YERSIN, H. Highly efficient luminescence of Cu(I) compounds: Thermally activated delayed fluorescence combined with short-lived phosphorescence. **Journal of the American Chemical Society**, *137*(1), 399–404, 2015.
 https://doi.org/10.1021/ja5109672

HOPF, H. My favorite aromatic compounds - A tribute to friedrich august kekulé. In **Chemical Record**, Vol. 14, Issue 5, pp. 979–1000, 2014. John Wiley and Sons Inc.
 https://doi.org/10.1002/tcr.201402056

HRBAC, J. et al. Immobilization of helicene onto carbon substrates through electropolymerization of [7]helicenyl-thiophene. **RSC Advances**, *4*(86), 46102–46105, 2014.
https://doi.org/10.1039/c4ra06283c

JABŁOŃSKI, A. et al. Anthracene-thymine luminophores: Synthesis, photophysical properties, and imaging in living HeLa cells. **Dyes and Pigments**, *170*(April), 107554, 2019.
 https://doi.org/10.1016/j.dyepig.2019.107554

JAKUBEC, M. et al. 2-Bromo[6]helicene as a Key Intermediate for [6]Helicene Functionalization. **Journal of Organic Chemistry**, *83*(7), 3607–3616, 2018.
https://doi.org/10.1021/acs.joc.7b03234

JAKUBEC, M., & Storch, J. Recent Advances in Functionalizations of Helicene Backbone. **Journal of Organic Chemistry**, *85*(21), 13415–13428, 2020.
https://doi.org/10.1021/acs.joc.0c01837

JØRGENSEN, K. B.. Photochemical oxidative cyclisation of stilbenes and stilbenoids-the Mallory-reaction. In **Molecules**, Vol. 15, Issue 6, pp. 4334–4358, 2010.
https://doi.org/10.3390/molecules15064334

KELLY, S. M., O'NEIL, M. **Liquid crystal for electro-optic applications**.Vol. 7, 2001.

KOTIAN, S. Y. et al. Small molecule based five-membered heterocycles: A view of liquid crystalline properties beyond the biological applications. **Journal of Molecular Liquids**, *297*, 111686, 2020.
https://doi.org/10.1016/j.molliq.2019.111686

KUMAR, S. et al. Structurally controlled singlet-triplet splitting for blue star-shaped thermally activated delayed fluorescence emitters incorporating the tricarbazoles-triazine motifs. ***Organic Electronics***. 84, 2020.
 doi.org/10.1016/j.orgel.2020.105783.

KUMAR, R. et al. Send Orders for Reprints to reprints@benthamscience.net 1,2,3-Triazine Scaffold as a Potent Biologically Active Moiety: A Mini Review. **Reviews in Medicinal Chemistry**, *14*, 72–83, 2014.
https://www.ingentaconnect.com/contentone/ben/mrmc/2014/00000014/00000001/art00007?crawler=true

KUMAR, S. **Chemistry of Discotic Liquid Crystals**, 2011.
https://doi.org/10.1201/b10457

LASCHAT, S. (2009). Progress in liquid crystal chemistry. *J. of Org. Chem*, *48*.

LEE, H. et al. Discotic liquid crystalline materials for potential nonlinear optical applications: Synthesis and liquid crystalline behavior of 1,3,5-triphenyl-2,4, 6-triazine derivatives containing achiral and chiral alkyl chains at the periphery. **Tetrahedron Letters**. 45(5):1019–1022, 2004.
doi.org/10.1016/j.tetlet.2003.11.085.

LIU, C. et al. Small molecule-mediated glass transition of acrylic copolymers: Effect of hydrogen bonding strength on glass transition temperature. **Journal of**

**Polymer Science**, *Part B: Polymer Physics*, *53*(6), 400–408, 2015. https://doi.org/10.1002/polb.23642

LIU, L., YANG, B., KATZ, T. J., & POINDEXTER, M. K. Improved Methodology for Photocyclization Reactionst. In **J. Org. Chem**, Vol. 56, 1991.

LI, YF et al. Two bipolar blue-emitting fluorescent materials based on 1,3,5-triazine and peripheral pyrene for organic light-emitting diodes. **Dyes and Pigments**. 145:43–53, 2017. doi.org/10.1016/j.dyepig.2017.05.017.

LI, Z., & TWIEG, R. J. Photocyclodehydrofluorination. **Chemistry - A European Journal**, *21*(44), 15534–15539, 2015. https://doi.org/10.1002/chem.201502473

MALLORY, F. B., & MALLORY, C. W. Photocyclization of stilbenes and related molecules. In **Organic Reactions**, Vol. 30, pp. 3–81, 1984.

MALLORY, F. B., MALLORY, C. W., BUTLER, K. E., & EVANs, A. C. (1997). Phenacenes: A Family of Grafite Ribbons. 2. Syntheses of some [7]Phenacene by Stilbene-like Photocyclizations. **J. Am. Chem. Soc.**, *119*(2), 2119–2124, 1997.

MALLORY, F. B., WOOD, C. S., GORDON, J. T., & F. Photochemistry of Stilbenes. 111. Some Aspects of the Mechanism of Photocyclization to Phenanthrenes'. **J. Am. Chem. Soc.**, *86*, 3094–3102, 1964.

MATULAITIS, T. et al. Synthesis and properties of bipolar derivatives of 1,3,5-triazine and carbazole. **Dyes and Pigments**. 127:45–58, 2016. doi.org/10.1016/j.dyepig.2015.11.001.

MOOIBROEK, TJ & GAMEZ, P. The s-triazine ring, a remarkable unit to generate supramolecular interactions. **Inorganica Chimica Acta**. 360(1):381–404, 2007.
 doi.org/10.1016/j.ica.2006.07.061.

MUELLER-GOYMANN, C. C. Drug Delivery — Liquid Crystals in. **Pharmaceutical Technolog**y*, 2002*.

NAVEEN, K. R., YANG, H. I., & KWON, J. H. Double boron-embedded multiresonant thermally activated delayed fluorescent materials for organic light-emitting diodes. **Communications Chemistry**, *5*(1), 2022. https://doi.org/10.1038/s42004-022-00766-5

PARDESHI, S. D. et al. Transition Metal-Free sp3 C–H Functionalization of Arylacetic Acids for the Synthesis of 1,3,5-Triazines. **European Journal of Organic Chemistry**, (18), 2098–2102, 2018. https://doi.org/10.1002/ejoc.201800178

PARKER, C. O., & SPOERRI, P. E. Photochemical Conversion of Stilbene to Phenanthrene. **Nature**, *166*, 603, 1950.

PERKIN, W. H. XI.—On the formation of coumarin and of cinnamic and of other analogous acids from the aromatic aldehydes. **J. Chem. Soc.**, *31*(0), 388–427, 1877.
 https://doi.org/10.1039/js8773100388

PESTOV, S., & VILL, V. Liquid crystals. In **Springer Handbooks**, 2018. https://doi.org/10.1007/978-3-319-69743-7_26

PRADHAN, B. et al. Star-shaped fluorescent liquid crystals derived from s-triazine and 1,3,4-oxadiazole moieties. **Journal of Materials Chemistry C**, *4*(25), 6117–6130, 2016. https://doi.org/10.1039/c6tc01260d

RAVAT, P. Carbo[n]helicenes Restricted to Enantiomerize: An Insight into the Design Process of Configurationally Stable Functional Chiral PAHs. In **Chemistry - A European Journal**, Vol. 27, Issue 12, pp. 3957–3967, 2021. Wiley-VCH Verlag.
 https://doi.org/10.1002/chem.202004488

ROBERT, A, DECHAMBENOIT, P, BOCK, H & DUROLA, F. A carboxyfunctionalized (24)-1,6-pyrenophane-tetraene by glyoxylic Perkin condensation. **Canadian Journal of Chemistry**. 95(4):450–453, 2017. doi.org/10.1139/cjc-2016-0585.

RYAN, S. T. J., & FUCHTER, M. J. Helicenes for Optoelectronic Applications and Devices. In **Helicenes**, pp. 473–503, 2022. Wiley. https://doi.org/10.1002/9783527829415.ch15

SAGARA, B. Y. et al. A stimuli-responsive, photoluminescent, anthracene- based liquid crystal: emission color determined by thermal and mechanical processes. **Advanced Functional Materials,** *19*(12), 1869–1875, 2009. https://doi.org/10.1002/adfm.200801726

SARKAR, P., DUROLA, F., & BOCK, H. Dipyreno- and diperyleno-anthracenes from glyoxylic Perkin reactions. **Chemical Communications,** *49*(68), 7552–7554, 2013.
 https://doi.org/10.1039/c3cc44044c

SCHEROWSKY, G., & CHEN, X. H. Ferroelectric Switching in Columnar Phases of Novel Chiral Discotic Liquid Crystals. In **J. Mater. Chem**, Vol. 5, Issue 3, 1995.

SHARMA, N. et al. Turn on of sky-blue thermally activated delayed fluorescence and circularly polarized luminescence (CPL): Via increased torsion by a bulky carbazolophane donor. **Chemical Science.** 10(27):6689–6696, 2019. doi.org/10.1039/c9sc01821b.

SMAKULA, A. **The photochemical transformation of trans-stilbene**. *B25*, 90–98, 1934.

STORCH, J. et al. The Photochemical Approach to Helicenes. In **Helicenes**, Wiley, pp. 1–52, 2022.
https://doi.org/10.1002/9783527829415.ch1

STORCH, J. et al. Synthesis and Characterization of a helicene-based imidazolium salt and its application in organic molecular electronics. **Chemistry - A European Journal**, *21*(6), 2343–2347, 2015. https://doi.org/10.1002/chem.201405239

STURM, L. et al (2022). The Perkin Strategy for the Synthesis of Large Carboxy-Substituted Polycyclic Aromatic Compounds. In **European Journal of Organic**

**Chemistry**, Vol. 2022, Issue 29. John Wiley and Sons Inc. https://doi.org/10.1002/ejoc.202200196

SUGIMURA, H. et al. Synthesis of 1,2,3-Triazines Using the Base-Mediated Cyclization of (Z)-2,4-Diazido-2-alkenoates [Rapid-communication]. **Organic Letters**, *20*(11), 3434–3437, 2018. https://doi.org/10.1021/acs.orglett.8b01445

TAING, H. et al. 1,3,5-Triazine(trithiophenylcarboxylate) esters form metastable monotropic nematic discotic liquid crystal phases. **Liquid Crystals**, *45*(8), 1147–1154, 2018. https://doi.org/10.1080/02678292.2017.1417506

TAN, X. F. et al. Comparative study of multi-functional luminogens with 1,3,5-triazine as the core and phenothiazine or phenoxy donors as the peripheral moieties for non-doped/doped fluorescent and red phosphorescent OLEDs. **Dyes and Pigments**. 173(September 2019):107793, 2020.
 doi.org/10.1016/j.dyepig.2019.107793.

TANAKA, H, SHIZU, K, MIYAZAKI, H & ADACHI, C. Efficient green thermally activated delayed fluorescence (TADF) from a phenoxazine–triphenyltriazine (PXZ–TRZ) derivative. **Chemical Communications**. 48(93):11392–11394, 2012. doi.org/10.1039/c2cc36237f.

TARBELL, D. S., SMITH, R. F., BOEKELHEIDE. **Synthetic Studies on the Colchicine Problem. The Preparation and Properties of Some Styryltropolonesl.** V., 76, V., & Smith, R. F 2470-2473, 1954.

TENOPALA-CARMONA, F. et al. Identification of the Key Parameters for Horizontal Transition Dipole Orientation in Fluorescent and TADF Organic Light-Emitting Diodes. In **Advanced Materials**, Vol. 33, Issue 37, 2021. John Wiley and Sons Inc.
https://doi.org/10.1002/adma.202100677

TOBER, N, RIETH, T, LEHMANN, M & DETERT, H. Synthesis, Thermal, and Optical Properties of Tris(5-aryl-1,3,4-oxadiazol-2-yl)-1,3,5-triazines, New Star-Shaped Fluorescent Discotic Liquid Crystals. **Chemistry - A European Journal.** 25(67):15295–15304, 2019.
doi.org/10.1002/chem.201902975.

UMAR, A & SHAMSUDDIN, M. Preparation and aggregation-induced emission of new 1,3,5-triazine-2,4,6-tricarboxamide with liquid crystal properties. **Oriental Journal of Chemistry**. 34(4):1741–1748, 2018.
doi.org/10.13005/ojc/340405.

VALEUR, B., & BERBERAN-SANTOS, M. N. *Molecular Fluorescence: principles and applications* (Second Edition, Vol. 1). Wiley-VCH Verlag GmbH & Co. KGaA, 2013.

VERBIEST, T. et al. **Electric-Field-Modulated Circular-Difference Effects in Second-Harmonic Generation from a Chiral Liquid Crystal\*\*.** http://www.angewandte.orgorfromtheauthor.

VIEIRA, A. A. et al. Nematic Triphenyltriazine Triesters and the Induction of the Columnar Mesophase by Fluorine Substitution. **Chemistry - A European Journal**, *27*(35), 9003–9010, 2021. https://doi.org/10.1002/chem.202005456

VYKLICKÝ, L., EICHHORN, S. H., & KATZ, T. J. (2003). Helical discotic liquid crystals. **Chemistry of Materials**, *15*(19), 3594–3601, 2003. https://doi.org/10.1021/cm034146j

WADA, Y. et al. Highly efficient electroluminescence from a solution-processable thermally activated delayed fluorescence emitter. **Applied Physics Letters**. 107(18), 2015. doi.org/10.1063/1.4935237.

WANG, S. et al. Towards high-power-efficiency solution-processed OLEDs: Material and device perspectives. **Materials Science and Engineering R: Reports**, *140*(February), 100547, 2020. https://doi.org/10.1016/j.mser.2020.100547

WANG, X. F. et al. Superconductivity at 5 K in alkali-metal-doped phenanthrene. **Nature Communications**, *2*(1), 2011. https://doi.org/10.1038/ncomms1513

WEBER, J., & CLENNAN, E. L. Origin of the Preferential Formation of Helicenes in Mallory Photocyclizations. Temperature as a Tool to Influence Reaction Regiochemistry. **Journal of Organic Chemistry**, *84*(2), 817–830, 2019. https://doi.org/10.1021/acs.joc.8b02671

WÖHRLE, T.et al. Discotic Liquid Crystals. **Chemical Reviews**, *116*(3), 1139–1241, 2016. https://doi.org/10.1021/acs.chemrev.5b00190

WONG, M. Y., & Zysman-Colman, E. (2017a). Purely Organic Thermally Activated Delayed Fluorescence Materials for Organic Light-Emitting Diodes. In **Advanced Materials,** Vol. 29, Issue 22, 2017. Wiley-VCH Verlag. https://doi.org/10.1002/adma.201605444

WUNDERLICH, B. Glass transition as a key to identifying solid phases. **Journal of Applied Polymer Science**, *105*(1), 49–59, 2007. https://doi.org/10.1002/app.26110

YANG, H.-N., & LU, Z.-H. **Glass Transition in Organic Semiconductor Thin Films**, 2021.

YANG, Q., OUYANG, K., & XI, Z. Synthesis of chrysenosiloles via Mallory photocyclization. **Tetrahedron**, *74*(48), 6878–6882, 2018. https://doi.org/10.1016/j.tet.2018.10.035

YANG, Z. et al. Recent advances in organic thermally activated delayed fluorescence materials. In **Chemical Society Reviews**, Vol. 46, Issue 3, pp. 915–1016, 2017. Royal Society of Chemistry. https://doi.org/10.1039/c6cs00368k

YASUDA, T., SHIMIZU, T., LIU, F., UNGAR, G., & KATO, T. Electro-functional octupolar π-conjugated columnar liquid crystals. **Journal of the American Chemical Society**, *133*(34), 13437–13444, 2011. https://doi.org/10.1021/ja2035255

YILDIRIM, A. et al. Multiple glassy dynamics in dipole functionalized triphenylene-based discotic liquid crystals revealed by broadband dielectric spectroscopy and advanced calorimetry-assessment of the molecular origin. **Physical Chemistry Chemical Physics**, *21*(33), 18265–18277, 2019. https://doi.org/10.1039/c9cp03499d

YOKOYAMA, D. Molecular orientation in small-molecule organic light-emitting diodes. **Journal of Materials Chemistry**, *21*(48), 19187–19202, 2011. https://doi.org/10.1039/c1jm13417e

YUVARAJ, A. R., RENJITH, A., & KUMAR, S. Novel electron-deficient phenanthridine based discotic liquid crystals. **Journal of Molecular Liquids**, *272*, 583–589, 2018. https://doi.org/10.1016/j.molliq.2018.09.120

ZHANG, L. et al. DBU-Catalyzed [3+3] and [3+2] Annulation Reactions of Azomethine Ylides with α-Diazocarbonyls as N-Terminal Electrophiles: Modular, Atom-Economical Access to 1,2,4-Triazine and 1,2,4-Triazole Derivatives. **Advanced Synthesis and Catalysis**, *360*(11), 2172–2177, 2018. https://doi.org/10.1002/adsc.201800030

ZASSOWSKI, P. et al. 1,3,5-Triazine and carbazole derivatives for OLED applications. **Dyes and Pigments**. 149(November 2017):804–811, 2018. doi.org/10.1016/j.dyepig.2017.11.040.

# 8. APPENDIX

$^1$H NMR of compound **F₃Et** in CD₂Cl₂, 400 MHz.
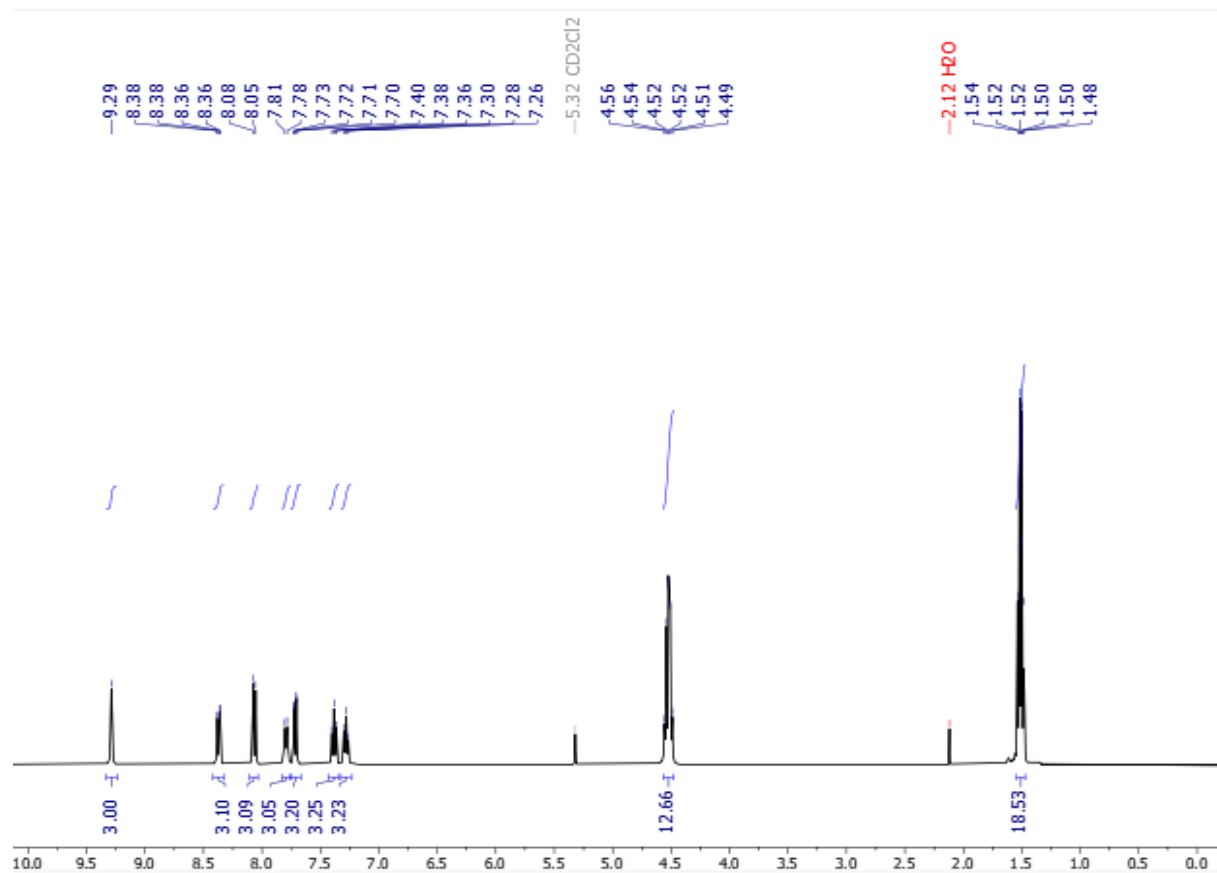


Expansion of the aromatic region of the $^1$H NMR of compound **F₃Et** in CD₂Cl₂, 400 MHz.
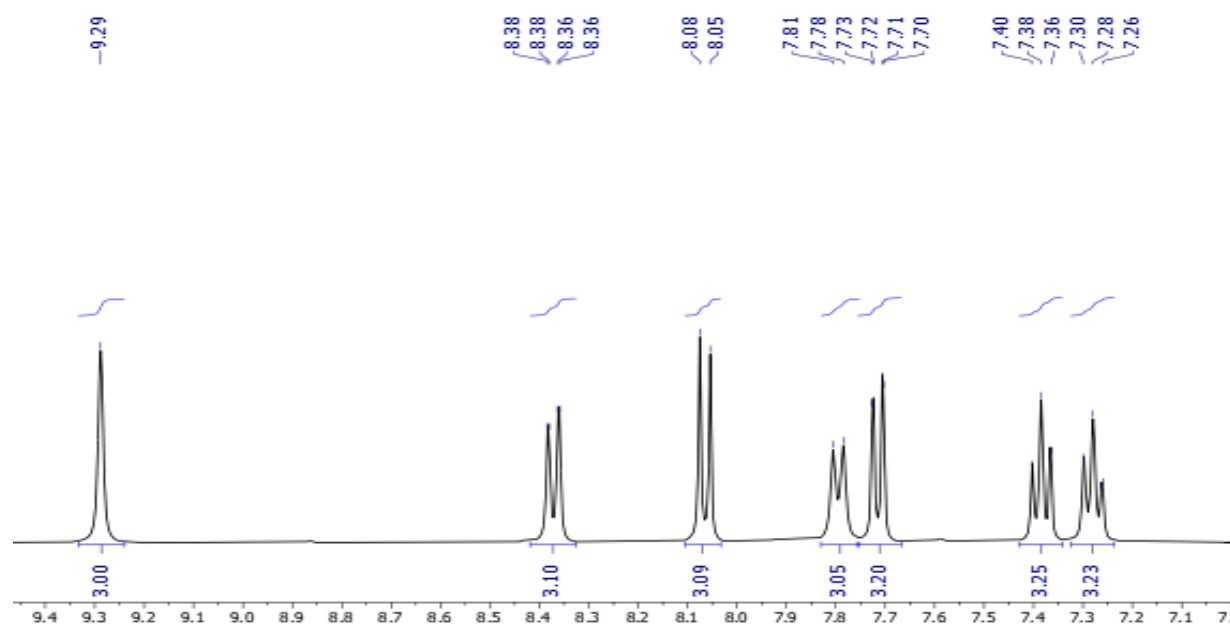
$^{13}$C NMR of compound **F$_3$Et** in CD$_2$Cl$_2$, 100 MHz.
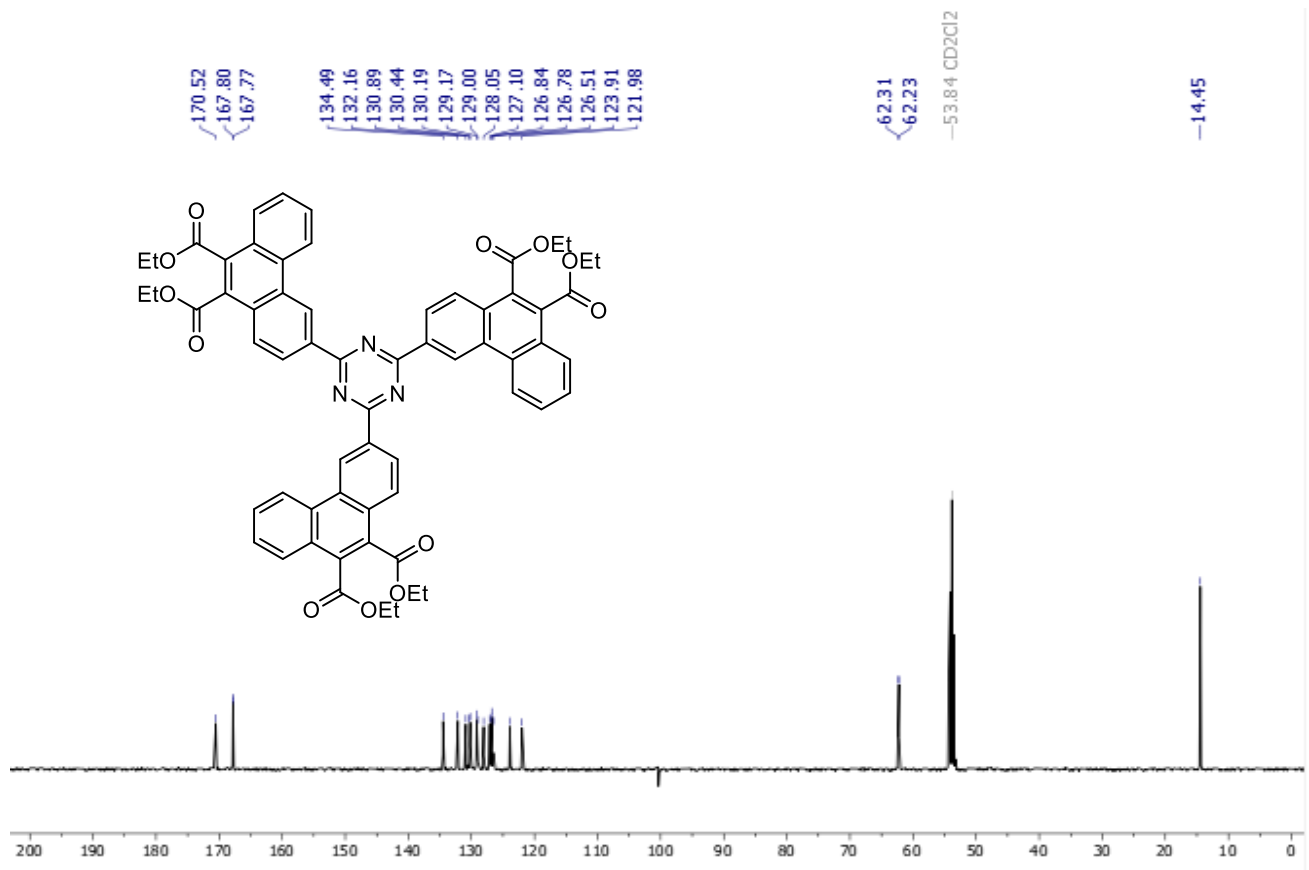


Expansion of the aromatic region of the $^{13}$C NMR of compound **F$_3$Et** in CD$_2$Cl$_2$, 100 MHz.
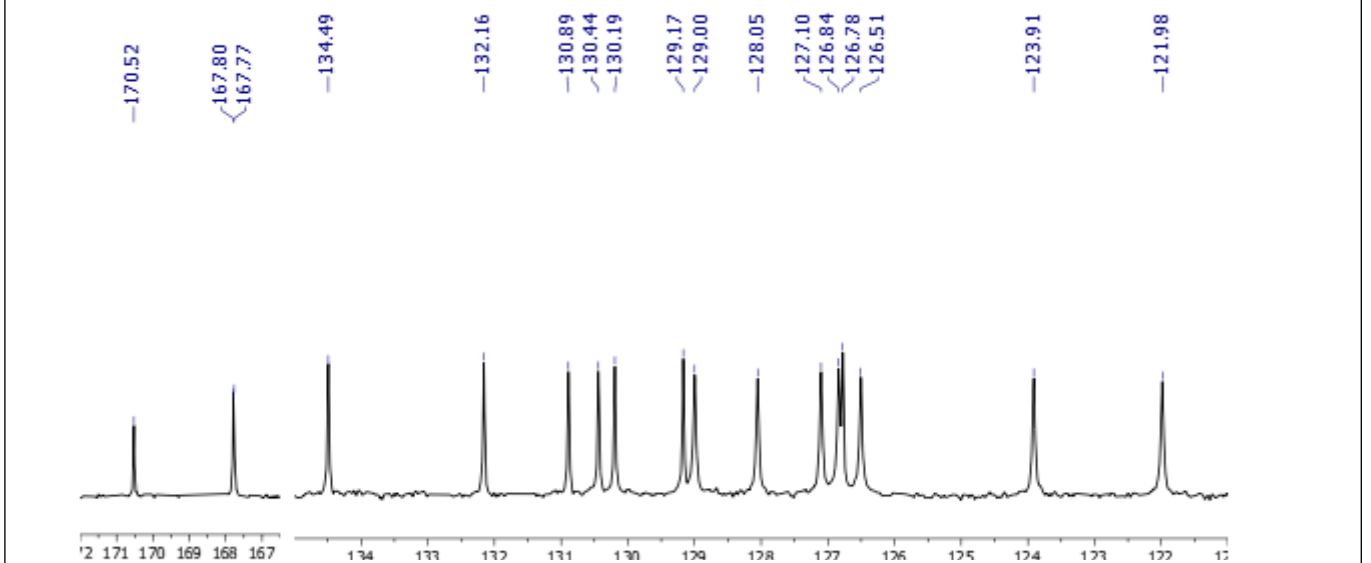
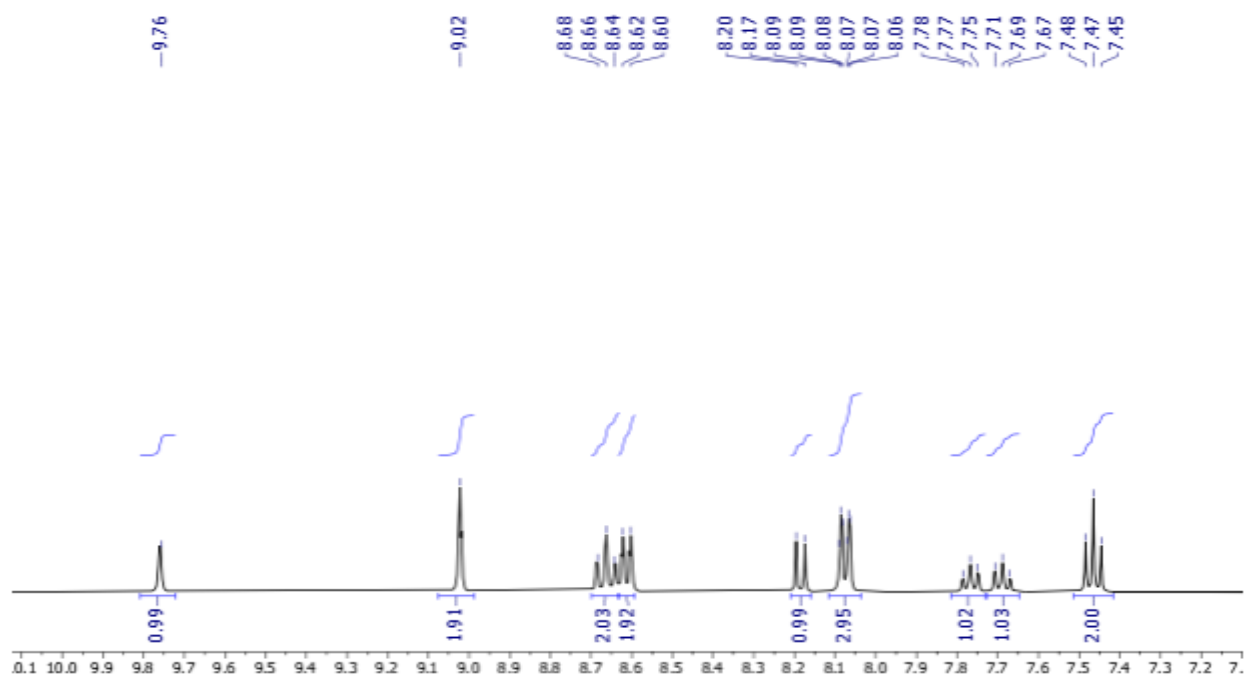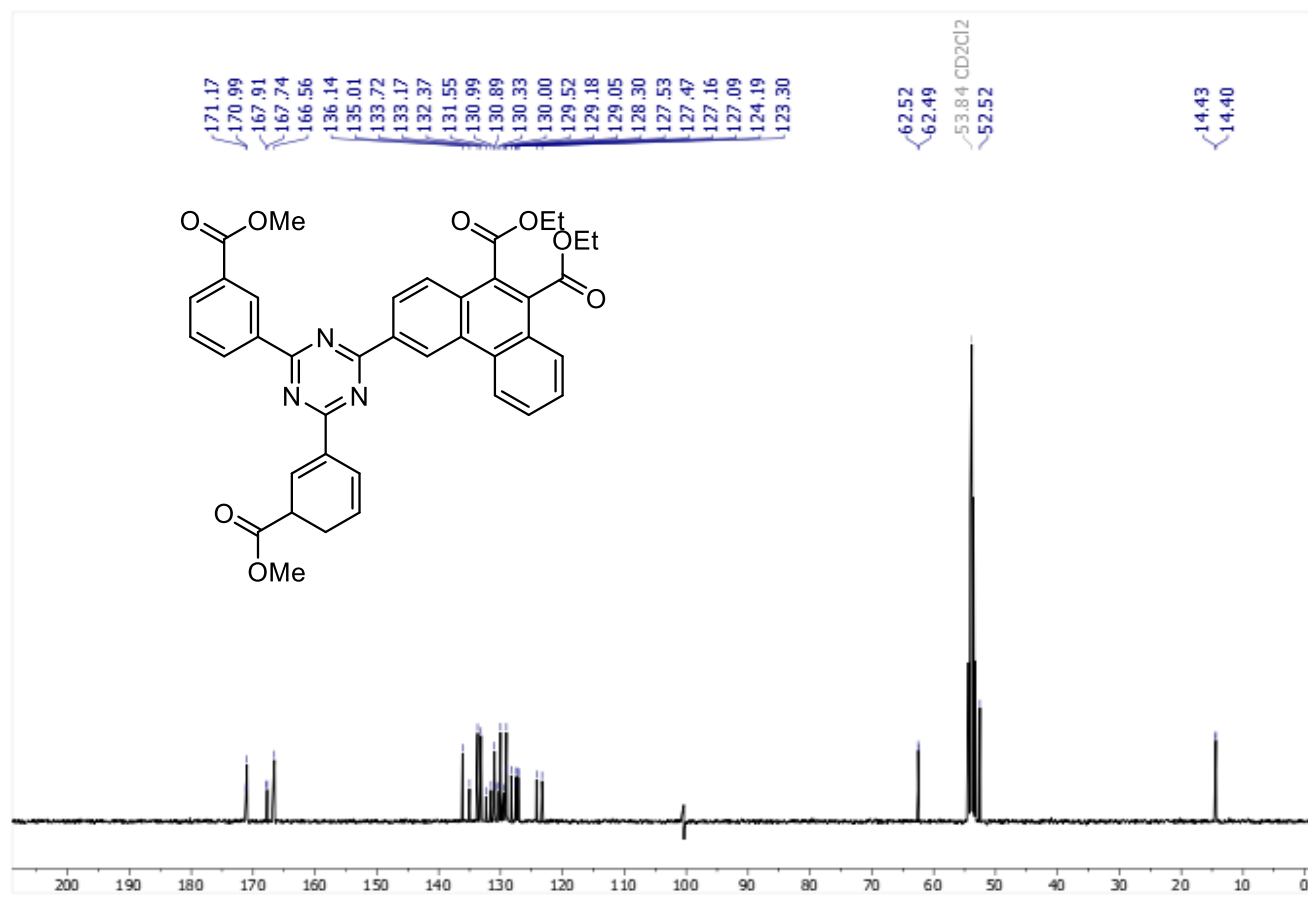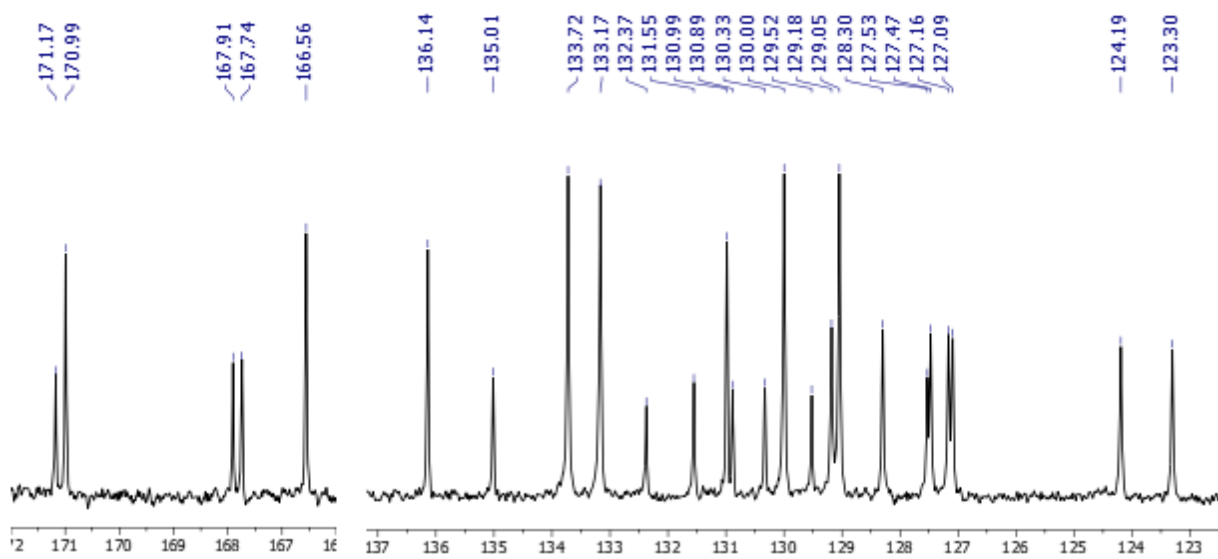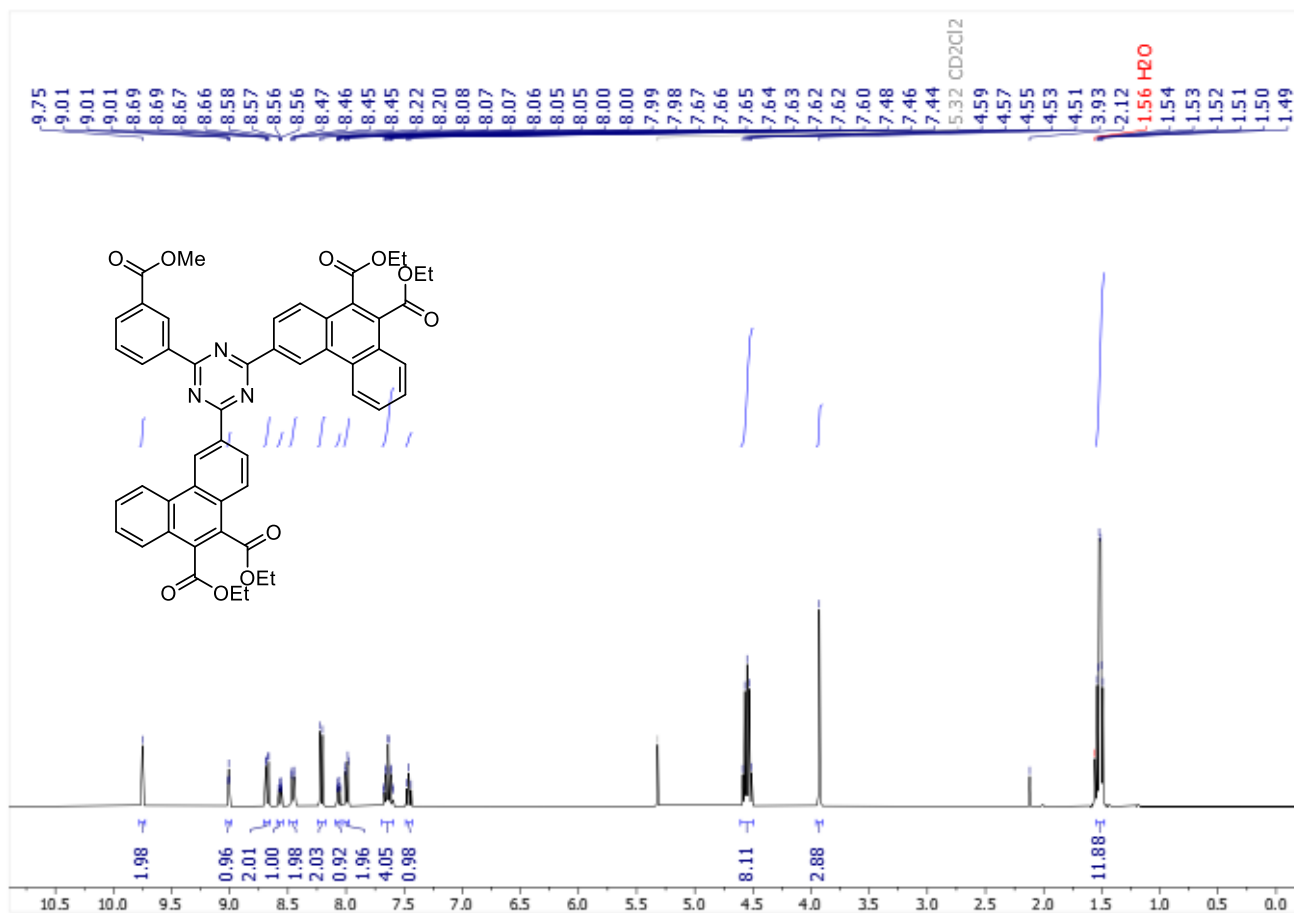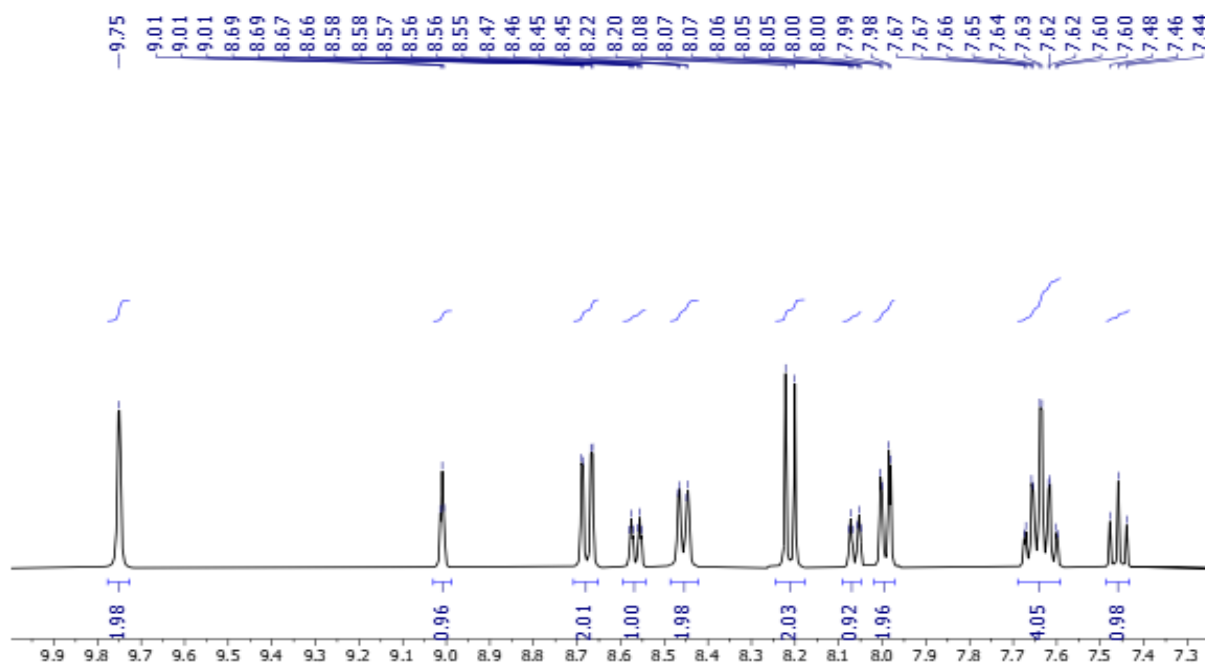<sup>1</sup>H NMR of compound **F₃Pr** in CD₂Cl₂, 400 MHz.
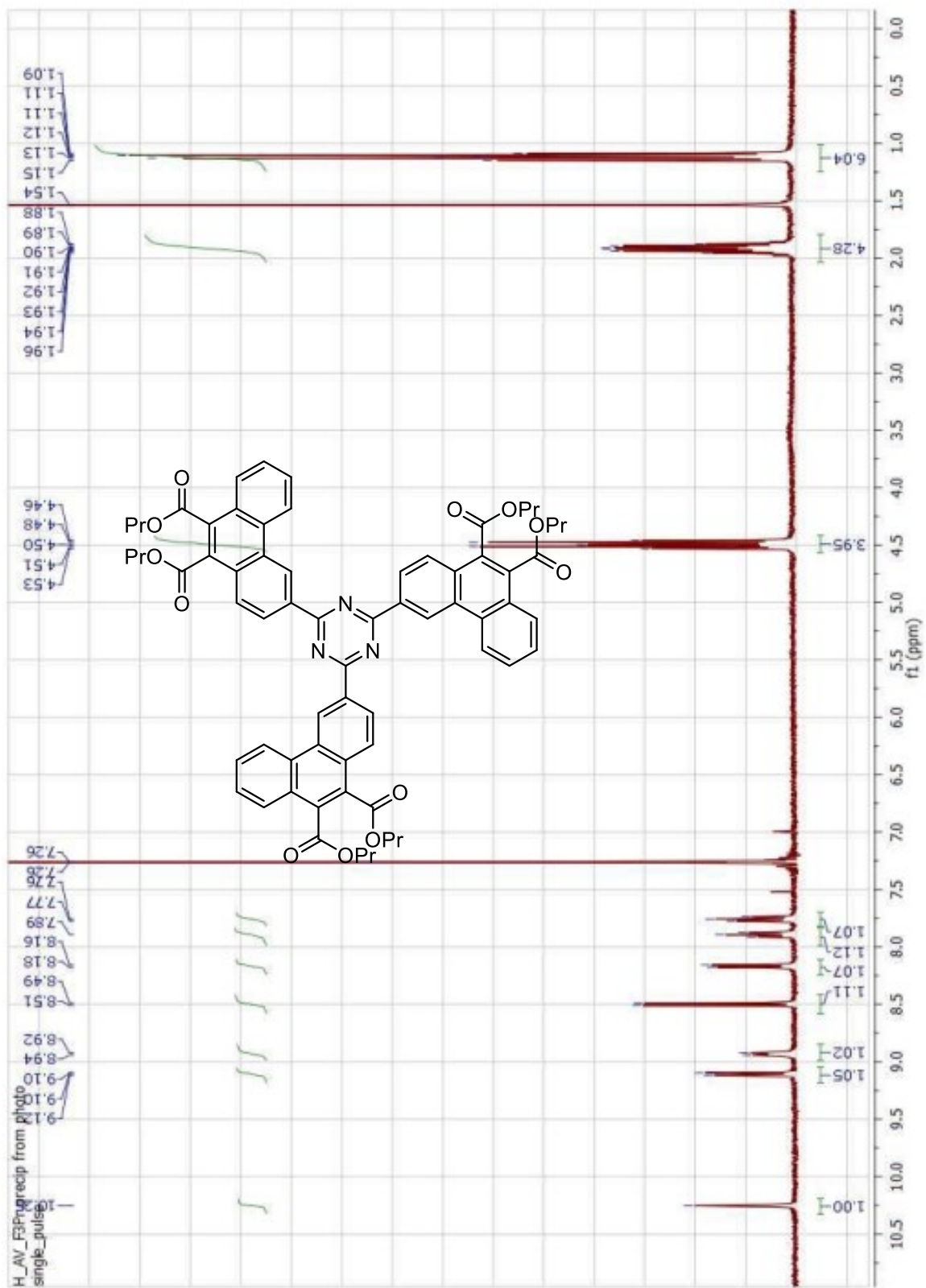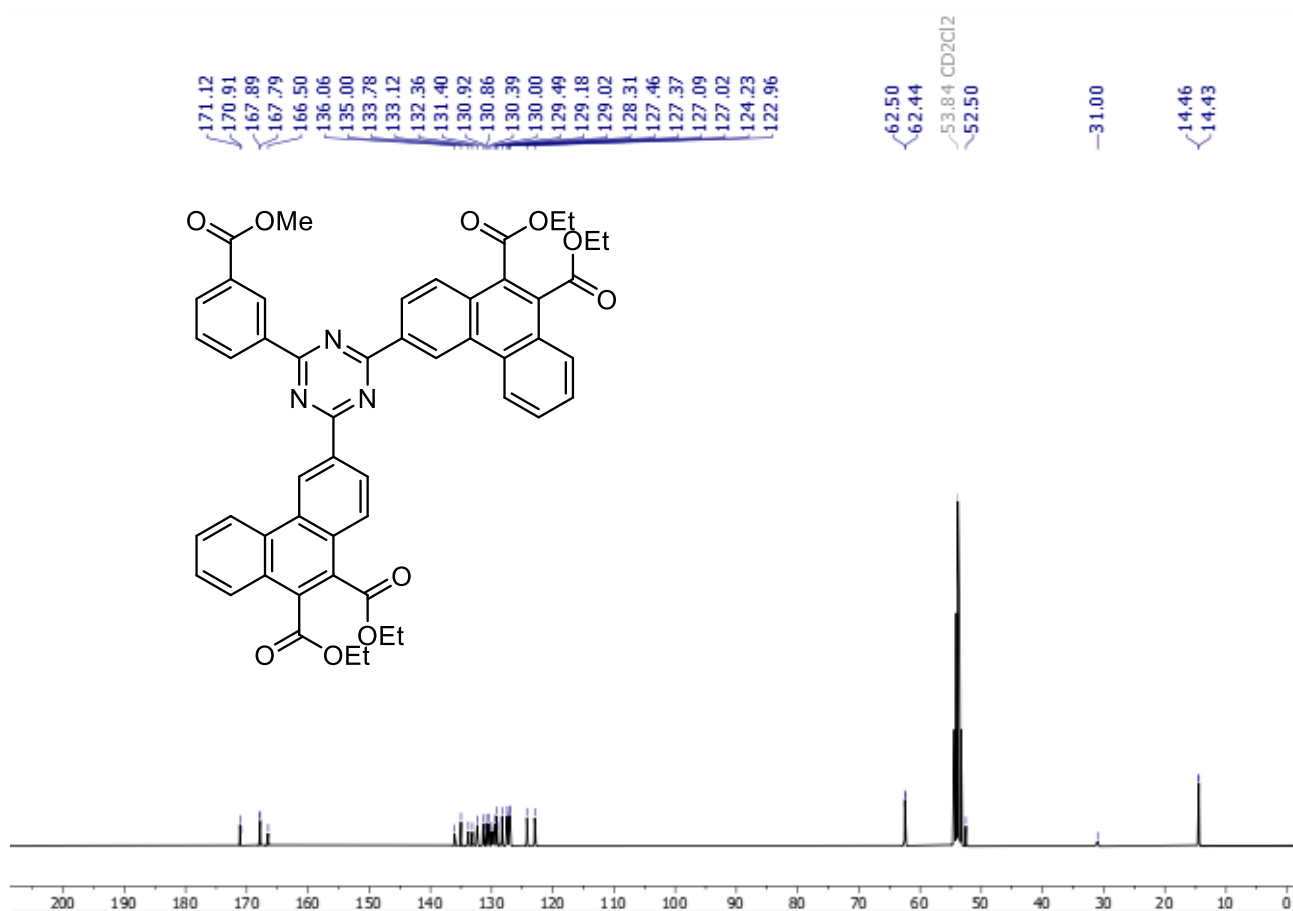
¹³C NMR of compound **F₃Pr** in CD₂Cl₂, 100 MHz.
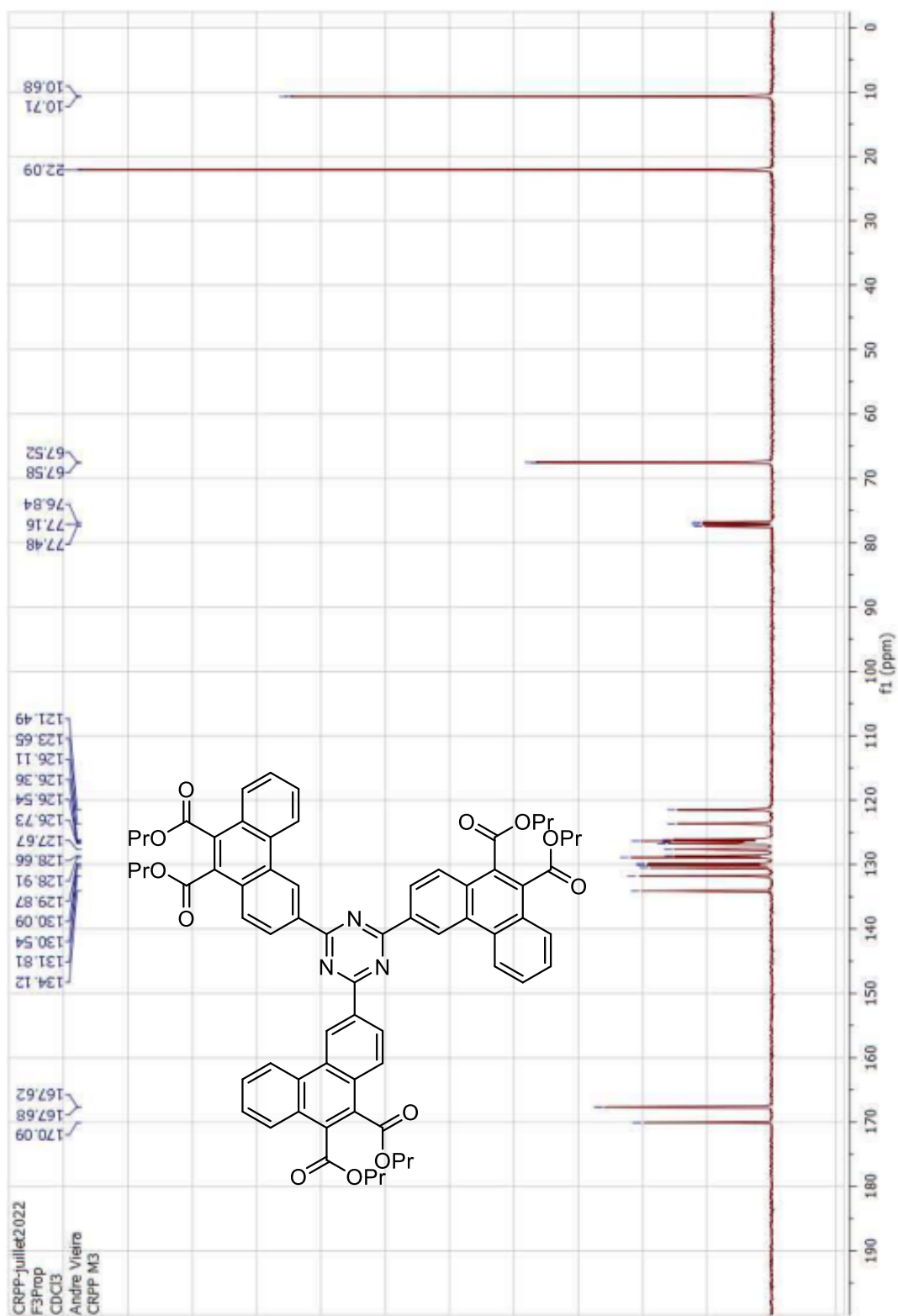
$^1$H NMR of compound **F₃Bu** in CD₂Cl₂, 400 MHz.
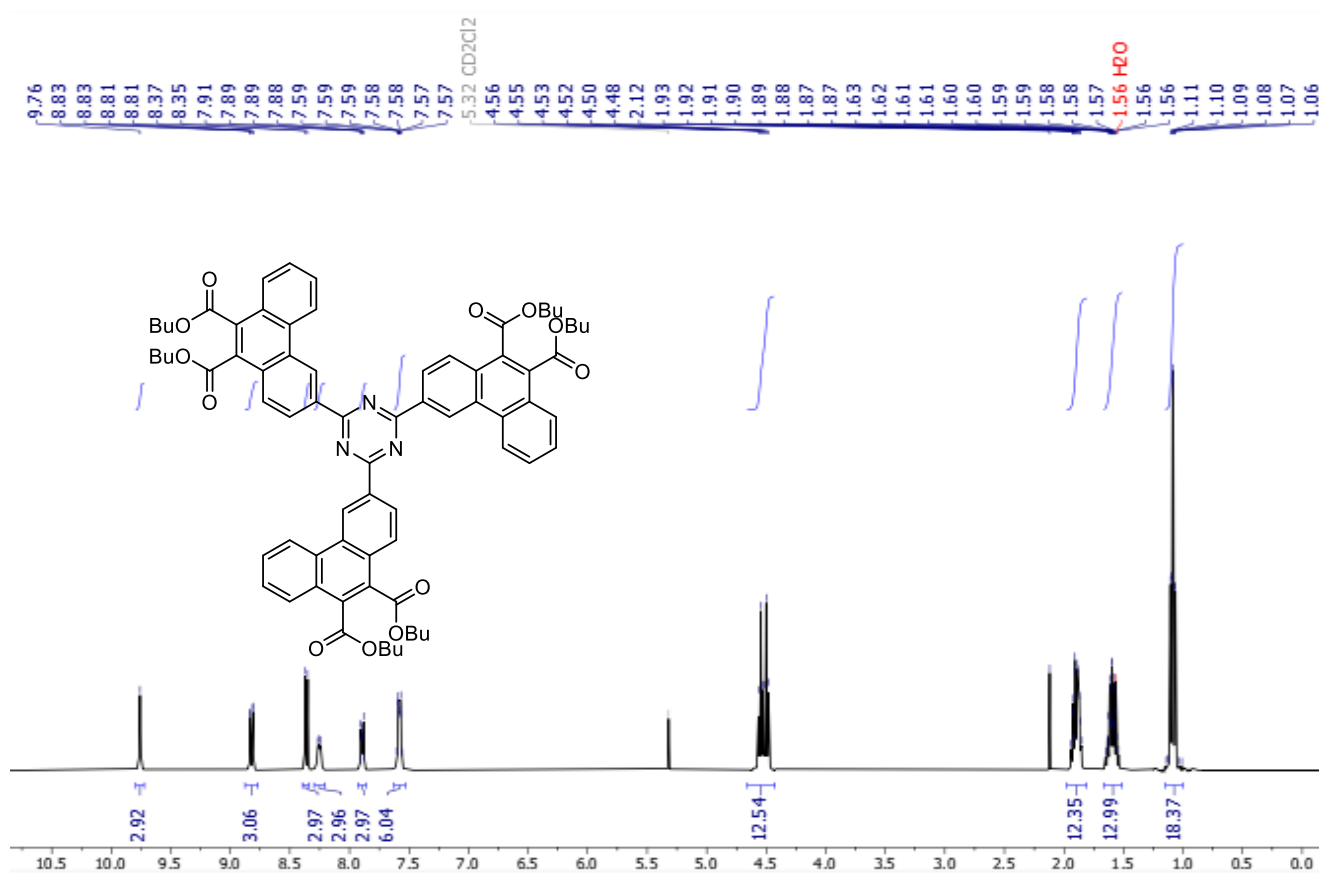


Expansion of the aromatic region of the $^1$H NMR of compound **F₃Bu** in CD₂Cl₂, 400 MHz.
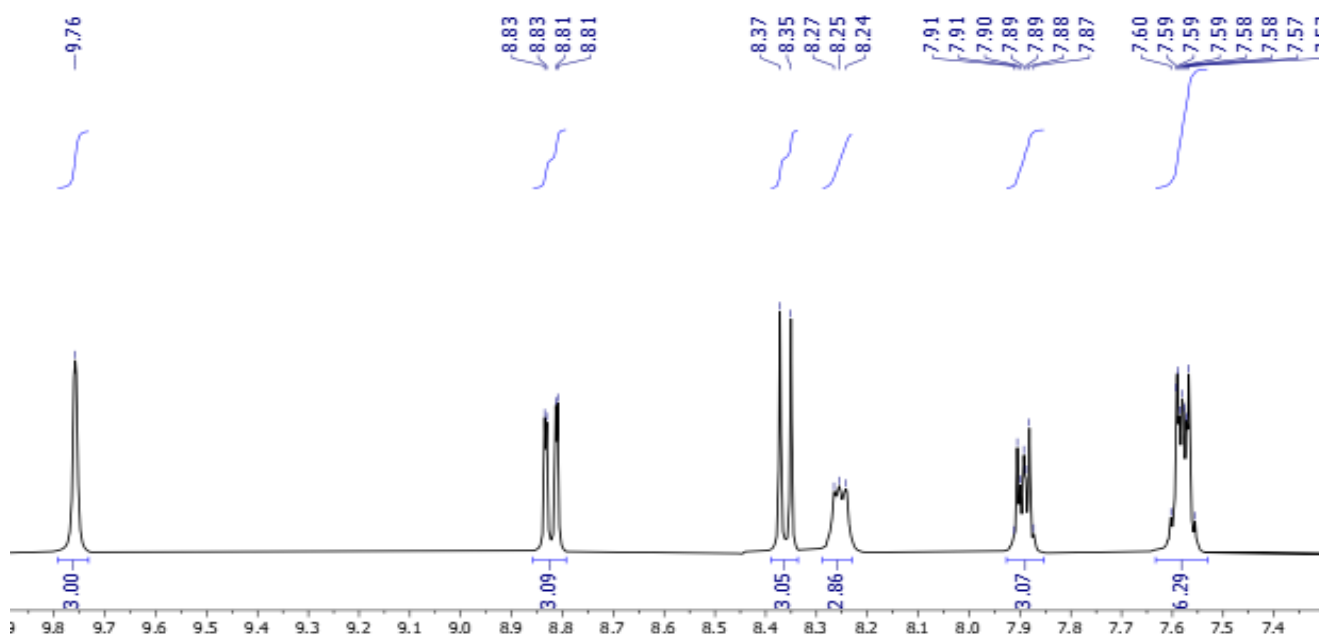
$^{13}$C NMR of compound **F₃Bu** in CD₂Cl₂, 100 MHz.
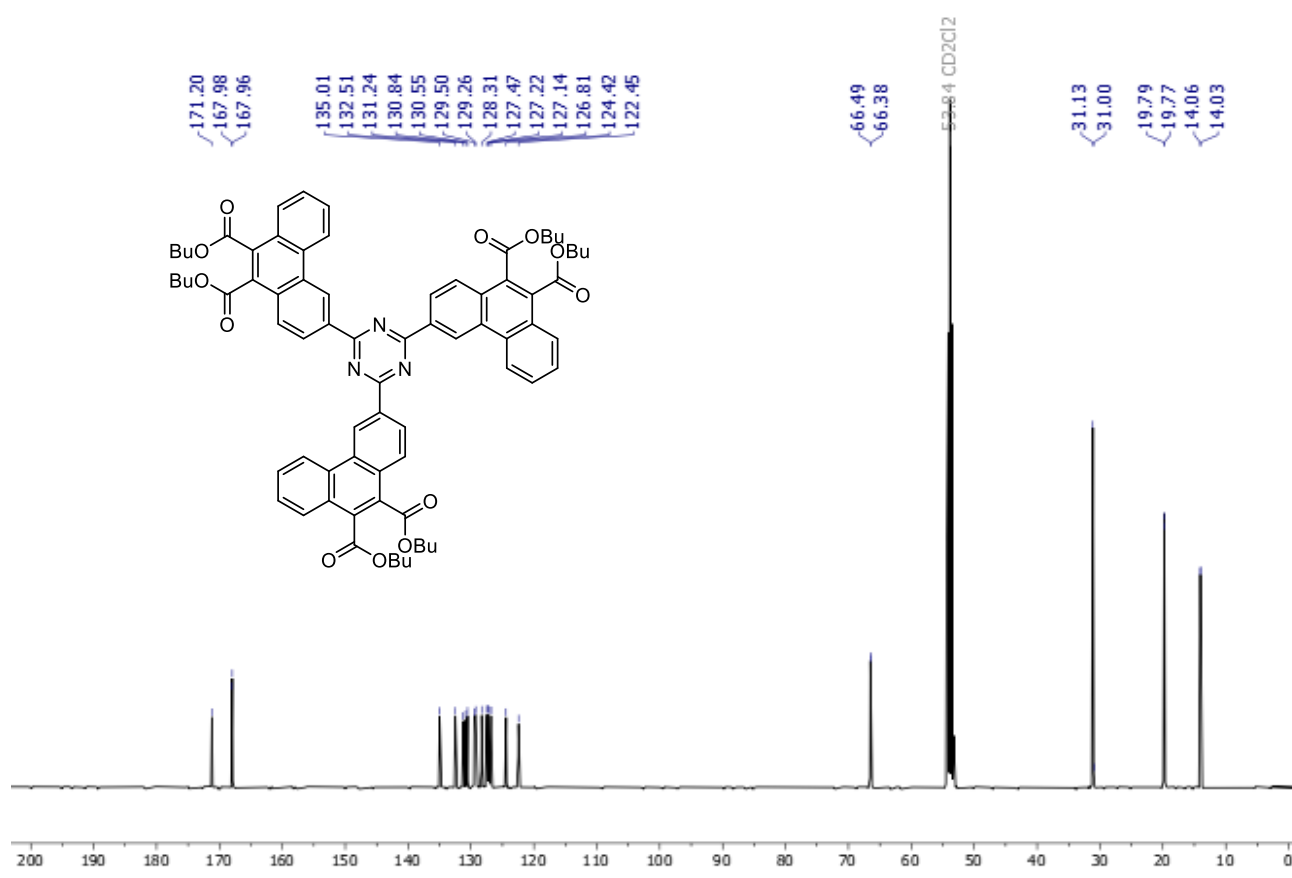


Expansion of the aromatic region of the $^{13}$C NMR of compound **F₃Bu** in CD₂Cl₂, 100 MHz.
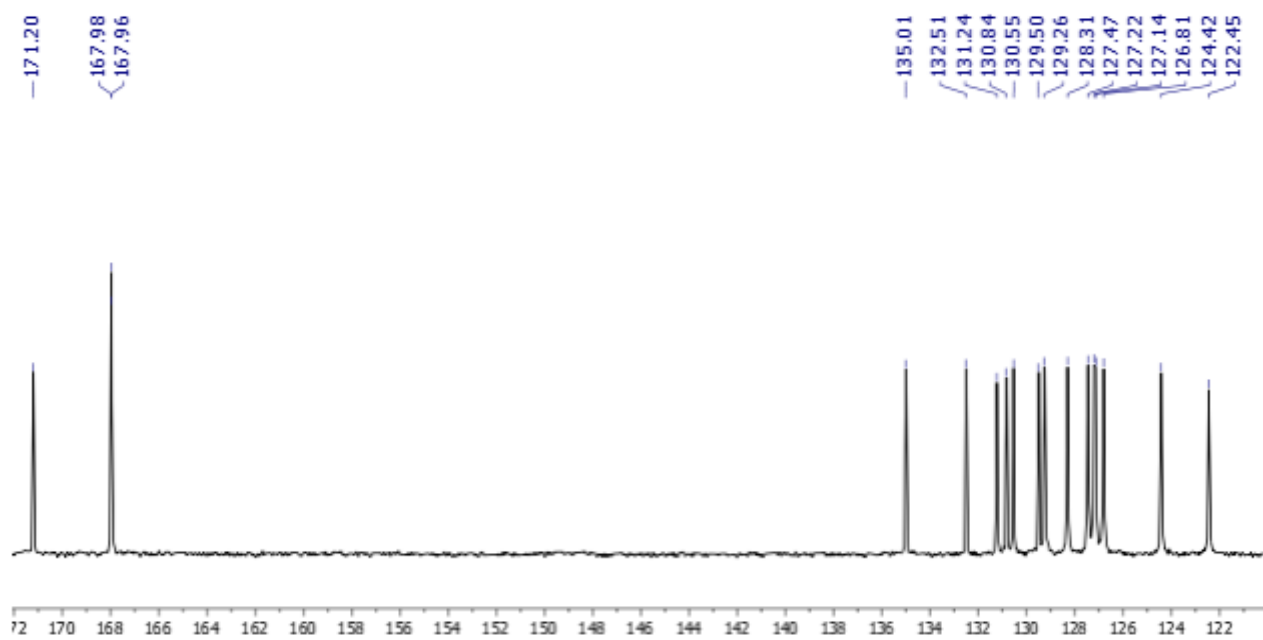
<sup>1</sup>H NMR of compound **H₃Et** in CDCl₃, 400 MHz.
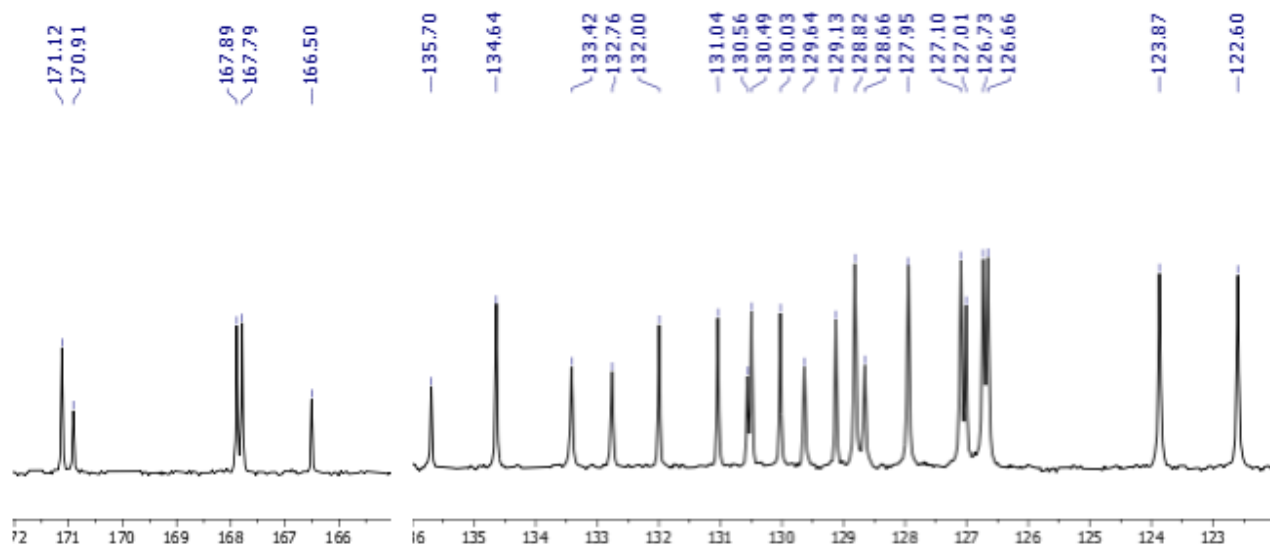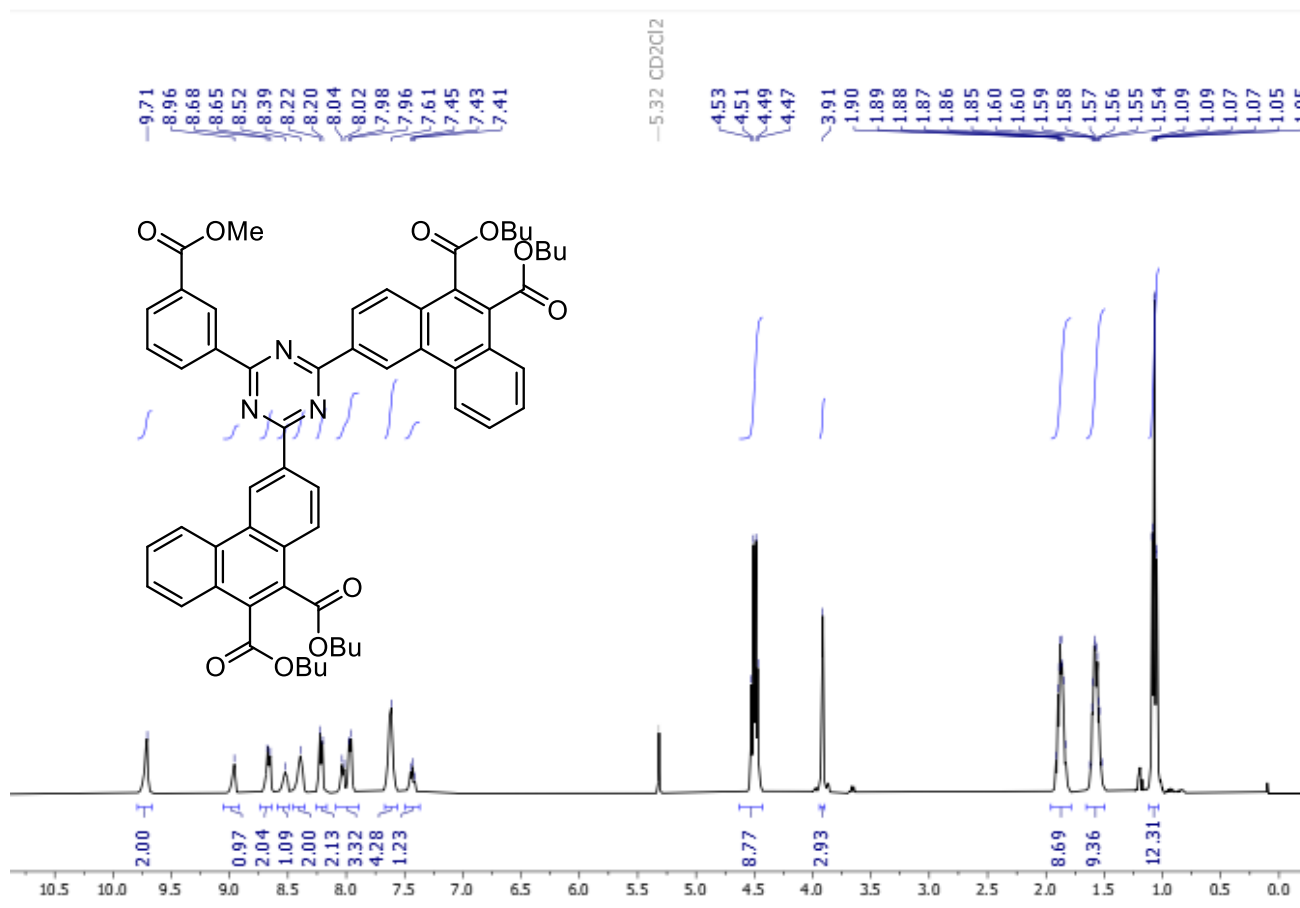
$^{13}$C NMR of compound **H₃Et** in CDCl₃, 100 MHz.

—14.38

—62.25

76.84
77.16
77.48

122.99
126.33
126.40
126.54
126.72
127.49
128.38
128.72
129.02
129.29
130.13
130.31
130.33
131.20
132.24
133.88
134.43

167.71
168.27
171.45

EtO

EtO

OEt

OEt

OEt

OEt

N

N

N

O

O

O

O

O

O

CRPP-juillet2022
H3Et
CDCl3
Andre Vieira
CRPP M3
13C

f1 (ppm)
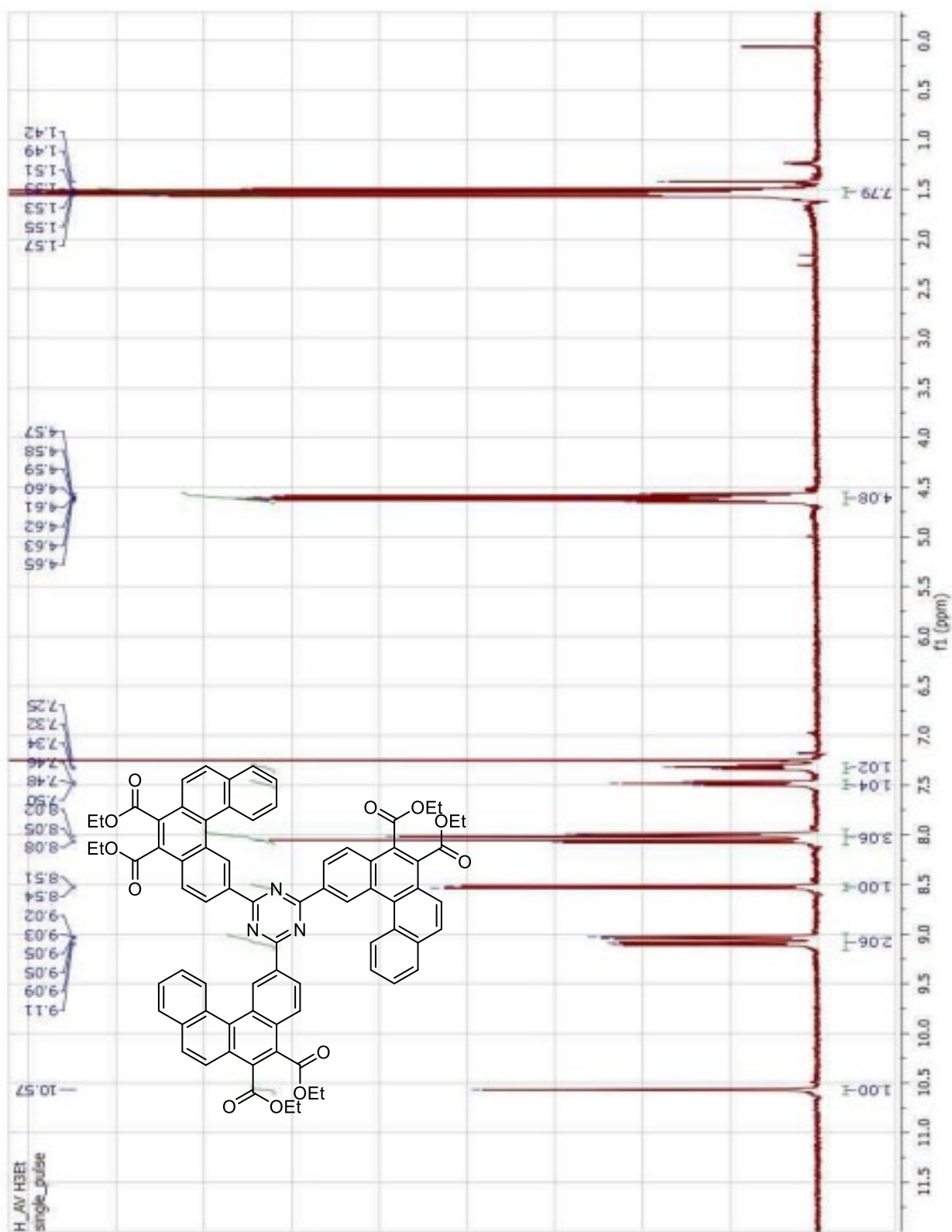
$^{13}$C NMR of compound **H₃Et** in CDCl₃, 100 MHz.
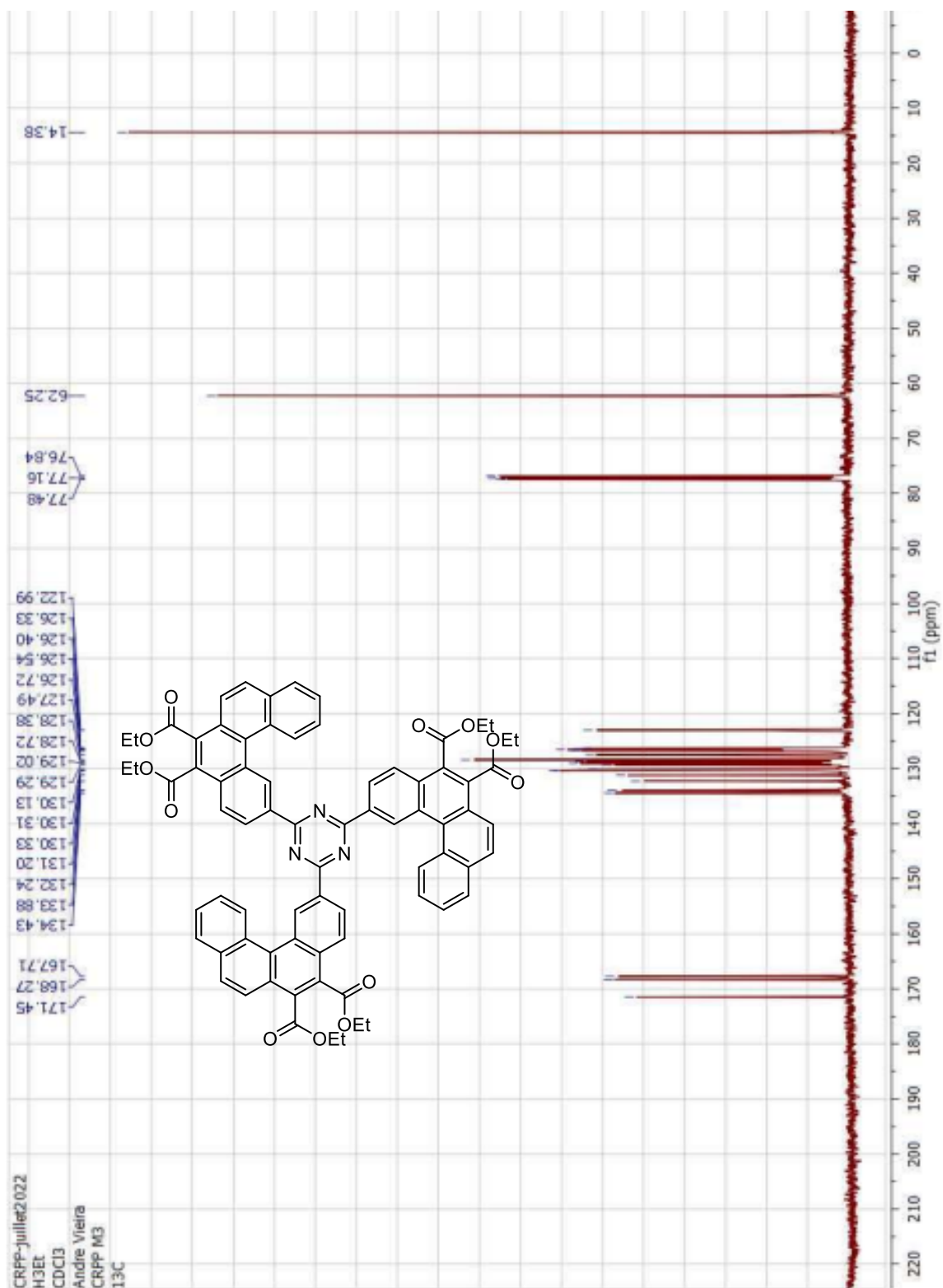
<sup>1</sup>H NMR of compound **H₃Pr** in CDCl₃, 400 MHz.
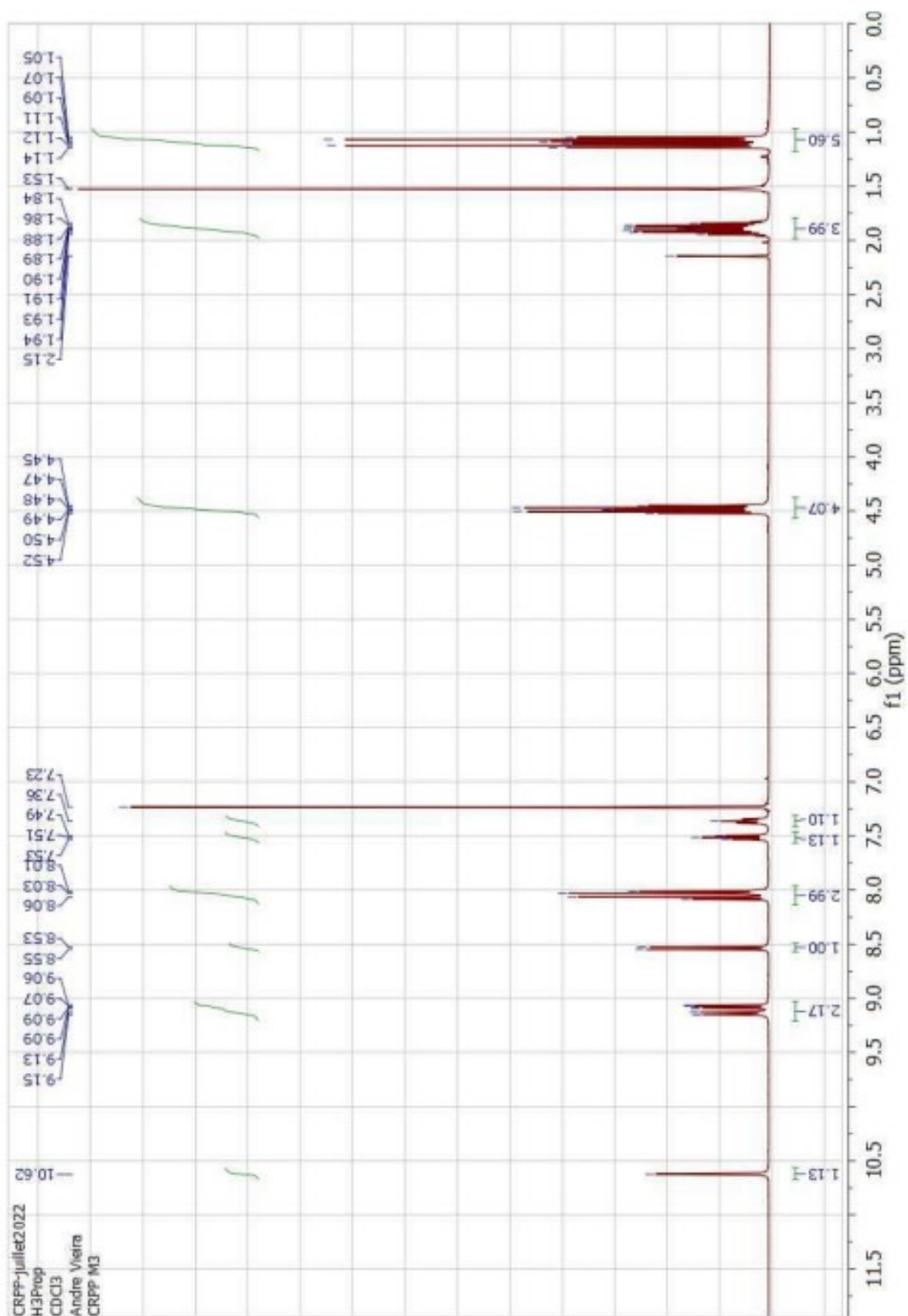
¹H NMR of compound **H₃Bu** in CD₂Cl₂, 400 MHz.
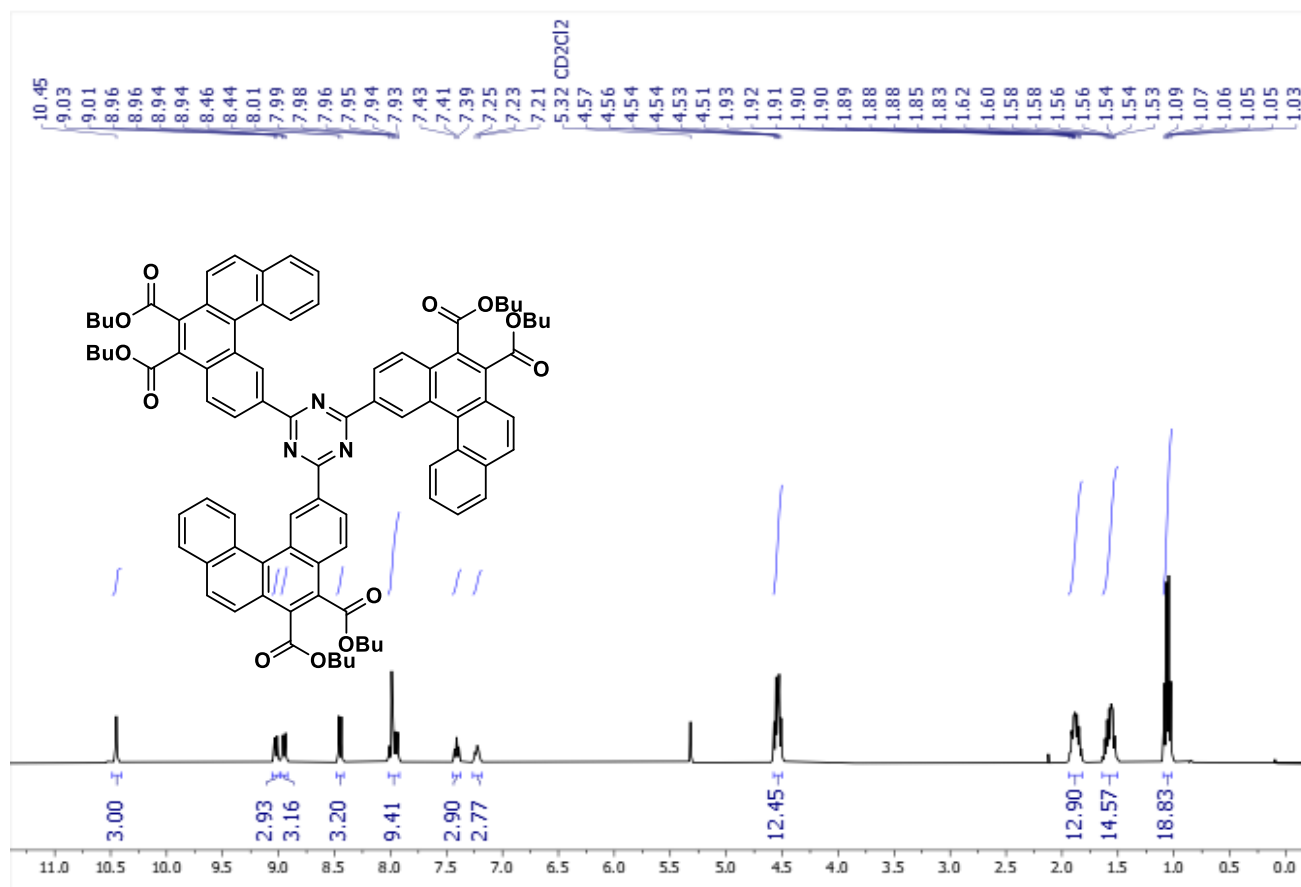


Expansion of the aromatic region of the ¹H NMR of compound **H₃Bu** in CD₂Cl₂, 400 MHz.
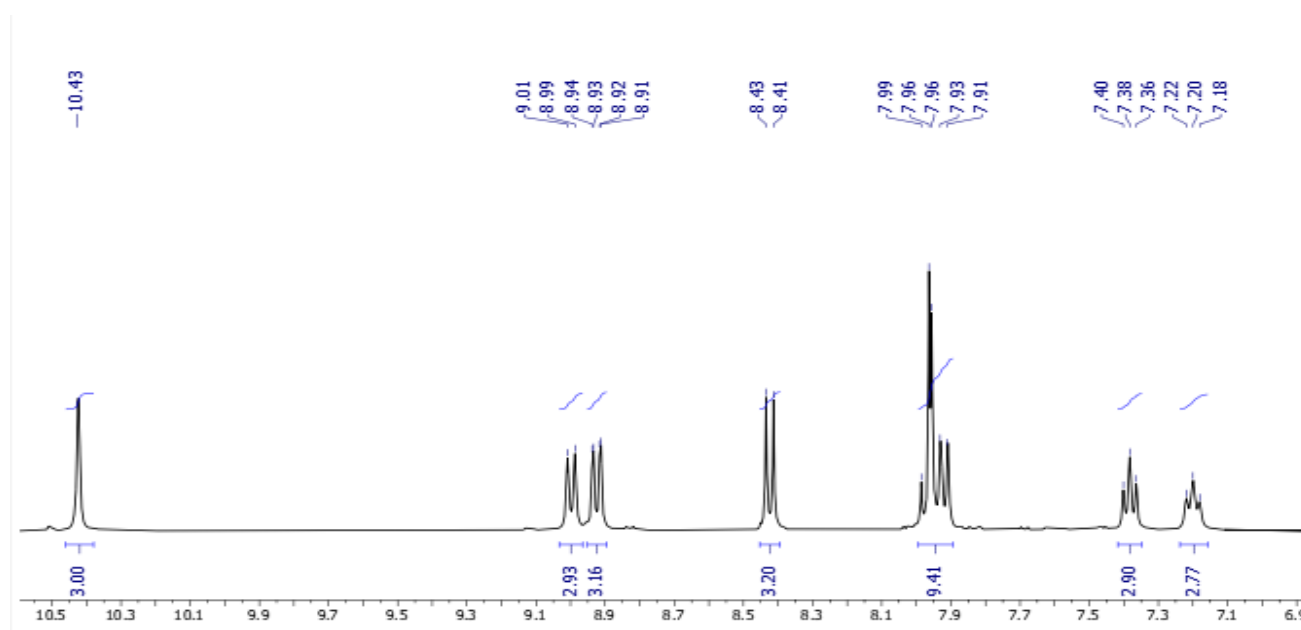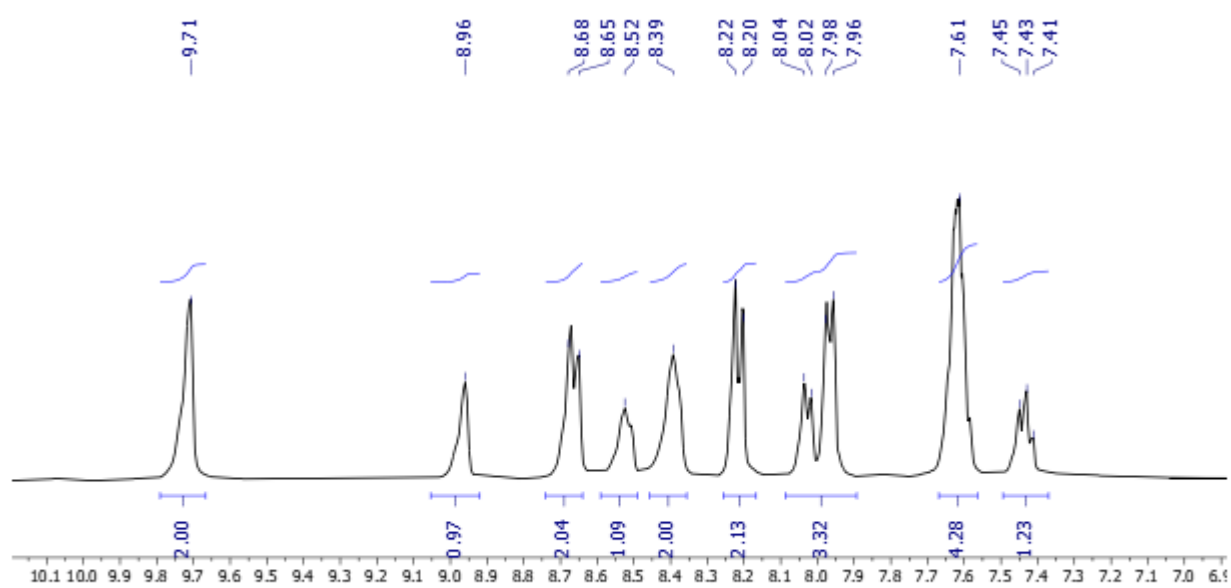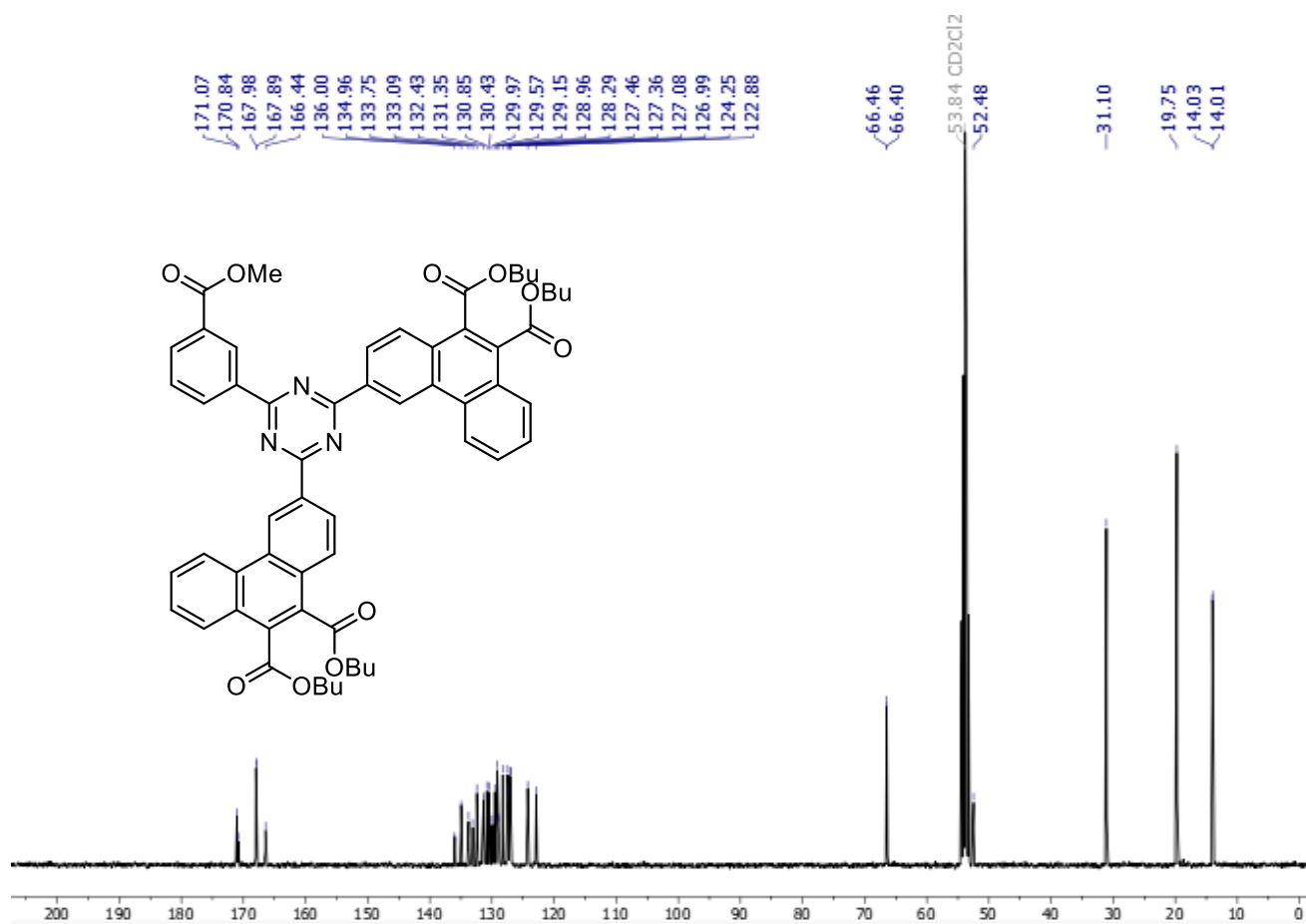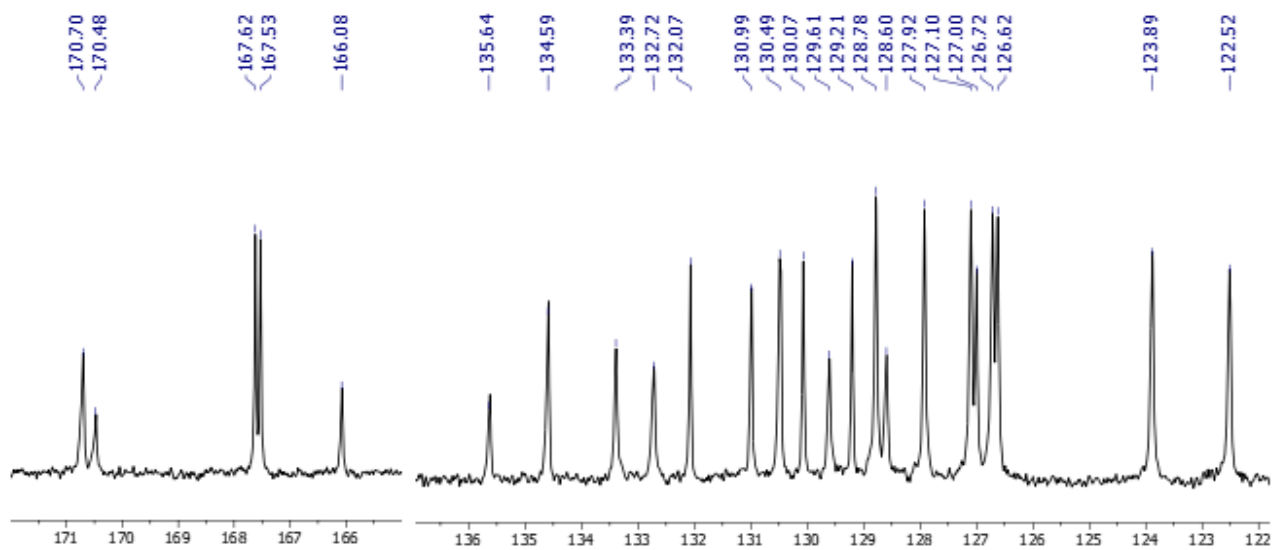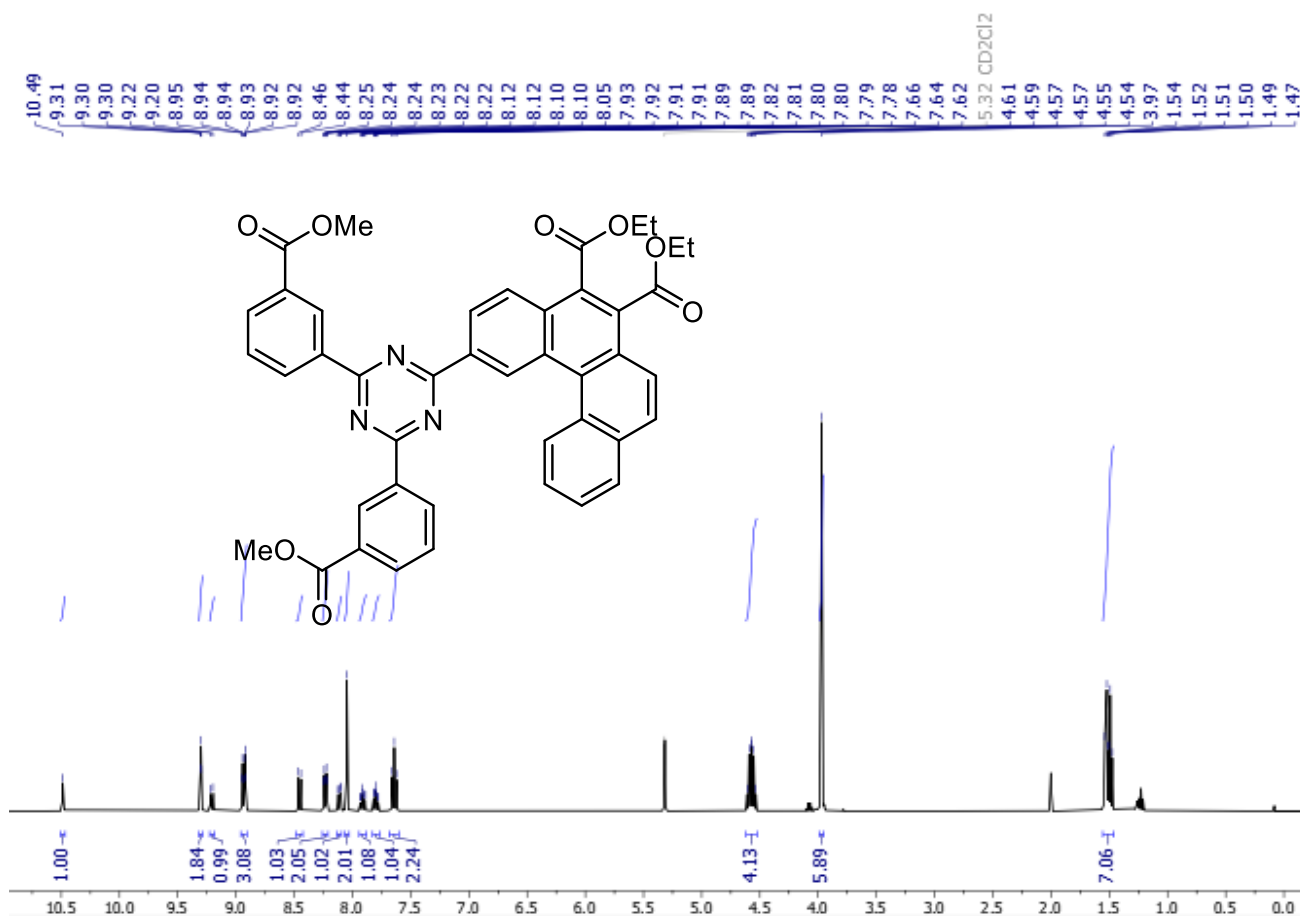
$^{13}$C NMR of compound **H₃Pr** in CDCl₃, 100 MHz.
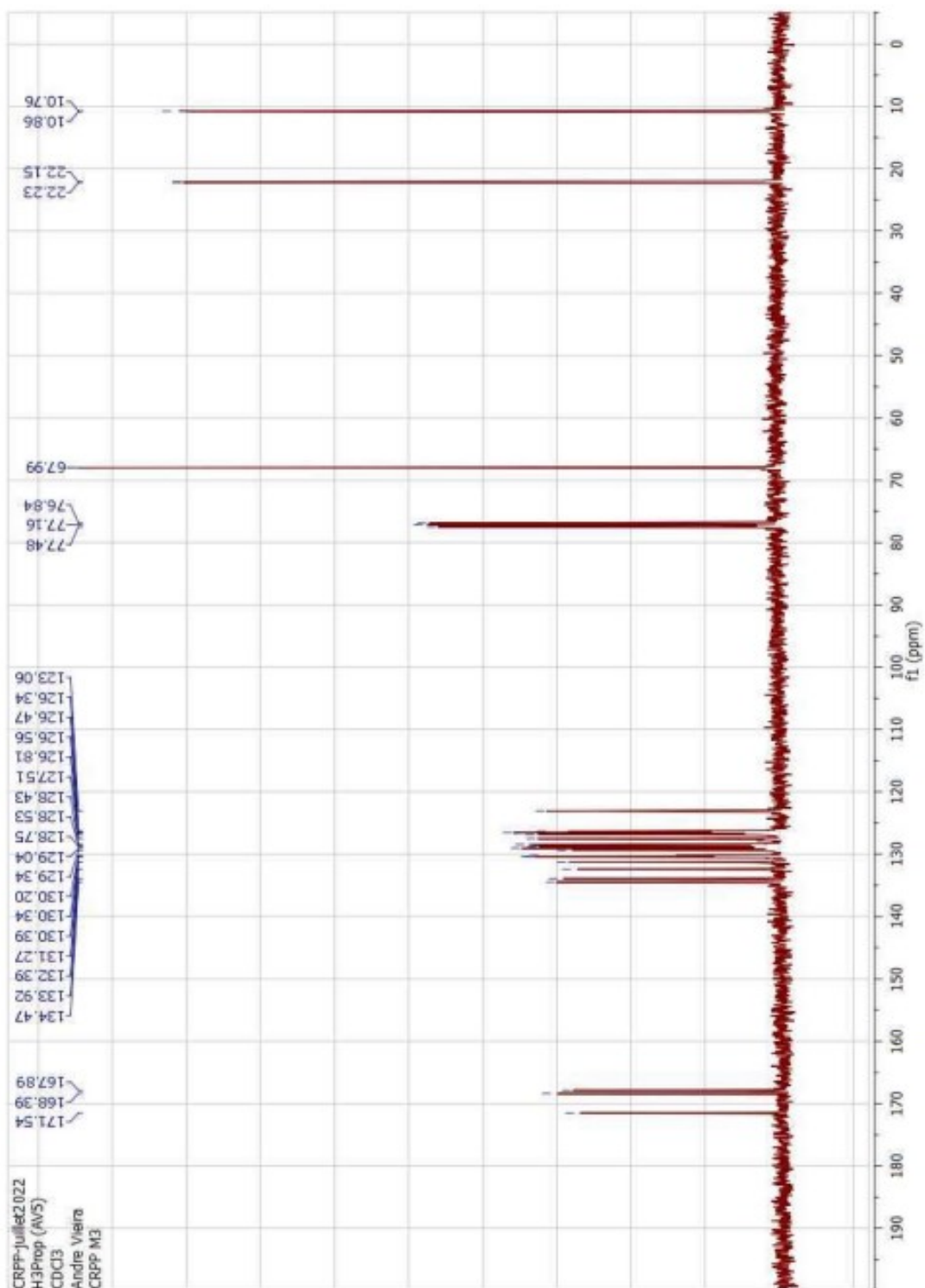
$^{13}$C NMR of compound **H₃Bu** in CD₂Cl₂, 100 MHz.
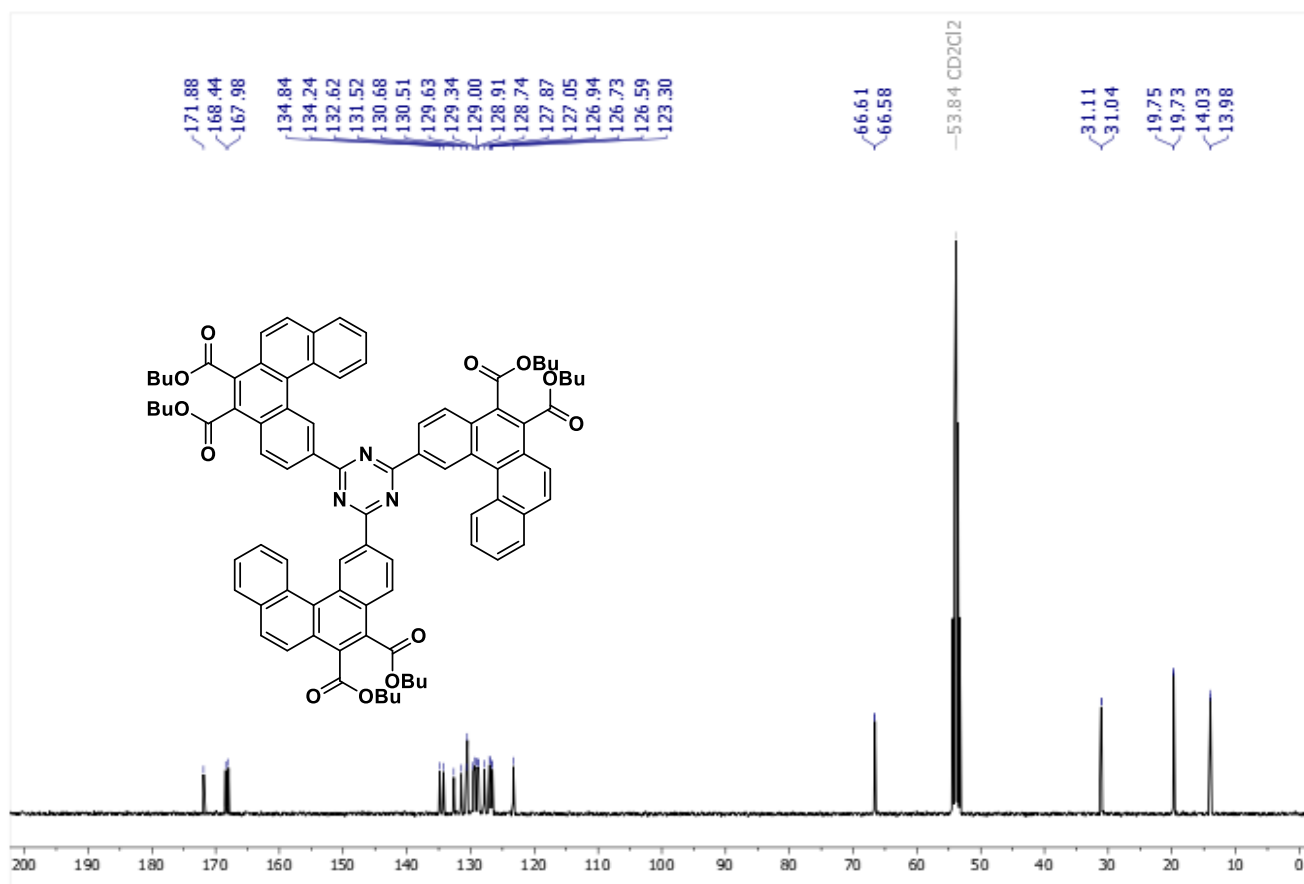


Expansion of the aromatic region of the $^{13}$C NMR of compound **H₃Bu** in CD₂Cl₂, 100 MHz.
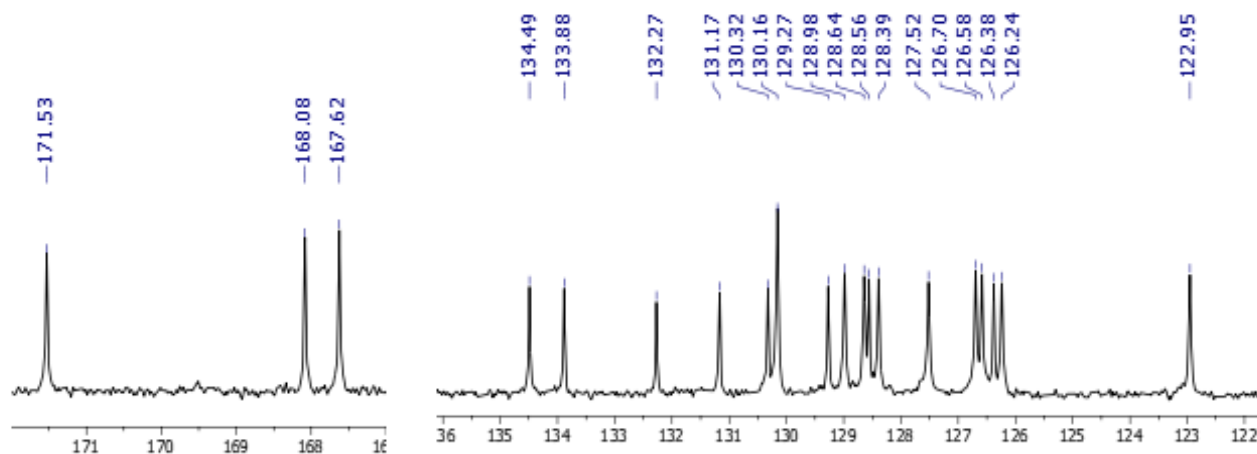
<sup>1</sup>H NMR of compound **H₃Hex** in CD₂Cl₂, 400 MHz.
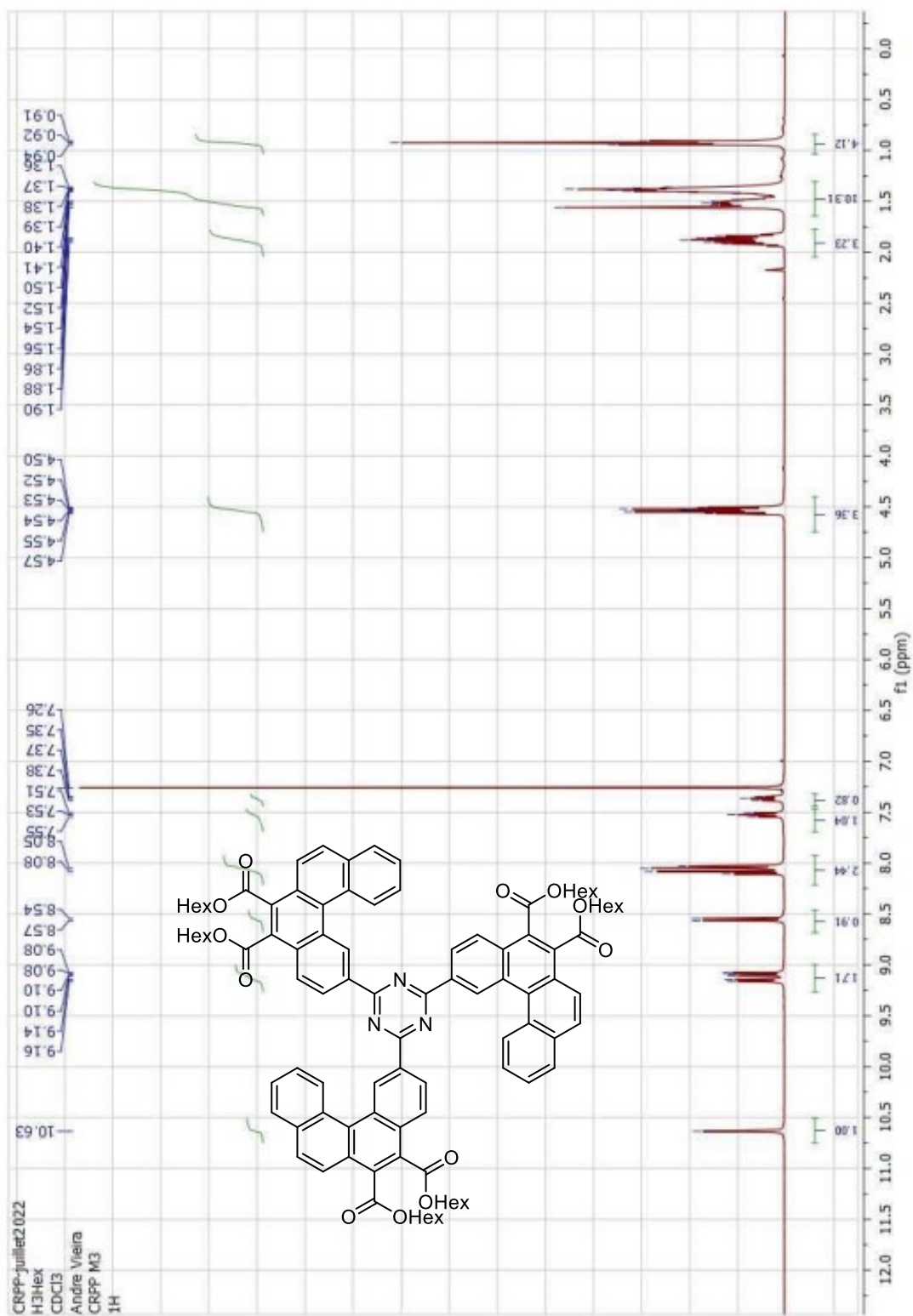
¹H NMR of compound **H₃Hex** in CD₂Cl₂, 100 MHz.

<sup>1</sup>H NMR of compound **F₁Et** in CD₂Cl₂, 400 MHz.



Expansion of the aromatic region of the <sup>1</sup>H NMR of compound **F₁Et** in CD₂Cl₂, 400 MHz.

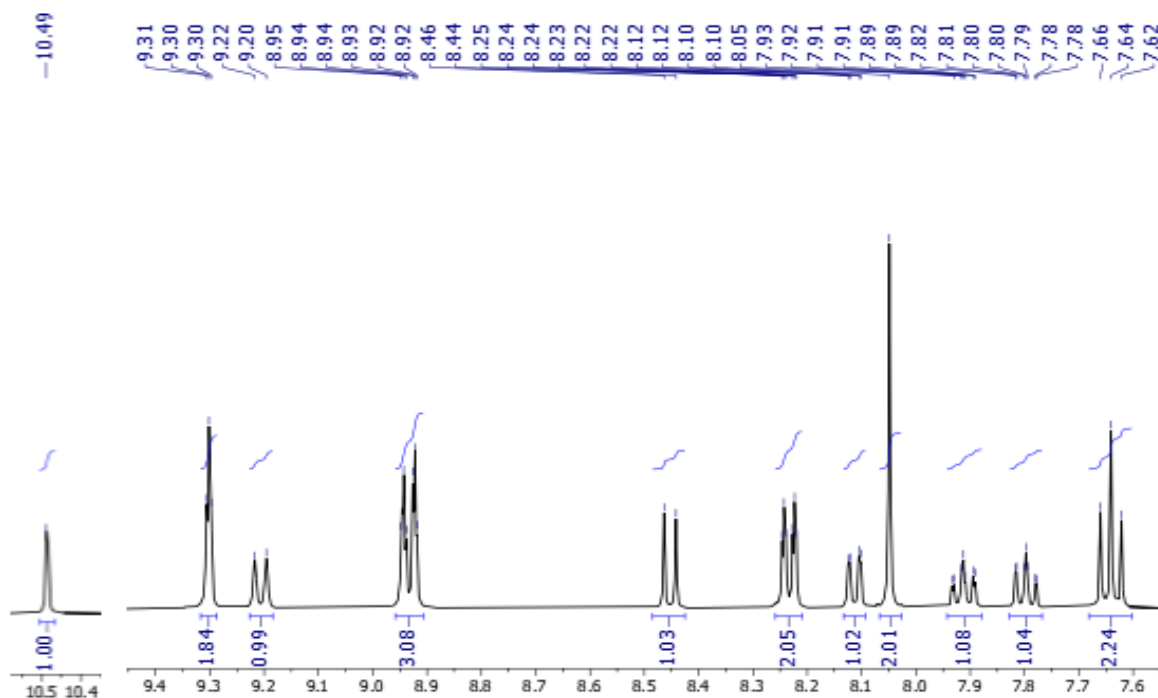$^{13}$C NMR of compound **F₁Et** in CD₂Cl₂, 100 MHz.



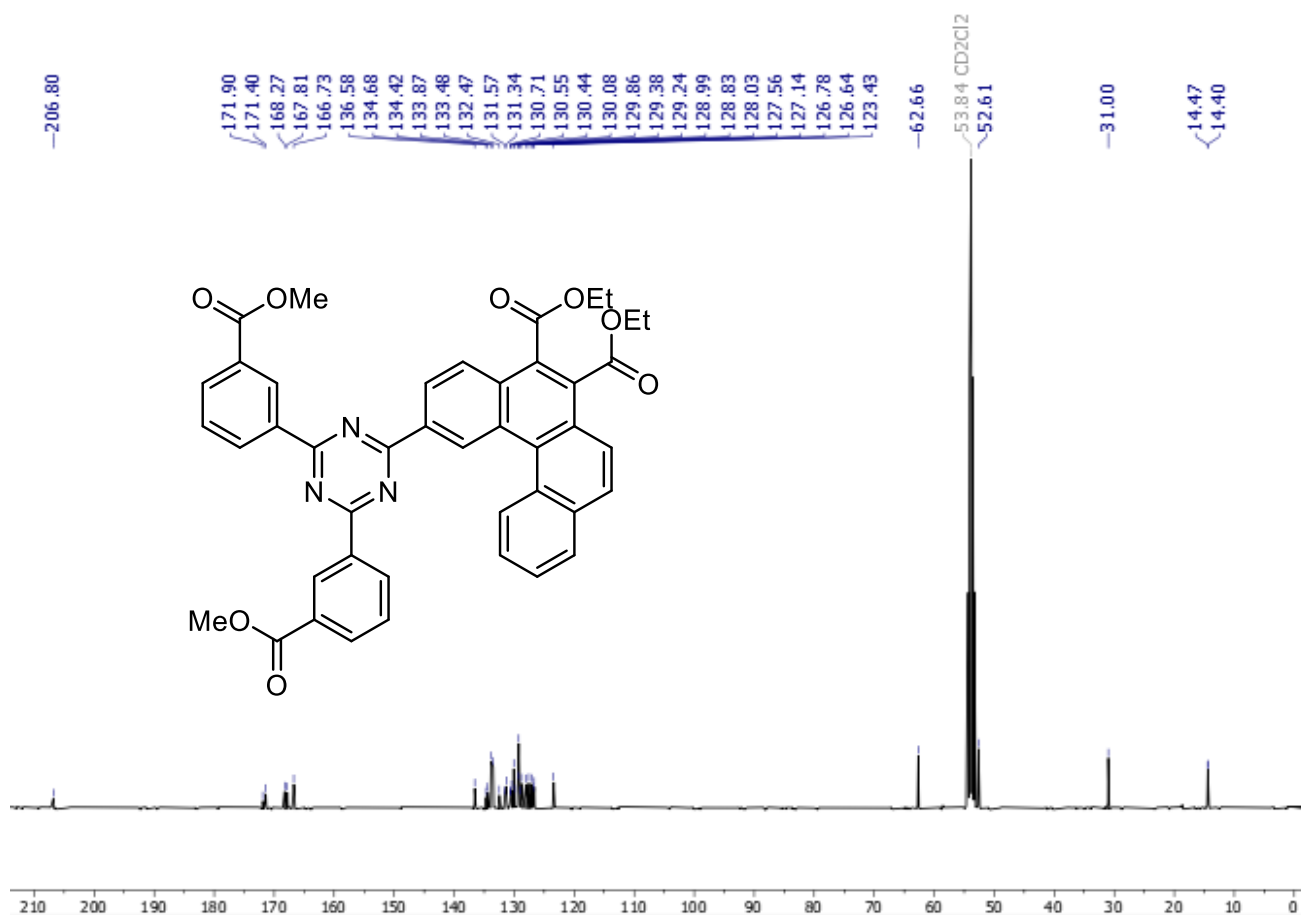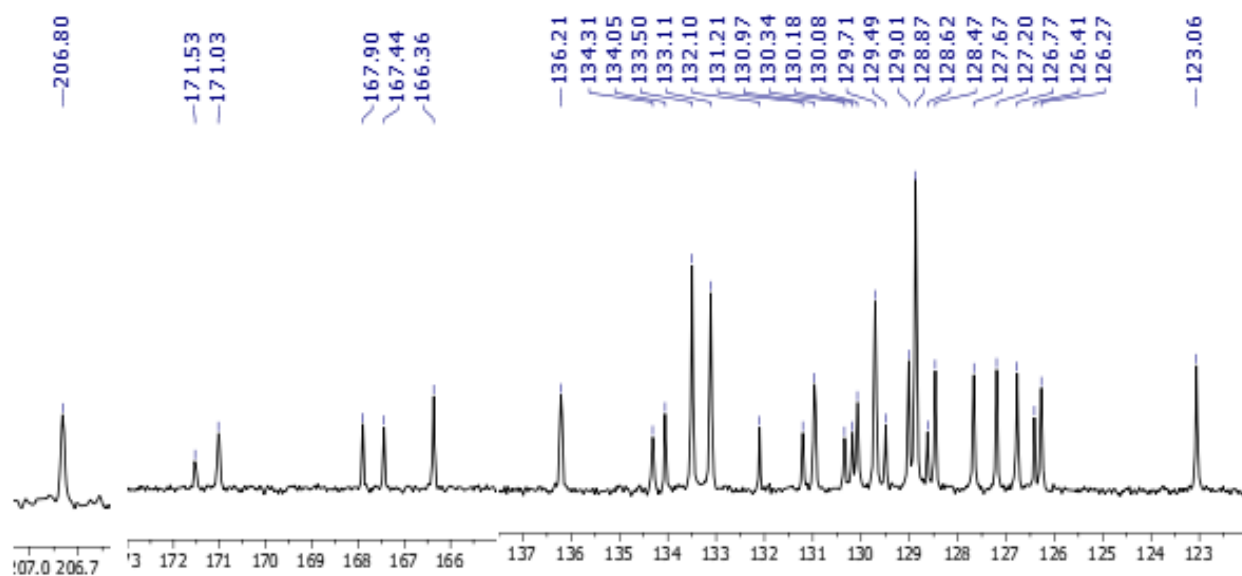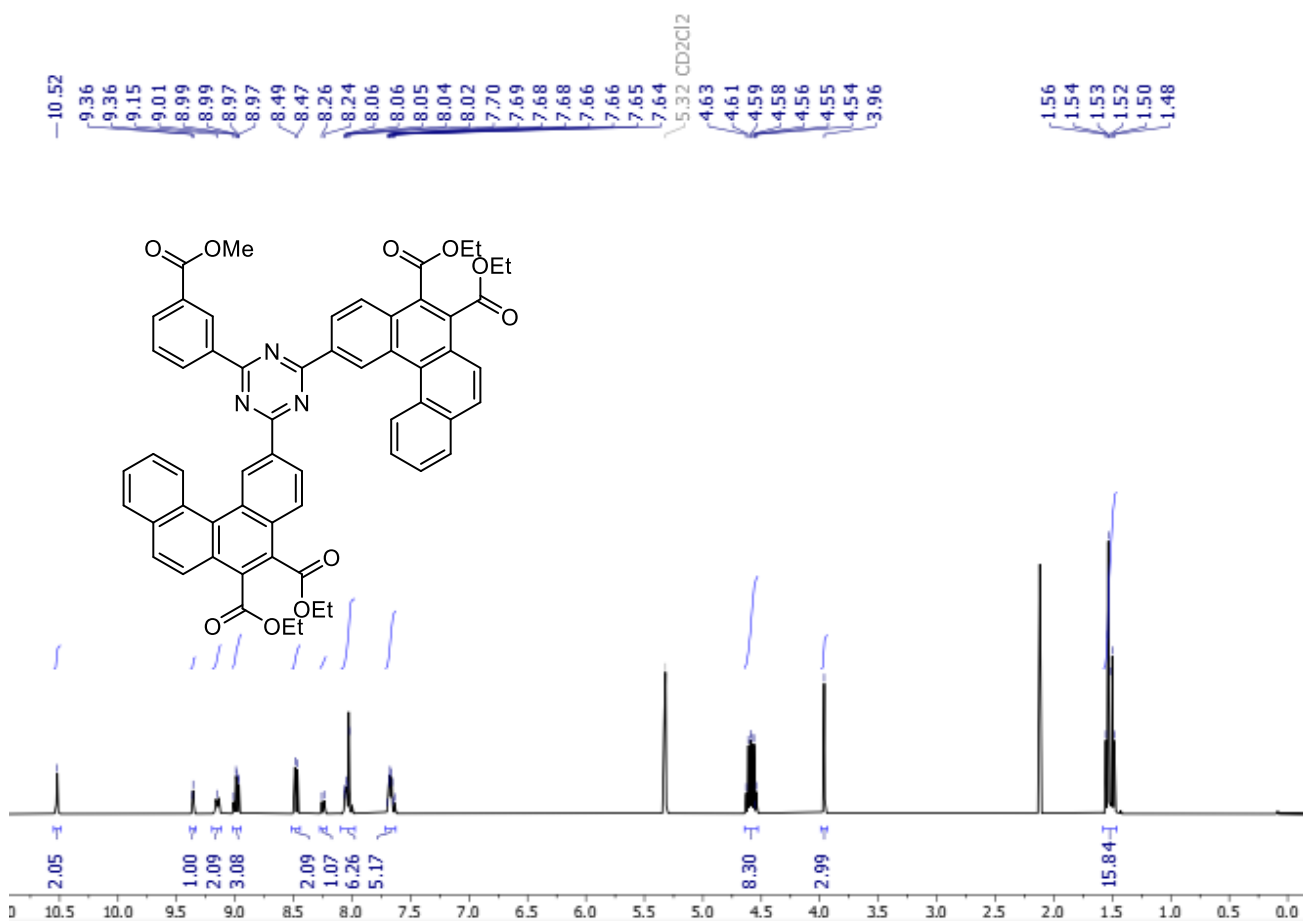Expansion of the aromatic region of the $^{13}$C NMR of compound **F₁Et** in CD₂Cl₂, 100 MHz.

<sup>1</sup>H NMR of compound **F₂Et** in CD₂Cl₂, 400 MHz.



Expansion of the aromatic region of the <sup>1</sup>H NMR of compound **F₂Et** in CD₂Cl₂, 400 MHz.

<sup>13</sup>C NMR of compound **F₂Et** in CD₂Cl₂, 100 MHz.

$^{13}$C NMR of compound **F₂Et** in CD₂Cl₂, 100 MHz.

171.12
170.91
167.89
167.79
166.50
136.06
135.00
133.78
133.12
132.36
131.40
130.92
130.86
130.39
130.00
129.49
129.18
129.02
128.31
127.46
127.37
127.09
127.02
124.23
122.96

62.50
62.44
53.84 CD2Cl2
52.50

31.00

14.46
14.43

200  190  180  170  160  150  140  130  120  110  100  90  80  70  60  50  40  30  20  10  0

Expansion of the aromatic region of the $^{13}$C NMR of compound **F₂Et** in CD₂Cl₂, 100 MHz.

171.12
170.91
167.89
167.79
166.50
135.70
134.64
133.42
132.76
132.00
131.04
130.56
130.49
130.03
129.64
129.13
128.82
128.66
127.95
127.10
127.01
126.73
126.66
123.87
122.60

172  171  170  169  168  167  166    136  135  134  133  132  131  130  129  128  127  126  125  124  123

<sup>1</sup>H NMR of compound **F₂Bu** in CD₂Cl₂, 400 MHz.



Expansion of the aromatic region of the <sup>1</sup>H NMR of compound **F₂Bu** in CD₂Cl₂, 400 MHz.

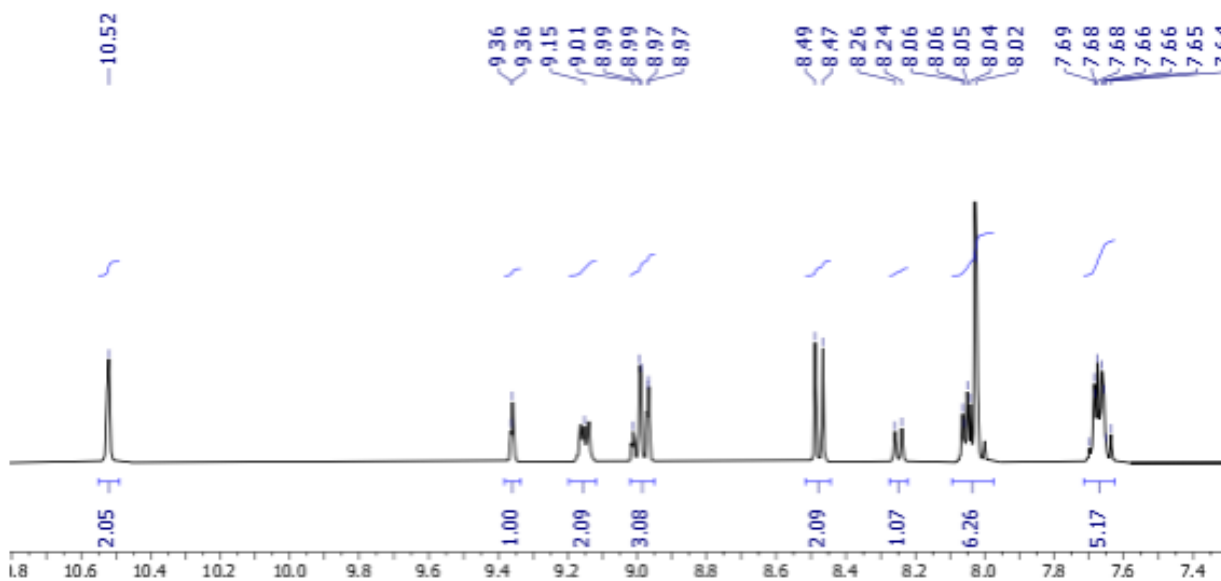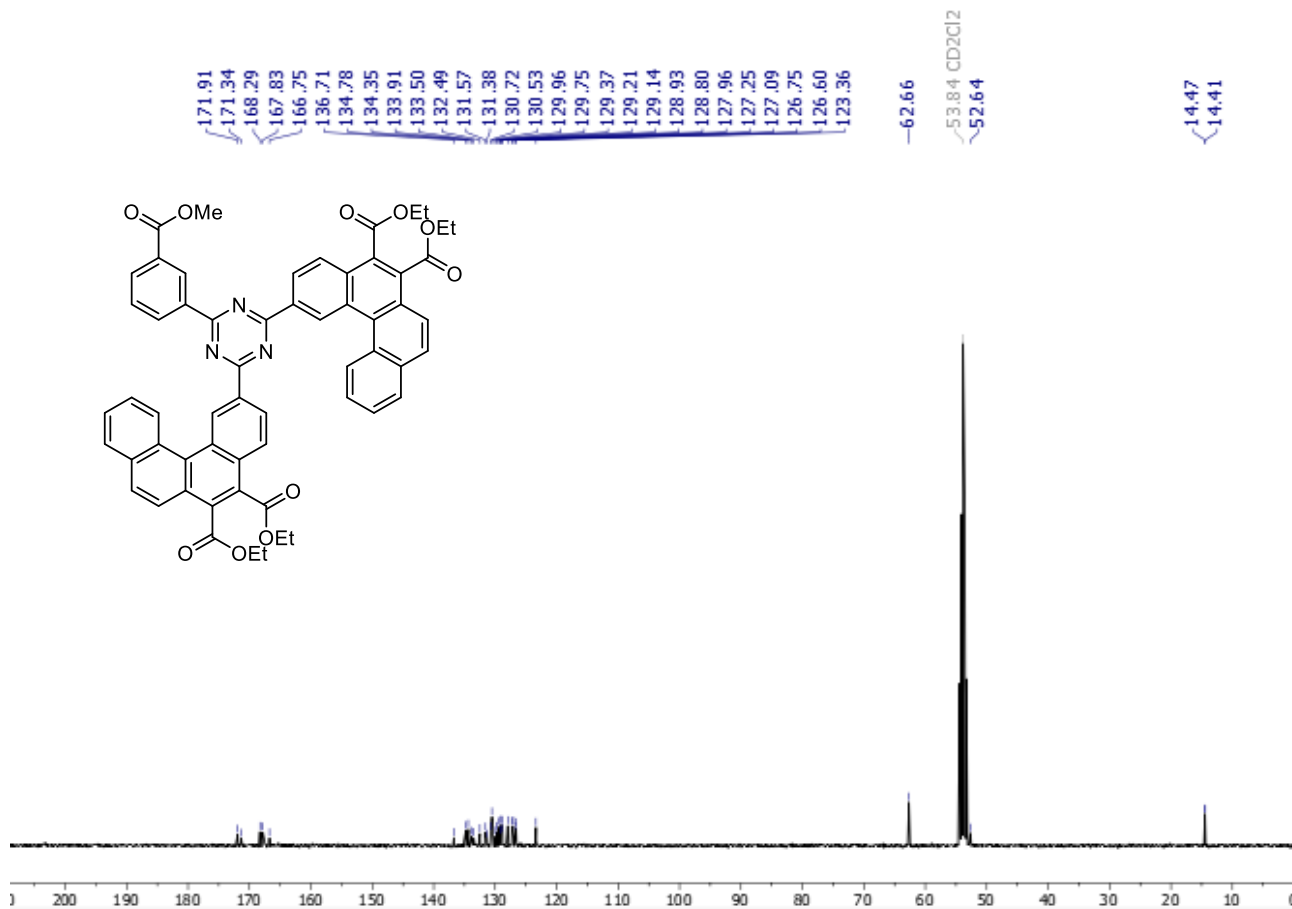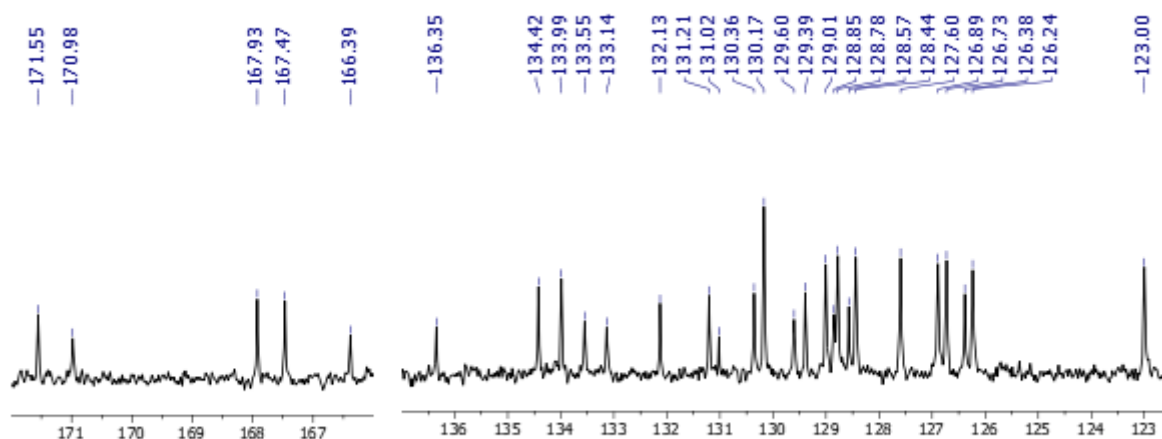$^{13}$C NMR of compound **F₂Bu** in CD₂Cl₂, 100 MHz.



Expansion of the aromatic region of the $^{13}$C NMR of compound **F₂Bu** in CD₂Cl₂, 100 MHz.

<sup>1</sup>H NMR of compound **H₁Et** in CD₂Cl₂, 400 MHz.



Expansion of the aromatic region of the <sup>1</sup>H NMR of compound **H₁Et** in CD₂Cl₂, 400 MHz.

<sup>13</sup>C NMR of compound **H₁Et** in CD₂Cl₂, 100 MHz.



Expansion of the aromatic region of the <sup>13</sup>C NMR of compound **H₁Et** in CD₂Cl₂, 400 MHz.

<sup>1</sup>H NMR of compound **H₂Et** in CD₂Cl₂, 400 MHz.



Expansion of the aromatic region of the <sup>1</sup>H NMR of compound **H₂Et** in CD₂Cl₂, 400 MHz.

<sup>13</sup>C NMR of compound **H₂Et** in CD₂Cl₂, 100 MHz.



Expansion of the aromatic region of the <sup>13</sup>C NMR of compound **H₂Et** in CD₂Cl₂, 100 MHz.
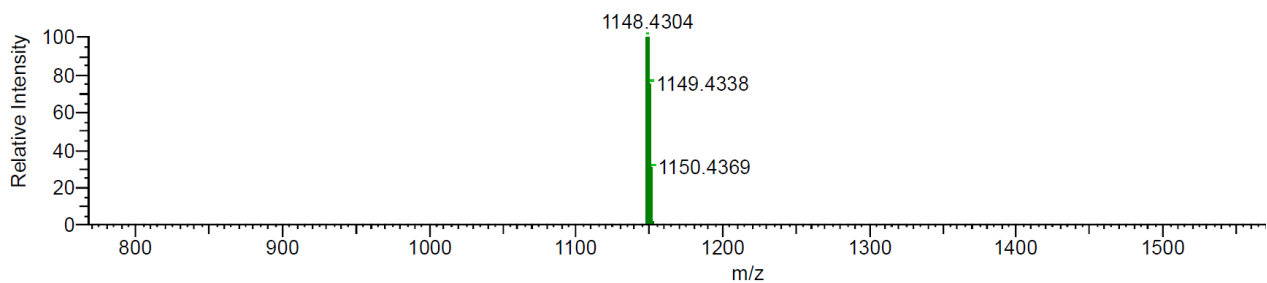
**ESI-HRMS analyses were performed on all final compounds up to a molecular weight of 1300 g/mol:**

**F₃Et:** m/z calcd for $C_{63}H_{51}N_3O_{12}Na$ [M+Na]$^+$: 1064.33650, found 1064.3378 (100% relative intensity).
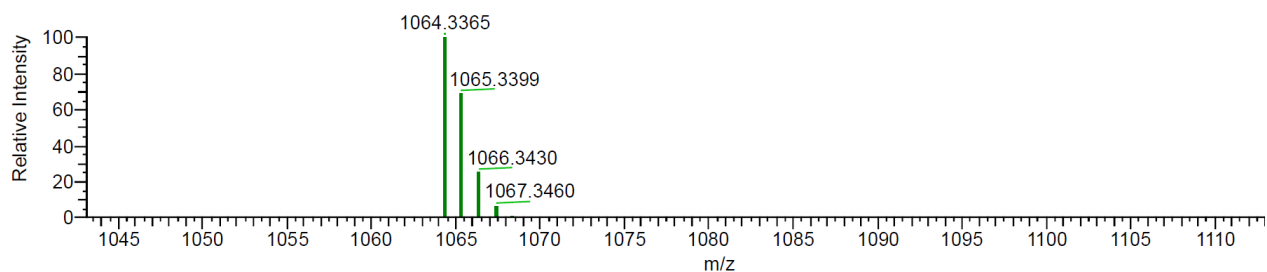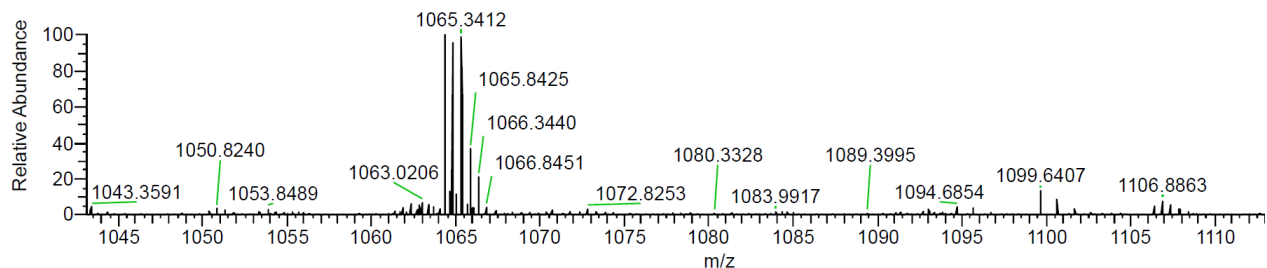


| Peak Mass | Display Formula | Delta [ppm] | Theo. mass |
|---|---|---|---|
| 1064.3378 | $C_{63}H_{51}O_{12}N_3{}^{23}Na$ | 1.21 | 1064.33650 |

**F₃Pr:** m/z calcd for $C_{69}H_{63}N_3O_{12}Na$ [M+Na]$^+$: 1148.43040, found 1148.4310 (65% rel. intens.).
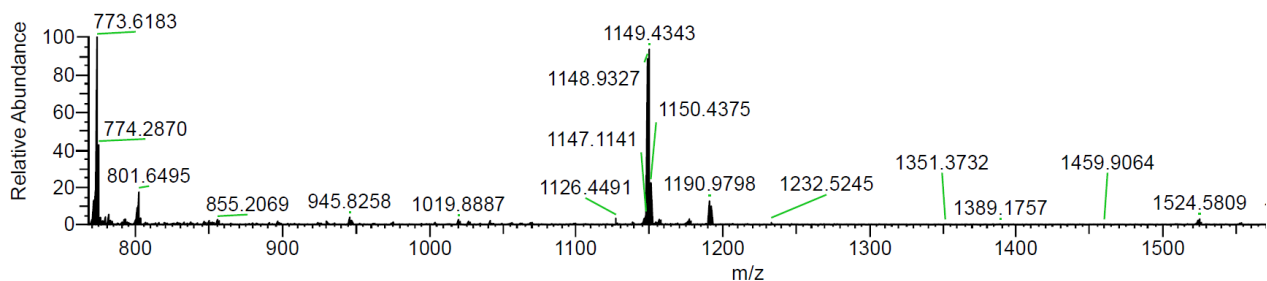


| Peak Mass | Display Formula | Delta [ppm] | Theo. mass |
|---|---|---|---|
| 1148.4310 | $C_{69}H_{63}O_{12}N_3{}^{23}Na$ | 0.49 | 1148.43040 |

**F₃Bu**: m/z calcd for $C_{75}H_{75}N_3O_{12}Na$ [M+Na]⁺: 1232.52430, found 1232.5245 (53% rel. intens.).
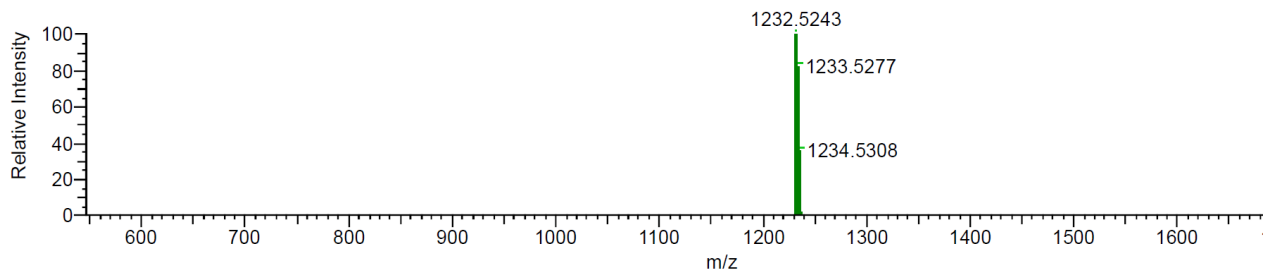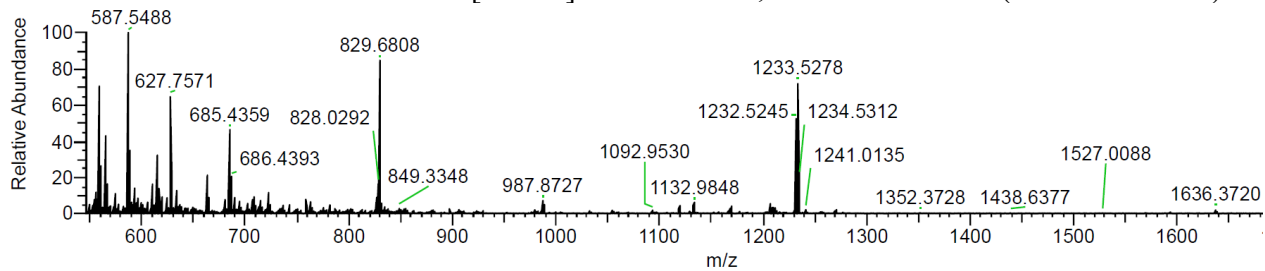


| Peak Mass | Display Formula | Delta [ppm] | Theo. mass |
|---|---|---|---|
| 1232.5245 | $C_{75}H_{75}O_{12}N_3{}^{23}Na$ | 0.17 | 1232.52430 |

**H₃Et**: m/z calcd for $C_{74}H_{64}N_3O_{12}Na$ [M+Na]⁺: 1209.43822, found 1209.4396 (9% rel. intens.).
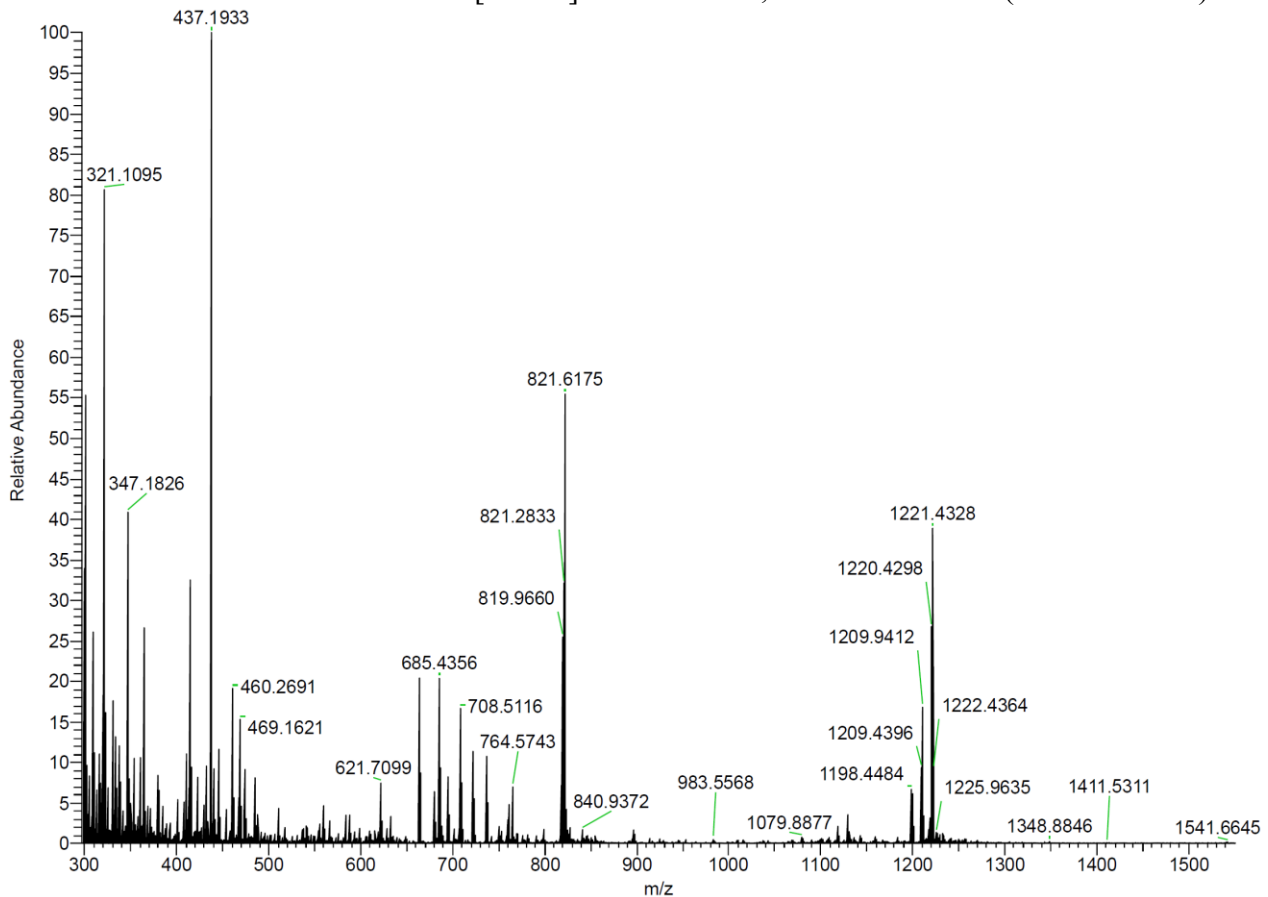
**H<sub>3</sub>Pr:** m/z calcd for $C_{81}H_{69}N_3O_{12}Na$ [M+Na]$^+$: 1298.47735, found 1298.4778 (55% rel. intens.).